



Department
Of
Mechanical
Engineering.

The Influence of Unsteady Wind on the Performance and Aerodynamics of Horizontal Axis Wind Turbines

A Thesis submitted for the degree of Doctor of Philosophy

By

Radwan Muhammad Addaiy Aljuhashy

Registration No.: 140234831

Department of Mechanical Engineering

The University of Sheffield

March 2019

Dedication

To your soul my beloved mum, I just want to say I will never forget you until I join you, where you are now. I am so grateful for what you did for me and I hope to achieve what you wished me to be.

Abstract

This study elucidates the work which has been undertaken in the field of horizontal axis wind turbine (HAWT) aerodynamics and performance. The main aim of the study is to obtain a better understanding of the characteristics of HAWTs operating with unsteady flow conditions. The literature review found that most research on the HAWT has not taken this unsteadiness into account and that will be the general objective of the current study.

The effects of steady and unsteady wind velocity upon the horizontal wind turbine performance have been studied numerically. Using a mesh independent CFD model, the NREL phase VI wind turbine was built utilising Ansys ICEM CFD and then simulated using FLUENT.

Firstly, steady wind simulations at 6 m/s were implemented, with a maximum power coefficient C_p of (0.4245) at the tip speed ratio of 6. Then, this process was repeated to test the performance of the scaled-down wind turbine.

The effect of the sinusoidal oscillating flow on the wind turbine performance was investigated using a user-defined function, or UDF. Initially a (1Hz) wind frequency was chosen to carry out this study. Then, the performance of the wind turbines was investigated in the flow of upstream mean velocity of $\bar{U}=6$ m/s and four different oscillating amplitudes (7%, 15%, 25% and 45%) of the mean upstream wind velocity. Moreover, various additional wind speed frequencies (0.5, 2, 5 and 10Hz) and their effects on the wind turbine's performance and aerodynamics were investigated. Similarly, the small scale wind turbine was also investigated to examine the performance of these sizes of machines.

The various wind speed performance trend was well-matched a previous experimental data trend. The constant wind speed performance trend also showed a good agreement with the QBlade data and CFD data of previous researchers. The results generally showed that the unsteady flow caused the performance to a relative drop compared to steady flow. Moreover, the findings revealed that small amplitudes improved the performance marginally. The small-scale rotor also presented high performance at small amplitudes whereas, high amplitudes could cause negative impact to its performance.

Declaration

Described in this dissertation is work performed in the Department of Mechanical Engineering, the University of Sheffield between October 2014 and September 2018. I hereby declare that no part of this work has been submitted as an exercise for a degree at this or any other university. This thesis is entirely the result of my own work and includes nothing which is the outcome of collaboration, except when stated otherwise. This thesis contains 81 figures and 18 tables and more than 39,000 words.

Signature:

Date: / /

Acknowledgements

I would like to express my massive and special gratitude to my supervisor Dr Robert J Howell who provided me a lot of guidance in academic and personal suggestions for my research. In addition, I strongly appreciate for his support and patience during my PhD study and without his support, I could not be able to reach my goal, so I wish him all the best in his life.

I wish also would thank whole of my family (my dear father, my beloved boy, my wife my brothers and sisters) who strongly stand beside me and regularly encourage me to achieve my research and I hope to be always at their best expectations. Many thanks to my relatives who always contact me and eagerly waiting my Ph.D.

I owe a special debt of gratitude toward my friends (Ahmed A. Al-rubaiy and Basim A. Al-bakri) and my colleagues at the University at the University of Sheffield (Feng Xie and Hao Chen) for their advice and support during the years of my study. Within Dr Howell's group, I am so thankful for Binoe Abuan, who was sitting next to, for his time when we discussed our results and that led to reform my PhD path. Also, many thanks to Dorit Sobotta for her useful and valuable advices.

Last and not least, I would like to pay special thanks to Ministry of Higher Education and Scientific Research (Iraq) for its financial support to complete my studies here in the United Kingdom.

Nomenclature

Symbols

A	Swept area of the wind turbine blades, m^2
A	Amplitude of the fluctuating wind speed.
A_b	Area of the wind turbine blade, m^2
a	Axial induction factor
c	Aerofoil chord length, m
C_L	Lift coefficient
C_D	Drag coefficient
C_L/C_D	Lift to drag coefficient
C_f	Friction coefficient
C_M	Pitching moment coefficient
C_m	Torque coefficient
C_P	Pressure coefficient
C_p	Instantaneous power coefficient
$C_{p_{av}}$	The average one cycle of the unsteady flow power coefficient
D	Drag force, N
D_R	Rotor diameter, m
dr	Strip span, m
dt	Time step size, s
k	Turbulent kinetic energy
k	Reduced frequency
L	Lift force, N

l	Aerofoil span, m
M	Mach number
N	Number of blade
N	Newton, kg m s^{-1}
N_{rev}	Number of rotor rotations
P_B	Extracted power, W
P_w	Available wind power, W
p	Pressure, N/m
p_n	Normalised pressure
r	Radius and radial direction, m
R	Blade tip radius, m
Re	Reynolds number
St	Strouhal Number
s	Second
T	Torque, N.m
T_h	Thrust, N
t	Flow time, s
tn	The normalised flow time
t	Time step size, s
U	Blade velocity, m/s
\bar{U}	Average wind speed, m/s
\acute{u}	Fluctuated wind speed, m/s
V_∞	Mean free stream velocity, m/s

V_R	Relative velocity, m/s
V_t	Instantaneous wind speed, m/s
W	Watts
y^+	Non-dimensional wall distance
$^\circ$	Degree

Greek symbols

α	Angle of attack, degree
β	Pitch angle, degree
∇	Vector of partial derivative operators, denotes the gradient of a vector field
ε	Rate of dissipation of turbulence energy, $m^2 s^{-3}$
f	Frequency of the oscillating wind, Hz
θ	Relative flow angle onto blades, degree
λ	Tip speed ratio
μ	Dynamic viscosity, $N s m^{-2}$
μ_T	Eddy-viscosity, $N s m^{-2}$
ρ	Air density, kg/m^3
τ_w	Shear stress, Pa
ω	Specific dissipation rate, s^{-1}
ω	Rotating blade speed, m/s

ABBRIVATIONS

2D	Two dimensional
3D	Three dimensional
ANSYS	Analysis Systems
AOA	Angle of attack
BEM	Blade Element Momentum theory
CFD	Computational fluid dynamics
FEM	Finite element method
FVM	Finite volume method
HAWT	Horizontal wind turbine
ICEM	Integrated Computer Engineering and Manufacturing
KARI	Korea Aerospace Research Institute
NACA	National Advisory Committee for Aeronautics
NREL	National Renewable Energy Laboratory
NS	Navier–Stokes equations
RANS	Reynolds Averaged Navier–Stokes equation
S-A	Spalart and Allmaras turbulence model
SST	Shear Stress Transport
TSR	Tip Speed Ratio
UDF	User-defined function
URANS	Unsteady Reynolds Averaged Navier–Stokes equation
VAWT	Vertical wind turbine

Table of Contents

Chapter 1: Introduction	1
1.1 Background	2
1.2 Utility of wind energy	2
1.3 Modern machines of wind energy	3
1.4 Winds configuration	6
1.4.1 Unequal solar heating	6
1.4.2 Coriolis Effect	7
1.5 Effect of winds' loads	7
1.6 Objectives and Scope	10
1.6.1 Objectives	10
1.6.2 Scope	11
1.7 General outline of the thesis	11
Chapter 2: Literature Review	12
2.1 Introduction	13
2.2 Aerodynamics of the HAWT	13
2.2.1 Momentum theory	13
2.2.2 Aerodynamics and Reynolds number	14
2.3 The turbine geometry	16
2.3.1 Aerofoil for current turbine wind	16
2.3.2 Blade design for current turbine wind	20
2.4 The effect of rotor size and feature	21
2.4.1 Effect of the rotor size	21
2.4.2 Effect of the rotor feature	23
2.5 Modelling and Numerical Simulation of Wind Turbines	25
2.5.1 Computational fluid dynamics (CFD).....	25
2.5.2 Blade-Element Momentum (BEM) Model.....	33

2.6 Unsteady flow conditions	35
2.6.1 Overview	35
2.6.2 The unsteady wind flow form	36
2.6.3 Wind turbine operating in unsteady flow	37
2.7 Summary of this chapter	40
Chapter 3: Numerical Modelling of NREL Phase VI Rotor	41
3.1 Introduction	42
3.2 Methodology	42
3.2.1 Specification of NREL Phase VI wind turbine	42
3.2.2 Angle of attack along the blade	44
3.2.3 Building the model geometry	45
3.2.4 Generating mesh	47
3.2.5 Reynolds number along the blade	53
3.2.6 Solution Procedure (Fluent Settings)	54
3.3 Steps in creating the model of this study	57
3.4 Summary of this chapter	58
Chapter 4: Computational Fluid Dynamics (CFD) Validation	59
4.1 Introduction	60
4.2 Mesh size case study results	60
4.3 The boundary layer and the turbulence model	61
4.4 Torque of the rotor	63
4.5 Time step size checking	65
4.6 Friction coefficient (C_f) and Pressure coefficient validation	66
4.7 Surface limiting streamlines distribution	70
4.8 Blade element momentum theory (BEM) Validation	75
4.9 Summary and findings of this Chapter	77
Chapter 5: Steady Flow Simulations	78

5.1 Introduction	79
5.2 Validation of the constant wind speed case	79
5.3 Analysis of study wind flow simulations	80
5.3.1 The power trend for the turbine at 75% of the blade	81
5.3.2 The power trend for the turbine at 30% of the blade	81
5.4 The effect of Reynolds number on wind turbine performance	84
5.4.1 The power trend for the turbine at 75% of the small size blade	85
5.4.2 The power trend for the turbine at 30% of the small size blade	85
5.5 Summary of this chapter	88
Chapter 6: Unsteady Flow Simulations	89
6.1 Introduction	90
6.2 Simulation of unsteady flow	90
6.3 Characteristics of unsteady wind flow	94
6.3.1 Reduced frequency (k)	94
6.3.2 Strouhal number (St).....	94
6.3.3 Amplitude of wind speed (\hat{u})	95
6.4 Power performance of the wind turbine with amplitude variations	95
6.4.1 Power curve at $f=1\text{Hz}$ and 7% amplitude	98
6.4.2 Power curve at $f=1\text{Hz}$ and 15% amplitude	102
6.4.3 Power curve at $f=1\text{Hz}$ and 25% amplitude	106
6.4.4 Power curve at $f=1\text{Hz}$ and 45% amplitude	110
6.5 Power performance of the wind turbine at different TSR	114
6.5.1 Power performance of the wind turbine at $\lambda=4$	114
6.5.2 Power performance of the wind turbine at $\lambda=8$	119
6.6 Effects of amplitudes in summary	124
6.7 Power performance of the wind turbine with frequency variations	127
6.7.1 Power curve at $f=0.5\text{Hz}$ and 25% amplitude	130
6.7.2 Power curve at $f=2\text{Hz}$ and 25% amplitude	134

6.7.3 Power curve at $f=5\text{Hz}$ and 25% amplitude	138
6.7.4 Power curve at $f=10\text{Hz}$ and 25% amplitude	142
6.8 Summary of findings	146
6.9 The effect of changes in wind turbine scale in unsteady flow	147
6.10 Summary of this chapter	155
Chapter 7: Conclusions and Recommendations	156
7.1 Introduction	157
7.1 Conclusions	157
7.3 Recommendations and potential plans for future work	160
References	163
Appendices	171
Appendix A	172
Appendix B	173

LIST OF FIGURES

Figure	Page
1.1 The development of HAWTs through time (http://www.irena.org).....	3
1.2 (left) A HAWT's parts (right) wind turbine with ($D_R=40$ m and $P_B = 1$ MW), (Image captured at Wallis Way, Catcliffe, Sheffield).....	5
1.3 Hypothetical atmosphere circulation (left) and the Coriolis Effect (right) (images by Byron Inouye captured from https://manoa.hawaii.edu).....	7
1.4 The aerodynamic loads of HAWTs through time (Erich, 2006).....	9
2.1 Stream line tube around the rotor.....	14
2.2 A cross-section of the S809 aerofoil with forces and velocities distribution.....	15
2.3 A cross section of the S809 aerofoil with its camber line (Butterfield et al., 1990).....	16
2.4 Comparison of S809 with NACA aerofoils for $Re=3$ million (Somers, 1997).....	17
2.5 Aerodynamics coefficients (C_L and C_D) of 2D S809 aerofoil with different Re (Kyoungsoo et al., 2017).....	19
2.6 Boundary layer affected by desirable and adverse pressures (sited in Manwell, 2012).....	19
2.7 The full scale of NREL Phase VI Blade.....	20
2.8 The full scale NREL Phase VI Blade operating at $V_\infty = 8$ m/s with λ (Sobotta, 2015)..	21
2.9 Power coefficient for several scales of NREL wind turbine Cho, et al. (2010) and (2014).....	22
2.10 Effects of solidity on the performance of HAWT (Burton, et al., 2001).....	24

2.11 Validation of NACA 654-421 aerofoil for S-A, k- ϵ and k- ω models at Re = 400k and $\alpha = 0^\circ$, Sobotta, (2015).....	29
2.12 (a) 360° mesh domains configuration, Xie, et al. (2012) and (b) 360° mesh domains configuration, Sobotta, (2015).....	31
2.13 Blade element scheme, Manwell et al., (2009).....	33
2.14 Characteristics of air flow incident on a wind turbine (Jonkman, 2003).....	36
2.15 A wind speed measured with time (Erich, 2006).....	37
2.16 Effect of steady and unsteady flow on the performance of VAWT (Danao et al., 2013).....	38
2.17 How performance of HAWT is affected by the wind frequencies at designed $\lambda = 5$, Toshimitsu, et al., (2012).....	40
3.1 The NREL blade.....	43
3.2 The trailing edge mesh, sharp edge (left), modified edge (right) and 75% cut plane....	44
3.3 Angle of attack along the blade for various wind speeds.....	44
3.4 The full geometry of blades and the disk	45
3.5 The full geometry of the current study.....	46
3.6 The cut plan mesh at 75% along the blade and wall mesh above the blade (top) and leading and trailing edges (bottom).....	50
3.7 The full structured mesh of the blade and the surrounding disk	51
3.8 Display of pre-mesh quality in ICEM-CFD.....	51
3.9 The full unstructured mesh of the wind tunnel.....	52
3.10 Cut plane mesh of the wind tunnel at the hollow disk.....	53
4.1 Comparison of different numbers of grids at various wind speeds.....	61

4.2 Comparison of three different turbulence models at various wind speeds.....	62
4.3 Torque coefficient against wind speeds.....	64
4.4 Comparison of torque coefficient of two different turbulence models at wind speed =15m/s.....	64
4.5 Torque coefficient history at $\lambda = 5.4$ for three-time step sizes.....	65
4.6 Skin friction coefficient (suction side) at wind speed 7m/s (a), 10m/s (b), 13m/s (c) and 15m/s (d).....	68
4.7 Comparison of pressure coefficient at wind speed 7, 10, 13 and 15 m/s.....	70
4.8 Current CFD data obtained at 75% of the blade span.....	72
4.9 Limiting streamlines distribution on pressure side (left) and suction side (right) of the blade at various λ	75
4.10 Full scale NREL wind turbine in QBlade.....	76
4.11 Validation of full scale NREL wind turbine in QBlade at various wind speeds.....	76
5.1 Validation of full scale NREL wind turbine in QBlade at constant wind speed.....	80
5.2 Performance trend of the full scale NREL wind turbine with constant wind speed (a) at 75% and (b) at 30% of blade.....	83
5.3 The small and large-scale turbines operating at $V_{\infty} = 6\text{m/s}$	84
5.4 Performance trend of the scaled-down NREL wind turbine with constant wind speed (a) at 75% and (b) at 30% of blade.....	87
6.1 Performance of the unsteady flow at 1 Hz frequency and its amplitude 25% at the full complete rotation of the turbine.....	91
6.2 Performance of the turbine for one cycle of unsteady wind velocity.....	92

6.3 Comparison between the available wind power and the extracted power by the turbine at unsteady wind flow.....	93
6.4 Effect of steady and unsteady flow on the performance of the HAWT at various amplitude.....	97
6.5 The plot and streamline performance curve of the full scale NREL wind turbine at 1Hz and 7% amplitude of unsteady wind speed (a) at 75% and (b) at 30% of the blade.....	100
6.6 The pressure distribution around the rotor blade at different locations around the hysteresis loop of the full-scale NREL wind turbine. Conditions are 1Hz and 7% amplitude of unsteady wind speed at 75% of the blade.....	101
6.7 The plot and streamline performance curve of the full scale NREL wind turbine at 1Hz and 15% amplitude of unsteady wind speed (a) at 75% and (b) at 30% of the blade.....	104
6.8 The pressure distribution around the rotor blade at different locations around the hysteresis loop of the full-scale NREL wind turbine. Conditions are 1Hz and 15% amplitude of unsteady wind speed at 75% of the blade.....	105
6.9 The plot and streamline performance curve of the full scale NREL wind turbine at 1Hz and 25% amplitude of unsteady wind speed (a) at 75% and (b) at 30% of the blade.....	108
6.10 The pressure distribution around the rotor blade at different locations around the hysteresis loop of the full-scale NREL wind turbine. Conditions are 1Hz and 25% amplitude of unsteady wind speed at 75% of the blade.....	109

6.11	The plot and streamline performance curve of the full-scale NREL wind turbine at 1Hz and 45% amplitude of unsteady wind speed (a) at 75% and (b) at 30% of the blade.....	112
6.12	The pressure distribution around the rotor blade at different locations around the hysteresis loop of the full-scale NREL wind turbine. Conditions are 1Hz and 45% amplitude of unsteady wind speed at 75% (of the blade.....	113
6.13	Effect of unsteady flow on the performance of the HAWT at 45% amplitude and $\lambda=4$	115
6.14	The plot and streamline performance curve of the full-scale NREL wind turbine at 1Hz and 45% amplitude of unsteady wind speed at $\lambda= 4$ (a) at 75% and (b) at 30% of the blade.....	117
6.15	The pressure distribution around the rotor blade at different locations around the hysteresis loop of the full-scale NREL wind turbine at $\lambda=4$. Conditions are 1Hz and 25% amplitude of unsteady wind speed at 75% of the blade.....	118
6.16	Effect of unsteady flow on the performance of the HAWT at 25% amplitude and $\lambda=8$	120
6.17	The plot and streamline performance curve of the full scale NREL wind turbine at 1Hz and 25% amplitude of unsteady wind speed at $\lambda= 8$ (a) at 75% and (b) at 30% of the blade.....	122
6.18	The pressure distribution around the rotor blade at different locations around the hysteresis loop of the full-scale NREL wind turbine at $\lambda=8$. Conditions are 1Hz and 25% amplitude of unsteady wind speed at 75% of the blade.....	123
6.19	Effect of various amplitudes at 1Hz unsteady wind flow on the wind turbine.....	125

6.20	The hysteresis curve for the three unsteady cases at $\lambda=4, 6,$ and 8	126
6.21	Effect of steady and unsteady flow on the performance of the HAWT at 25% amplitude and various wind speed frequencies.....	129
6.22	The plot and streamline performance curve of the full scale NREL wind turbine at 0.5Hz and 25% amplitude of unsteady wind speed at $\lambda= 6$ (a) at 75% and (b) at 30% of the blade.....	132
6.23	The pressure distribution of the hysteresis loop of the full-scale NREL wind turbine at 0.5Hz and 25% amplitude unsteady wind speed at 75% of the blade.....	133
6.24	The plot and streamline performance curve of the full-scale NREL wind turbine at 2Hz and 25% amplitude of unsteady wind speed at $\lambda= 6$ (a) at 75% and (b) at 30% of the blade.....	136
6.25	The pressure distribution of the hysteresis loop of the full-scale NREL wind turbine at 2Hz and 25% amplitude unsteady wind speed at 75% of the blade.....	137
6.26	The plot and streamline performance curve of the full scale NREL wind turbine at 5Hz and 25% amplitude of unsteady wind speed at $\lambda= 6$ (a) at 75% and (b) at 30% of the blade.....	140
6.27	The pressure distribution of the hysteresis loop of the full scale NREL wind turbine at 5Hz and 25% amplitude unsteady wind speed at 75% of the blade.....	141
6.28	The plot and streamline performance curve of the full scale NREL wind turbine at 10Hz and 25% amplitude of unsteady wind speed at $\lambda= 6$ (a) at 75% and (b) at 30% of the blade.....	144
6.29	The pressure distribution of the hysteresis loop of the full scale NREL wind turbine at 10Hz and 25% amplitude unsteady wind speed at 75% of the blade.....	145

6.30 Operation of the small NREL rotor at $V_{\infty} = 6\text{m/s}$ against various wind speed amplitudes.....	148
6.31 Effect of steady and unsteady flow on the performance of the HAWT at 25% amplitude and 17.2Hz wind speed-scaled down NREL.....	149
6.32 The plot and streamline performance curve of the scale-down NREL wind turbine at 17.2Hz and 25% amplitude of unsteady wind speed at $\lambda = 6$ (a) at 75% and (b) at 30% of the blade.....	151
6.33 The pressure distribution of the hysteresis loop of the scaled-down NREL wind turbine at 17.2Hz and 25% amplitude unsteady wind speed at 75% of the blade....	152
6.34 The hysteresis curve for the small-size rotor at three unsteady cases at $\lambda = 4, 6,$ and 8 and at 25% amplitude 17.2Hz.....	153
6.35 Performance of the small rotor at three tip speed ratios at 17.2Hz and 25% amplitude	154

LIST OF TABLES

Table	Page
3.1 NREL Phase VI blade fundamental form.....	43
3.2 The lift to drag coefficient of 2D S809 aerofoil against angles of attack.....	48
3.3 Reynolds number values.....	54
4.1 Numbers of iterations per time.....	66
6.1 The area under the pressure curve at each point on the loop ($f=1\text{Hz}$ and $A=7\%$).....	102
6.2 The area under the pressure curve at each point on the loop ($f=1\text{Hz}$ and $A=15\%$)....	106
6.3 The area under the pressure curve at each point on the loop ($f=1\text{Hz}$ and $A=25\%$)....	110
6.4 The area under the pressure curve at each point on the loop ($f=1\text{Hz}$ and $A=45\%$)....	114
6.5 The area under the pressure curve at each point on the loop ($f=1\text{Hz}$, $A=25\%$ and $\lambda=4$).....	119
6.6 The area under the pressure curve at each point on the loop ($f=1\text{Hz}$, $A=25\%$ and $\lambda=8$).....	124
6.7 Performance at various amplitudes.....	124
6.8 The area under the pressure curve at each point on the loop ($f=0.5\text{Hz}$ and $A=25\%$)..	134
6.9 The area under the pressure curve at each point on the loop ($f=2\text{Hz}$ and $A=25\%$)....	138
6.10 The area under the pressure curve at each point on the loop ($f=5\text{Hz}$ and $A=25\%$)...141	
6.11 The area under the pressure curve at each point on the loop ($f=10\text{Hz}$ and $A=25\%$).145	
6.12 Performance at 25% amplitudes and various frequencies.....	146
6.13 The area under the pressure curve at each point on the loop ($f=17.2\text{Hz}$ and $A=25\%$).....	153
6.14 Coefficient of torque from three different tip speed ratio.....	155

CHAPTER 1

Introduction

1.1 Background

Since the dawn of history, wind energy has been used to propel sailboats and grind wheat. Later, with the development of modern lifestyle, water pumps were powered through the use of wind energy, the first well-known design being the vertical axis direction system used in ancient China and the Middle East. The drag-type rotor mill machine, one of the first documented forms of wind mill, was commonly set inside a building to force the incoming wind hit the rotor, (Wind energy, 2018). The current way of using kinetic power from the wind is to generate electricity.

1.2 Utility of wind energy

For human being development to continue, it is essential to use sources of renewable energy that do not warm the planet. Several hundred years of coal and natural gas consumption have led to depletion these traditional sources and contributed to global warming through the release of Carbon. Fortunately, using renewable sources like solar, wind, hydro, and underground energies for large-scale generation of power might be sufficient to support or even completely replace the traditional sources. However, these renewable sources have lacked support from society because they could damage the usual views of nature and sometimes installation and maintenance can be expensive. Furthermore, in the case of mechanical devices like wind turbines, there could be a lack of incoming wind in some areas. However, the cost of wind is dropping all the time and it may now be cheaper than many other forms of power.

Recently, the use of wind energy has expanded across most of the world due to the oil market fluctuates a lot that changed the global energy picture. Additionally, in the current century, small wind plants, which are suitable for a few homes, and giants scale inshore and offshore wind farms that could be linked to global or local electricity transmission systems, have been established.

The dramatic increase in the cost of oil since the 1970s has led to the development of the alternative energy sources such as wind turbines (Rosa, 2009). The cost of oil has had to be taken into account by many industrialised countries which are dependent on fossil fuels for producing much of their energy. Burning fossil fuels leads to the emission into the atmosphere of greenhouse gases such as carbon dioxide, methane and ozone, which cause

harm to the environment by raising the Earth's temperature through trapping heat (Zulfequar Ahmad Khan, 2017). Hence renewable energy like wind energy can play a valuable role in replacing fossil fuels (International Renewable Energy Agency, 2018). There has, over the last three decades, been significant growth in the capacity of wind power generation as a source of alternative energy. This growth has not just been seen in numbers of installations but also in their size. For example, in the 1990s, average capacities were 100kW with heights of about 100 m and rotor blades' diameters around 50 m to 2MW capacity, whilst nowadays the height can be around 200m (Ryi, J. et al., 2014), as shown in Figure 1.1.

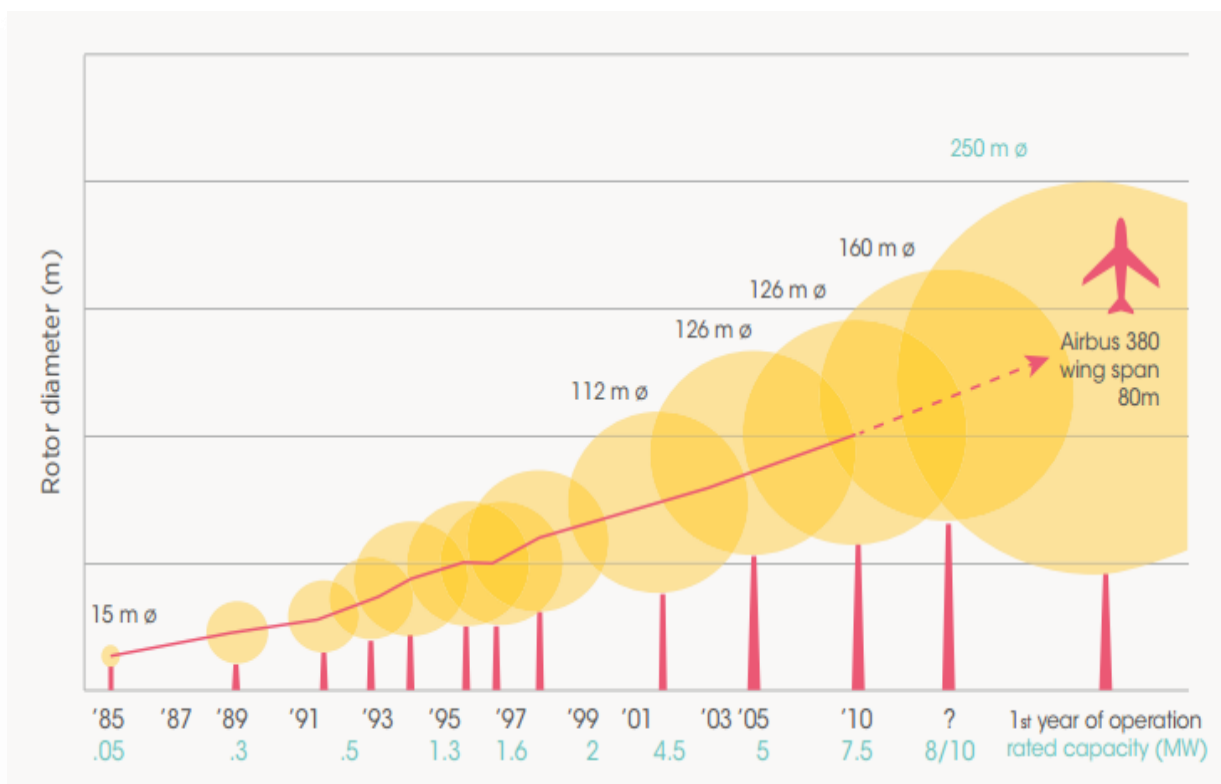


Figure 1.1: The development of HAWTs through time (image is captured from <http://www.irena.org>).

1.3 Modern wind energy machines

Generally, wind machines are divided into lift-type and drag-type machines. The lift-type machines such as power generation wind turbines achieve high coefficient of performance at lower tip speed ratios with low blades speed. On the other hand, the drag-type machines

such as water pump for irrigation achieve low coefficient of performance at lower tip speed ratios with low blades speed. In addition, unlike the drag machines, the blade of lift-type machines can have different aerofoil shapes (Eboibi, 2013).

Lift-type machines can be divided into two types according to the way in which the blades are mounted on the rotating shaft: a horizontal-axis wind turbine (HAWT), where the shaft is in the horizontal view, and a vertical-axis wind turbine (VAWT), where it is in the vertical view (Hansen, 2008). HAWTs can also be classified into upwind or downwind configuration, depending on the orientation of the rotors (wind speed direction).

The horizontal wind turbine is made up in general of the following main parts: rotor (blades and hub), nacelle (gears, ball bearings and generator), and tower with base and control system, as shown briefly in Figure 1.2.

The energy of wind is harnessed to cause the blades to rotate and generate power. The profile of the blades has been improved to extract the maximum kinetic energy from wind; hence, the modern rotor has various aerofoil sections along the blade's span (Han, 2011). Meanwhile, the blades, with symmetrical or asymmetrical aerofoils, are twisted and tapered from their root to the tips with length can reach to several tens of meters, making their manufacture and transportation complex and costly (Eboibi, 2013). In addition, large size wind turbines have a significant mechanism which is employed to control the stall, known as pitch control.

The rotating blades turn the nacelle, which contains the gearbox that connects the high-speed shaft to the low-speed rotor shaft, working as a speed converter. Then, the increased speed drives a generator or generators to produce power. Although gearboxes are heavy and occupy a space, they are still required in modern generators, in particular with high-speed rotating shaft. Hence, because of the high load and fluctuating winds, the design of these parts should be given special consideration. The nacelle has a mechanism called a yaw control that is used to control the rotor blades direction and to provide braking where necessary.

The support tower is built of various materials (for example concrete, steel or truss tube) depending on the size and location of the wind turbine. To avoid the failure, the height of the tower is normally at least 1 time greater than the full diameter of the rotor (Manwell et al., 2009). Due to the atmospheric boundary layer profile, the high the tower,

the higher the mean wind speed and so energy yield of the turbine. The atmospheric boundary layer can be defined as a region when the wind flow interacts with the surface of the earth and could reach to approximately 0.5-1km. The velocity gradient can be formed by that interaction starts from zero velocity at the surface to 0.99 of the free stream velocity which is called the boundary layer thickness. (Gilooly S. and Taylor-Power G., 2016)

With regard to the wind turbine control system, it typically contains electrical equipment such as sensors, actuators, and intelligence equipment. These parts are necessary to enhance the power generation further maximise the life of the rotor and the wind turbine in general.

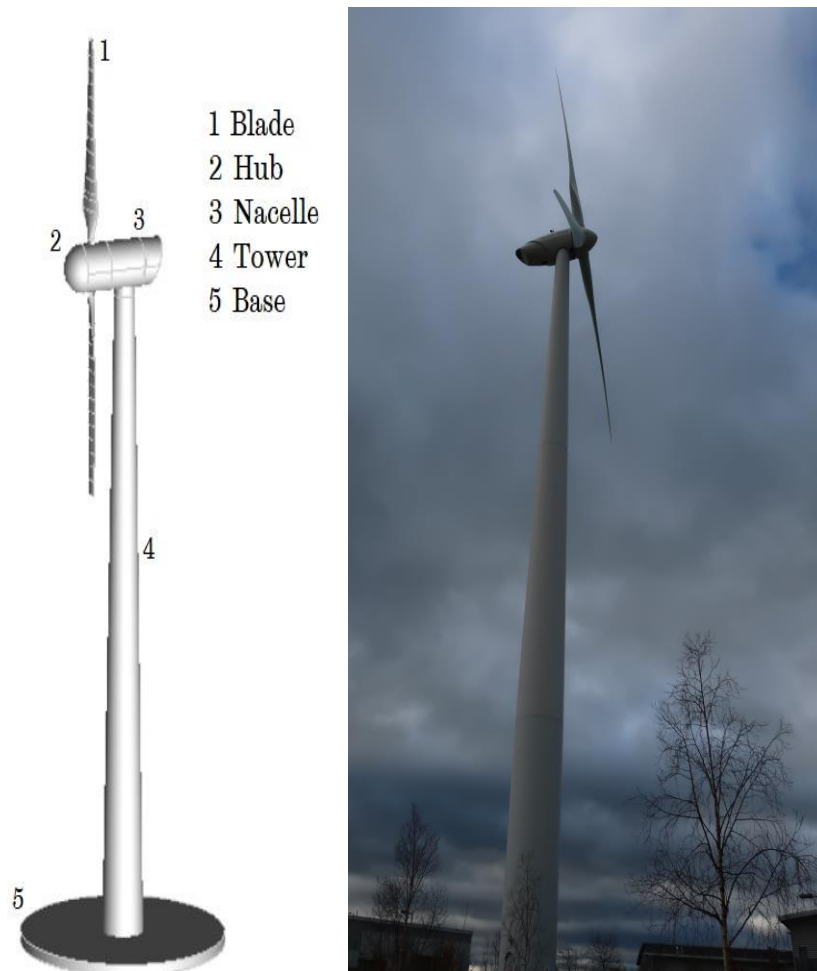


Figure 1.2: (left) A HAWT's parts (right) wind turbine with ($D_R=40$ m and $P_B = 1$ MW), (Image captured at Wallis Way, Catcliffe, Sheffield).

HAWT's have many advantages compared to vertical axis wind turbines (VAWT's), for instance, the profile of the blade can be optimized aerodynamically to enhance the lift force (Erich, 2006). This can be achieved flexibly by pitching the blades in high winds. Moreover, the long tower enables the HAWT to access high wind speeds, whereas this is not possible with the VAWT because the tower is too short. Since VAWTs are more complex aerodynamically and mechanically, they have been used less frequently.

According to Han (2011), before the invention of computers the design of HAWTs was primarily depending on theoretical and experimental studies. Development of computer models has allowed new techniques to be used to analyse the aerodynamics and performance of wind turbines. In fact, there is no single unique design for the horizontal wind turbine. The design most commonly used around the world is the three-bladed turbine, but sometimes the two-bladed shape can perform more efficiently, and it has the benefit of a lightweight structural design. Turbine designers have faced many issues ranging from the intended power capacity, location, behaviour of wind speed, noise from the wind machine and the size.

Regarding problems with aerodynamics, these can be analysed through computational fluid dynamics techniques employing numerical solutions. The blade structure, furthermore, can be investigated by using finite element methods (FEM) (Zhu et al., 2016). FEM is a numerical method for solving partial differential equations numerically. Concisely, the purpose of seeking numerical solutions is to save money by saving time.

1.4 Winds configuration

1.4.1 Unequal solar heating

Air temperature and air pressure are the two main concepts to be taken into account regarding generation of wind. Since solar energy warms the atmosphere in an uneven manner, when the heated air rises, the motion of the air molecules could be very slow, mild or very quick, depending on the location. Any changes in air pressure over the indicated area push high air pressure toward an area of low pressure. It is this difference in pressure that leads in general to differences in climate; for instance, the tropics are hot all the time, while it is extremely cold in the poles (Wind energy, 2018).

1.4.2 Coriolis Effect

The Coriolis Effect, Figure 1.3, is an apparent force that generates air masses that move in curves. The Coriolis Effect deflects the horizontal winds, causing them to blow toward the Poles so that winds circulate in opposing directions at the northeast and the southeast of the Earth, as shown in Figure 1.3.

To sum up, wind occurs due to differences in the atmospheric pressure which resulted in air moving from a higher to a lower pressure area. Moreover, warm air, which weighs less than cold air, then moves up and replaces the heavy cold air, thereby making the wind blow.

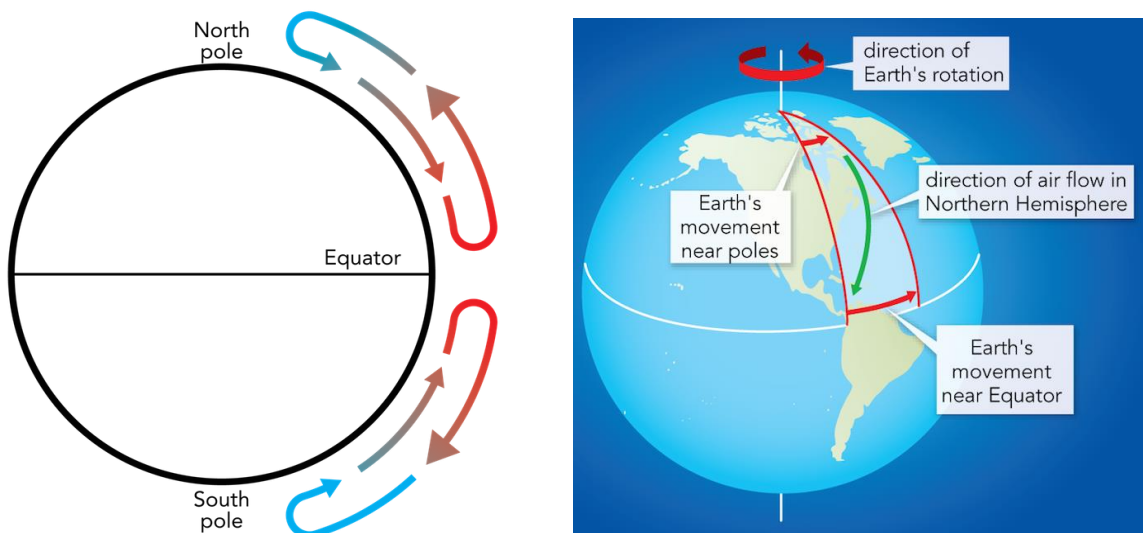


Figure 1.3: Hypothetical atmosphere circulation (left) and the Coriolis Effect (right) (images by Byron Inouye captured from <https://manoa.hawaii.edu>).

1.5 Effect of wind loads

The nature of wind inevitably has an effect on wind turbines, in particular, the sudden, brief fluctuations (gust). This could lead to low performance or even shorten the life of the machine when it experiences high loads and stresses. As the density of air in general is low, the swept surface of the blade should be large enough to capture a large stream tube and then convert it into a useful energy form. Therefore, the structure of wind turbines must be well-designed to counteract these undesired variables.

Loads on the rotor mainly derive from the aerodynamics, inertial and gravitational forces, and the effect of aerodynamic loads on the rotor of horizontal wind turbines is highlighted in the current study.

Steady flow in wind is clearly the ideal case and this is not available in the real environment. The aerodynamic load in this case is relatively uniform along the blade, whereas at high wind speeds, a separation in flow will occur near the root of the blade and causes considerable changes in the aerodynamic loads, as shown in Figure 1.4. (Erich, 2006).

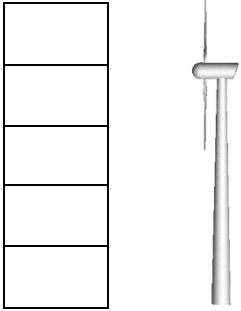
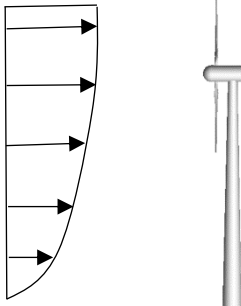
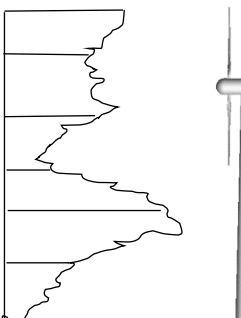
		Aerodynamic forces	
Steady loads		Average wind speed(steady)	
	Cyclic loads	Shear wind	
	Non-cyclic loads	Turbulence in wind	

Figure 1.4: The aerodynamic loads of HAWTs through time (Erich, 2006).

Turbulent flow or unsteadiness, on the other hand, is the form of wind that occurs in the real surrounding atmosphere. Mathematically, the wind speed can generally be considered as mean wind speed, which is used normally with steady flow calculations, or high and low deviations from the mean wind speed, with along the average value are used to calculate the

unsteady flow. Because of the shape complexity of the unsteady flow, an idealised form, for instance, like rectangular, trapezoidal and sin or cos can be employed to simplify this complication and thereby allow interpretation of oscillations with large or small amplitudes (Erich, 2006).

1.6 Objectives and Scope

1.6.1 Objectives

Wind turbines are exposed to many complicated phenomena in the environment, such as changes in wind direction, turbulence, and the effects of the ground boundary layer (Leishman, 2002). With the majority of research focusing on the steady flow cases, there is a lack of research analysis of wind flows in reality (Wekesa et al., 2015). However, the effects of unsteady wind flow on horizontal rotor wind turbines (HAWT) have recently become a significant topic as manufacturers try to make their products more competitive.

The main objective of this thesis is to fill some of the gaps in the literature through studying the influence of the unsteadiness of the wind on aerodynamics and assessing performance of a full scale HAWT numerically. There has been only a little research conducted on the effects of unsteadiness on the horizontal wind turbine. The computational fluid dynamics CFD data reference turbine used in this study is Tadamas and Zangeneh, (2011), while the experimental data for some scales of National Renewable Energy Laboratory (NREL) wind turbines in particular the full scale (10.058m) of NREL phase VI turbine geometry, are derived from Mo and Lee (2012). For numerical solution, ANSYS ICEM 16.1 meshing commercial software and FLUENT program are employed to understand the physics of the boundary conditions and aerodynamics of the wind turbine. The following procedures will be applied in constructing the CFD model for comparison with the experimental data:

- Conducting an acceptable CFD validation which can be performed by comparing the CFD results with the NREL Phase VI wind turbine experimental results and the blade element method Blade Element Momentum method (BEM) which can be derived from QBlade tool findings.

-
-
- Both structured and unstructured mesh will be used to simulate this study, structured grid for the blade and unstructured mesh for the outer domain.
 - Developing and achieving a mesh independent study using different numbers of grids and different turbulence models.
 - Investigating the three well-known turbulence models (k- ω SST, Spalart -Allmaras and k- ϵ) in order to indicate which model can capture highly the specified conditions in the cases of steady and unsteady flow conditions.

1.6.2 Scope

To the best of the author's knowledge, no research has been conducted to consider the effect of unsteady flow conditions with different adequate frequencies of wind speed fluctuations on performance and aerodynamics of the horizontal wind turbine, numerically or in the lab. Therefore, in this thesis, the effect of steady and unsteady wind velocity upon the horizontal wind turbine's performance will be studied numerically. The main key points of this work are:

- Plot the performance curve at each tip speed ratio employing an average wind speed at 6m/s.
- Study the effect of sinusoidal oscillating flow on the wind turbine's performance.
- A 1 Hz wind frequency will initially be assessed and then this will be halved and then doubled to investigate the influence of various frequencies on the performance.
- Investigate the performance of the wind turbine in the flow of upstream mean velocity of $\bar{U}=6$ m/s and various oscillating amplitudes (7%, 25% and 45%) of the mean upstream wind velocity.
- Study the influence of Reynolds number on performance of the wind turbine in the flow of upstream mean velocity of $\bar{U}=6$ m/s and also various oscillating amplitudes (7%, 25% and 45%) of the mean upstream wind velocity.

1.7 General outline of the thesis

A short summary description of each chapter in the thesis is provided in the following paragraphs:

Chapter 1: provides an introduction to the historical development of wind energy and wind machine as well as their potential as an alternative energy source and clarifies the scope of this study.

Chapter 2: this literature review presents ideas from many recent studies on horizontal wind turbines. Numerical solutions Ansys FLUENT and unsteady wind flow are particularly highlighted and analysed. First, some principles of aerodynamics of horizontal wind turbines are explained and then discussion moves to the physics and design of these machines. CFD validation and QBlade software, representing the blade element method, are discussed in details to define the area of the current study and, finally, displaying its motivation.

Chapter 3: the full NREL phase VI wind turbine blade feature is built according to the coordinates mentioned in many previous works.

Chapter 4: presents in full the CFD validation of the NREL phase VI wind turbine, which is built in chapter three, based on widely available NREL/NASA experimental work.

Chapter 5: reveals the findings for the CFD validation of the NREL phase VI wind turbine with QBlade results at constant wind speeds and steady flow conditions. The performance curve of wind turbine at average wind speed is also highlighted in the chapter, as well as the performance of the scale-down rotor.

Chapter 6: investigates numerically and analyses the effects of unsteady flow on the full and small size NREL phase VI wind turbines, in accordance with the main aim of the thesis. Different amplitudes and frequencies are presented in and compared to the trend of the performance at average wind speed which was obtained in chapter four.

Chapter 7: presents the conclusions of the thesis and provides recommendations based on this study.

CHAPTER 2

Literature Review

2.1 Introduction

Characteristics of the unsteady wind such as flow direction, non-uniformity in time and space, turbulence have become important topics of study. In eastern countries like Japan, for example, wind is more unsteady than western countries (Toshimitsu, K. et al, 2012). Although the performance of a vertical axis wind turbine with fluctuating wind flow has been studied by Danao et al., (2013), most studies, whether numerical and experimental, have been conducted on the assumption of steadiness of flow. Many research projects have been conducted on the assumption of steadiness of flow, however, few have simulated environment conditions in the unsteady winds in the urban field.

Several recently published studies have given an impression of the effects of steady and unsteady flow on wind turbines by using experimental laboratory work and numerical solutions. This review will highlight most of these studies, with the focus on how the fluctuating flow affects HAWTs. The following sections have been divided into numerous sub-sections in order to cover all fundamental details; first, the aerodynamics of HAWTs will be considered, then the geometry of the NREL selected for this study, followed by the effect of unsteady wind flow on both HAWTs and VAWTs, and finally, numerical studies relating to NREL wind turbines will be reviewed.

2.2 Aerodynamics of the HAWT

This section describes the distribution of velocities and forces on the rotor of the HAWT. These characteristics play a significant role in production power from the rotor.

2.2.1 Momentum theory

To analyse the power from a wind turbine in the simplest terms, a stream tube boundary can be assumed around the rotor, as shown in Figure 2.1. The force of wind on the turbine, which is thrust T_h , is equal to the opposite side of the net force (Manwell, 2012):

$$T_h = (\rho AV^2)_1 - (\rho AV^2)_2 \quad \text{Equation 2-1}$$

Bernoulli's equation can be applied for both upstream and downstream of the disc rotor when a fluid, which in this case is air, is not shifting any energy to other entity such as a rotor:

$$p + \frac{1}{2} \rho V^2 = \text{Constant} \quad \text{Equation 2-2}$$

By assuming no pressure difference and that the velocity is still the same on both sides of the rotor, $p_1 = p_4$ and $V_2 = V_3$.

The axial induction, a , can be defined as the fractional factor of the decrease in wind velocity; therefore, the coefficient of performance of wind rotor, C_p , can be represented by both:

$$P = 0.5 \rho A (1 - a)^2 V^3 \quad \text{Equation 2-3}$$

$$C_p = (\text{Rotor power/power in wind}) = \frac{P_B}{P_W} = \frac{NT\omega}{\frac{1}{2}V^3\rho A} \quad \text{Equation 2-4}$$

where N is the number of blades of the wind machine. T generated torque by the rotor, and A is the area of the swept area of the rotating blades. Betz's limit represents the maximum power that can be harnessed from wind turbines. It states that no turbine can extract more than (0.593) of the kinetic energy in the wind flow.

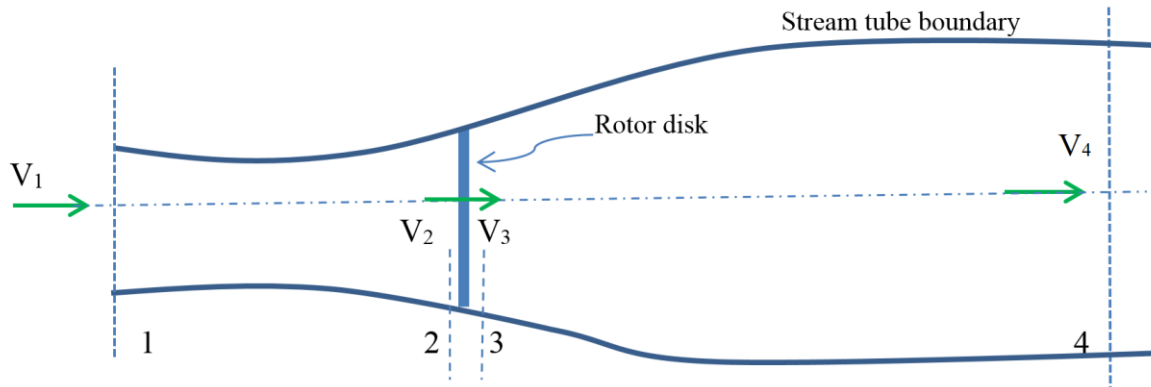


Figure 2.1: Stream line tube around the rotor.

2.2.2 Aerodynamics and Reynolds number

Forces are distributed over the aerofoil surface because of the air flow passing over it. The velocity of flow over the upper surface of the aerofoil, which is called suction side, increases due to the curvature of a blade. However, on the lower surface, which is called pressure side, the flow passes slowly then the pressure is higher than in the suction side. Therefore, as a result of this difference in pressure, lift and drag forces and a pitching moment are produced (Manwell, 2012):

$$CL = \frac{L}{0.5 A_b \rho V^2} = \frac{\text{Lift force}}{\text{Dynamic force}} \quad \text{Equation 2-5}$$

Equation (2-5) represents the lift coefficient in two dimensions, while the drag force is:

$$CD = \frac{D}{0.5 A_b \rho V_\infty^2} = \frac{\text{Drag force}}{\text{Dynamic force}} \quad \text{Equation 2-6}$$

The same applies for the moment:

$$CM = \frac{T}{0.5 A_b \rho V_\infty^2 c} = \frac{\text{Moment of force}}{\text{Dynamic moment}} \quad \text{Equation 2-7}$$

There is also a dimensionless coefficient that is significant for the design and analysis of wind turbines:

$$CP = \frac{p - p_\infty}{0.5 \rho V_\infty^2} = \frac{\text{Static pressure}}{\text{Dynamic pressure}} \quad \text{Equation 2-8}$$

The Reynolds number, Re , is considered the most non-dimensional considerable parameter to describe fluid flow behaviours:

$$Re = \frac{V_\infty c \rho}{\mu} = \frac{\text{Inertial force}}{\text{Viscous force}} \quad \text{Equation 2-9}$$

The income velocity V_∞ with its magnitude and direction and also the blade geometry(c) produce the Reynolds number and the angle of attack (α). The angle of attack is the angle between the chord line of the blade and the vector line representing the relative wind velocity between the wind turbine and the atmosphere. Moreover, the relative velocity relies on both the incoming wind speed, V_∞ , and the rotational blade velocity, U .

$$V_R^2 = V_\infty^2 + U^2 \quad \text{Equation 2-10}$$

Figure 2.2 below shows the aerodynamics characteristics of the S809 aerofoil in more details:

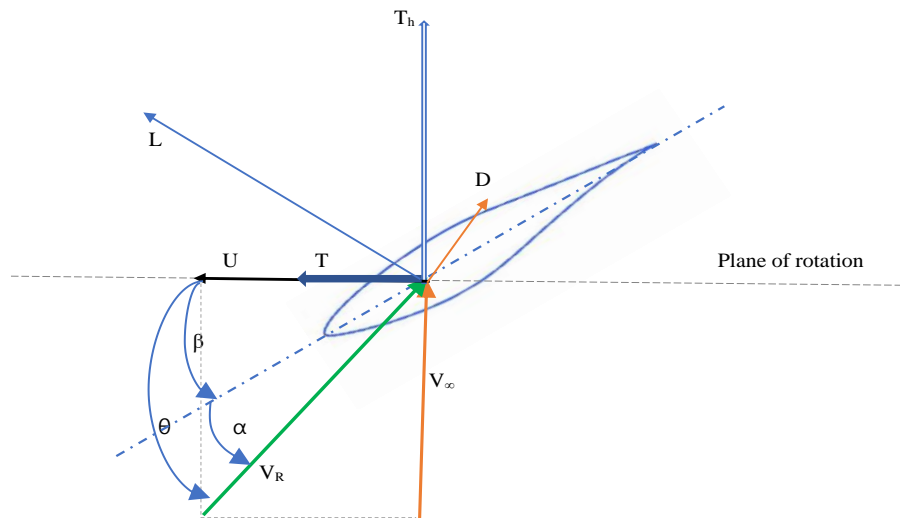


Figure 2.2: A cross-section of the S809 aerofoil with forces and velocities distribution.

2.3 The turbine geometry

2.3.1 Aerofoil for current wind turbine

The coordinates of the S809 aerofoil have been used by many of researchers, for example, (Butterfield et al., 1990). Generally, this aerofoil consists of a maximum thickness reaching 21% at roughly 40% along the chord length and it has been designed for wind turbines applications. (<http://wind.nrel.gov/airfoils/>).

As can be seen clearly below in Figure 2.3, the camber line of S809 fluctuated twice around the chord line; one at roughly at 20% chord and the other beyond 60% up to the leading edge, while the negative position extends from 20 to 50% of chord's length.

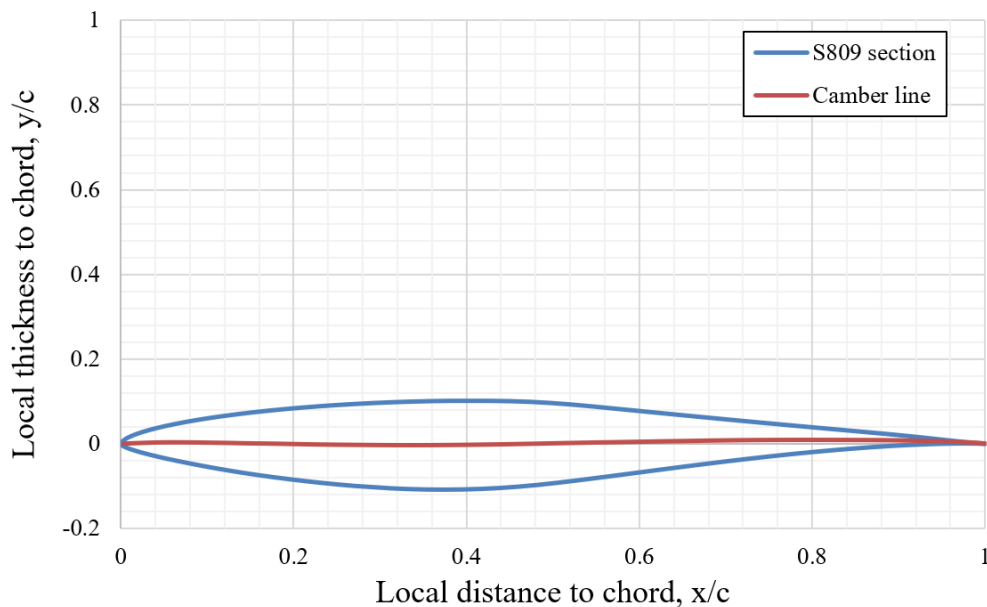


Figure 2.3: A cross section of the S809 aerofoil with its camber line (Butterfield et al., 1990).

Somers (1997) compared the moderate 21% thickness aerofoil of the S809 family with both NACA 4421 and 23021 aerofoils, as presented in the curves in Figure 2.4. The results illustrated that the S809 aerofoil achieves important objectives such as restrained maximum lift coefficient and low drag coefficient in comparison to the chosen NACA group. Therefore, eventually this aerofoil could confidently be used to build a full wind turbine. In addition, Douvi and Margaris (2012) confirmed that the S809 aerofoil revealed higher lift coefficients than that of NACA0012 at various angles of attack and at two high Reynolds numbers.

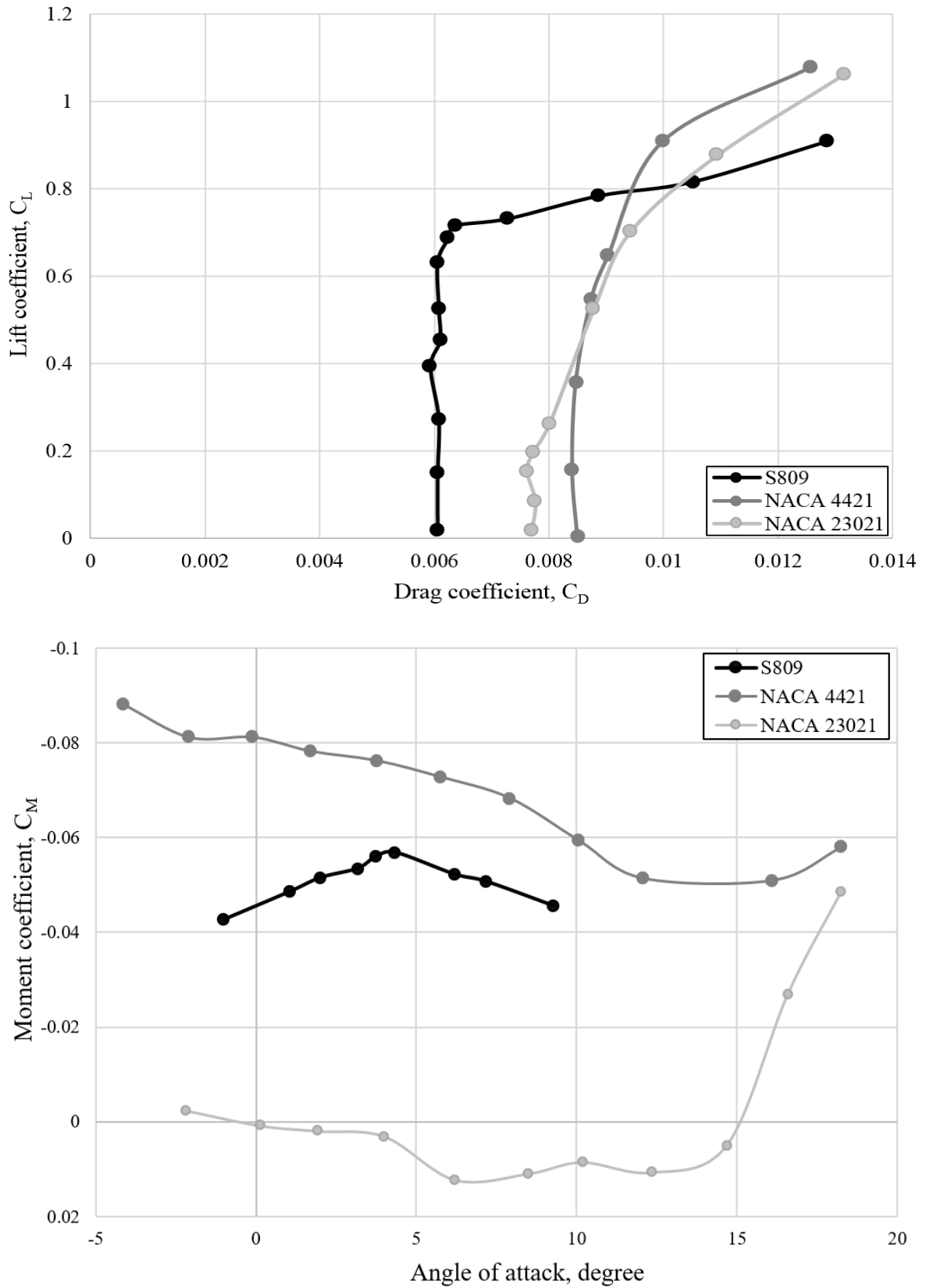


Figure 2.4: Comparison of S809 with NACA aerofoils for Re=3 million (Somers, 1997).

The Figure 2.5 below shows that the behaviour of the lift and drag forces curves of the S809 aerofoil does not vary considerably with four different high Reynolds numbers. It can be seen that the lift coefficients increase linearly from -6° to 7° AOA which represents a fully attached region. Then, they go up until a point called the separation point is reached which is about 15° . The range between 7° to 15° AOA is called pre-stall or transition region. The angle of attack 15° is called stall point at which stalling occurs. C_L values then decrease from their maximum point at 15° to the lowest value at 20° AOA. This region is well-known as the dynamic stall region. The dynamic stall can be defined as fluctuating in the angle of attack when the blade subject to unsteady wind flow conditions. (Johnson and Gharali, 2012 and Leishmann, 2006). Beyond this point, the flow above the aerofoil is fully separated from the suction side of the aerofoil and causes the deep stall region (Kyoungsoo et al., 2017). In addition, C_L and C_D values increase highly together due to more surface area of the blade will face the incoming wind flow by increasing the angle of attack.

The separation often occurs when the flow detaches from the surface of the aerofoil, leading to a low velocity region and then rapid increase in drag and stall of the flow, as illustrated in Figure 2.6. Both increasing and decreasing pressure have influence on the region of flow next to the aerofoil surface, which is known as the boundary layer. The boundary layer is a very thin layer of fluid in contact with the surface of the blade where the velocity has a value zero at the surface to the free stream value away from that surface. The pressure gradient could be favourable in the flow way along the surface, whereas a negative pressure gradient is unfavourable, and with assistance of the friction of the surface the viscid flow might reverse the direction, causing separation and then the stall. The lift to drag ratio with the angle of attack is known as the lift to drag coefficient C_L/C_D . Hence, when the angle of attack increases, the lift to drag ratio increases and then decreases with decrease in the lift force. The maximum lift to drag ratio is called the optimal lift to drag coefficient. Furthermore, with increasing of wind speed, maximum lift to drag ratio also increases due to increase in Reynolds number leads to increase in lift coefficient.

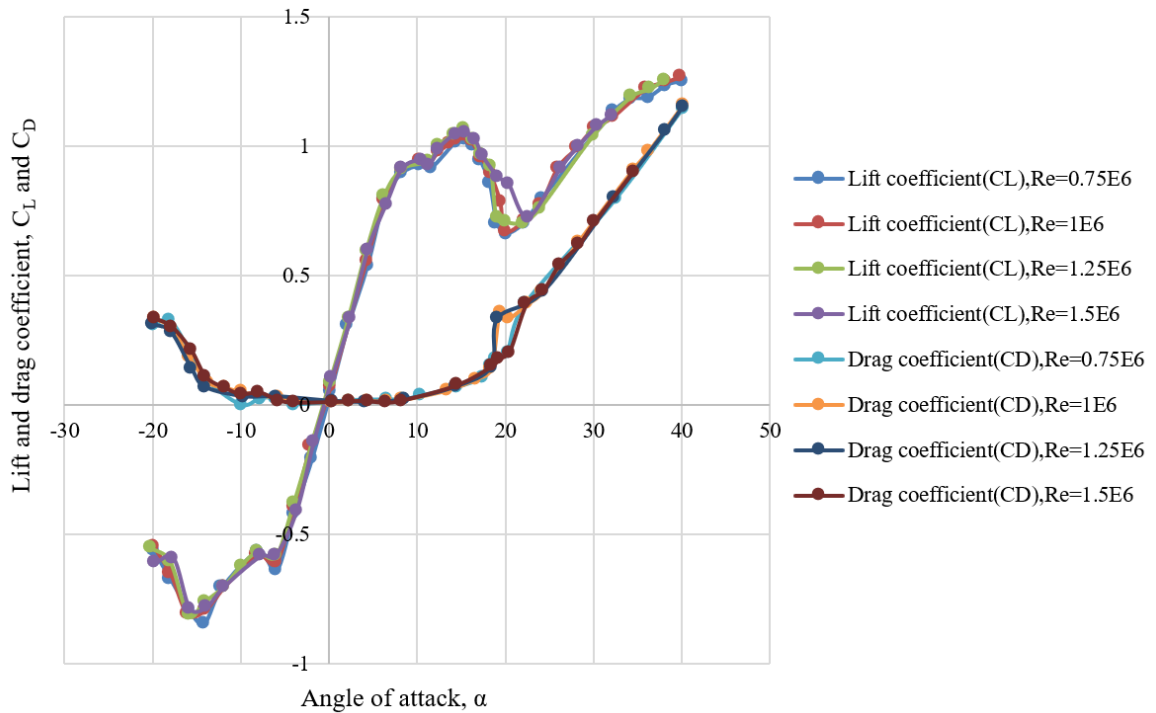


Figure 2.5: Aerodynamics coefficients (C_L and C_D) of 2D S809 aerofoil with different Re (Kyoungsoo et al., 2017).

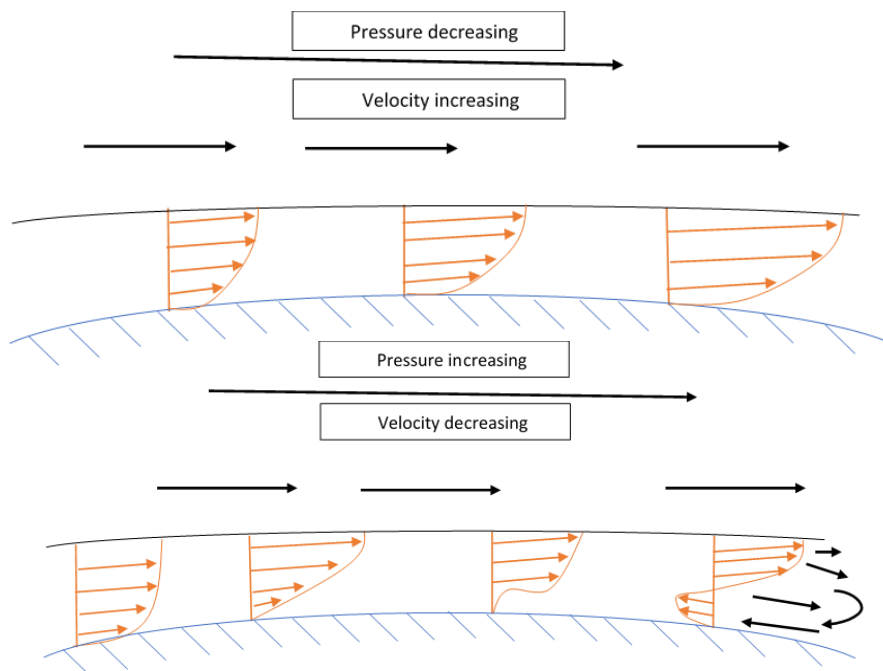


Figure 2.6: Boundary layer affected by desirable and adverse pressures (sited in Manwell, 2012).

2.3.2 Blade design for current wind turbine

Even though the flow around a wind turbine is of greater complexity than that around a 2D aerofoil, the performance of both is critically dependent on the tip speed ratio and the angle of attack between the aerofoil and the incoming wind. The tip speed ratio (TSR) is of vital importance in the design of wind turbine machines. The importance lies in the fact that if the rotor of the wind turbine spins too slowly or too quickly, the wind will pass between the rotor blades or utterly stagnate respectively. Hence, modern wind turbines are generally designed with optimal tip speed ratios to extract as much power out of the wind as possible. The tip speed ratio is calculated by dividing the speed of the tips of the rotor by the speed of the incoming wind. Furthermore, this ratio depends on the number of blades in the wind turbine rotor. This is because the fewer the number of blades, the faster the wind turbine rotor needs to spin to harness maximum power from the wind.

$$\lambda = \frac{\omega R}{V_{\infty}} \quad \text{Equation 2-11}$$

The blade root is exposed to low relative velocity at high angle of attack, whereas at the tip, the relative velocity is high with low attack angle, which stimulates creation of high lift and low drag.

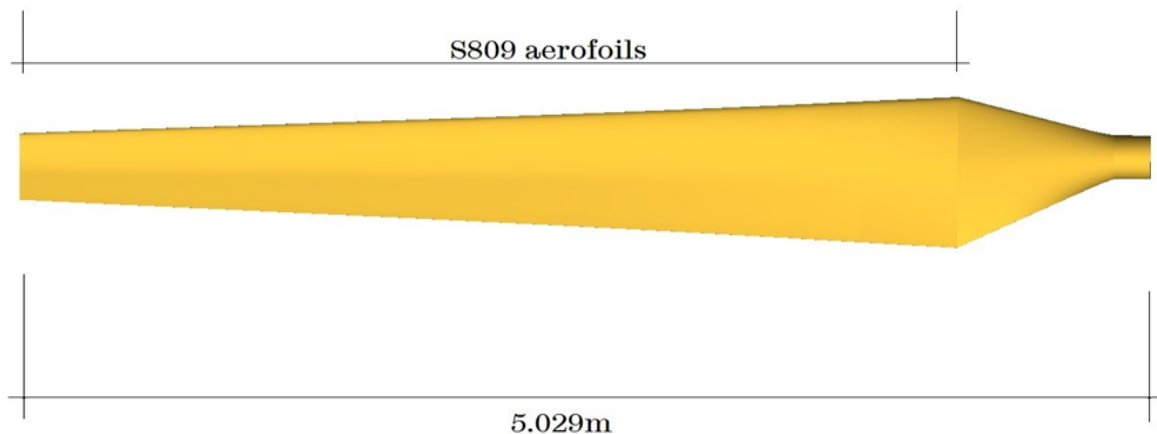


Figure 2.7: The full scale of NREL Phase VI Blade.

In spite of the chord distribution and radius of the NREL Phase VI turbine being linear, the radial distribution of Re is non-linear. This is as a result of the non-linear twist distribution of the NREL Phase VI blade in addition to the non-linearly change of the angle between V_R and V_{∞} (Sobotta, 2015). The Figure 2.8 below illustrates the geometric Re

along the blade r/R with variation of λ . It can be seen that Re increases proportionally with λ along the blade. Furthermore, Re is affected by V_∞ when λ is constant according to equations (9) and (10).

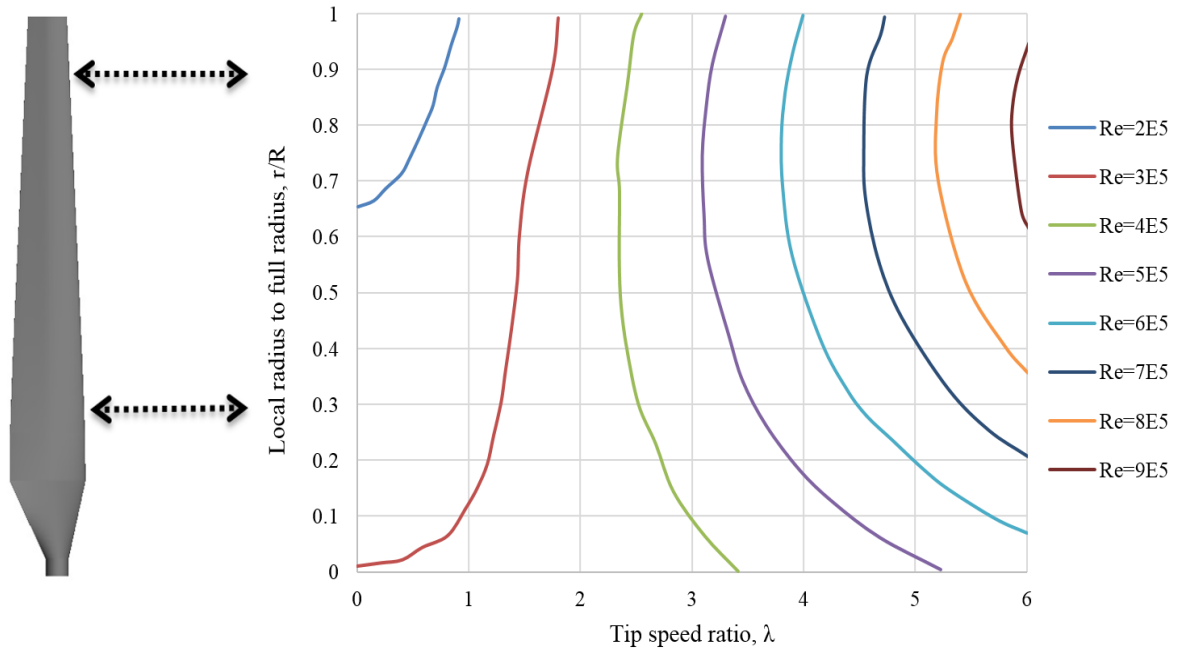


Figure 2.8: The full scale NREL Phase VI Blade operating at $V_\infty = 8\text{m/s}$ with λ (Sobotta, 2015).

2.4 Effects of rotor size and shape

2.4.1 Effect of the rotor size

Sobotta (2015) has analysed numerically three NREL Phase VI wind turbines scales using an identical un-pitched angle. The torque and static pressure around the blade were measured for a full-scale machine in the NREL laboratory (Hand et al., 2001).

The full-scale machine has a rotor of 10.058 m diameter and two blades. At the root, the blade has a circular section which extends from the hub between $0.101 < r / R < 0.176$ and twisted S809 aerofoils along the blade with a maximum thickness of 21%. The full scale of this structure with a pitch angle of 0° will be used as the reference turbine in this study, see Figure 2.7. The scaled down NREL Phase VI turbine blades will be used to investigate torque and aerodynamics in the test section, of height 1.2m and width 1.2m, in a wind tunnel at the University of Sheffield. Relatively, the influence of blockage might be

maintained at a low level when the wind turbine is scaled down. Meanwhile, Cho, et al. (2010) described work the Korea Aerospace Research Institute (KARI) to measure, at lower than 0.1% turbulence intensity, the torque of the 12% two blades scale rotor and compared with that of the 100% scale which means full scale of NREL phase VI turbine. The results showed that there was a similarity in power slope for the NREL turbine 100%, 20% and 12 % scales, Figure 2.9.

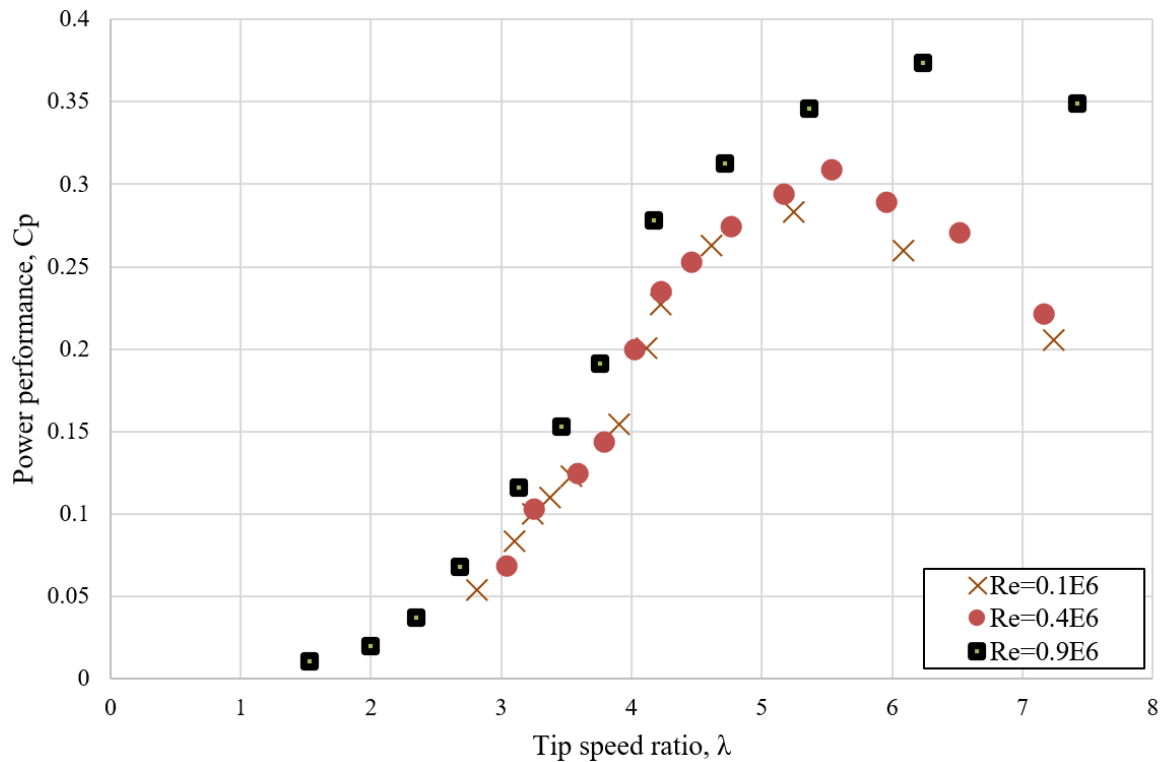


Figure 2.9: Power coefficient for several scales of NREL wind turbine Cho, et al. (2010) and (2014).

However, the results demonstrated that the increase in C_L is paralleled the increase of Re and the C_D decreases. Therefore, the Re positively affected on the L/D trend and that can rise highly the C_p value for the full size rotor.

In addition, a simulation study by Park et al. (2007) examined scale effect of NREL phase VI wind turbine. Wind turbine model scales of (6%, 12%, 50%, 100%, 400%, 800% and 1600%) were investigated numerically: likewise, experimental tests for 12% and 20% scaled down models were performed by Cho et al. (2010) Cho et al. (2014) respectively.

The main finding of this study, was that for large scales rotors, performance was higher than that of small scale models.

Sobotta's numerical study (2015) comparatively investigated the scaling down (from 100% to 6%) of NREL wind turbine. The velocity of flow was constant at 6 m/s with a range of λ from 0 to 6. The results of that comparison indicated a reduction in the coefficients of performance and moment of up to 27% and 29% respectively. In addition, at the tip of the blade, Reynolds number decreased from 8.15×10^5 for the large scale wind turbine to 0.53×10^5 for the small one.

Owing to the size limitations of the wind tunnel at the University of Sheffield, the design of a scaled down wind turbine model becomes significant. At similar TSRs to that of full scale HAWTs, the small-scale wind turbine needs to be rotated at Re lower than full scale model. Furthermore, a blockage ratio, which is the ratio of frontal swept area to wind tunnel cross-section area, could affect the experiment or the simulation results (Du Gang and Wu Chun Kau, 2015). Therefore, Brawley, (2008) and Edwards et al. (2012), who utilised the University wind tunnel, kept it to a value that would not intensely alter the flow physics.

2.4.2 Effect of the rotor shape

The geometrical design of the rotor plays an influence role in capturing the kinetic energy from the wind. The optimal design of the modern blade depends on many manufacturing factors, for example, the outer area of the blade. The rotor's solidity, which is the percentage of total blade area to the swept area, can be affected by the outer area and that is expressed in the following equation:

$$\sigma = (\text{Whole area of the blade to the swept area by blade}) = \frac{N c}{\pi R} \quad \text{Equation 2-12}$$

where N is the number of wind turbine blades.

The major influence of the solidity on performance of horizontal wind turbines can be seen in Figure 2.10.

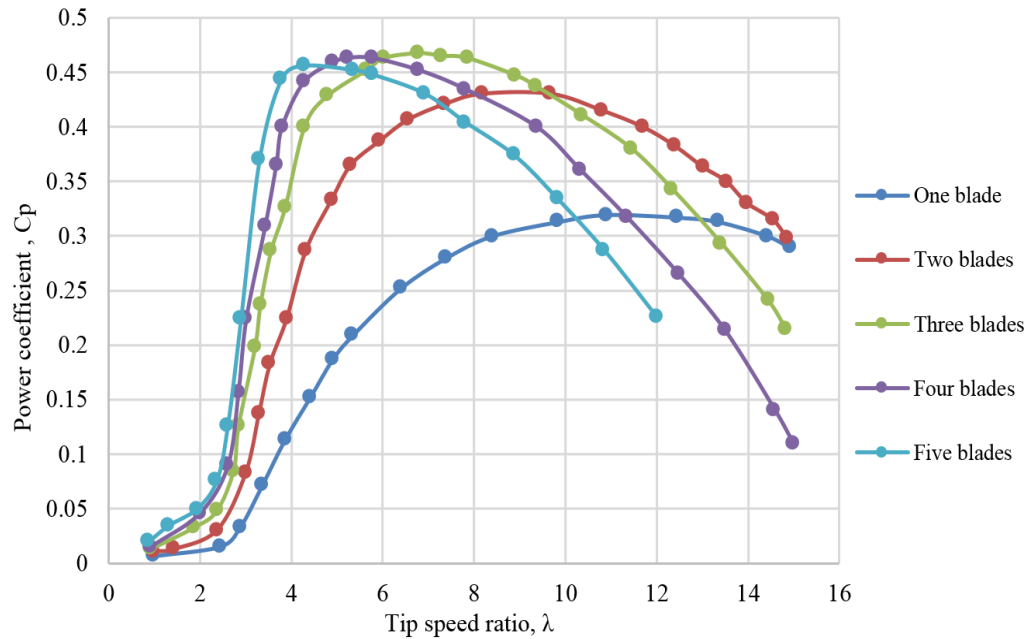


Figure 2.10: Effects of solidity on the performance of HAWT (Burton, et al., 2001).

Increases in the number of blades will lead to higher rotor solidity, so the performance of the turbine will drop in direct proportion to the number although the maximum power coefficients increase. The solidity of a three blades wind turbine, for instance, could reach to 0.0345; however, this number might alter by changing the number of blades and also the chord of the blade (Burton, et al., 2001). Figure 2.10 shows that high solidity curves are relatively shorter than that of the low solidity. It was because the high solidity shifted the performance curve into the lower range of λ when it decreases the rotational blade velocity, U . High solidity turbines could work like a solid wall which impedes incoming wind speed from freely passing through the blades and that causes low performance.

Hau (2006) mentioned that a wind turbine with three blades can produce 3 to 4% more power than one with two blades. Apparently, the curves of a high solidity turbine tend to become narrow with a sharp peak with increasing tip speed ratio. Additionally, the maximum performance coefficient C_p changes slightly with high solidity, even though high drag forces accompany by high solidity. Optimum performance is likely to be achieved with the three blades turbine design; nevertheless, the two blades turbine may also achieve acceptable performance. This is due to the peak being widely spread along the performance curve, in spite of the C_p being slightly lower than that of three blades version (Burton et al., 2001). Moreover, the increase in solidity expands the stream tube that may cause deviation

of incident flow from geometric angle of attack as well as affecting turbine loading, which then strengthens the wake, according to Danao et al., (2013).

2.5 Modelling and Numerical Simulation of Wind Turbines

2.5.1 Computational fluid dynamics (CFD)

General overview

Computational fluid dynamics (CFD) can be defined generally by employing computer codes to study and analyse numerically multi- features of the flow. This entails the prediction of the behaviour of flow past objects by numerical methods rather than lab work and analytic solution. Computational fluid dynamics has offered a significant but inexpensive way to test the fluid flow system and solve such complex equations as Navier-Stocks equations (NS).

CFD makes it possible to test flow conditions that cannot be measured easily in experimental work (Versteeg and Malalasekera, 2007). In the field of wind machines research, CFD has been evolving recently because of its capability to model phenomena of these machines such as root losses, dynamic stall and the effect of rotation for both 2D aerofoils and 3D blades (Delbaere, 2015).

The various stages of CFD analysis can be summed up as follows. First, post-processing involves building the geometry and mesh generation once the flow domain has been broken down into sufficiently small elements. The next stage is the solver which defines the flow domain, sets the fluid properties, applies the boundary conditions, and specifies initial conditions. Once the results have been obtained, the final stage involves analysis of these results using methods that include contour and vector plots, and streamlines.

CFD governs the mathematical equations, namely, the mass continuity equation, and the momentum equations or Navier-Stokes equations. These equations could be seen, in another view, as application of Newton's second law of motion for fluids. Assuming the flow is an incompressible Newtonian fluid, this yields the following equation, which represents the combination of three components in Cartesian coordinates in one vector form equation:

$$\rho \frac{DV}{Dt} = -\nabla p + \rho g + \mu \nabla^2 V \quad \text{Equation 2-13}$$

These equations are in the form of partial differential equations (PDEs) and they are partial due to changes of the variables involved within. The PDEs are typically combinations of flow variables and the derivatives of these variables. These equations are a group of coupled differential equations and can be solved numerically by using modern mathematical methods. However, as these equations are practically complex to solve, further approximations and simplifications have in the past been made to solve these equations analytically.

Reynolds-Averaged Navier-Stokes Equations (RANS) could be defined as an open, time-dependent equations by which instantaneous variables (as velocity) can be decomposed into the mean and fluctuations. To some extent, these equations simplify the NS equations to enable simulation of many engineering fluid flow applications such as wind turbines. Furthermore, these equations produce a set of terms known as the Reynolds stresses, which are functions of fluctuations, and require a turbulence model that will be discussed later.

Nowadays, high speed computers are being used to solve these equations approximately. The partial differential equations are transformed into numerical forms. The solution can be reached by separating the flow domain into small cells via three main methods which: the finite difference method, the finite element method and the finite volume method. Ansys software bases on the finite volume method (FVM) which is a numerical method that converts the partial differential equations into discrete ordinary algebraic equations over elements or cells (Moukalled et al., 2016). The solution can be considered as convergent as the values of the variables at the points in the domain tend to move towards some constant value as the solution is being progressed.

All in all, a CFD package consists of three main software processes: pre-processor, solver and post-processor. Pre-processing represents configuration and mesh generation. The numerical solution is run to calculate the numerical solution to the flow problem in what is the solver stage. Then last process is analysing the results and checking whether they are acceptable for determining the required flow data.

Turbulence models

The time-averaging of the instantaneous Navier-Stoke equations means they decompose into two quantities: an average and a fluctuation component. Decomposing equation 2-13 produces a term owing to the fluctuating velocity field, generally represents what is known as the Reynolds stress that will be modelled to solve and close the RANS equation. The Reynolds stress refers to the rate of strain of the mean velocity multiplied by the eddy-viscosity μ_T , which is a coefficient that represents the average shear stress within a turbulent flow to the vertical gradient of velocity. Fluid flow applications have recently utilised many turbulence models. However, three active models are especially used in aerodynamics applications, namely, the Spalart –Allmaras (S-A) model, the standard $k-\varepsilon$ and the standard and shear stress transport of the $k-\omega$ SST, and these will be overviewed in the following sections. These sections will consecutively provide a short definition of these models and their applications, especially in relation to NREL phase VI wind turbine.

Spalart -Allmaras model

The new one-equation, economic model has recently started to be more widely used and was employed firstly by Spalart and Allmaras (1994) for directly computing the eddy-viscosity. This model, which was developed at Boeing, produces a good perspective on boundary layers in pressure gradients, especially in aerospace fields. In general, it is hard for this model to capture a separation in the flow field, in particular at the leading-edge, (Spalart and Allmaras, 1994). Song and Perot (2015) later employed the (S-A) model directly in their numerical simulation of the NREL Phase VI rotor work, without any comparison to other models. The CFD results were good compared to the experimental data, especially when fine mesh was made at the leading-edge of the blade.

$k-\varepsilon$ model

This two-equation eddy-viscosity model was firstly used by Jones and Launder (1972). k and ε refer to the turbulence kinetic energy and turbulence rate of dissipation respectively and these are gained from solving differential equations numerically in order to compute the eddy-viscosity. This model showed an ability to satisfactorily simulate the flow behaviour on the distance outside the viscous sub-layer. Derakhshan1 et al. (2015)

conducted a further numerical investigation study and it was validated by the NREL Phase VI rotor work using this model.

k- ω SST model

In 1988, Wilcox designed a two-equation model (k- ω) which can be utilised in the sub-layer of the boundary layer, while Menter (1994), whose work has priority over that of other researchers in terms of using the SST model, constructed this model which works near walls with the previous mentioned model (k- ϵ) in the free flow stream near the boundary layer edges. The new combined model has enhanced the ability of the RANS to predict the separation and wake region in the boundary layer (Cebeci, 2003). Furthermore, Ekaterinaris and Menter (1994) applied the k- ω SST model and various turbulence models in their study to investigate the effects of complex flow conditions on wings or slender bodies. The k- ω SST model produced more satisfying prediction than other models for the flow separation and stall cases.

Similarly, Tominaga (2015) examined the k- ω SST model and other turbulence models to investigate the performance of the unsteady part of the RANS, with the k- ω SST model showing high ability to predict the fluctuation and flow separation. In addition, numerically, results produced by Danao et al. (2013) showed that both fully k- ω Shear Stress Transport (SST) and the 4-equation Transitional SST model gave an accuracy than other turbulence models such as the one-equation Spalart-Allmaras (S-A) and the two-equation renormalization group RNG k- ϵ . In the case of 2D simulation, a 2D S809 aerofoil was modelled by Han (2011) and the SST k- ω turbulent model in ANSYS-Fluent displayed adequate convergence with the experimental data.

For reasons beyond those mentioned above, the k- ω SST model is still frequently used, especially in the simulation of NREL phase VI wind turbines, according to many recent published studies. Though the k- ω SST model has been mostly applied to the NREL Phase VI, Park et al. (2007) found that the k- ϵ model performed in torque predictions better than other turbulent models over a wide range of wind speeds. The k- ω SST model was also adopted by Johnson (2012) to study the effect of unsteady flow on the erosion of the S809 aerofoil after comparing it to the realisable k- ϵ model. Following is a selection of studies which dealt with this model and type of horizontal wind turbine.

According to Sørensen et al. (2002), the $k-\omega$ SST model was selected because of its successful application in prediction of flow separation and valuable connection with the NREL/NASA Ames experiment data. Moreover, Tadamas and Zangeneh (2011) selected this turbulence model only on the basis of past successful experiences at different operating conditions and, similarly, Lynch and Smith (2013) and Zhou et al. (2013). Additionally, Velamati et al. (2016) selected three turbulent models for conducting their numerical study, including the $k-\omega$ SST model. In term of the CFD, the other two models performed less well compared to the SST $k-\omega$ model. Furthermore, Yelmule and Anjuri (2013) carried out a comparison between their CFD results and the NREL experimental data and then the CFD results with those produced by researchers. The SST model they used showed high agreement among all the results. Although the prediction of the aerodynamics of the blade could be affected at high angle of attacks, the $k-\omega$ SST model achieved well at these massive degrees and matched with the experimental work (Lee and Ho 2012). Finally, Sobotta (2015) conducted an independent case study and then compared the data with those from the experimental study done by Devinant et al. (2002). The numerical work simply involved measuring the aerodynamics of the NACA 654-421 aerofoil. The main aim was to analyse the turbulence models from the S-A, $k-\epsilon$ and $k-\omega$ model groups, as shown in Figure 2.11.

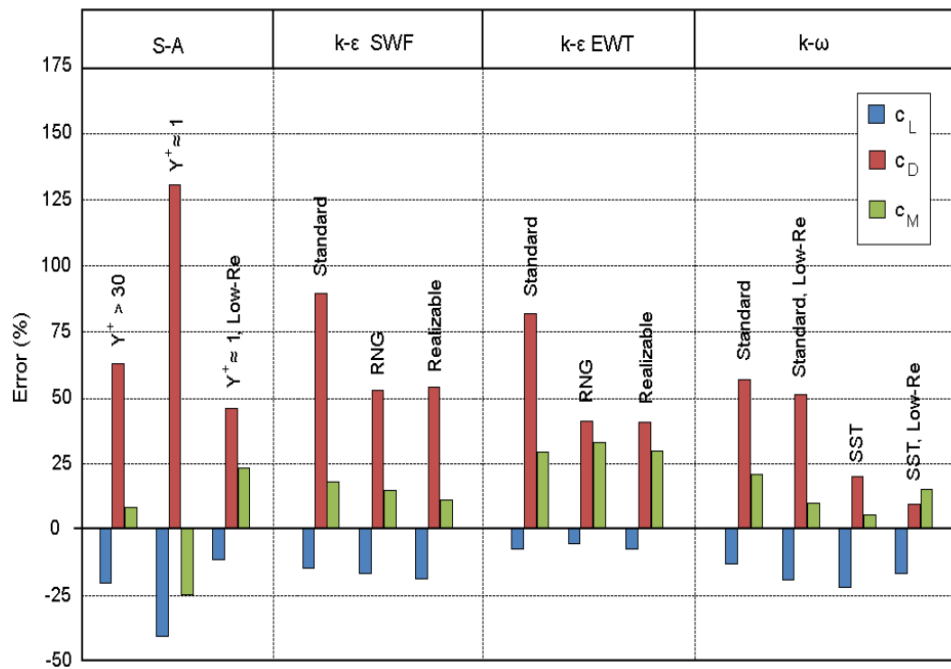


Figure 2.11: Validation of NACA 654-421 aerofoil for S-A, $k-\epsilon$ and $k-\omega$ models at $Re = 0.4E6$ and $\alpha = 0^\circ$, Sobotta,(2015).

The $k-\omega$ model group revealed consistent prediction, in particular with SST low-Re model, which showed relatively small deviations from the experimental data compared with other models. Hence, Sobotta (2015) chose the $k-\omega$ model to simulate starting sequences of the NREL Phase VI rotor wind turbine.

In contrast, the CFD data gained by Moshfeghi (2012) revealed that the $k-\omega$ SST model could not always anticipate the separation point, in particular, when it occurred far from the leading edge; however, it was able to predict the flow details beyond this point.

ANSYS Fluent and ICEM Software and CFD Simulation Studies

ANSYS Fluent software could be considered the most dependable and widely-used CFD tool for physical modelling validation in terms of providing prompt, accurate results for many academic and industrial applications. Meanwhile, the ANSYS ICEM tool might be considered as flexible and powerful software which can offer a schematic view of a geometry in various forms of mesh generation. Following are some samples of research studies and articles which have functioned the CFD to achieve their study aims.

Computational domain configuration

Song and Perot (2015) built a double-bladed full scale NREL Phase VI rotor inside a rotating cylinder. Similarly, Xie et al. (2012), Figure 2.12(a), configured two concentric computational cylindrical domains: the inner fine mesh dynamic domain and outer coarse mesh stagnant domain. On the other hand, many researchers have utilised a single-bladed wind turbine, to minimise the mesh size and save time (for example, Yelmule and Anjuri, 2013; Sørensen et al. 2002; Sørensen et al. 2015; Mo and Lee 2012; Sobotta, 2015), as seen in Figure 2.12(b). All of these constructed only a 180° sector, used various software packages and included one blade of the doubled-bladed turbine of the NREL Phase VI rotor.

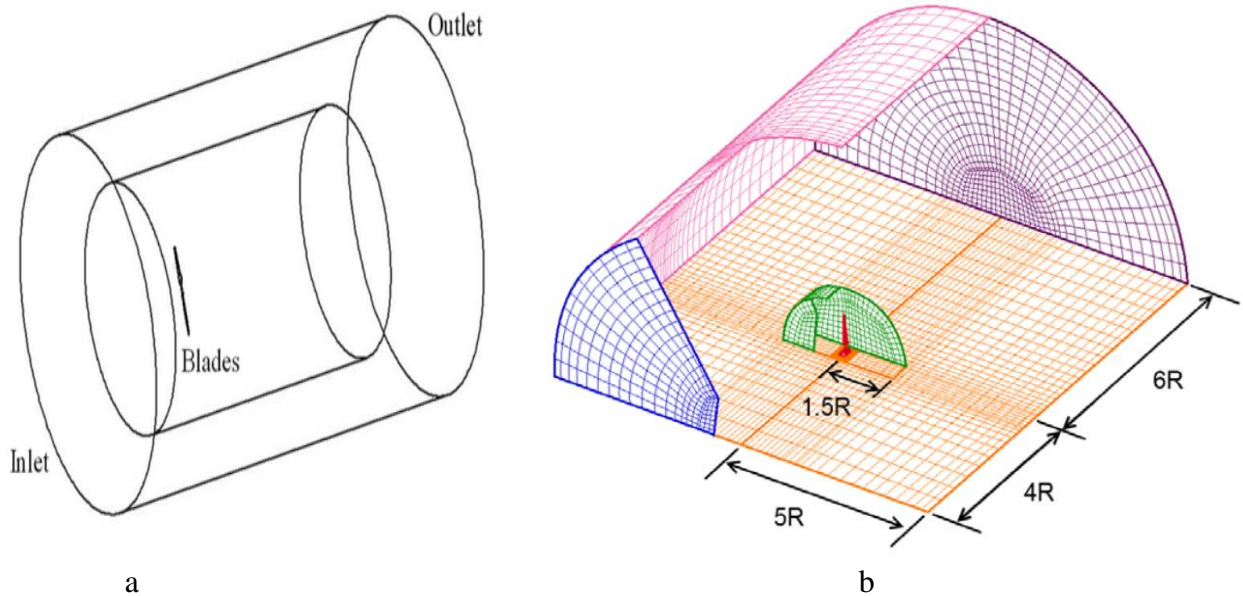


Figure 2.12: (a) 360° mesh domains configuration, Xie et al., (2012) and (b) 180° mesh domains configuration, Sobotta,(2015).

Number of mesh cells

A thesis submitted by Han (2011) modelled the 2D S809 aerofoil. Both structured and unstructured mesh were applied separately for the accuracy test. A large number of cells were set close to the aerofoil where the gradient in the flow needed to be captured, while the mesh of far field was coarse. The structured mesh consisted of 5×10^4 quadrilateral cells whereas the unstructured mesh comprised 1.5×10^4 triangular cells, with 300 cells set on the aerofoil surface in both cases. Compared with experimental work, the unstructured mesh exhibited high accuracy at high angles of attack ($-10^\circ \geq \alpha \geq 10^\circ$). In contrast, structured mesh showed precise results at low AOA, owing to unaligned cells and according to the flow direction and keeping the aerofoil at 0° pitch angle relative to the plane of blade rotation.

Another study, by Park et al. (2007), utilise CFD to examine the effect of the same blade scales, including the 6 % scale. The structured quadrilateral and hexahedral mesh type were used around the wind turbine surface and boundaries from the hub to positions on the blade respectively. A tetrahedral mesh type was also used to fill intermediate boundaries; therefore, the overall mesh was about 3.3×10^6 cells. Additionally, an article

submitted by Song and Perot (2015) reported that using of CFD to simulate the aerodynamics of tapered, twisted and rotating NREL, for instance, presents exciting possibilities. The study's simulation was based on the experimental work of Hand et al. (2001) and the results were validated against the findings of Robinson et al. (1999). The full scale NREL blade was covered by a rotating cylinder and everything was set inside a cube which represented the wind tunnel. An unstructured refined mesh was applied in a thin layer next to the surface of the blade at massive Reynolds number of up to 10^5 . In order to avoid high aspect ratio, very flat prisms were set next to the surface. Whereas, for the remaining geometries a coarse mesh was used. Different mesh densities 4, 6.3 and 10 million cells were tested. The results showed that the high quantity mesh can capture the solution accurately. In their study, Mo and Lee (2012) used a total of 3.0×10^6 hexahedral grids. Of these, 200 grids were meshed in a chord-wise direction on the both sides of the blade and the majority of these grids were around the leading and trailing edge and another 200 grids were set up along the blade. Hexahedral mesh was also employed by Chaviaropoulos et al. (2003) and in total more than 1.0×10^6 hexahedral grids and 64 grids totally were meshed in a chord-wise direction on the both sides of the blade and another 167 grids were set up along the blade. Furthermore, Xie et al. (2012) used a number of hexahedral grids ranging from 3.6×10^6 to 5×10^6 .

Performance of wind turbines

CFD method has also been used to analyse the effect of unsteadiness and physics of wind speed on performance of a Vertical Axis Wind Turbine (VAWT). This has been done by solving the unsteady RANS equations and applying Reynolds decomposition as well as taking time-average of the continuity and momentum equations, leading to the unsteady RANS equations for incompressible flows. The obtained results then compared with experimental data of Danao et al. (2013). The final results showed that high fluctuating wind speeds have a negative effect on the performance of the VAWT. The C_p for steady flow was 33% better than that of unsteady flow at mean velocity 11m/s, while the figure dropped negatively to 1.6% from C_p for steady flow at 3.42 m/s. Therefore, high fluctuating winds might detrimentally affect the performance of the VAWT. The performance of the horizontal wind turbine was tested using Fluent code by Velamati et al. (2016)

investigating the influence of different pitch angles (-10° , 0° , 5° , 10° , 20° , 30° and 40°) at three different wind speeds against the work on the NREL phase VI wind turbine. The performance of the wind turbine showed improvement when the pitch angle was increased due to the low drag generated by this pitching.

2.5.2 Blade-Element Momentum (BEM) Method

This approach can be generally defined as a mathematical method used to calculate the aerodynamics and then the performance of a wind turbine at different wind flow conditions. Moreover, this method has been used recently to ultimate the design of the rotor (Manwell et al., 2009). Use of the Blade-Element Momentum method was first promoted in 1935 by Glauert from a combination of two main theories; momentum theory and blade element, and over time its use has been modified. The momentum theory was briefly mentioned earlier in section 2.2.1 in this chapter in relation to how the turbine can simply be shown as a disk generates a difference pressure in a stream tube, as shown previously in Figure 2.2. Meanwhile, according to the blade element theory, a rotor blade is initially divided into small strips where no aerodynamic synergy between them, as seen in Figure 2.13. Then forces are calculated from the lift and drag forces on the strip.

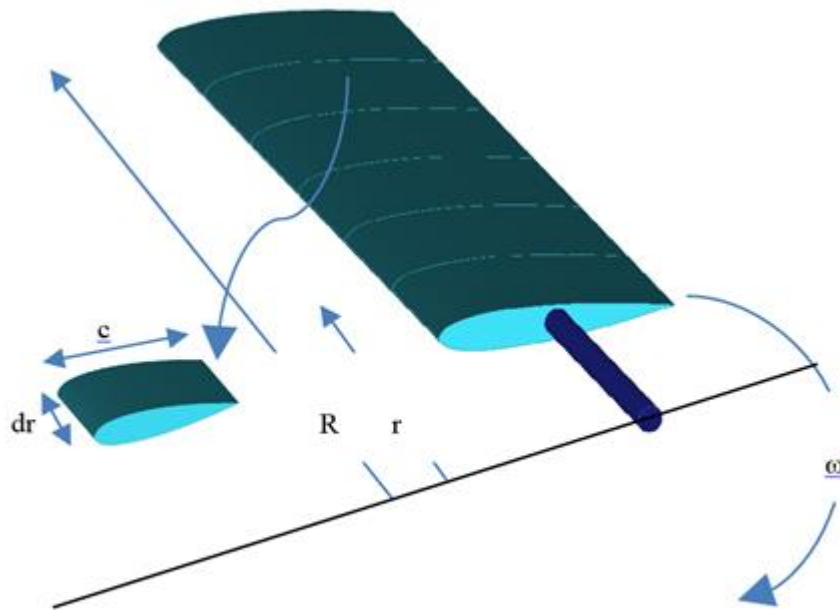


Figure 2.13: Blade element scheme, Manwell et al. (2009).

Where c and dr are the chord and the strip-span from axis of rotation, the aggregates of forces acting on each strip and moments are gained by integrating the individual forces and moments on each strip.

Recently, many researchers have successfully implemented BEM in their work, especially in the wind turbine field. The BEM has been productively used to design a small size horizontal wind turbine by Bai et al. (2013). Lanzafame and Messina (2007) conducted a comparison study to investigate the validity of the BEM with the experimental NREL work (Lindenbug, 2003) and their results displayed acceptable agreement with the experimental work. Similarly, Taehwan and Cheolwan (2014) conducted a comparison study with the scaled down NREL phase VI wind turbine and their results also showed agreement with the experimental data. Moreover, Yelmule (2013), who conducted a comparison of CFD results from the NREL Phase VI turbine with those from other CFD predictions studies and also the BEM, observed satisfactory results for BEM predictions in comparison with experimental CFD results.

In this study, the BEM will be applied in another form, namely the QBlade software. This new tool, which harnesses the Blade Element Momentum method, was firstly used by the Technical University of Berlin in 2010 and it has steadily been validated by researchers to simulate performance of both HAWTs and VAWTs.

The aim, behind this open source tool is to enable engineers and researchers to stimulate and design various types of wind turbines Marten et al. (2013). QBlade has, moreover, been successfully validated against computation results from the BEM. The QBlade software tool is used for simulating and for designing wind turbines (Marten, 2013). It includes several modules such as design and analysis of aerofoils, lift and drag polar extrapolation, design of blade and turbine simulation. Mahmuddin (2017) developed a computational method which depends on the Blade Element Momentum theory and compared the results with data gained from the QBlade tool. The findings derived by the two different methods showed a good agreement, thereby indicating that the QBlade tool is a trustworthy tool for conducting the present comparison.

2.6 Unsteady flow conditions

2.6.1 Overview

A wind flow that is only a function of space is called steady flow; in other words, time-dependent flow, so turbulent flow is considered unsteady by definition. Steady flow is practicably more tractable than the unsteady flow (Erich, 2006). Unsteady flow, however, prevails in the environment and that should be taken into consideration when designing wind turbines. The atmosphere is dominated by fluctuating air flow, and thus wind turbines frequently face unsteady air-loads (Leishman, 2002).

The flow of air can be considered as steady even though boundary layer flow has turbulent characteristics such as fluctuations in velocity and pressure. Mountains, buildings, plants and other bumpy terrain might generate non-uniformities, even at low wind speeds, that will then affect the wind flow that passes through the wind turbines (Jonkman, 2003), Figure 2.14. The shape of the high-frequency wind flow (turbulent flow) can be represented in idealised shapes such as rectangular, trapezoidal and sinusoidal shapes, which can be described by either a sine or cosine function with convenient frequency and amplitude, to calculate loads on wind machines. The sinusoidal shape, in addition, was identified as the best example of unsteady flow behaviour in a study by Scheurich and Brown (2013).

Sine waves are relatively simple and allow researchers to understand the fundamental aerodynamics that occur with unsteady flows. Some papers have looked at very complicated flows, but these are very hard to then understand and even harder to understand the effect of the performance of unsteady flow.

Thus, the current researchers has chosen a sinusoidal shape to represent the unsteady flow that will be used to rotate the NREL Phase VI turbine rotor as described in chapter six.

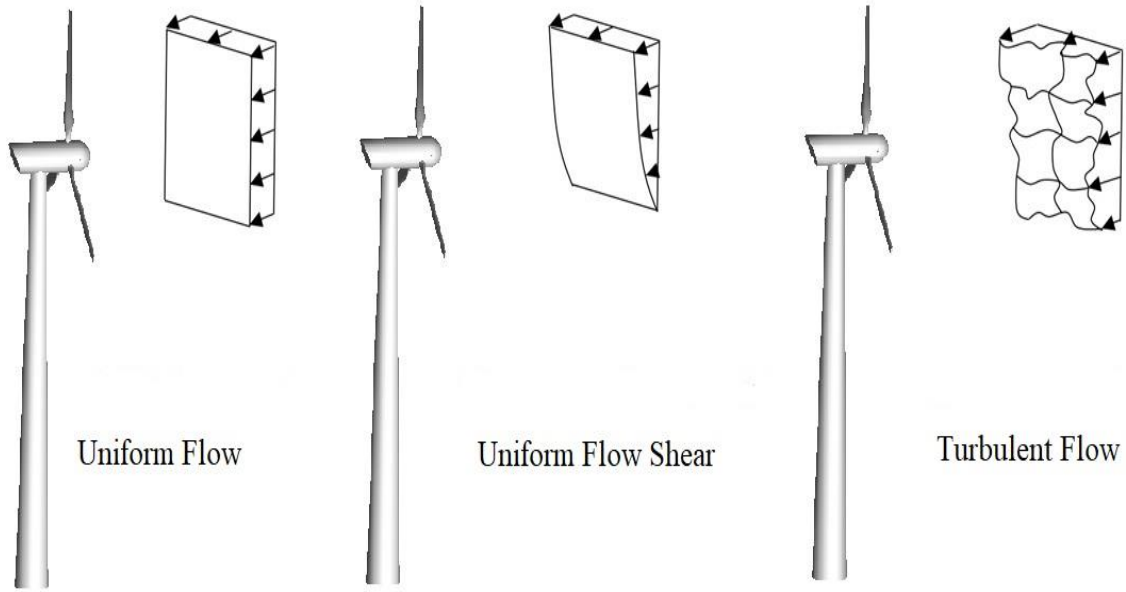


Figure 2.14: Characteristics of air flow incident on a wind turbine (Jonkman, 2003).

2.6.2 The unsteady wind flow form

The unsteady wind flow has been frequently used as an argument against harnessing the power of wind (Hau, 2006). The fluctuations in wind speed from season to season have been considered very significant issue in terms of wind turbines investments. In addition, theoretically, the energy in wind depends on the third power of the averaged wind speed; therefore, it is logically to study the fluctuations in wind energy.

The following specified equation represents, at a local point in time, the instantaneous wind speed:

$$V(t) = \bar{U} + \acute{u}(t) \quad \text{Equation 2-14}$$

The term $V(t)$ refers to the fluctuating wind speed, \bar{U} is the average wind speed and $\acute{u}(t)$ is the fluctuating wind speed which occurs due to the wind speed's turbulence. Turbulence, thus, can be defined as the instantaneous wind speed deviating randomly from the averaged wind speed, as shown in Figure 2.15.

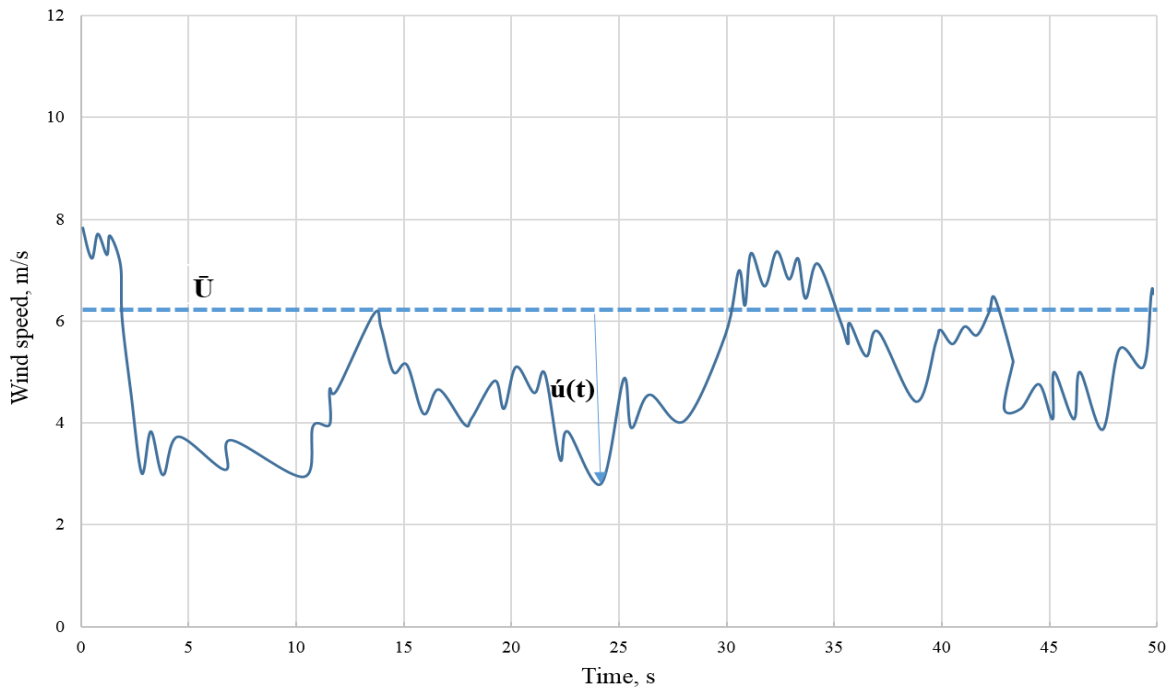


Figure 2.15: A wind speed measured with time (Erich, 2006).

Moreover, the percentage of the standard deviation of the wind speed from the averaged wind speed represents the degree of turbulence or turbulence intensity. This ratio has been measured over the sea as being 5% or less, while it has been measured as 20% or more in forests or urban regions (Hau, 2006).

The instantaneous inlet velocity can be modelled more specifically using modified (equation 2-14) to obtain the equation below which represents generally the sinusoidal form (Danao et al, 2013; Wekesa et al, 2015; Toshimitsu, et al., 2012):

$$V(t) = \bar{U} \pm \acute{u} \sin(2\pi ft) \quad \text{Equation 2-15}$$

Where f is the frequency of the oscillating wind in Hz, while t is the flow time in second.

2.6.3 Wind turbine operating in unsteady flow

To the best author's knowledge, it is only recently that unsteady wind effects studies have been taken into consideration and this field of study is still not completely mature. Largely, steady wind flows are still the dominate research area in horizontal wind turbines studies. Following is discussion of several selected researches that have dealt with the unsteady wind condition.

Danao et al. (2013) conducted both experimental work and numerical simulation to investigate the influence of unsteady wind on performance of a vertical wind turbine. This was a significant step forward in the understanding of VAWT performance in unsteady wind conditions. Unsteady wind flow was obtained by using the shutters in a low speed open system wind tunnel. A Reynolds number of up to 5×10^4 , of 7 m/s mean wind speed was utilised, with 7% and 12% fluctuated from wind velocity at frequency of 0.5 Hz. Fluctuations of rotational speed of the VAWT were conducted to produce power. Both steady and unsteady power performance were tested utilising unsteady Reynolds Averaged Navier–Stokes Computational Fluid Dynamics. The results from the laboratory showed that the unsteady wind gives rise to a fall in performance of the VAWT, Figure 2.16.

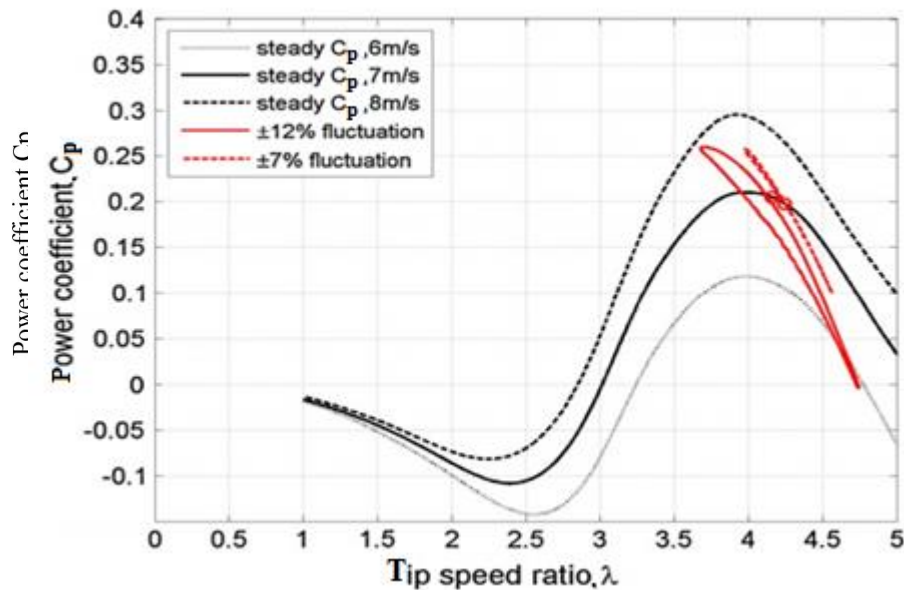


Figure 2.16: Effect of steady and unsteady flow on the performance of VAWT (Danao et al., 2013).

The same VAWT model was utilised again in a numerical study by Danao and Howell, (2012). The wind conditions in their study were set at three different frequencies (1.16, 2.91 and 11.6 Hz) with 50% amplitude of the average wind speed. The findings showed that the highest frequency reduced the average performance of the turbine by half, while the performance decreased by 75% with other two frequencies.

A case study conducted by Wekesa et al. (2015) illustrated that the unsteady flow is prevailing in the real environment and further studies are still continuing. The yearly mean

velocity and standard deviation were measured to give the amplitude of fluctuation of unsteady wind for two locations in Kenya which have offer good wind speeds and therefore potentially good energy harvesting using wind turbines. The values were 11.00 m/s and 3.42 m/s with standard deviations of 4.26 m/s and 2.60 m/s.

Experimentally and theoretically, examinations of the influence of gusts (high turbulence) on a VAWT inside a wind tunnel were conducted by Hara et al. (2012). Then, this wind turbine model was subjected to various average wind speed ranging from 7 to 13m/s, with amplitudes of the fluctuating wind of between 1 and 2m/s. One finding of their study was that the turbine's performance increased when the wind amplitude was low.

Likewise, the performance of the three types of the VAWT, in steady and unsteady wind flow, was researched by Scheurich and Brown (2013). In the case of unsteady wind speed, a frequency of 1 Hz at average wind speed 5.4 m/s was used, based on an experiment done by Bertényi (2010, cited in Scheurich and Brown, 2013). Moreover, the researchers utilised two amplitudes: 10% and 30%. The findings showed that in terms of the C_p , the straight blade and the curved blade turbine were less efficient than twisted blade turbine. However, the C_p of these blades showed instability at different attack angles.

A Japanese engineering group, Toshimitsu et al. (2012), researched the performance of both a flanged-diffuser shroud and only rotor wind turbine, which has high performance (Ohya et al., cited in Toshimitsu et al., 2012) in both steady and unsteady wind conditions. The tip speed ratios were 3.7 and 5 whereas the frequencies of the wind speed fluctuations were $f = 0.033, 0.05, 0.083$ and 0.25 Hz for unsteady flow. The numerical analysis was based on the $k-\epsilon$ turbulence model. A multi-blocks unstructured 3-D mesh of 6.4 million grids was utilized. The lab and CFD results showed a comparative agreement. From Figure 2.17, it can be seen that the performance of wind turbine with only rotor (no shroud) was high with low fluctuations. High frequency, in addition, enhanced the performance of the shrouded wind turbine. Nevertheless, the width of the curves in the case of the shrouded wind turbine in comparison with the rotor only has not been fully explained in their study.

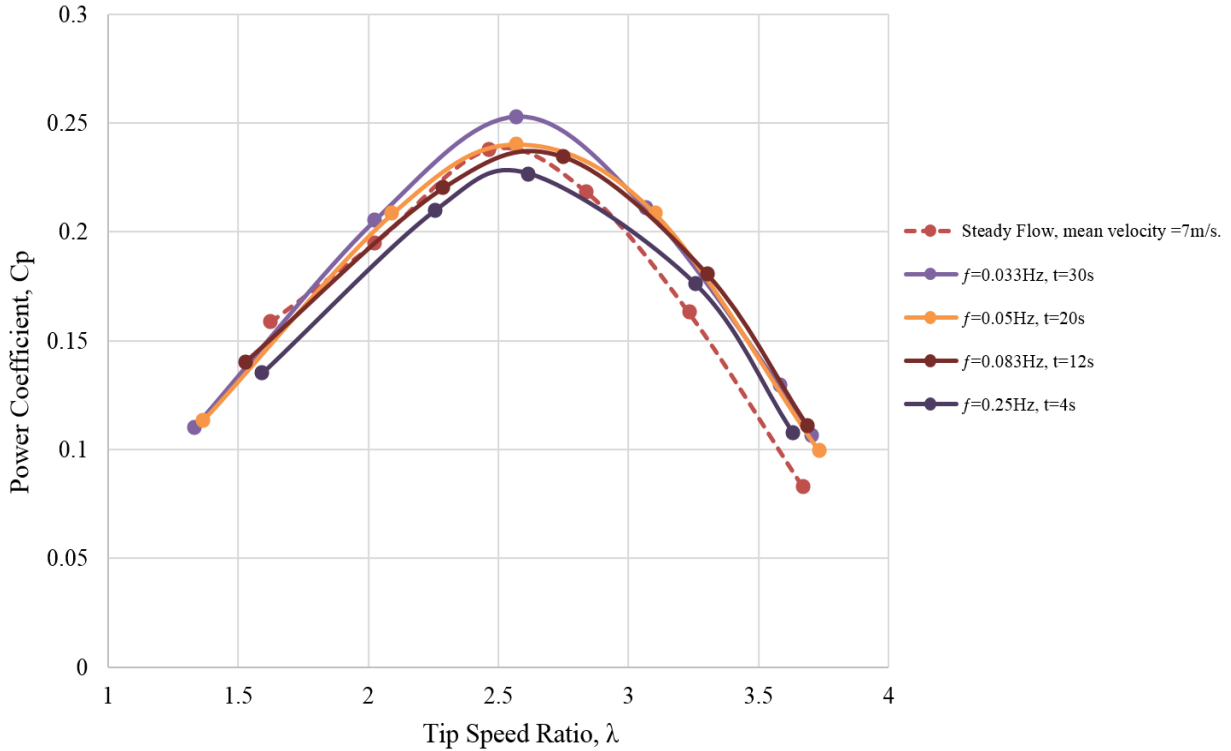


Figure 2.17: How performance of HAWT is affected by the wind frequencies at designed $\lambda = 5$ (Toshimitsu et al., 2012).

2.7 Summary of this chapter

As introduced earlier, the two-bladed NREL Phase VI horizontal rotor machine was chosen, with a full diameter of 10.058m and an aerodynamic blade section that has been exclusively built for many S809 aerofoils. The literature review has demonstrated that computational fluid dynamics is a powerful tool for solving numerically the equations of motion and has shown an ability to mimic many aspects of experimental research. Moreover, it revealed that the SST $k-\omega$ model with low-Reynolds corrections option made more satisfying predictions than other turbulent models. Furthermore, CFD can provide some required outstanding details in the understanding of the steady and unsteady wind flow and predict precisely the physics of air flow that influence the overall performance of a HAWT. Therefore, ANSYS FLUENT CFD software simulation will be fully utilised in the current research to solve the output of the ICEM tool using the hybrid (mostly structured grids) mesh.

The prevalent studies in recent times have limited their focus to, or even assumed, steady wind conditions. A finite number of efforts, however, have been made to study experimentally or numerically, or both the behaviour of HAWTs that work in fluctuating wind conditions and then compare the findings to steady wind data. From the available body of researchers work, a noticeable gap has been observed in the fundamental aerodynamics of HAWTs in unsteady flow. This gap provides substantial motivation for carrying out the current research. The aims of the current research can be summed up as follows:

- There is lack of experimental work on the effects of fluctuating winds. This lack of understanding of the flow physics surrounding blades in the fluctuating wind could be addressed through applying CFD modelling.
- The estimated frequency of the fluctuations in wind conditions in the current study will range between 0.5 and 10 Hz in various amplitudes (7, 15, 25, and 45 %) and it is expected that using these frequencies will assist to address the gap in the literature.
- Further to the above point, these wind conditions will be selectively applied in order to obtain a better understanding of the impact of Reynolds number on the output power of the HAWT.

CHAPTER 3

Numerical Modelling of NREL Phase VI Rotor

3.1 Introduction

The NREL phase VI was successfully tested experimentally on the NREL/ NASA-Ames wind tunnel in 2000. This work has remained as unique and vital since it was first conducted. However, there has been much recent experiments work to develop scaled down NREL phase VI wind turbines. The data of the full scale NREL wind turbine were considered substantially accurate and trustworthy, and many researchers have hence been utilising these data in their validations and further studies. Nevertheless, some key points need to be examined, such as the effect of unsteady flow on the wind turbines. CFD analysis has demonstrated effectiveness in prediction of this phenomenon and will be used in the same way in this research. Therefore, the current research adopts the same blade shape used in the NREL Phase VI tests as an analysis target for CFD simulation using the released information and the ANSYS ICEM CFD software package which is used for CAD and mesh generation. The major objective from this work is to calculate numerically the coefficient torque (C_m) and then convert it to the torque to compute the power that can be generated by the wind turbine.

3.2 Methodology

The CFD module is a numerical simulation tool for accurate descriptions of fluid flow processes in addition to engineering designs. The simulation work in general includes the following steps: building or importing the model geometry, generating mesh elements, and selecting solvers. Finally, a full NREL rotor with a hybrid mesh has been modelled in ICEM for use in the Fluent tool.

3.2.1 Specification of NREL Phase VI wind turbine

According to Seige (1999), there are in general two reasons for designing the blade: scientific and commercial. Choosing the blade design is logically based on scientific rather than the commercial reason, although the first produces thinner aerofoils. Therefore, the S809 aerofoils blade could capture energy more effectively. Fundamental building features of the NREL are presented in the table below. The NREL model in this research was built with 13 equally spaced S809 aerofoils from the root at 0.459 m radius to the tip at 5.029 m

radius except for a short transition area near the root which has a maximum thickness of 21% of the chord length. Figure 3.1 displays the change of size and angle with increasing the main radius. The selected blade cross section geometry data are presented in Appendix A.

Table 3.1 NREL Phase VI blade fundamental form.

Number of blades	2
Full Rotor diameter	10.029 m
Velocity of blades	Up to 72 RPM
Blade aerofoils	S809 along the span
Blade feature	Twisted, linear and tapered
Angles of twist	Non-linear twist from -20.04(root) to 2.5(tip).

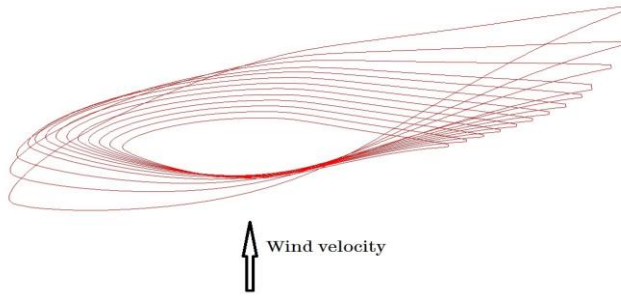


Figure 3.1: The NREL blade.

Additionally, the NREL phase VI blade has a sharp trailing edge. However, in this study a small blunt modification is applied to the blades. This bluntness has played a decidedly significant role in enhancing the quality of the mesh. According to Song (2015), blunting about 2% of the total blade chord at trailing edge allows for higher quality cells than a sharp trailing edge. The same technique was applied by Yelmule (2013) at 1 mm along the blade. Similarly, Lee (2012) created a blunt leading edge by truncating 1 % from the whole aerofoil chord to ease the construction of the hexahedral grids. Therefore, the trailing edge of the present work was modified in order to reduce the skewness of the cells as is shown in Figure 3.2. The quality of the mesh has been improved massively by applying this technique. Hence, it will be used as well for the current wind turbine mesh by trimming less than 4% from the whole chord without any aerodynamic consideration.

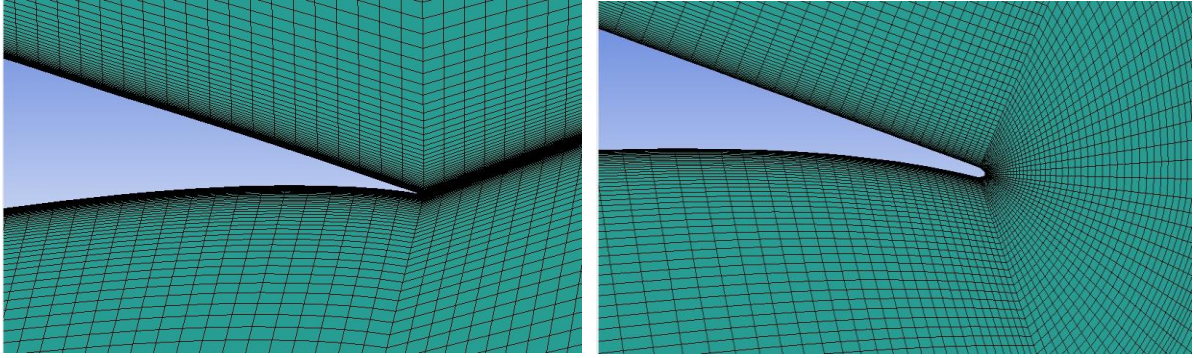


Figure 3.2: The trailing edge mesh, sharp edge (left), modified edge (right) and 75% cut plane.

3.2.2 Angle of attack along the blade

The design of the modern wind turbine blade depends on a maximum ratio of lift to drag ratio at various wind speeds along the blade. Moreover, since the rotor blade shape would need to be twisted to generate a maximum output power at an optimal angle of attack, it would be necessary to investigate mathematically the angle of attack along the blade. Various wind speeds (5, 7, 10, 13, 15, 20, and 25 m/s) were examined at different locations along the blade. Figure 3.3, shows the distributions of the angle of attack of these seven wind speeds from the top to the bottom of the blade using the following formula with 3° is the global pitch angle of the blade:

$$\alpha = \theta - \beta - 3^\circ$$

Equation 3-1

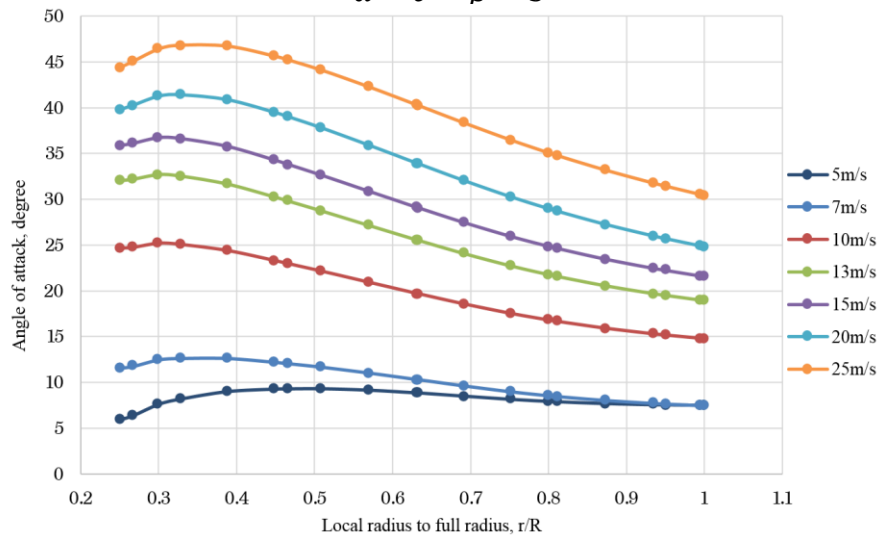


Figure 3.3: Angle of attack along the blade for various wind speeds.

3.2.3 Building the model geometry

A full scale NREL of S809 aerofoils, full details of which are provided in Figure 2.7 and Appendix A, is used to create the blades for this study. The literature survey of methodologies used in previous research work showed that a single blade model with full structured or unstructured mesh in periodic boundary conditions and a two blade version inside a rotating disk with full unstructured mesh were built and utilised. For the current study, a full-scale double-blade NREL wind turbine was built with an entirely separated structured mesh around both of its blades, as shown in Figure 3.4.

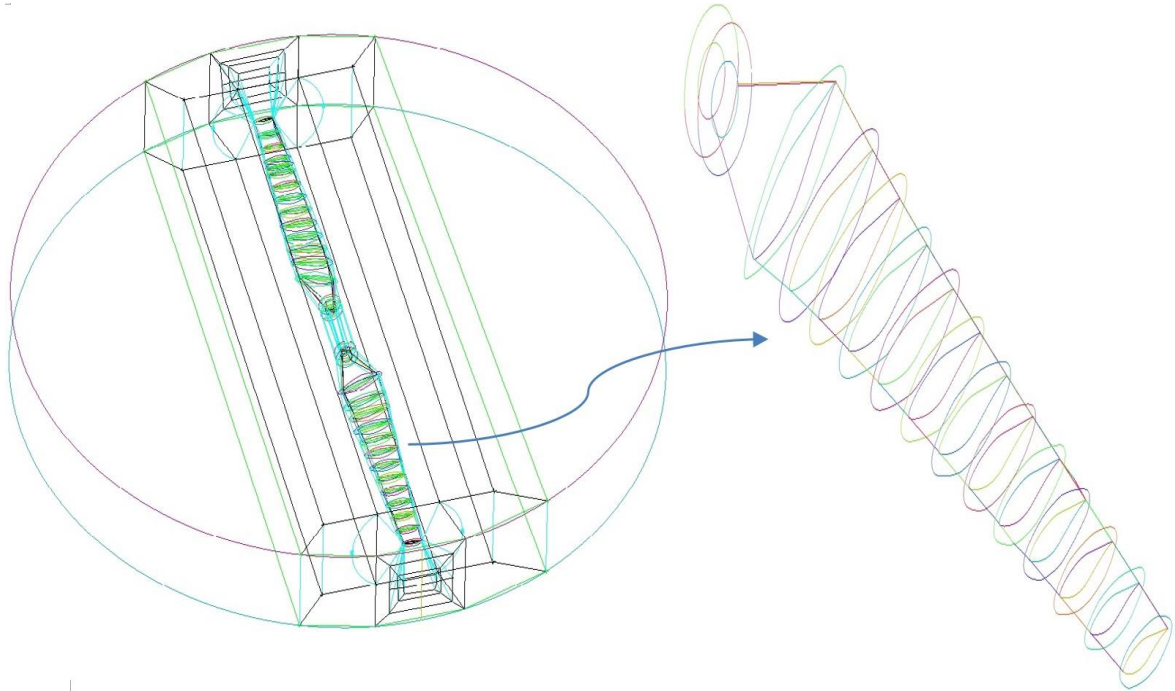


Figure 3.4: The full geometry of blades and the disk.

The two rotors that were built consist only of the blade and root, eliminating the hub in the middle in order to obviate skewed grids and reduce their numbers. In a previous study by Hsu et al. (2014) that used the NREL phase VI wind turbine without a hub, the overall findings closely matched the experimental data. Moreover, Carrica et al. (2012), who built the same wind turbine model numerically but with a hub, found that inclusion of a hub did not substantially affect the results. Moreover, other studies have found that the direct effect of both tower and nacelle on the aerodynamics of wind turbines can be negligible (Sørensen

et al., 2002; Tadamasa et al., 2011; Song and Perot, 2015), so these components are not simulated in this study.

Before generating mesh for the whole geometry, the two blades, each of 5.029 m in length from the centre of rotation to tip, were formed using Ansys ICEM 16.1. Blocking was used to cover the blades and was split into small pieces, with one at the tip, one at the root and one at each aerofoil section. Blocking is the last main step before meshing the parameters. The blades were both surrounded by a disk with a circular base slightly wider than the diameter to be covered by the two blades when rotating. Each face of this disk was given different name from those in the outer domain in order to make an interface between them later, as shown in Figure 3.5

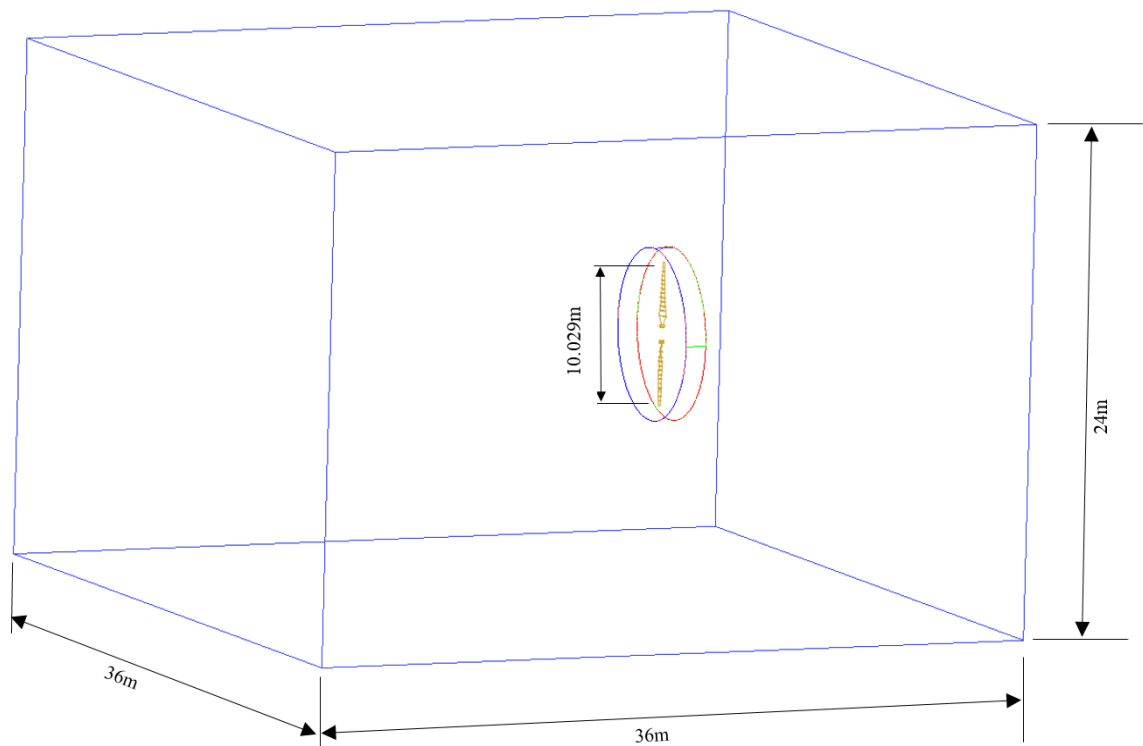


Figure 3.5: the full geometry of the current study.

The outer computational domain, which represents the wind tunnel test section, includes two regions: an inner region in which the blades would be set up and the outer region which would be stationary. The disk-shaped space, where blades are placed, is located in 4R from the inlet in order to mimic the test section of the NREL/ NASA-Ames lab. No blocking

would be used to build the test section because the tetrahedral mesh would be fully employed and that would save time and memory storage capacity.

3.2.4 Generating mesh

According to Ali and Tucker (2014), it is necessary to consider a compromise between structured and unstructured meshes when choosing mesh for non-flexible geometries like turbo-machinery flows. Therefore, and to benefit from the advantages of both types, a hybrid mesh approach was chosen for application in the present work.

2D Independent case study

A study into the aerodynamic characteristics of a two-dimensional S809 aerofoil was conducted to test the density of the mesh around the blade required to capture the flow details like the pressure gradient at the boundary layer. For the S809 aerofoil at 75% along the blade span, a numerical simulation was carried out and validated by experimental work of Jonkman (2003), Mo and Lee (2012), using the same boundary conditions as the Reynold's number (Re), namely, 3×10^5 at various angles of attack (AOA).

A mesh around the S809 aerofoil was generated by using ICEM 16.1 ANSYS module to mimic the viscose flow behaviour around the blade surface. The orthogonal mesh has many points as (200, 280, 320 and 380 cells), chosen in order to determine how many cells are required to accurately capture the flow. The wall coordinate (y^+), which depends on the Re , is 5.3×10^5 . The $k-\omega$ SST turbulent model was applied in the solution because of its high accuracy in case of the turbulent flow (Ryi, J. et al., 2014). In addition, the same boundary conditions were applied as those used experimentally. Many iterations of the solution, which were up to 1800 iterations, were carried out until convergence was reached. An O-mesh type was modelled in the ICEM ANSYS and then solved in ANSYS, the results of which are shown in Table 3.2.

Table 3.2 The lift to drag coefficient of 2D S809 aerofoil against angles of attack.

Angle of attack α , degree	Lift to drag ratio, C_L/C_D				
	Experiment, Mo and Lee, (2012)	CFD			
		200 Grids	280 Grids	320 Grids	380 Grids
0	8.974	4.632	7.701	7.720	7.721
2	26.465	17.072	23.629	23.740	23.744
4	45.407	29.100	33.510	34.220	34.220
10.2	33.217	22.210	23.200	25.440	25.445
12.2	18.229	16.320	17.500	17.980	17.988
15.15	11.383	11.121	11.852	11.320	11.322

A good agreement can be observed between the findings of the experimental work and the Fluent results. Table 3.2 shows the 2D results for the ratio of lift force coefficient (C_L) to the drag force coefficient (C_D) along with their experimental counterparts at attack angles (0° , 2° , 4° , 10.2° , 12.2° and 15.5°). However, there are noticeable differences at the angle of attack 4° where the C_L/C_D value is high. The mesh density may not be enough to capture the flow details at this angle. Moreover, the thickness of the S809 aerofoil at 75% along the blade could be less than in the experimental work and that could affect the results, since Jonkman (2003) did not provide any more details about the aerofoil. The CFD values in this table follow the experimental curve and increasing the grids around the aerofoil caused no change in the results, indicating that 320 grids are appropriate for this study.

Setting up the mesh

The main components of the mesh are illustrated in Figures 3.6 and 3.7. The mesh domain, which includes the blades and the rotating disk, is divided into two main blocks. The first block contains stationary mesh and the other a mesh that rotates at the same angular velocity as the blades. The mesh throughout the domain was tested with three cases: 4,500,000, 6,400,000 and 8,700,000 quadrilateral grids. Below this range, the mesh was of low quality, albeit of sufficient quality to run the jobs quickly in super computers. On the other hand, while using a large number of grids would obviously increase the quality, the

CPU time required to achieve convergence would be relatively large. The mentioned range was therefore selected as the base of the current research. More than 6×10^6 grids were selected that achieved the Determinant $3 \times 3 \times 3$ and the Eriksson skewness above 0.3, which is good indicator of the mesh quality according to Hao (2016), as shown in Figure 3.8. The Determinant is the ratio of the smallest determinant of the Jacobian matrix, which is the matrix of all first-order partial derivatives of a vector-valued function, to the largest determinant of it. The Determinant value is defaulted between 0 to 1, when 1 indicating a high regulated mesh element, whereas 0 indicating a higher regulated mesh element in one or more edges and the inverted element is indicated by a negative sign. The skewness of the mesh element refers to the mesh quality and suitability when it represents a criterion of the shape of grid distorted from a standard shaped one. Hence, large skewness of a grid compromises the accuracy of the generated mesh. However, the aim is to obtain low skewness as much as possible. The Eriksson skewness is an empirical criterion for the hexahedral mesh.

An H-mesh shape was used surrounding the aerofoils, with an O-mesh shape created around the whole structure, and these were fitted to the outermost part of the blade. Up to 153 grid points were located in the span wise direction, while 320 grid points were applied in the chord-wise direction. This mesh size was selected after conducting a grid independence case study as mentioned in the previous section. The density of the mesh was set up near the leading and trailing edge in order to capture precisely all flow details in the boundary layer, in particular the pressure gradient on the blade surface. In addition, the $k-\omega$ SST turbulence model with low-Re corrections was used and the thickness of neighbouring cells to the blade surface was adjusted to be 0.05 mm, matching the value used by Belamadi et.al. (2015). Hence, y^+ value was founded to be acceptable, and more than 70% of the results fell within the range of 1 to 5, as reported by Mo and Lee (2012).

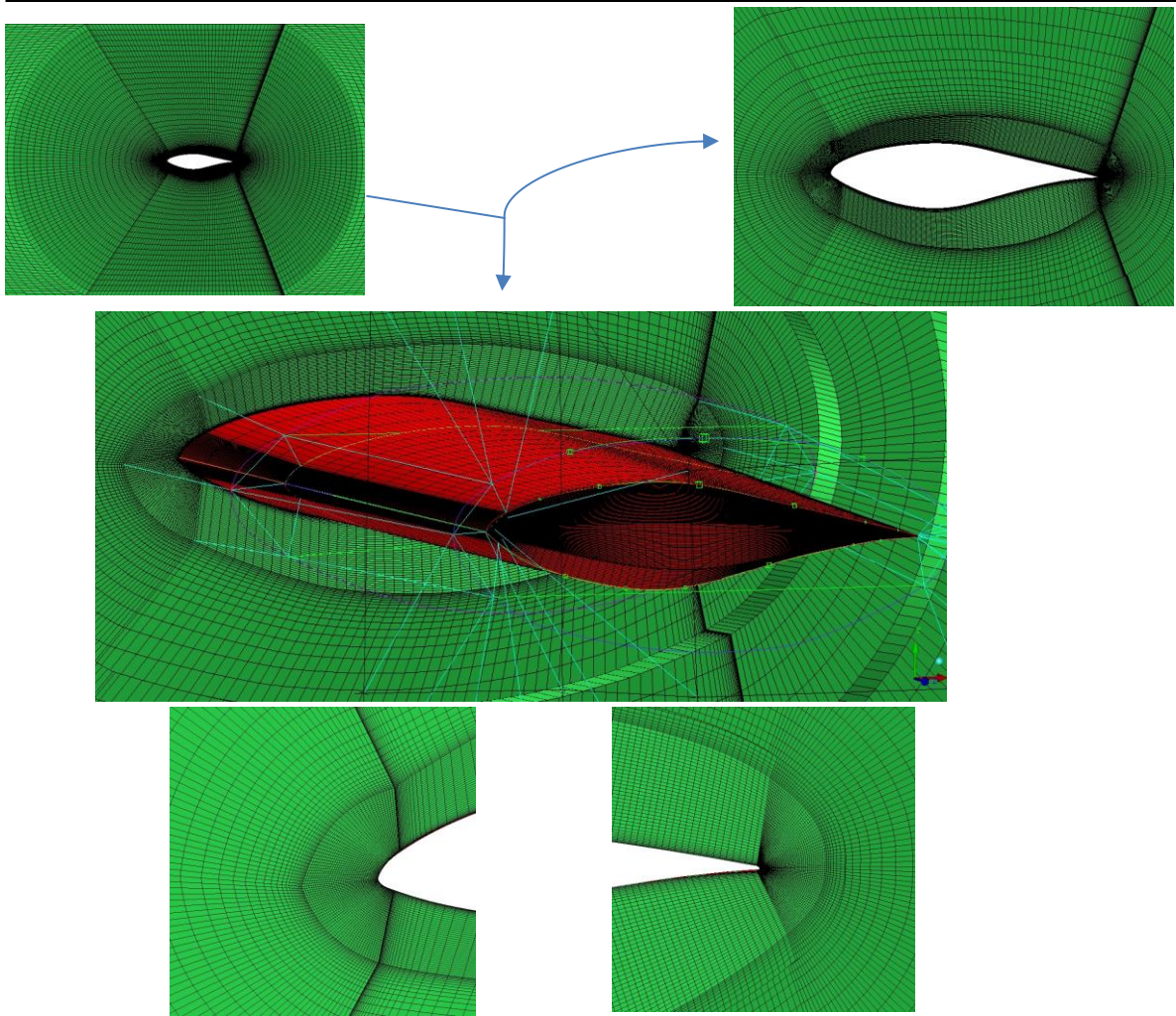


Figure 3.6: The cut plan mesh at 75% along the blade and wall mesh above the blade (top) and leading and trailing edges (bottom).

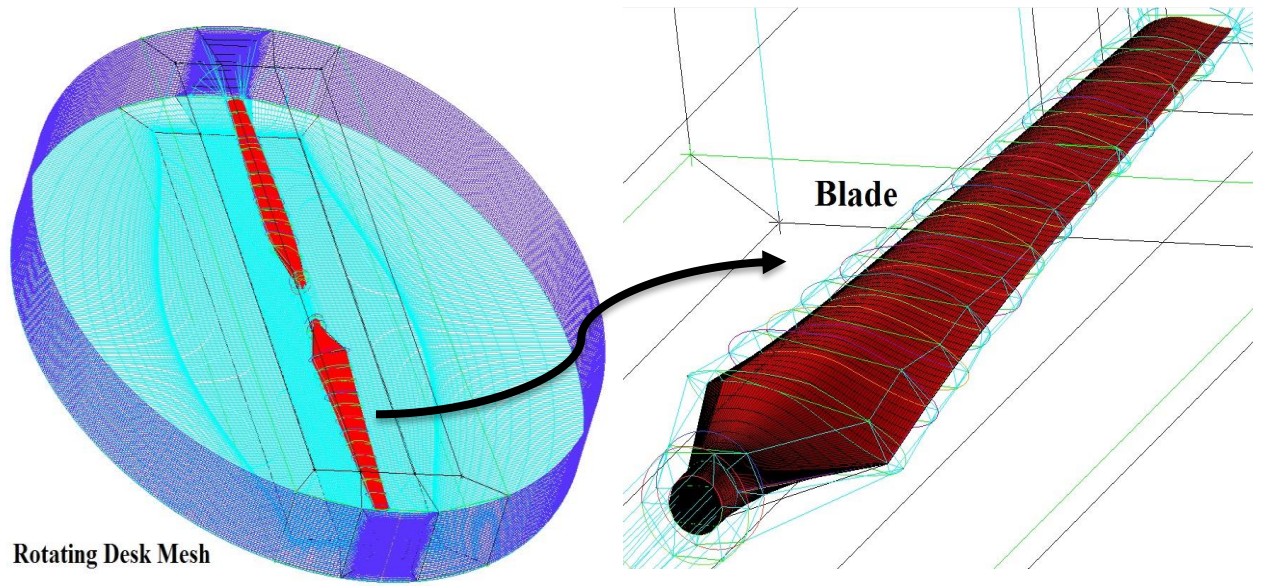


Figure 3.7: The full structured mesh of the blade and the surrounding disk.

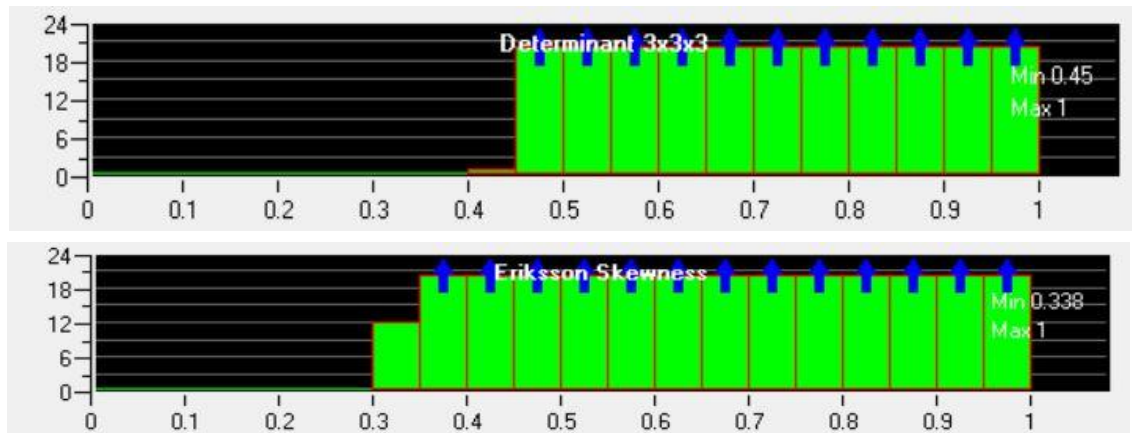


Figure 3.8: Display of pre-mesh quality in ICEM-CFD.

A disk made of dynamic mesh was then placed around the blades so as to enable them to rotate with respect to the outer mesh of the wind tunnel in the Fluent tool. Next, the turbine was set inside a rotating disk as an interface. This rotating disk was positioned inside a box which was used to represent the test section of the NREL/NASA Ames wind tunnel. In addition, an interface was added between the rotating cylinder mesh and the wind tunnel mesh. A (24.4×36.6 m) wind tunnel test section was established with an inlet, an outlet, and

an internal disk-shaped space which was built to house the rotating disk, and where the rotating disk and the blades would be rotated with respect to the inlet wind velocity and the blade speed, as shown in Figure 3.9. In order to minimise the mesh size and thereby reduce drastically the time taken on meshing and obtaining results, an unstructured mesh was used for the whole region, comprising 770,000 tetrahedral meshes and including 12 layers of prisms around the position of the blades. The interface boundary conditions were applied between the inner and outer region. Similarly, Song and Perot (2015) used unstructured meshes with $(4, 6.3 \text{ and } 10) \times 10^6$ tetrahedral cells that included flat prisms set out vertically to the surface of the blade. The high of the Prisms was set at 5×10^{-5} m to capture the flow details around the blades, as shown in Figure 3.10. As the inner mesh (dynamic mesh) rotates, at each time step the solution is interpolated between the inner and outer zones across the sliding interface boundary.

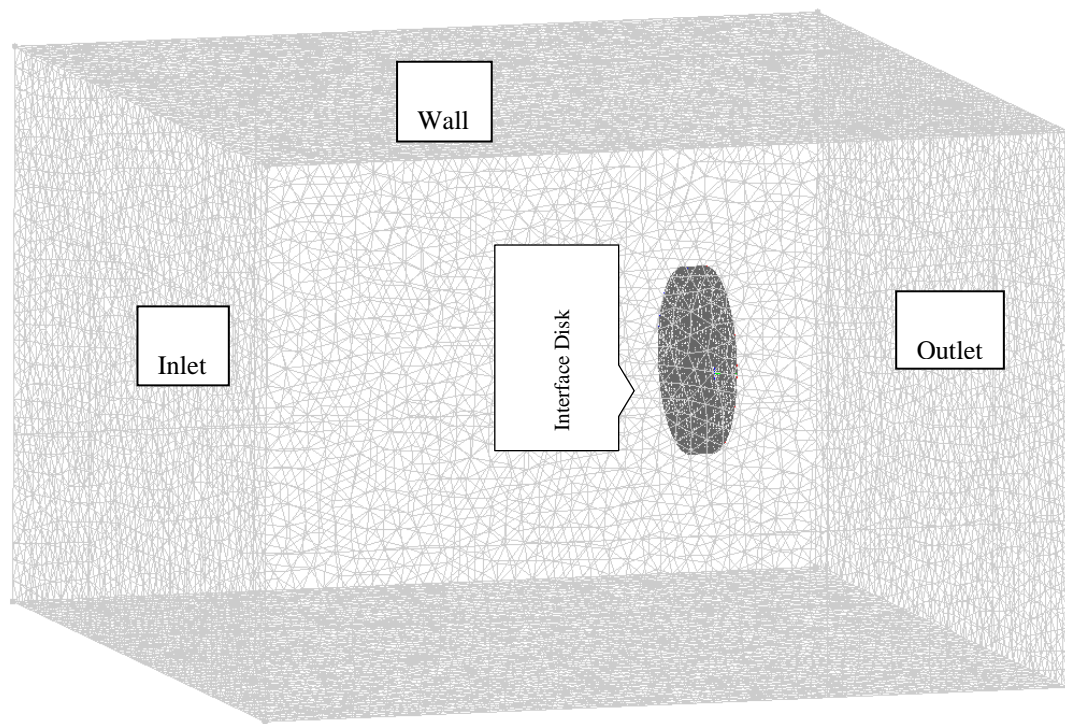


Figure 3.9: The full unstructured mesh of the wind tunnel.

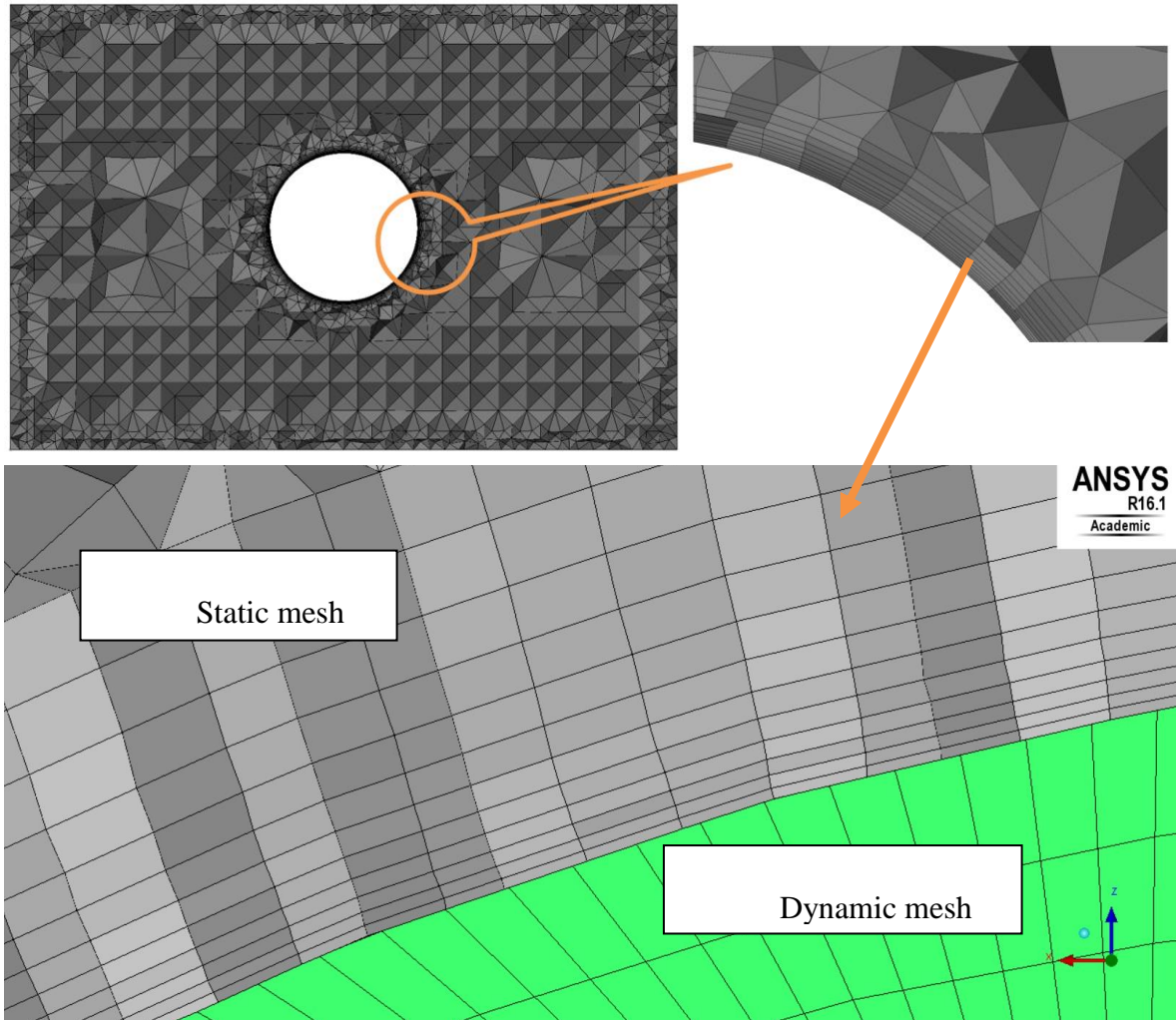


Figure 3.10: Cut plane mesh of the wind tunnel at the hollow disk.

3.2.5 Reynolds number along the blade

In general, Reynolds number (Re) is an indicator of whether the flow is laminar or turbulent flow, or possibly even an in between transitional flow. The following well-known equation can be used to calculate the Reynolds number:

$$Re = \frac{\rho c V_R}{\mu} \quad \text{Equation 3-2}$$

Where V_R is the relative velocity used when the blades are rotating and non-stationary to employ the stream flow (V_∞) instead of V_R . The denominator μ is the dynamic viscosity.

Reynolds number was calculated at the root, where the chord of the aerofoil in the cross-section is longer than other points, and at the tip, where the chord length along the blade is shortest, and the results are shown in Table 3.3:

Table 3.3 Reynolds number values.

Wind speed (m/s)	Re at the root	Re at the tip
7	593,057	907,763
10	685,074	923,033
13	792,991	943,472
15	871,037	959,682

The results showed that the flow is turbulent at the two selected locations when the Re at each point exceeds a typical value of Re (5×10^5), from which point the Re can be considered high according to (Burton et al., 2001); therefore, the flow is completely turbulent along the blade span.

3.2.6 Solution Procedure (Fluent Settings)

The software used in this research is Ansys Fluent 16.1. The coupled algorithm, which combines the momentum and pressure-based continuity equations, was used to solve the Reynolds's Averaged Navier-Stokes equations. The Courant number, which represents the transfer of flow particles from one computational cell to another within one time step, was specified at 1 (FLUENT user guide). The Ansys Fluent 16.1 is the flow solver for the current study and it is the newest academic version the University of Sheffield has available for download to standalone computers. The boundary conditions of this study will be detailed in the following paragraphs.

The velocity inlet was set to indicate the velocity of wind sucked into the test section and an absolute reference frame was selected for when flow was normal to the boundary. As the entrance was exposed to the atmosphere, the initial gauge pressure was 0 kPa. Assuming this study would be conducted under incompressible flow conditions ($M < 0.3$), the temperature would be stable roughly at the room temperature so that the density was remained largely unaffected. Because of the density of fluid is independent of the

temperature in (incompressible flows) and then independent of the energy equation, a pressure-based solver could be used to solve these equations.

As regards the two wall boundary conditions (blades and wall of the test section), the no-slip wall category of boundary conditions was utilised. The no-slip wall boundary condition was kept as default at the blades and slip wall boundary condition for the wall of the test section, when the wall shear effects at these boundaries could be ignored, and the coarse mesh was applied (ANSYS Fluent user guide).

Whereas, because the flow had already been considered to be subsonic, the static pressure at the outlet boundary condition was adjusted to 0 kPa. Generally, flow can be described as subsonic when the flow motion is lower than the speed of sound everywhere in that flow, in other words where the Mach number less than 1. The Mach number (M) is defined as the ratio of the wind velocity to the speed of sound. According to Hand et al. (2001), the maximum velocity of the NREL/NASA Ames wind tunnel is 50 m/s and this velocity causes the Mach number to be lower than 1, so the flow in that tunnel is permanently subsonic. In addition, due to the Mach number in the flow in the wind tunnel not exceeding 0.3, compressibility effects could usually be ignored.

The symmetric and possible in this study the periodic boundary conditions could not normally adequate when the aim is to investigate the effect of the unsteadiness of the wind velocity. At the beginning of this study, the direction of the fluctuating flow would be intended to be simulated, hence the decision was taken to build a full model wind turbine but this idea was then cancelled.

For moving of the blades, two cases of rotating the dynamic mesh were applied; one with various wind speeds and the other with the mean wind speed. For the CFD validation and to mimic the experimental work, seven various wind speeds from 5m/s to 25m/s were employed and the blade speed was fixed at roughly 7.54 rad/s (72 rpm) to compute the power coefficient at various tip speed ratios. Whereas in the unsteady flow cases, the mean wind speed of 6m/s was constantly used for all conditions. According to Chen (2016), the turbulence intensity and turbulent length scale of the experimental work were 0.1% and 0.02 m respectively, which is similar to Edwards et al. (2012). A turbulence intensity value of 0% can never occur on earth, hence it should be adequate for unsteady wind flow simulations. The turbulence intensity can be considered as the ratio of the root-mean-square

of the velocity fluctuations, to the mean flow velocity which also indicated the turbulence level. The turbulent length scale is a physical quantity in Fluent which represents the size of the active large eddies in the turbulent flow.

A mesh interface was set between the surfaces of the hollow of the disk in the test section and the surfaces of the rotating disk around the blades so as to enable the disk to spin when running. In this step, the mesh interface created between the hexahedral and tetrahedral meshes and the interface options were kept being as default.

The pressure-based solver was chosen in the current study. This solver includes two manner of solution: segregated or coupled. The coupled algorithm, which is used in this study, solves the momentum and pressure-based continuity equations simultaneously, whereas, the pressure-based segregated algorithm solves them separately. The solution method was set as a coupled scheme, then the second order upwind for the momentum, turbulent kinetic energy, and specific dissipation rate. The second order upwind is an approach which is used by FLUENT to solve numerically algebraic equations at cell faces. Although the second order upwind approach is more difficult to converge, it provides more accurate results than the first order one. The turbulent kinetic energy is generated in then transferred from the mean flow to the fluctuating flow and it is lost as heat energy due to interactional forces between the motions of different scales what is called eddies. Specific dissipation rate, like ω and ε , for example, is a parameter which refers to the energy lost by the viscous forces in the turbulent flow.

The steady flow condition simulations were primarily run at a constant wind speed of 6 m/s. After that, various wind speeds from 5m/s to 15m/s were tested in order to validate the current simulations. At highs above 13m/s, the blade displayed large scale flow separation and the torque curve fluctuated with flow time. Additionally, unsteady simulations were run for the mean velocity of 6m/s wind speed with different amplitudes and oscillating wind periods. In unsteady flow cases, the time-step size was set to be 1°, from 0.00182s at 8 TSR to 0.0164s at 1 TSR with 30 sub-iterations per time step. All the simulations were performed on the University of Sheffield HPC ICEBERG system in order to minimise the time taken. For the different wind speeds the rotational speeds of the wind turbine with constant wind speed are 1.193 to 9.544 rad/s for the tip speed ratios 1 to 8

respectively, while the rotational speed of the wind turbine is 7.54 rad/s, leading to tip speed ratios from 2.78 to 7.6.

In each of the simulations conducted in this research, air would flow in through the inlet of the wind tunnel and some of the air would pass through a refined mesh that was stuck around the blades in the rotating disk. Therefore, the blades inside this disk would rotate with respect to the disk circumference while the rest of the air flow would go through the outer wind tunnel mesh and then to the outlet and so on.

3.3 Steps in creating the model of this study

The modelling and mesh generation mapping in this study can be summarised as follows:

1. Prepare the geometry by modifying the S809 aerofoil at each blade cross-section (thickness and twist) after simplifying the aerofoil's geometry as much as possible to avoid the sharp trailing edges.
2. Create a surrounding binding disk that is wider than the blades span-wise.
3. Generate blocks as either solid (blades) or fluid (around the blades).
4. Split the main block into four O-grid blocks around the blades.
5. Deform two blocks to fit aerofoils geometry and two others to go around the aerofoil as an O-Grid.
6. Associate block vertices and edges to points of the aerofoil geometry.
7. Edit meshing parameters by inserting grids in each block elements.
8. Test the mesh quality and, in the presence of the cells have a big distortion, deform them to obtain better mesh quality.
9. Compute the Jacobian's $3 \times 3 \times 3$ determinant and Eriksson Skewness to test the mesh quality.
10. The above steps apply to the structured mesh, while generating the unstructured mesh for the outer box is less complex. Create the elements of the wind tunnel and leave a space to enable the disk to fit around the blades, then compute a volume mesh and delete the mesh inside the space to avoid overlapping between the cells.
11. After testing for cells with determinant below 0.3, export the ICEM file to the solver (Fluent).

3.4 Summary of this chapter

To sum up the work implemented in this chapter, a full size of NREL Phase VI was configured using Ansys ICEM package. The two blades of the wind turbine were inserted inside a mesh box to simulate the lab work of the NREL/ NASA-Ames. In this study, interface boundary conditions were chosen rather than periodic or symmetric conditions which would not have been convenient for carrying out the next unsteady flow simulation. In addition, a hybrid mesh technique was employed which combines the hexahedral grids on the blades and on the rotating interfaces around them with the tetrahedral grids for the surrounding box which also has many prisms layers generated on the circumference of the internal hole. The size of the mesh was investigated in an independence case study and 6.6×10^6 grids approach to the experimental data. The mesh refinement was achieved by modifying the sharp edge of the blades and setting up the O- shape mesh around the blades to make the grids non-orthogonal and thereby avoid an inaccurate or fluctuated CFD solution. The mesh files were then ready to set up in FLUENT for initialising solutions. All the solutions with 200, 280, 320 and 380 cells showed good similarity with results from the experimental work; however, the $280 < n < 380$ range emerged as probably the best choice for this study.

CHAPTER 4

Computational Fluid Dynamics (CFD) Validation

4.1 Introduction

In this chapter, the results of the modelled wind turbine described in chapter three will be discussed and analysed and then compared with the findings of the NREL/ NASA-Ames lab and QBlade data. The results of this chapter will pave the way to the next essential part of the present study which is to investigate the effect of unsteady flow on the wind turbine, covered in the next chapter.

The optimum total number of grids for the rotating cylinder will be examined. In addition, the appropriate turbulence models will also be tested and validated by experimental work. Then, the main findings of this chapter will be shown consecutively.

4.2 Mesh size case study results

Before initiating the jobs in Fluent, the quality of the mesh needed to be checked to ensure the solutions were independent of that mesh. Three mesh sizes were examined, at 4 million, more than 6 million and roughly 9 million grids, and these were tested at wind speeds of 7, 10, 13 and 15 m/s with $k-\omega$ SST turbulence model. The computed power coefficients of the blade were compared with those from the NREL phase VI rotor. Generally, in all cases, the computed power values followed the same trend as those in the experimental work. In the 4 million grids case, however, there was only slight agreement with the experimental power values except at low Reynolds's number and tip speed ratios below 3, when all values were relatively identical, as can be seen in Figure 4.1. This could mean that this number of cells, is not sufficient to capture the flow details around the blades. Whereas the other two larger mesh grids agreed more closely with values from the experimental results except in the case of an obvious divergence at the tip speed ratio =3.8. Since 9 million is quite a high number of cells and there would have been significant additional time to reach convergence for each case run, the 6 million cell mesh was selected for the current study.

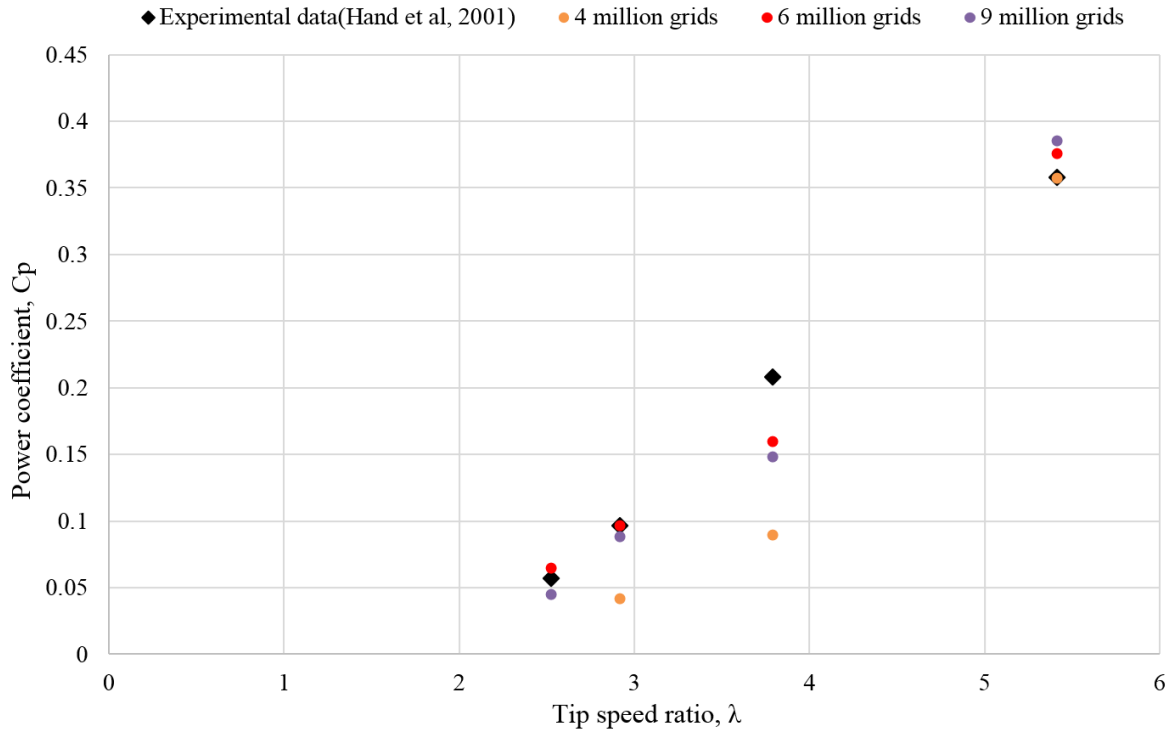


Figure 4.1: Comparison of different numbers of grids at various wind speeds.

4.3 The boundary layer and the turbulence model

The y , which is a distance from the blade surface, was calculated using the following formula and the y^+ value is within the viscous and buffer layers:

$$y = \frac{y^+ \mu}{\rho V_\infty} \quad \text{Equation 4-1}$$

This was used to capture the flow details near the wall (viscous sub-layer), where viscous effects are dominant, and to model the viscous sub-layer and the buffer layer. For the current work, the SST $k-\omega$ model with low Re correction was chosen in the current work which requires a wall y^+ to be around or less than 5 for accuracy. In this study, the wall y^+ varies from 2.5 to 15 along the blade and the average value of y^+ generally is about 7 at 7 m/s, which is acceptable, according to Mo and Lee (2012).

A comparison study of turbulence models was done to indicate which model is most appropriate for the requirements of this work and two popular turbulence models $k-\omega$ SST and $k-\epsilon$, were tested. The reason for choosing these models is that they are the models most frequently used by researchers who have utilised the NREL phase VI within their works.

The equation used to obtain the performance of the wind turbine is shown below:

$$C_p = \frac{T \cdot \omega}{0.5 \rho A V_r^3} \quad \text{Equation 4-2}$$

This equation refers to the ratio of the produced power from the wind machine to the kinetic energy available in the wind flow. As mentioned earlier, in chapter two, the maximum achievable theoretical value of the power coefficient is 0.593 (Betz's limit), so it is not possible to exceed this value. The simulation with respect to experimental data was assessed, and as shown in Figure 4.2, there is high agreement between the simulations and the experimental values of the performance achieved for many wind speeds. All the results followed the same trend as the experimental findings; however, one tip speed ratio (3.85) displays an obvious deviation, which is similar to the finding by Yelmule and Anjuri (2013) of reasonable agreements with experimental data except at 10 m/s wind speed, where the flow separated over the whole blade pressure side. Similarly, Park et al. (2007) reported high agreement between their numerical solution with the experimental work except at 10 m/s wind speed. This wind speed was considered as “critical point” when the hard to predict stall started to appear. Moreover, separate CFD studies by Sørensen et al. (2002) and Derakhshan et al. (2015) produced results that were highly conformable to the experimental data, excepting the 10m/s result which showed clearly over-prediction.

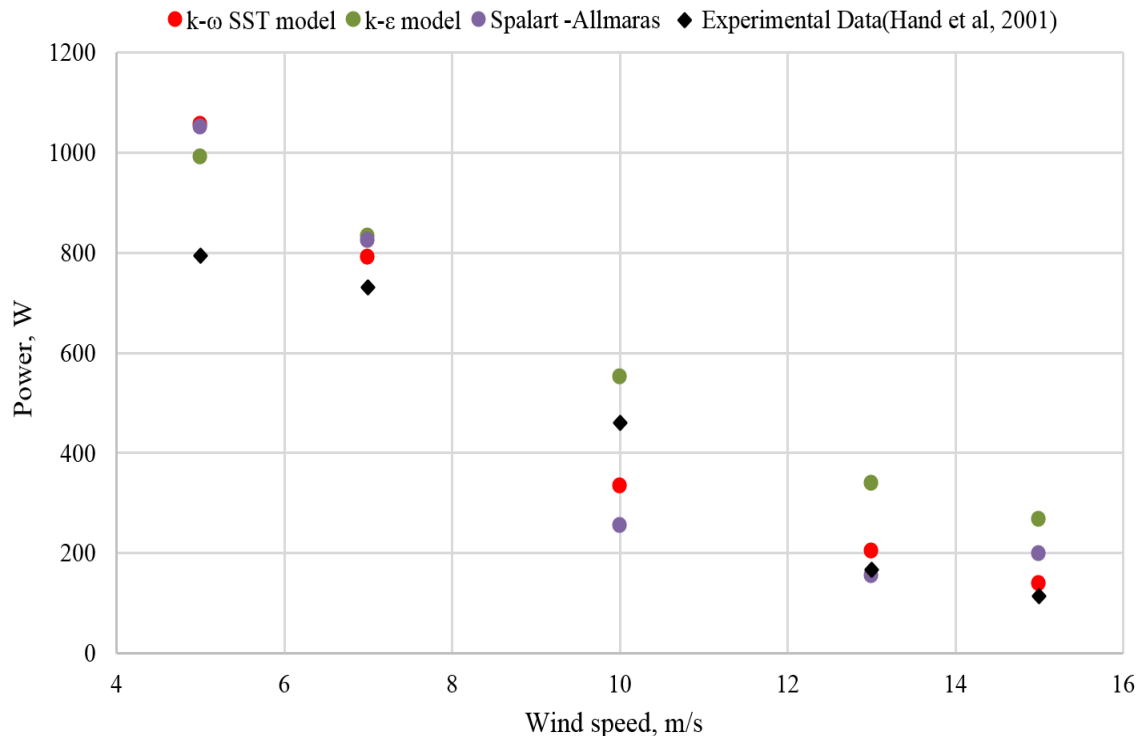


Figure 4.2: Comparison of three different turbulence models at various wind speeds.

Comparison of these turbulence models with the NREL experimental work at various wind speeds illustrated clearly visible difference between the k- ϵ model and the experimental data. The k- ω SST and Spalart–Allmaras models, however, are closer to the experimental work over most of the range tested. To sum up, although all the models showed similar trends to the experimental data, the k- ω SST model showed much better results and matched the experimental power values at all wind speeds closely except at 10 m/s where the curves clearly diverged for the reason mentioned above. At the wind velocity 5 m/s, the CFD predictions could not perfectly followed the experiment data up to 7 m/s, where the results converge. Since 25m/s is used very rarely, more realistic, and common speeds were run. The current CFD study was not able to run 20 m/s and 25 m/s and this also happened to Hao (2016). The current CFD results, however, are generally acceptable and could be considered adequate for performing the next studies.

4.4 Torque of the rotor

The coefficient of torque C_m from the CFD simulation was used to calculate the torque developed by the turbine and calculated using equation (4-3). The results were compared to the experimental data.

$$C_m = T/0.5 \rho R A_b V_r^2 \quad \text{Equation 4-3}$$

The data in Figure 4.3 shows a large difference between simulations and experimental results at wind speed ranging between 5 and 15 m/s. At 10 m/s, however, there is an obvious inconsistency with the experiments achieved. All in all, the results of the current simulations work follow the same performance and torque trends as the experimental work to an appreciable extent.

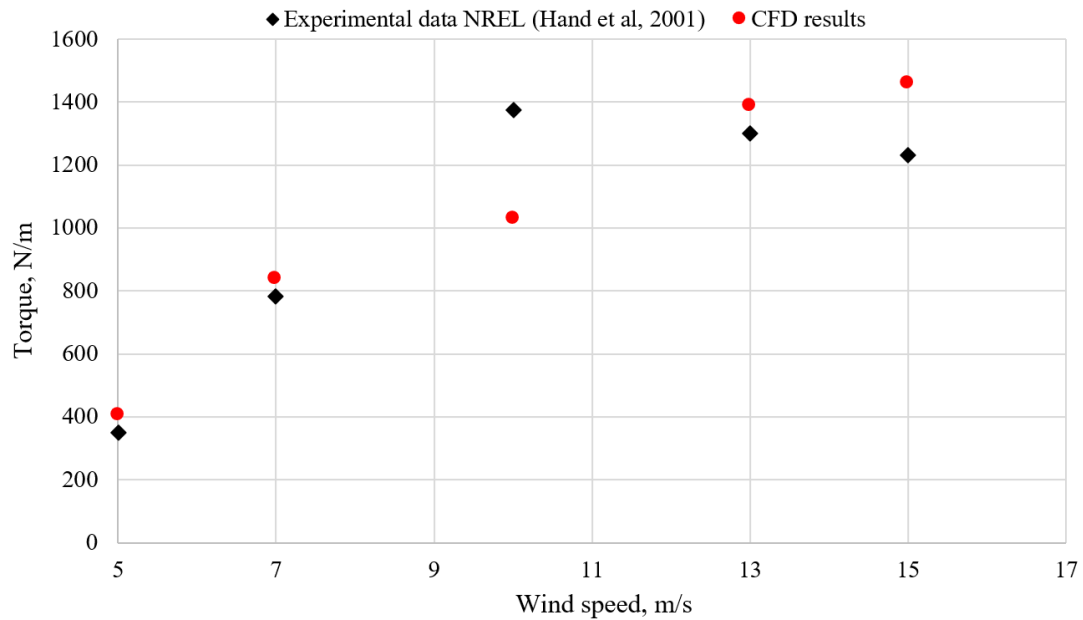


Figure 4.3: Torque coefficient against wind speeds.

Another comparison between two turbulence models was conducted to investigate the behaviour of the C_m at high wind speed and the results were presented in Figures 4.4. It seems clear from the figure that the curve of the torque is fluctuating in the $k-\omega$ SST model, whereas in the $k-\epsilon$ model the curve is steady. This likely means that the $k-\omega$ SST turbulence model captured highly the boundary layer details around the blade when compared to the other turbulence model.

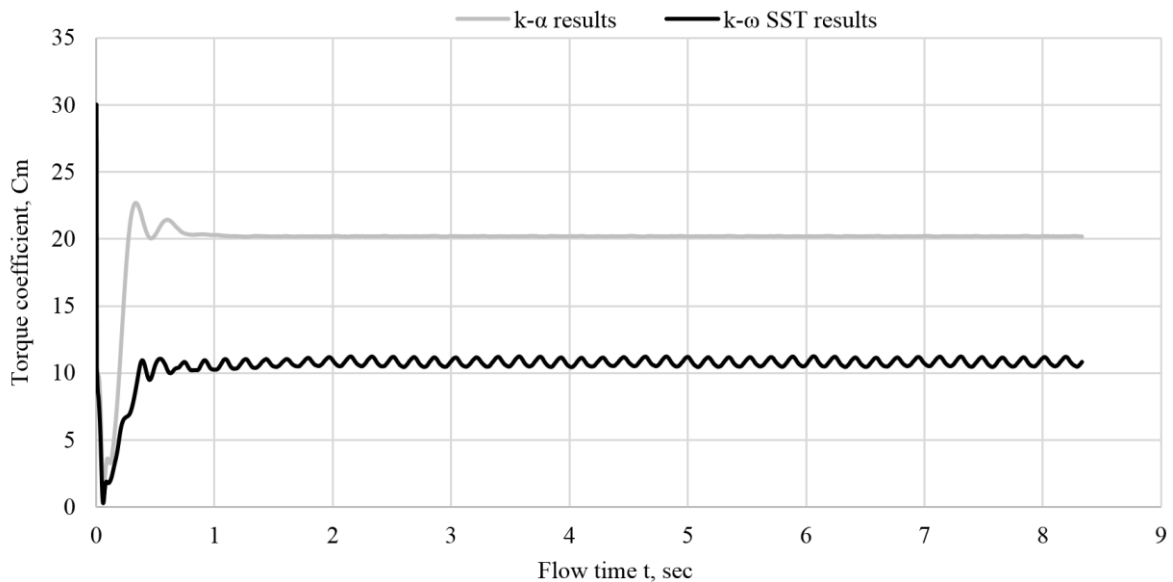


Figure 4.4: Comparison of torque coefficient of two different turbulence models at wind speed = 15m/s.

4.5 Time step size checking

The time step (Δt) is the gradual change in flow time for which the governing equations are being solved, in other words a time for a rotation. To capture all the flow fluctuations, using a small time-step size would be advised, but the smaller the time step the longer the time to convergence. In this case the solver time in Fluent should be set to be transient.

A study case was conducted to investigate the effect of time step size on the accuracy of the CFD results. Three-time step sizes were examined at three different degrees of rotation: 0.5, 1 and 2 degrees. All of three-time steps were run at a chosen wind speed which was 7 m/s ($\lambda=5.4$).

The results, as shown in Figure 4.5, illustrates a slight disparity in torque coefficient between these three degrees of rotation, although the 0.5 degree result seems more accurate but was more time-consuming. In addition, the continuity convergence line reached 10^{-4} , which is close to the default value 10^{-6} , for both 0.5 and 1 degree, while it did not exceed 10^{-3} with 2 degrees. So, a 1 degree time step size was adapted for the next runs.

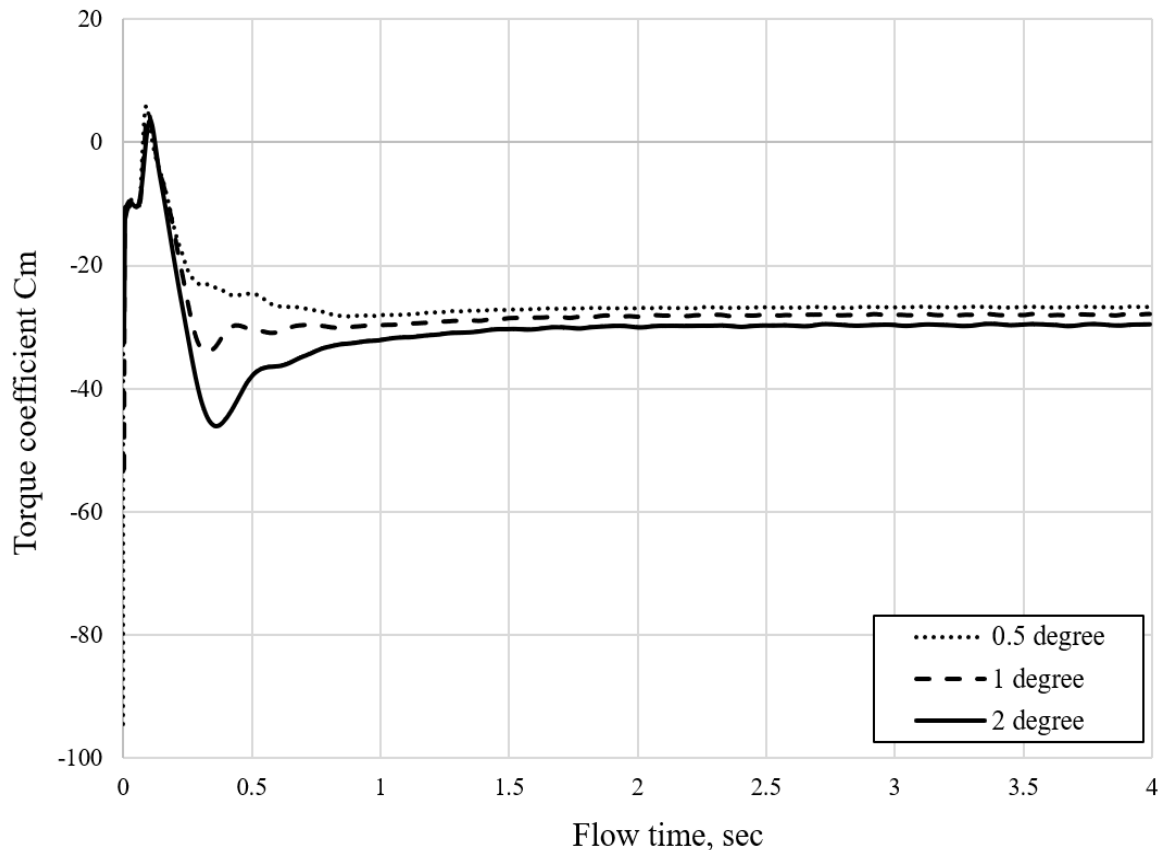


Figure 4.5: Torque coefficient history at $\lambda = 5.4$ for three-time step sizes.

The solver was computed for 30 iterations to simulate the process of the experimental work. However, this number of iterations was not chosen randomly but based on an independent case study, and the findings are demonstrated in Table 4.1.

Table 4.1. Numbers of iterations per time.

Wind speed at 7 (m/s)	C _p , CFD	C _p , NREL experimental data	Difference %	Computational time, hr
10 iterations/time	0.417754	0.35859	5.92	20
20 iterations/time	0.390627	0.35859	3.2	63
30 iterations/time	0.37842	0.35859	1.98	88
40 iterations/time	0.36966	0.35859	1.11	124

Regarding the number of iterations in this case study, three numbers of iterations were employed in order to find the best converged solution. From table 4.1, it is obvious that the first of these, 10 iterations, and possibly 20 iterations also, did not capture the flow details accurately, but once the number of iterations was raised to 30 or 40 the results were closely convergent with the experimental data. This indicate that it was unnecessary to test more than 30 iterations, which would also have increased the calculation time for the simulation and is no noticeable change in the numbers of the power performance.

4.6 Friction coefficient (C_f) and Pressure coefficient validation

In this section of the study, friction coefficient could provide more information regarding the flow attachment case. The friction coefficient C_f is defined as:

$$C_f = \frac{\tau_w}{0.5 \rho V_r^2} \quad \text{Equation 4-5}$$

where τ_w is the component of cross-sectional shear stress tangential to the surface.

The friction coefficient C_f along the blade span-wise in Figure 4.6 for four various wind speeds ranging from 7 to 13 m/s. Contours for the C_f, obtained only from the k- ω SST turbulence model, are shown. The surfaces are coloured by the value of the skin friction coefficient which is the non-dimensional value associated to the wall shear stress. In the

region near the leading edge, the flow starts with a maximum pressure value at the stagnation point then decreases up to a minimum value, while the flow velocity increase along the surface. This is the favourable pressure gradient region ($dp/dx < 0$) and ($dV/dx > 0$) and there is no chance for separation in this region ($C_f > 0$).

After that the pressure is recovery and begins to increase along the surface, while the velocity decrease ($dp/dx > 0$) and ($dV/dx < 0$) so, there is a risk of separation ($C_f \leq 0$).

It is observed that in the case of 7 m/s wind speeds, the flow stays attached except for the middle section close to trailing edge which shows local separation. At 10 m/s, the previous local separation moves towards the root of the blade. The flow also detached on the suction side in a region in the front of the blade.

Finally, the plot for the wind speed of 13 m/s reveals, to some extent, has an analogous behaviour to the previous case.

The pressure coefficient CP at some specific points along the blade chord was investigated numerically and then compared to the experimental work. Before highlighting the results, this coefficient needs to be determined, since it has a significant aerodynamical effect. In general, the pressure coefficient can be defined to be a dimensionless term which represents the ratio of the static pressures into the dynamic pressure throughout a flow field. The pressure coefficient is widely used in aerodynamics when the lift force generated due to the difference between the pressures up and down around the blades' surface (Anderson, 2008). This coefficient is commonly applied to study the flow of incompressible fluids, and the low-speed flow of compressible fluids. Mathematically it is expressed as:

$$CP = (p - p_{\infty}) / (0.5 \rho_{\infty} V_r^2) \quad \text{Equation 4-6}$$

This equation was actually mentioned in chapter two, but the relative velocity used here instead of the incoming wind speed.

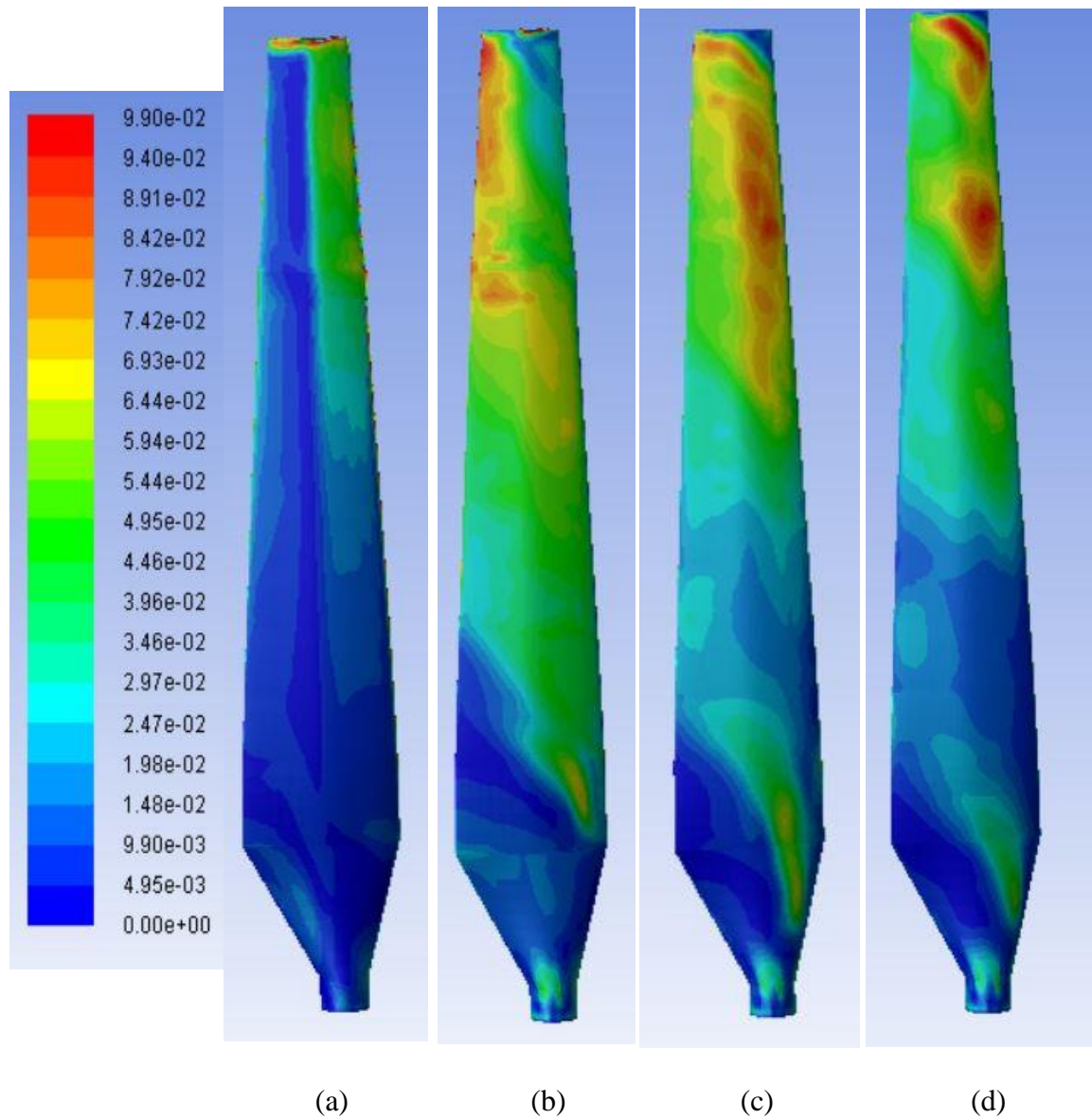


Figure 4.6: Skin friction coefficient (suction side) at wind speed 7m/s (a), 10m/s (b), 13m/s (c) and 15m/s (d).

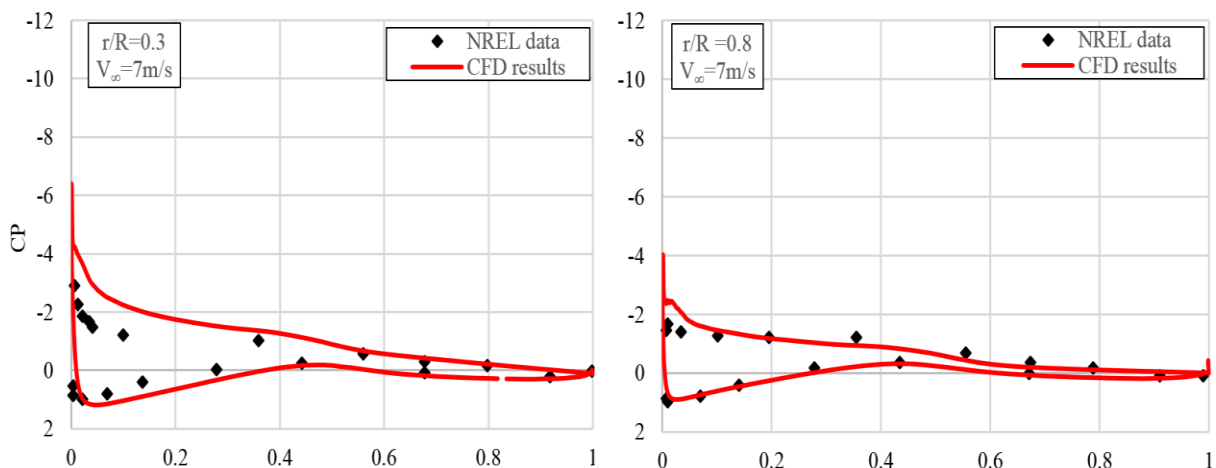
In this study, two sections along the blade were selected for comparison to the pressure coefficients (CP) at each ratio of the aerofoil length to the chord (x/c) that was taken from the NREL experimental work, as shown in Figure 4.7. The first section is 30 % along the blade, which is near the root where the angle of attack is high. The second section is 80 % along the blade, which is near the 75 % point of the blade where much of the power is generated.

As shown in Figure 4.7, for the low wind speed of 7m/s, high agreement is shown for two span-wise sections except the leading edge at 30% where a minor discrepancy between the two curves is likely owing to high angle of attack.

Similarly, the CFD data of the 10 m/s case satisfactorily predicted the pressure distribution along the blade, excluding the leading edge separation at the $r/R = 30\%$ section, which is relatively similar behaviour to that shown in the other CFD results. There is a noticeable discrepancy between the computed results and the measured results. This could be due to the unsteady behaviour of the flow around the aerofoil, in particular at the suction side of 30% span-wise case. The Reynolds numbers are higher, which might make the flow more unstable.

Looking at Figure 4.7 again, it is obvious that for the higher wind speeds (13 and 15 m/s), the blade reveals much separation and the flow is no still steady. The CFD results showed good agreement with the measured data, in particular, at the tip better than at 10m/s.

On the whole, the CFD findings were highly predictive in relation to the NREL results, although there were slight disagreements at $\lambda = 7.58$ (5m/s). Meanwhile, at $\lambda = 2.53$ (15m/s), low momentum keeps the turbulent boundary layer attached entirely to the surface of the blade. Moreover, when wind turbine experiences a stall it could vibrate the blade and that could lead to lowering of the CP. When λ increases at 2.92 and 3.8, an obvious tolerance can be seen between the data and that could be due to high unstable flow around the blade; however, greater separation is likely along the suction side of the blade.



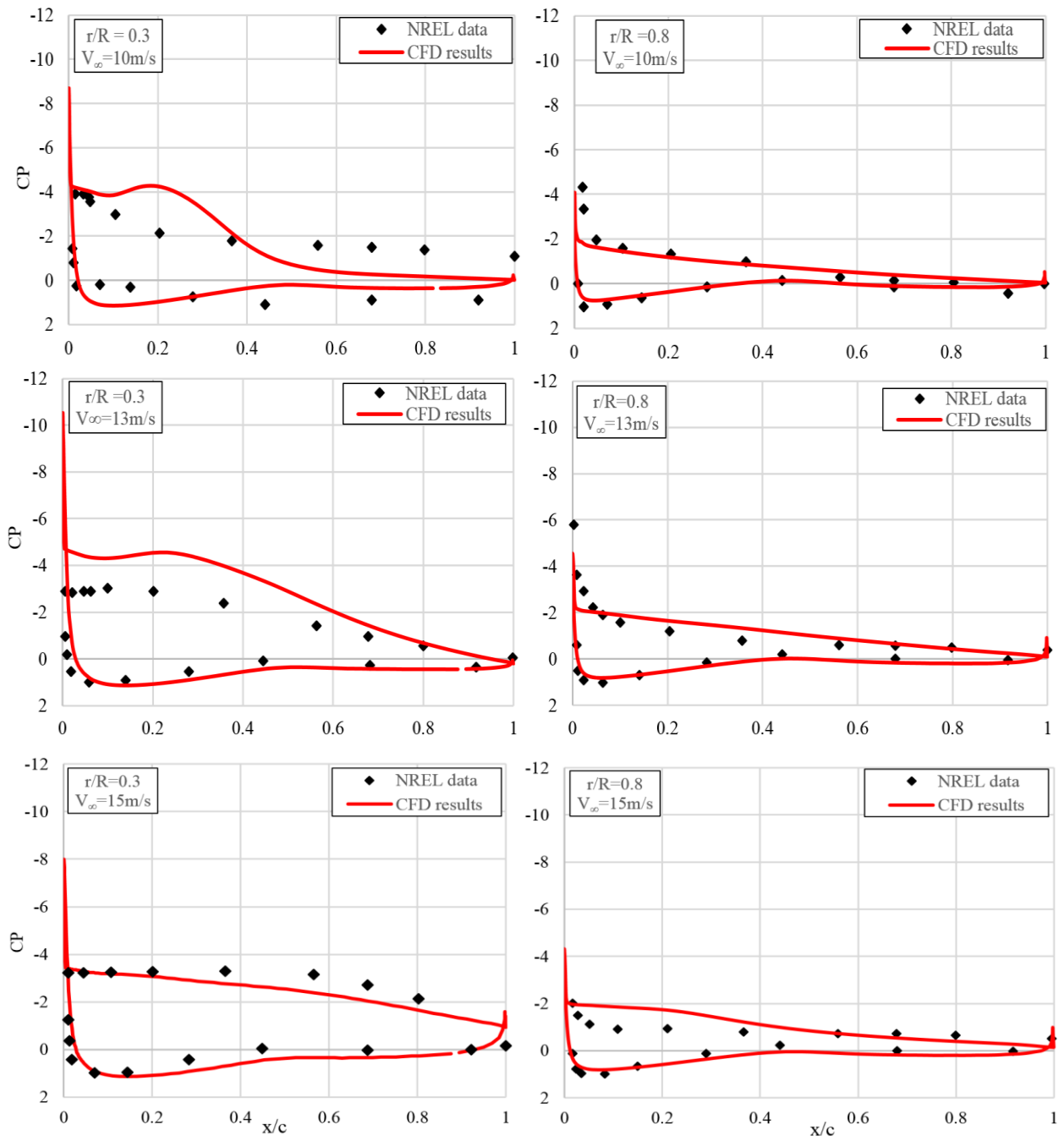


Figure 4.7: Comparison of pressure coefficient at four wind speeds 7, 10, 13 and 15 m/s.

4.7 Surface limiting streamlines distribution

Figure 4.8 displays the streamlines of the wind velocity around the rotor blade at 75% of the blade span, showing both the attached and separated flow on the suction side of the blade. Similar to the NREL experimental work, five wind speeds were tested at 75% spanwise of the blade, to reveal the flow behaviour above the blade. At 5 m/s (point **a**), it can be

seen that the flow is still attached on the blade surface; when the angle of attack is low then the lift force is also low. With further increase in wind speed specifically at 7m/s (point **b**), angle of attack increases and then the flow starts to separate near the trailing edge. At high wind speeds (points **c**, **d** and **e**), a remarkable flow separation occurs when the stagnation point on the pressure side surface is seen near the leading edge; in addition, the lift to drag ratio drops rapidly (because of high drag) and the blade stalled fully as a result of high angle of attack.

Figure 4.9 displays an overview of the flow behaviour on both blade surface (pressure and suction side) at five different wind speeds. Starting with high tip speed ratio at 7.58, it is clear that the streamlines direction is entirely parallel to the chord, which means that the flow around the blade is attached to the whole blade surface. Nonetheless, in a small area in the root, as indicated by the red circle, it appears the flow is unable to attach the surface. With further decrease of the tip speed ratio to 5.428, the flow begins to separate near the trailing edge in the pressure side of the blade as indicated by the red ellipse, while on the suction side flow separation clearly takes place at the mid-span area of the blade. At $\lambda=3.8$ the separation line shifts afterward towards the trailing edge of the blade. Similarly, at low tip speed ratios $\lambda=2.92$ and $\lambda=2.53$, air flow separation can be seen further away from the leading edge on the pressure side. Moreover, flow separation still predominates and covers most of the suction side area and the centrifugal force can pull the stagnation point line up over the suction side area of the blade. According to Hansen (2008), Coriolis Effect and centrifugal force both have an effective and influential role in the boundary layers beyond the stall. The Coriolis Effect, which was mentioned briefly in chapter one, accelerates the wind flow in the chord-wise from the leading edge. Meanwhile, the centrifugal force, which can be defined as an outward force that likely affects rotating wind turbines, forces the air to flow radially from the root to the tip of the blade (Du et al., 2005 and Carcangiu, et al., 2007). The prediction of the flow in the tip (end of the blade) region could be considered complicated when three-dimensional effects are dominated there.

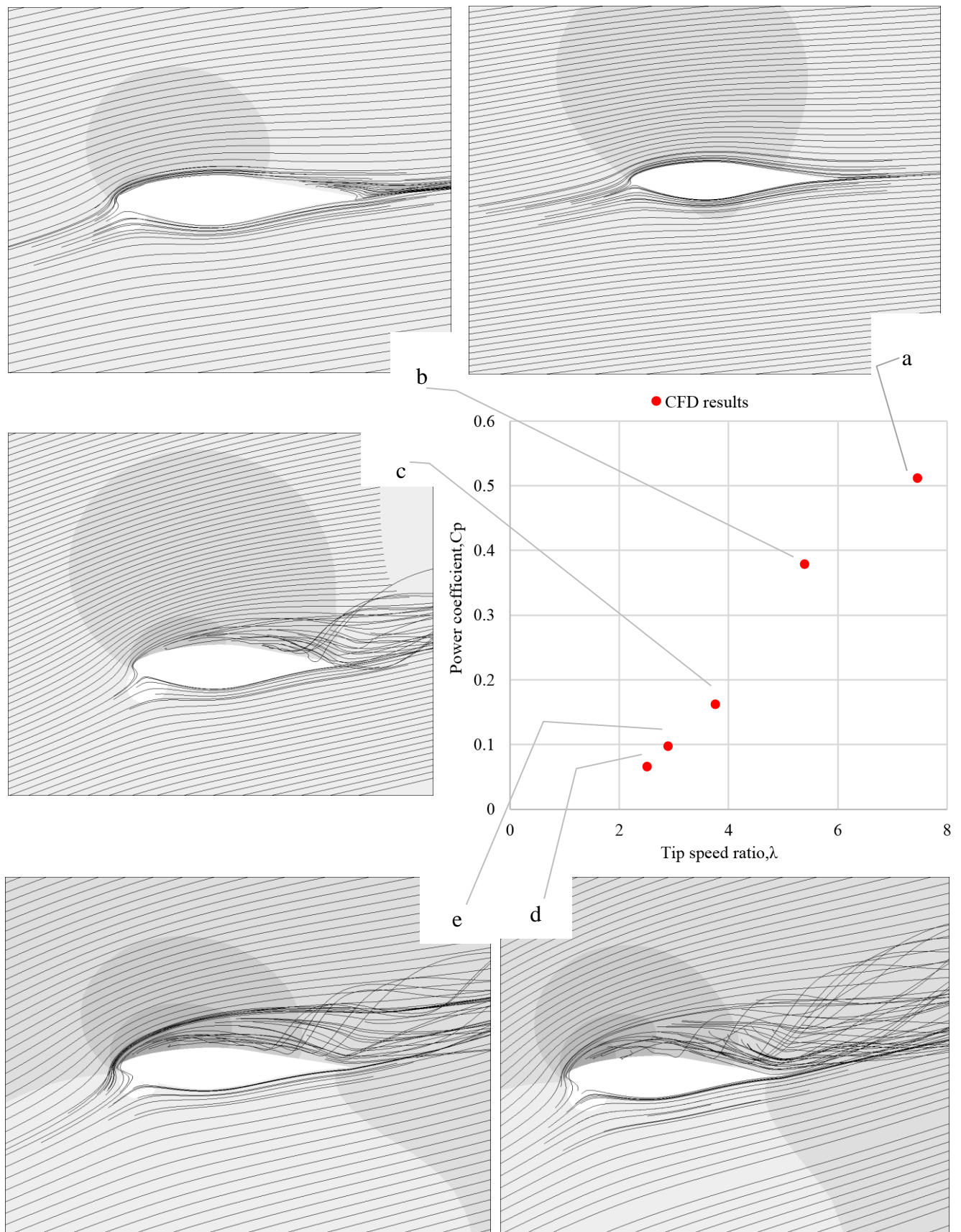
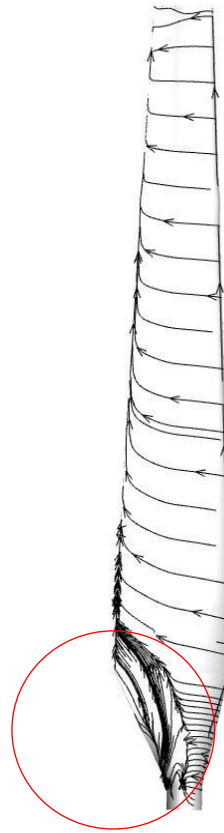
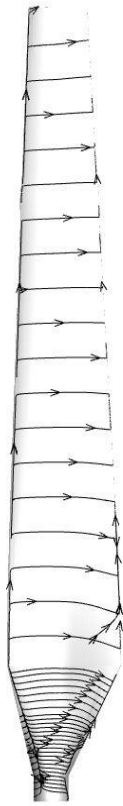
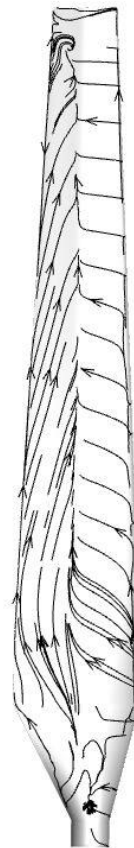
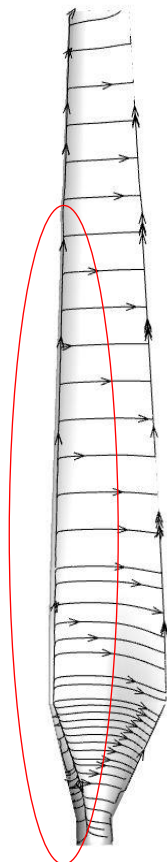


Figure 4.8: Current CFD data obtained at 75% of the blade span.

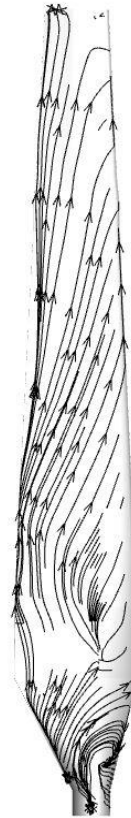
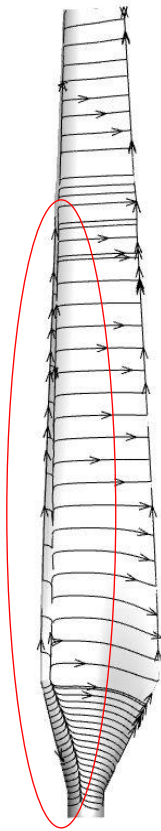
$\lambda=7.58$



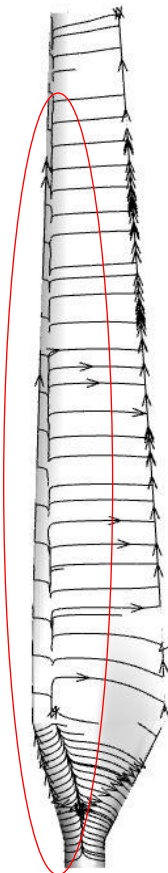
$\lambda=5.428$



$\lambda=3.8$



$\lambda=2.92$



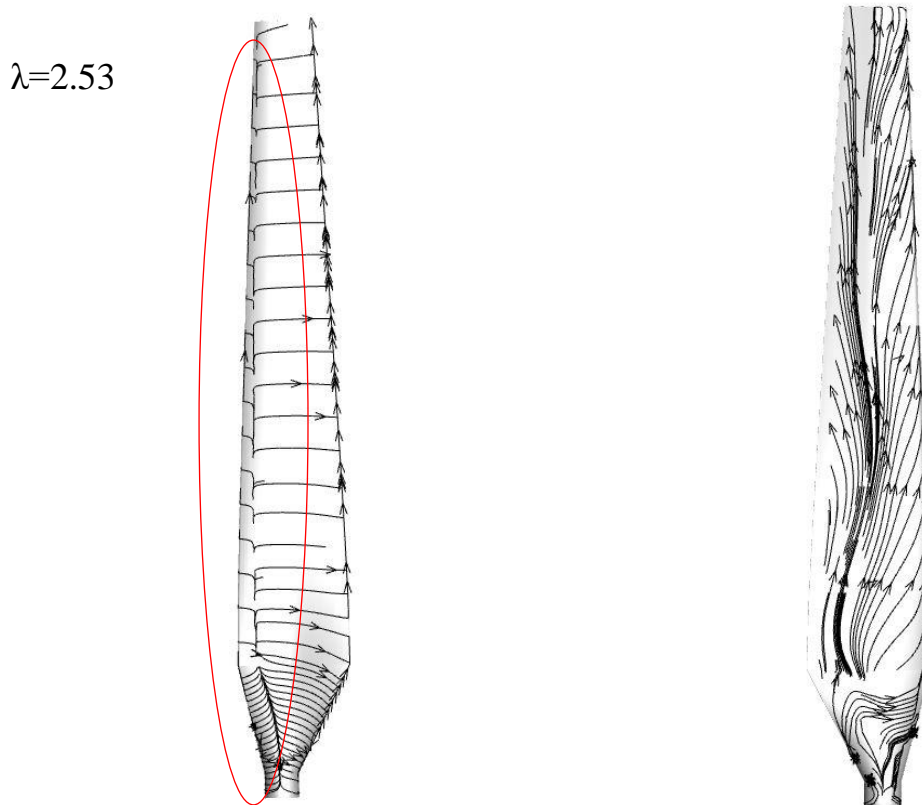


Figure 4.9: Limiting streamlines distribution on pressure side (left) and suction side (right) of the blade at various λ .

4.8 Blade element momentum theory (BEM) Validation

The QBlade is run by creating a rotor when all its aerofoils are defined. These aerofoils can be formed via a NACA aerofoil generator within the QBlade tool or imported other aerofoils are unavailable.

The flow around the aerofoils can be mimicked by the XFOIL and then analysed for a limited range of AOA values. Then, the rotor can be designed and optimised in the HAWT and VAWT command. The final full geometry over a range of wind speeds can be simulated, after setting the simulation parameters.

XFOIL is a software program used to compute and analyse flow details around a 2D aerofoil section. The XFOIL code is used to compute lift and drag coefficient polar for aerofoils. A full scale NREL wind turbine model was built in QBlade as shown in Figure 4.10.

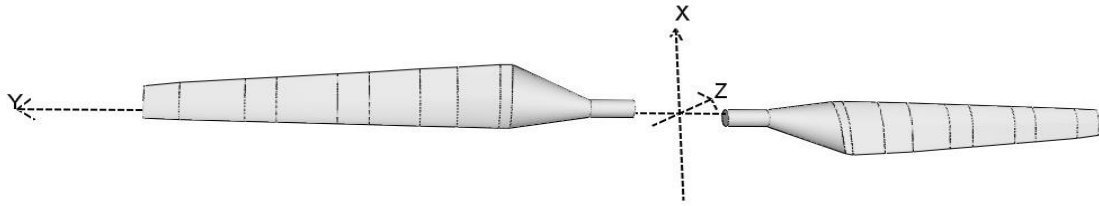


Figure 4.10: Full scale NREL wind turbine built in QBlade.

The validation of QBlade was initially conducted using the various wind speed experimental work and then CFD results were compared to the constant wind speed QBlade results as shown in Figure 4.11. This procedure was followed due to the lack in the experimental work at constant wind speed for this wind turbine model.

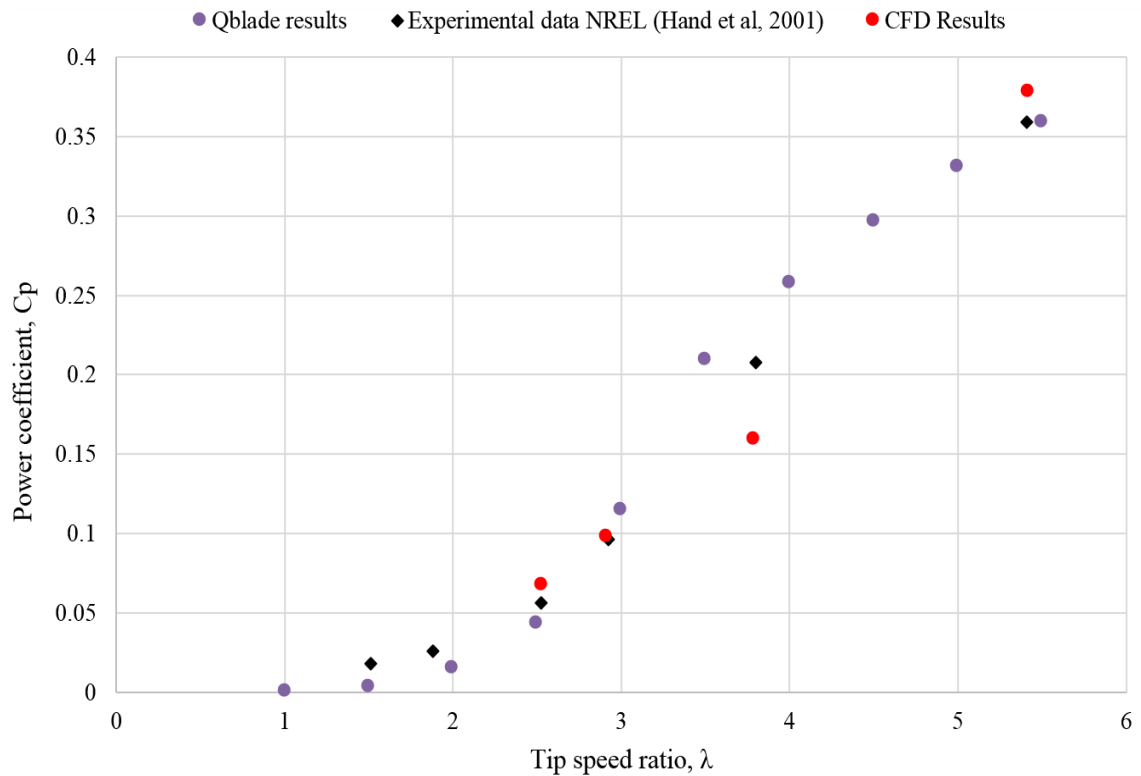


Figure 4.11: Validation of full scale NREL wind turbine in QBlade at various wind speeds.

In figure 4.11, there are missing points for tip speed ratio of 1.5 and 2, which should be available, due to CFD limitations at high wind speeds as mentioned earlier. However, CFD results demonstrated the ability to come close to matching the experimental data except at $\lambda=3.8$, which was not so much, when the C_p value seems under prediction. It seems that the

CFD cannot reliably predict the stall at this tip speed ratio then the power value diverges from the experimental value.

All in all, Figure 4.11 shows a good agreement between all the curves; therefore, QBlade tool can be relied on for use in the next phase of the study. Moreover, the current findings can support that were obtained from a study conducted by Mahmuddin (2017) that mentioned earlier in chapter two.

4.9 Summary and findings of this Chapter

To sum up the work carried out in this chapter, the performance of the NREL phase VI was obtained from FLUENT using the three most widely used fully turbulent CFD turbulence models ($k-\omega$ SST, $k-\varepsilon$ and Spalart–Allmaras) over a wide λ range of 1 to 10, at intervals of 1. The $k-\omega$ SST turbulence model was found to be the most accurate turbulence model for this study, when compared with the measured C_p data for a wind turbine with the same scale of wind and specifications. The mesh near the wall, in addition, was needed to be properly sized in order to achieve a desired y^+ then that would capture a more accurate simulation of the flow field. The power coefficients were compared at four wind speeds and data were examined numerically against experimental data of the NREL phase VI. The $k-\omega$ SST model was considered the most appropriate to this study because it best captured the full flow details. In addition, the mesh quality was investigated previously with three grids and the grid containing around 6 million cells was considered to be most suitable for the next studies. Further comparison work was performed with experimental power coefficient results of the wind turbine. The simulation work showed, in general, acceptable prediction of the performance and computed torques at the all tip speed ratios, although for $V_\infty=10\text{m/s}$ there was an obvious discrepancy with the experimental work. These findings paved the way for the main part of this work. Moreover, the BEM simulation results showed an acceptable agreement with the NREL experimental results.

CHAPTER 5

Steady Flow Simulation

5.1 Introduction

This chapter will highlight the results gained from using the CFD model at constant average wind speed. The results trend will be utilised when the influence of unsteady flow on the performance of the NREL phase VI wind turbines is examined in the next chapter. The performance of a scaled-down turbine will, in addition, be examined.

5.2 Validation of the constant wind speed case

Due to a lack of experimental data at constant wind speed, the QBlade tool was employed in order to obtain data to use in comparison with the performance of the HAWT model.

An independent simulation case study was conducted to validate the performance of a wind turbine at the constant wind speed of 6m/s, with the QBlade tool, Figure 5.1. The results of odd numbers tip speed ratios are hidden, and the even numbers could be sufficient to show the results. The full scale NREL wind turbine CFD results follow the trend of the QBlade results except at TSR 6 and 8, where there is a clear difference between the data points. However, the optimum performance of the NREL wind turbine phase VI is still within the TSR range $5.5 < \lambda < 7$ and that mentioned in Eau (2006) and Tadamasa and Zangeneh (2011) for all models shown. Furthermore, the QBlade software code is limited in that it cannot capture flow details around the blade so a perfect match would not be expected.

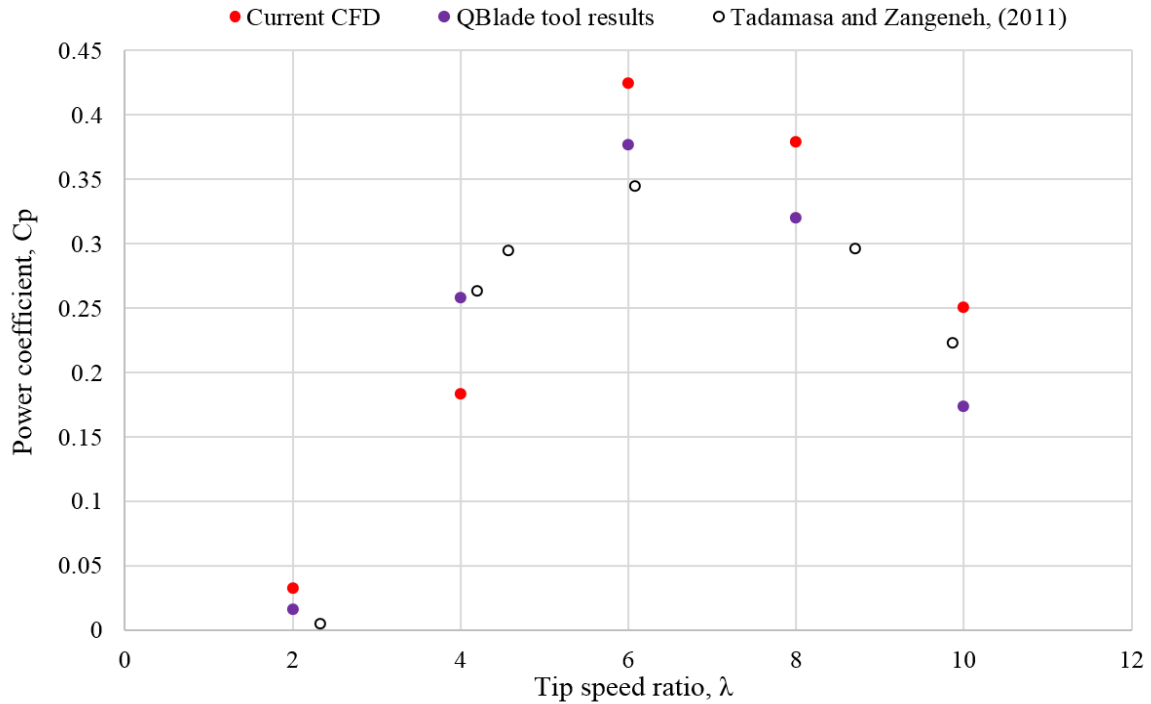


Figure 5.1: Validation of full scale NREL wind turbine in QBlade at constant wind speed.

As shown in Figure 5.1, it is obvious that the peak performance is $C_p=0.435$ at $\lambda=6$ and then it falls off, gradually showing a relatively high power trend region when compared to that from the QBlade tool and data from Tadamas and Zangeneh (2011) when the peak value ranges between $\lambda=6$ to $\lambda=7$. The point of peak performance is considered to be an essential value when designing wind turbines. The peak point of the current study is still within the same width compared to the above mentioned references. Moreover, Tadamas and Zangeneh (2011) stated that their wind turbine performed less well than that used in the actual environment. In general, the current CFD data showed a high degree of similarity to the comparative references, especially at low tip speed ratio $\lambda=2$. Nevertheless, there is a difference in results at $\lambda=4$ between the current study and the others and that could occur due to the hard stall initiating at this region of the tip speed ratio as was demonstrated and discussed in chapter four. All in all, the performance of the various tip speed ratios shows an acceptable trend and was still within the range cited also in Erich (2006).

5.3 Analysis of study wind flow simulations

Two locations along the blade span were selected to highlight the behaviour of the wind flow on the blades using streamlines. The selected locations are: 75% and 30% along the

blade span. The 75% location was selected because the blade at this point is thin and seems untwist, so the blade generates power and flow would be expected to be attached to the surface at this position. For the 30% location, which is relatively thicker than the previous aerofoil and next to the root, the angle of attack is higher, and separation is more likely to occur at lower wind speeds.

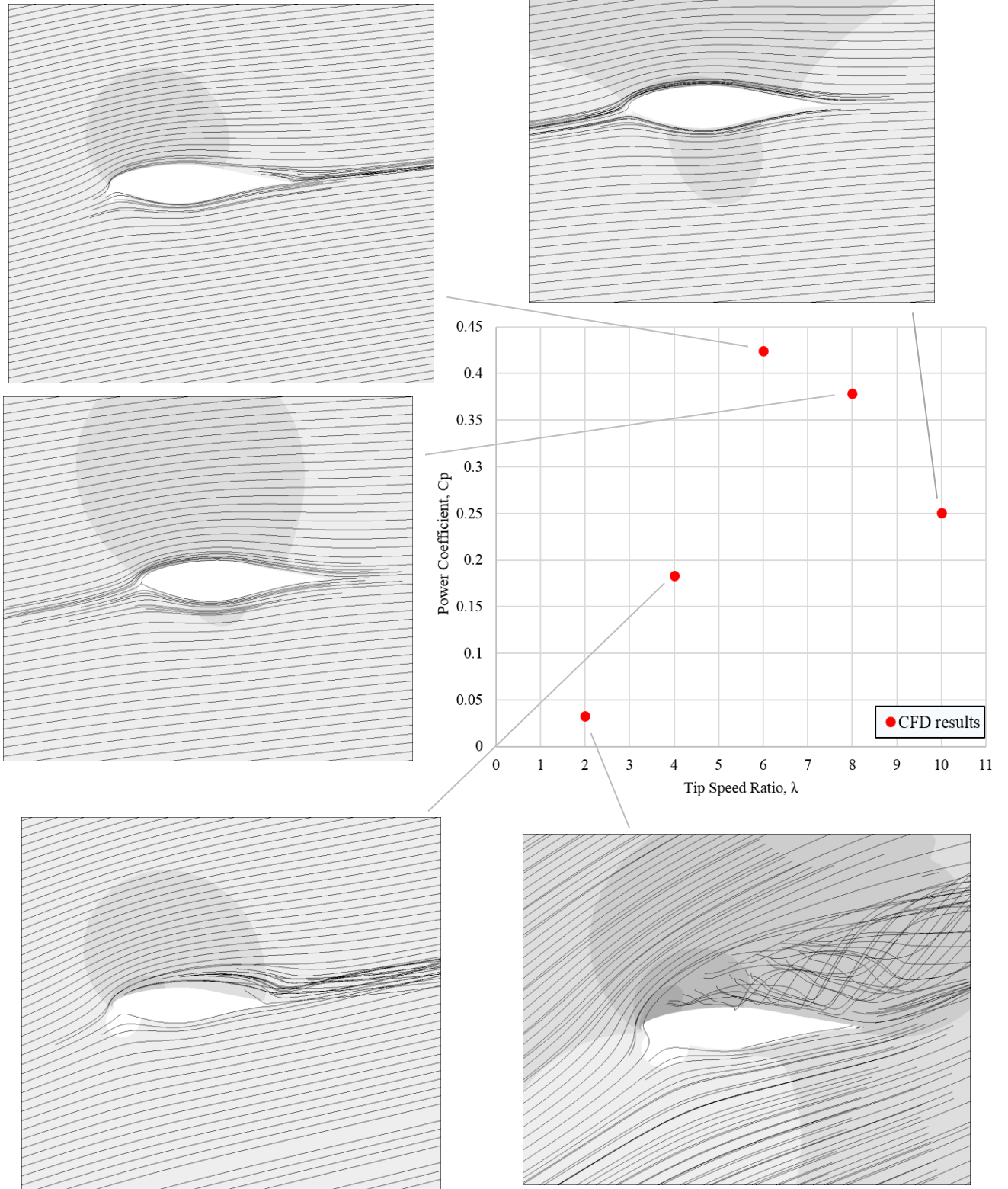
5.3.1 The power trend for the turbine at 75% of the blade

Five points of the power performance curve were chosen to show the streamlines plot of flow around a cross-section of the blade at 75% of the blade span. At each point of the power curve, there is an illustration of how the flow behaves, see Figure 5.2(a) In the Figure, the illustrations show clearly that the blade tends to separate at low tip speed ratios from $\lambda = 2$ until $\lambda=5$ and that separation leads to reduction of the overall performance of the wind turbine. Furthermore, the lift to drag ratio C_L/C_D increases slightly, which could explain why the C_p in that range is relatively low and the effect of stall is seen clearly. Following this, the trend moves further down with an increase in the tip speed ratios and with separation after $\lambda = 6$. Between $\lambda = 6$ and $\lambda = 10$, the flow was closely attached to the surface and the C_L/C_D ratio decreases after the optimum value at the range from $\lambda = 6$ until $\lambda = 7$ and that could happen as a result of flow resistance on separation with increase in Reynolds number.

5.3.2 The power trend for the turbine at 30% of the blade

Similar to the test 75% of the blade, the streamlines of flow around the cross-section of the blade at 30% of the blade span was plotted at five tip speed ratios. As in Figure 5.2(a), 5.2(b) also displays more details about the flow at this length of the blade. The illustrations show clearly that the blade tends to separate at low tip speed ratios from $\lambda = 2$ until $\lambda=5$. Separation initiates near the leading edge of the aerofoil and extends beyond the trailing edge. The lift to drag ratio C_L/C_D , moreover, rises until it approaches the peak of the curve at $\lambda=6$. The peak value of the performance ranges between $\lambda = 6$ to $\lambda = 7$. Beyond $\lambda=7$, no separation occurs to cause reduction of the overall performance; therefore, the streamlines are still attached to the surface. The blade could get to a certain tip speed where the angle of attack will no longer drive the rotation rather resist it

(a)



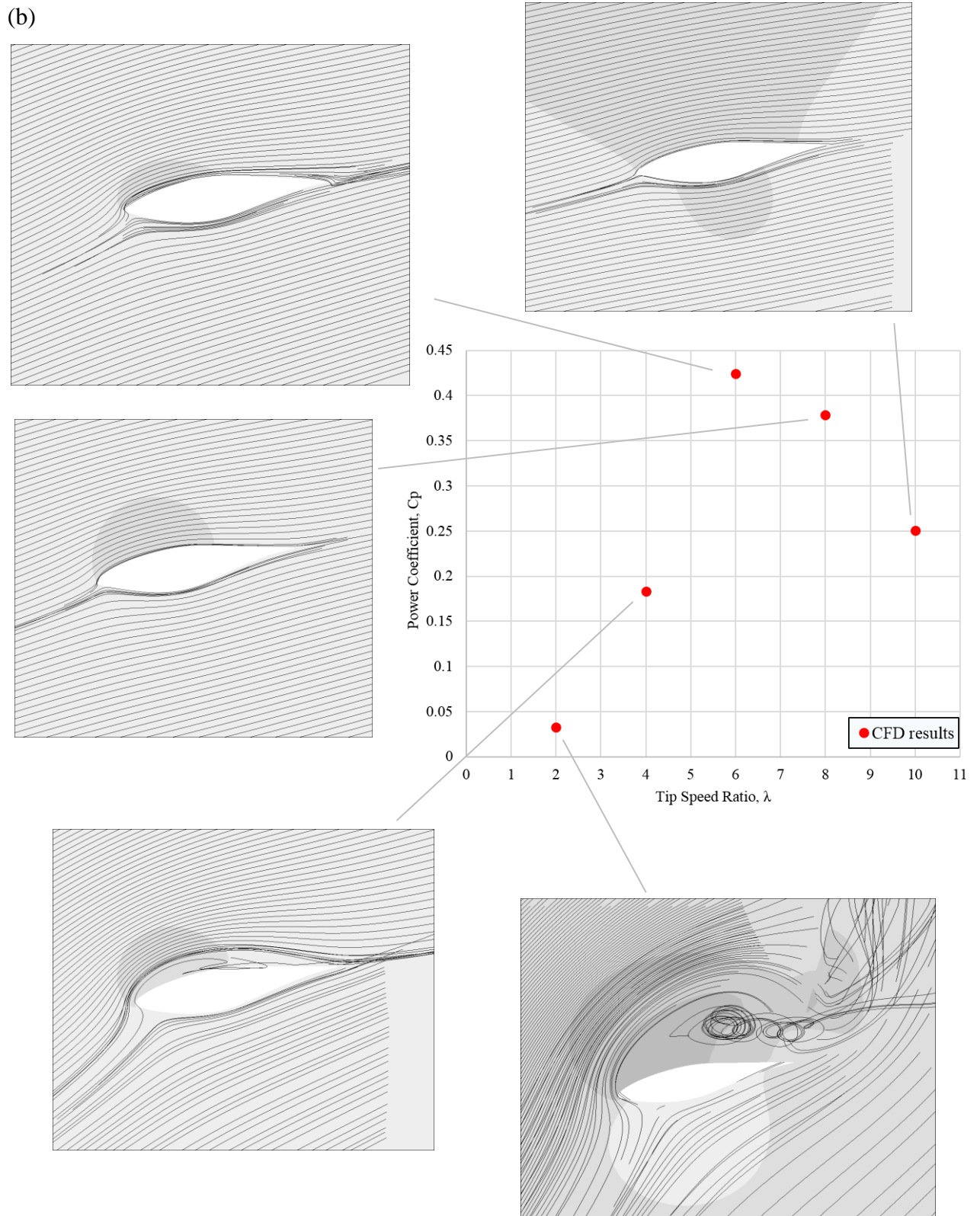


Figure 5.2: Performance trend of the full scale NREL wind turbine at constant wind speed (a) at 75% and (b) at 30% of blade.

5.4 The effect of Reynolds number on wind turbine performance

The influence of the wind turbine's size was tested at constant wind speed of 6 m/s. This test was conducted for both full-size model and a scaled down size 6% of the full -scale model, of 5.029m radius and 0.334m radius respectively. The performance of the two turbines differed when they encountered the incoming wind. Figure 5.3 shows the effect of these different scales on turbine performance at varying tip speed ratios from 2 to 10. The wind turbine's highest C_p performance for both sizes occurs at $\lambda=6$ but scaling the turbine up to full size increases its maximum performance up to 61 %, from 0.26 to 0.42 at roughly the same tip speed ratio. This increase in performance is roughly double that obtained from the 20% scale NREL phase wind turbine test done by Cho and Kim (2014). The trend of the performance of the two rotors is very similar at $2 \geq \lambda$ as Re is low and that causes the overall torque of the turbines to decrease then the performance to be low. It is also obvious that there is a large divergence between the two sizes at the maximum performance at the range that mentioned earlier.

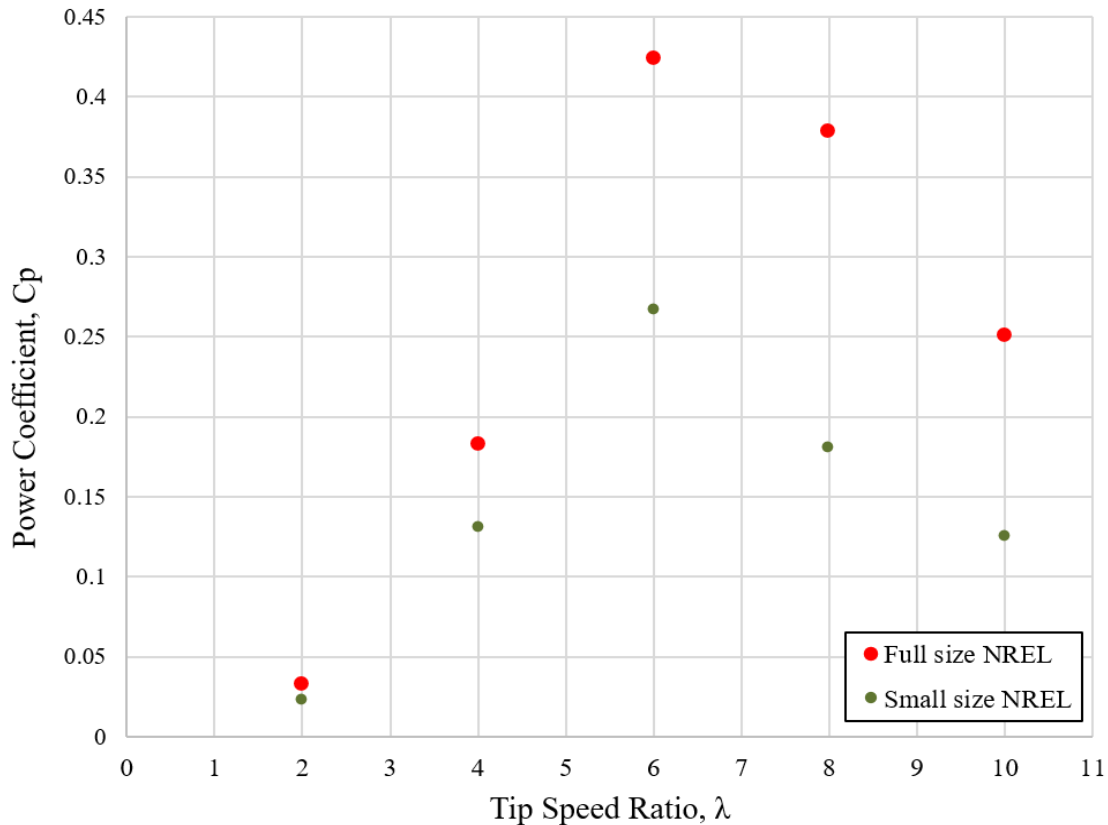


Figure 5.3: The small and large-scale turbines operating at $V_\infty = 6\text{m/s}$.

The computed Re for the small-scale wind turbine is 59,000 at the blade tip increases to 836,000 for the large-scale model (based on chord length at 75 % span of the blade). (Burton et al., 2001) stated that Reynolds number of about 200,000 can be considered a critical point. Above this value, the flow begins to be transition from laminar to turbulent type. The torque of the full-scale machine is higher than that of the small size turbine since the mass and the radius of the full-scale machine are large, even though the small turbine rotates faster than the larger one.

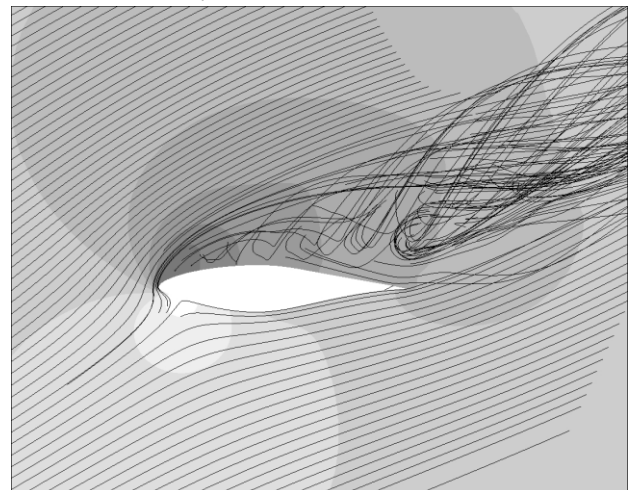
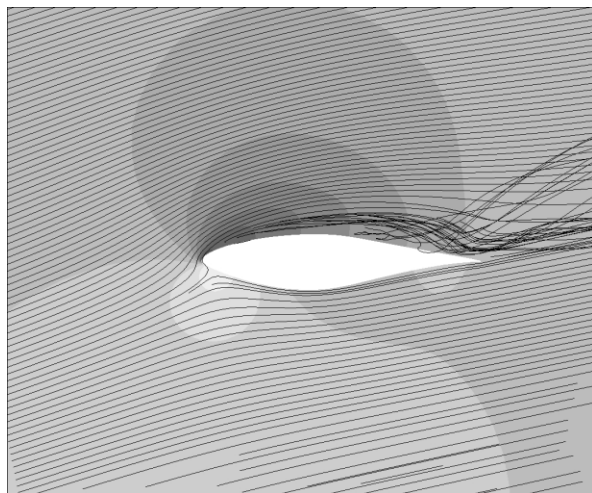
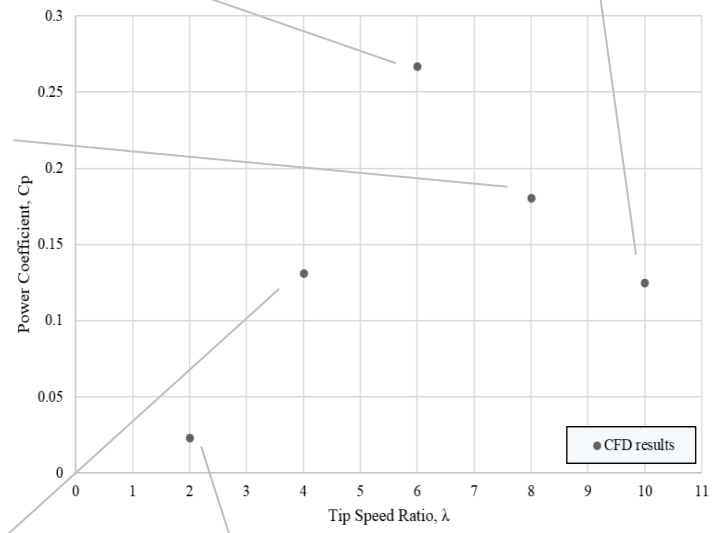
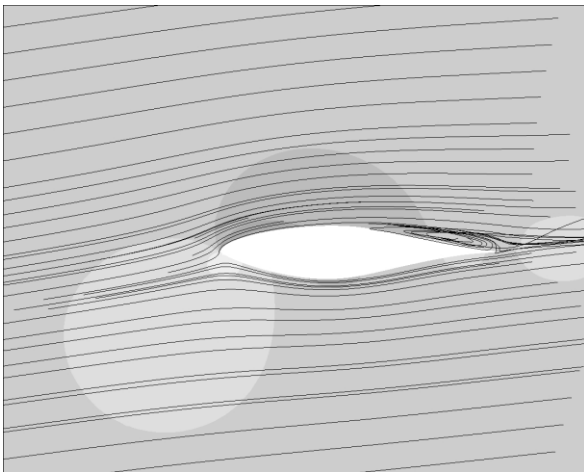
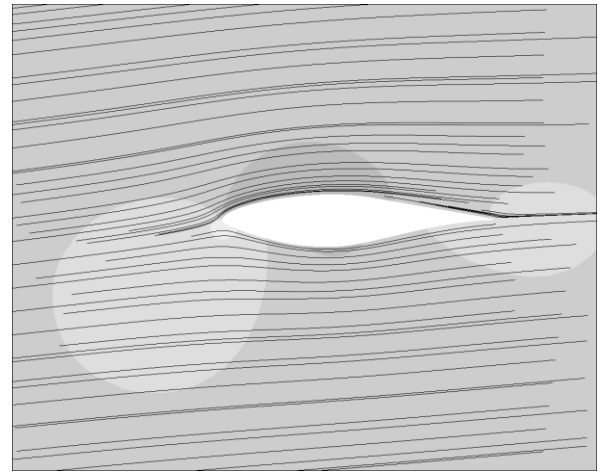
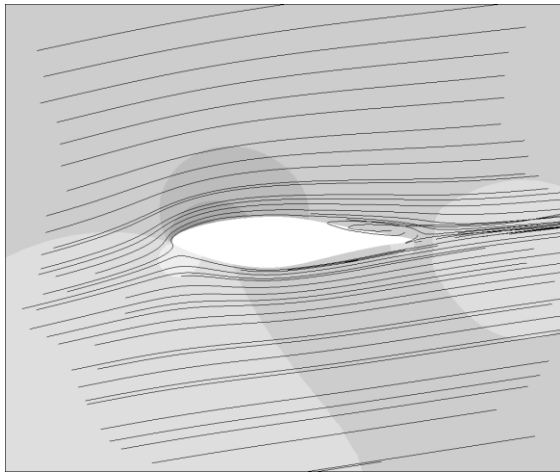
5.4.1 The power trend for the turbine at 75% span of the small size blade

Similar to section 5.3.1, five values of the scaled-down power performance trend were also selected to present the streamlines plot of flow around the cross-section of the blade at 75% of the blade span, as shown in Figure 5.4(a). It is fairly clear that the boundary layer is completely attached to the suction side of the aerofoil at high $\lambda = 10$. The same reason mentioned earlier could apply here, as the angle of attack is relatively low with a high Reynolds number. Whereas below this value, at the moderate $\lambda = 8$ and $\lambda = 6$, the flow begins to separate near the trailing edge and it continues to separate until a large-scale separation can be seen clearly at low tip speed ratios when the angle of attack is higher.

5.4.2 The power trend for the turbine at 30% span of the small size blade

This section reports similar behaviour to that described in section 5.3.2. The flow around the cross-section of the blade at 30% of the blade span at five tip speed ratios is shown in Figure 5.4(b). The attached flow over the aerofoil surface is still dominant at $\lambda \geq 6$. The behaviour of streamlines, however, changes, with the flow separates below that values and a big separation shown at low tip speed ratios and high angles of attack.

(a)



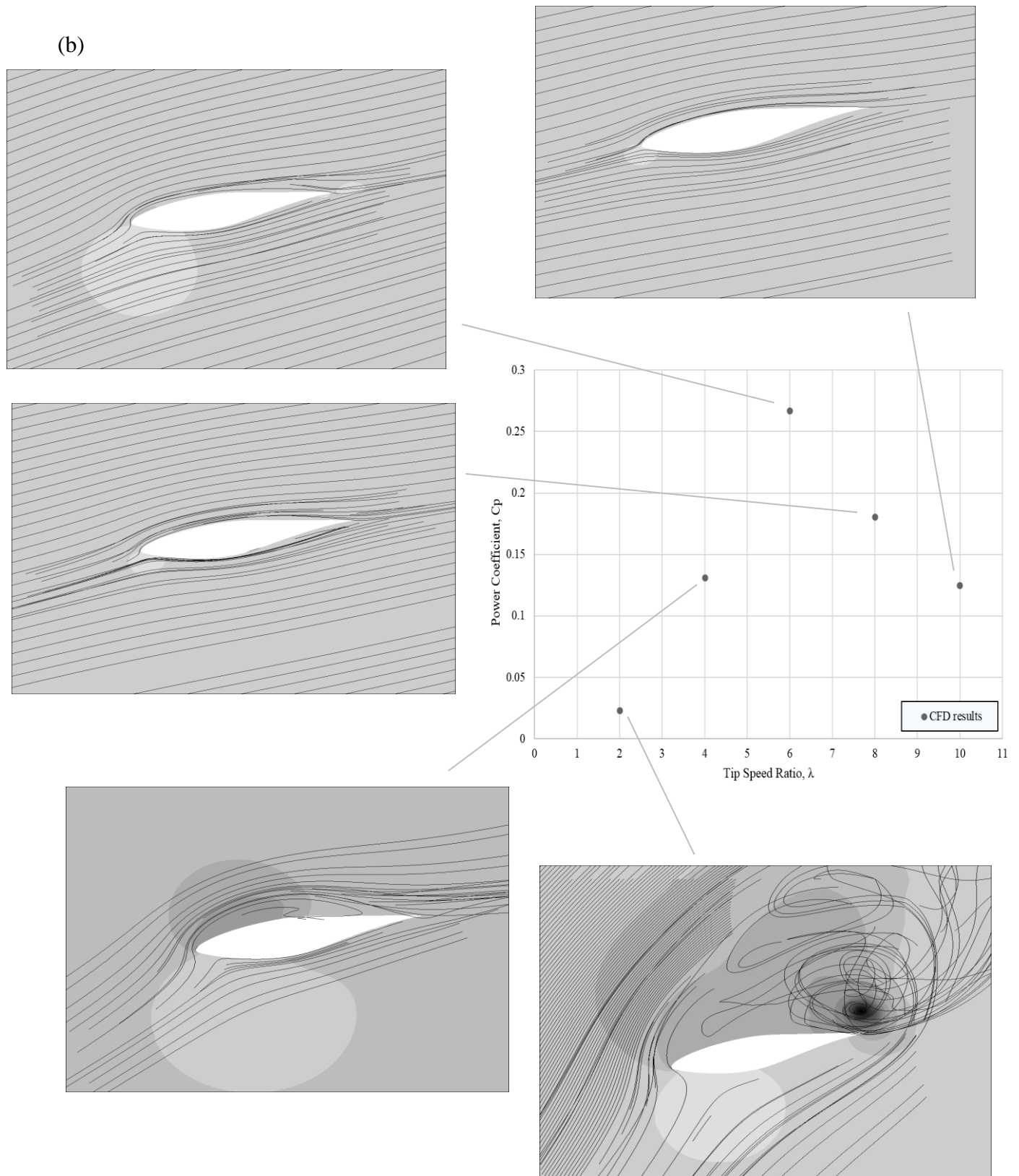


Figure 5.4: Performance trend of the scaled-down NREL wind turbine with constant wind speed (a) at 75% and (b) at 30% of blade.

5.5 Summary of this chapter

The performance of the NREL phase VI rotor was studied with steady inflow and the maximum performance value was identified with $C_p = 0.424$ at $\lambda=6$. The constant wind speed power curve closely follows the other performance trends. The plots of streamlines illustrate the behaviour of the flow around the blades and as expected at high angles of attack (at low tip speed ratios) the flow separates, while at low angles of attack (high tip speed ratios) the flow is still attached to the surface of the blades. Similarly, the effect of a 6% scale wind turbine was examined in this chapter at constant wind speed of 6 m/s. The performance was found to be generally affected by this scaling down, when the performance of the turbine increasing up to 61%, which was approximately twice as high as the results from research by Cho and Kim (2014). This percentage is higher than that obtained from Sobotta's numerical study (2015) which was up to 27%. The streamlines were also plotted, producing satisfactory results.

CHAPTER 6

Unsteady Flow Simulation

6.1 Introduction

In the previous chapter, the performance of the NREL phase VI wind turbine in steady flow conditions was investigated at five different tip speed ratios. The existing model geometry will be utilised again in this chapter in order to study the performance of the wind turbine but with unsteady flow conditions which is the essential aim of the current study.

The tip speed ratio 6, which was at the peak value of the wind turbine performance, will be the pivot point for the next comparative study. Furthermore, the effect of different amplitudes at various frequencies on the performance of the wind turbine rotor will be taken into consideration.

6.2 Simulation of unsteady flow

Initially, the unsteadiness needs to be fully discussed, so the following introduction will give clarification and a more in-depth view. Wind turbines generally operate in challenging conditions where wind speeds in the atmosphere vary in values and directions (Manwell, 2002 cited in Richardsa, 2011).

The same boundary conditions and turbulence model will again be employed in this chapter. However, the incoming wind speed that would hit the wind machine will be of sinusoidal shape and that wind speed needs a user-defined function (UDF) to be compiled in Fluent. The UDF is generally a routine programmed code which is written in C programming language and it is linked with the solver (Fluent 12.0 User's Guide and ANSYS FLUENT 12.0 UDF Manual). The objective of the programming language within this code is to translate the high-level C code into a machine language. The machine language is considered as a low-level programming language when it is well-known and widely-recognised for completely using numbers.

Oscillations in wind speed will be simulated numerically at average wind speed with period of fluctuation using equation 2-15, in chapter two, which was referred to in chapter two and can be applied in the following form:

$$V(t) = 5.985 + 0.41895 \sin(2f\pi t) \quad \text{Equation 6-1}$$

Then, this instantaneous wind speed value will be used to calculate the rotor torque from the torque coefficient. From the torque, performance of the wind machine can be obtained

by using the following equation, which is similar to some extent to equation 4-2 except the velocity was a constant value:

$$C_p = \frac{P_B}{P_W} = \frac{T \omega}{\frac{1}{2} V(t)^3 \rho A} \quad \text{Equation 6-2}$$

Returning to equation 6-1, this represents the final step in an iterative calculation that was performed. Iterative calculations were done at each available cyclic- averaged wind power (P_w) by calculating the non-dimensional normalised flow time (t_n). As mentioned earlier, the average wind speed (6m/s) was adopted to run steady flow cases and obtain the power. This iterative process therefore has to continue until a match in wind power values was obtained with the previous chapter. Therefore, the (5.985) value in equation 6-1 refers to the wind speed which is used to calculate the unsteady flow power to complement the steady flow case. Then, the second term is the fluctuating wind speed that is produced by multiplying the amplitude value of the wind speed by its average value, where f denotes the frequency of the wind flow. The base case of the current study was conducted by considering the fluctuation of the wind speed to be 1 Hz and its amplitude 25%, as surrounded by the green dashed cycle in Figure 6.1. In this case, the run of the simulation's jobs in ICEBERG (The University super computer) took roughly 144 hours and 4.5 rotations of the wind turbine to reach the full convergence where the residual of the cyclic-averaged wind power is highly consistent, as shown in Figure 6.1.

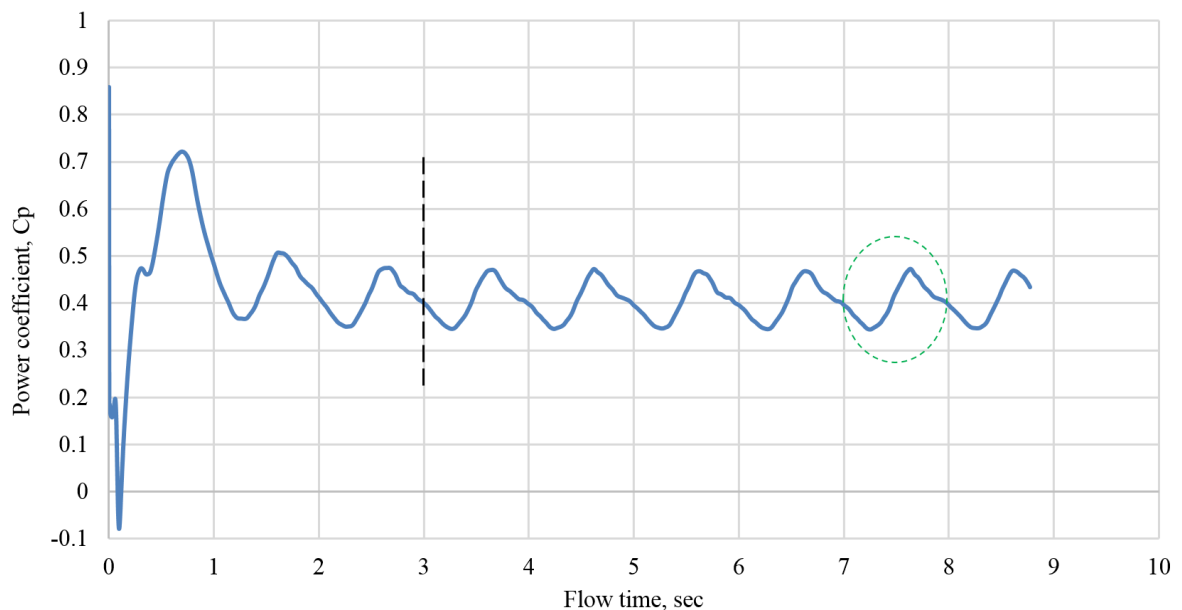


Figure 6.1: Performance of the unsteady flow at 1 Hz frequency and its amplitude 25% at the full complete rotation of the turbine.

In Figure 6.1, it can be seen that the performance curve is clearly fluctuating with the flow time as a result of the sinusoidal wind speed that hits the rotor. The performance curve, moreover, is observed to be a constant attitude in time after approximately 3 seconds from the starting point of the run which is also after about 1/3 turn of the wind turbine, as is indicated above by the black dashed line. In one full cycle of the wind fluctuation, the number of rotor rotations (N) can be calculated from the following form equation (McIntosh et al., 2008, cited in Wekesa, et al., 2014):

$$N_{rev} = \frac{\lambda \bar{U}}{2\pi f R} \quad \text{Equation 6-3}$$

Where λ refers to the tip speed ratio of the maximum power coefficient at the steady C_p - λ curve from chapter five, the symbol f refers to the frequency of the wind flow in Hz. The radius of the wind turbine is denoted by R in meter (m).

Figure 6.2, shows the two curves over the normalised flow time. The first path curve shows the average power coefficient of just one unsteady wind flow cycle. Each point in this curve represents an instantaneous power coefficient resulting from the instantaneous wind speed, while the second curve exhibits the variation of the tip speed ratio at each an instantaneous wind speed over the one cycle. The data of both curves were plotted to provide a good indication of the average λ power coefficient over one normalised flow time.

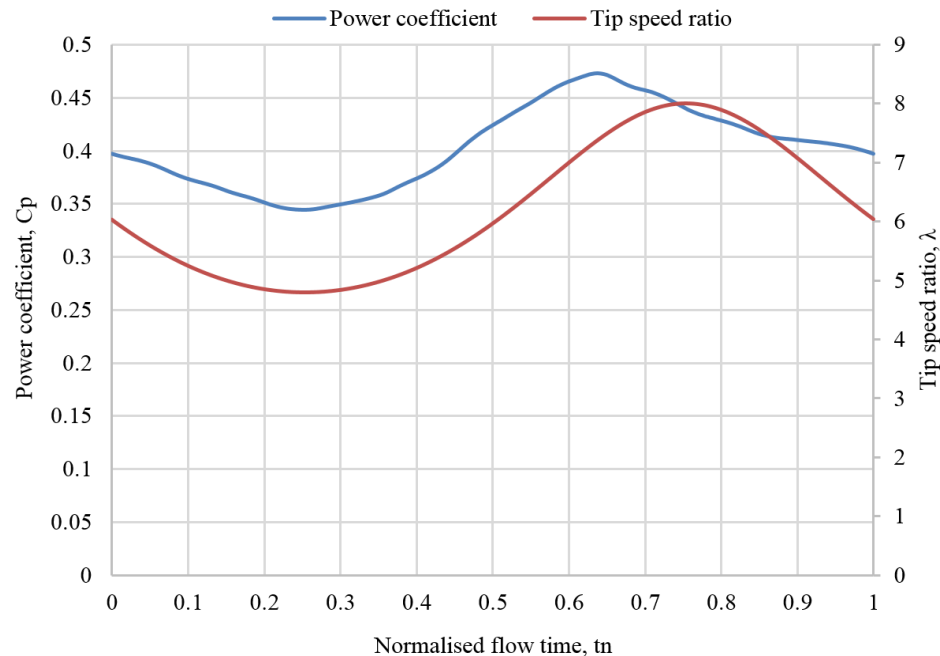


Figure 6.2: Performance of the turbine for one cycle of unsteady wind velocity.

In the same way, Figure 6.3, presents the behaviour of the power available in the incoming wind and that produced by the turbine. The sinusoidal wind flow shape is also shown over one cycle of flow time. Clearly, the unsteady flow curve and the extracted power curve that are both coming in and ending at the same normalised time are closely matched. The available power curve, however, shows higher amplitude than the other two curves when the available wind power based on the third power of wind speed.

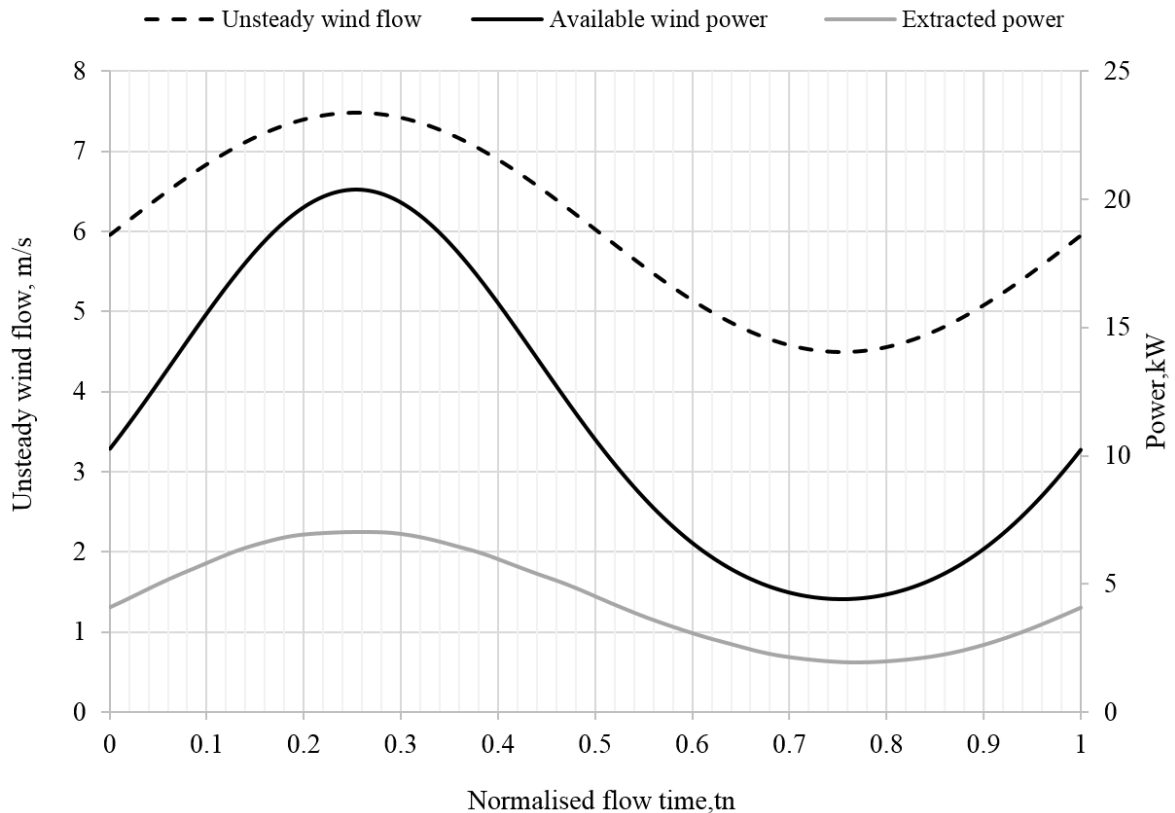


Figure 6.3: Comparison between the available wind power and the extracted power by the turbine at unsteady wind flow.

According to equation 6-2, power coefficient can be more affected in value by varying both P_B and P_W values. This effect is seen clearly by matching the results of Figure 6.2 and Figure 6.3. Figure 6.2 shows the lowest C_p value in the performance curve ($C_p=0.349$ at $t_n=0.248$) due to the convergence of two curves which produces a relatively low power. On the other hand, the second half of Figure 6.2 displays the maximum C_p values ($C_p=0.454$)

at t_n locates between 0.43 and 0.75 when the disagreement between the power curves is big.

6.3 Characteristics of unsteady wind flow

6.3.1 Reduced frequency (k)

Leishman (2006) considered reduced frequency (k) is an essential criterion to describe the level of the unsteadiness in the wind flow. The reduced frequency form can be drafted as the following equation mentioned by Milne et al. (2013):

$$k = \pi c f / \omega R \quad \text{Equation 6-4}$$

where c is the chord of the aerofoil in (m). The frequency of a wind (f) can generally be defined as the number of undulations which are produced by a source each second and the measurement unit is the hertz (Hz).

According to Moir and Seabridge (2008), the nominator, which is called frequency parameter, represents the oscillations of an aerofoil when it is subjected to a wind flow passing through it.

Consequently, the aerodynamic flow can be sorted into three types depending on the reduced frequency value: steady flow at $k = 0$, slight unsteady state effects when $k \leq 0.05$, while flow values above this can be considered to be fully unsteadiness. It was measured experimentally by Huyer et al. (1996) depending on the supplied wind flow normal to the swept area of the blade and also on oscillation of the blade.

By using the above equation, the calculated reduced frequency for the first chosen frequency of the wind flow (1Hz) is approximately equal to 0.05, which is in the unsteady flow region according to the definition of Leishman (2006). The other high values of the frequencies (2, 5 and 10Hz), which will be deliberated in the next section, are 0.084, 0.21 and 0.42 respectively. However, a small frequency (0.5) was chosen in order to gain more conception of the behaviour of the wind turbine in unsteady flow conditions.

6.3.2 Strouhal number (St)

There is a unit less quantity which can be essential when analysing unsteady flow problems called the Strouhal Number. It can be formulated as follows:

$$St = \frac{k A}{\pi c} \quad \text{Equation 6-5}$$

where A is the amplitude of the fluctuating wind speed.

As mentioned in section 6.3 above, five different wind frequencies: (0.5, 1, 2, 5 and 10 Hz), were chosen to achieve the aim of the current study. The reduced frequencies were calculated based on the velocity normal to the rotor disk and blade rotation frequency. It was varied between low value 0.021 and high value 0.42, depending on equation 6-4.

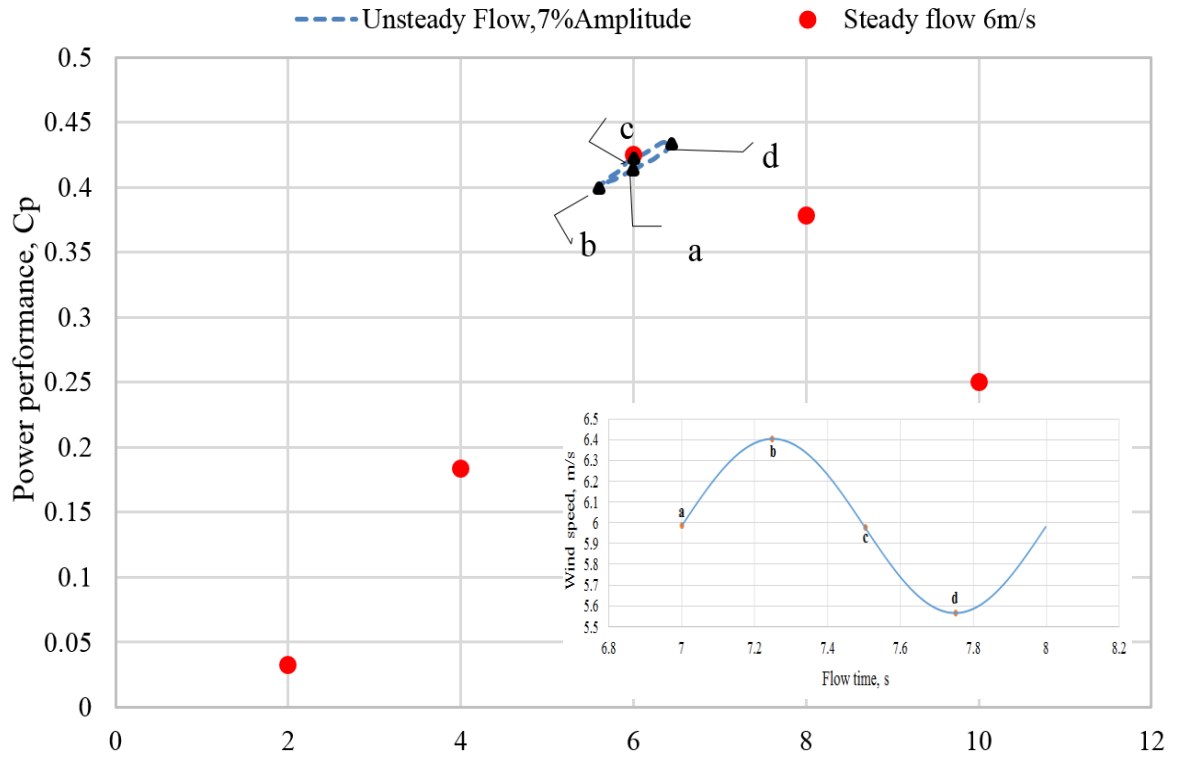
6.3.3 Amplitude of wind speed (\hat{u})

It is the maximum amplitude of the wind speed which can undulate from its mean value. It also can be expressed as the difference between the instantaneous velocity and the average wind speed. In this study, various amplitudes (7, 15, 25 and 45%) were applied in most of the next case studies.

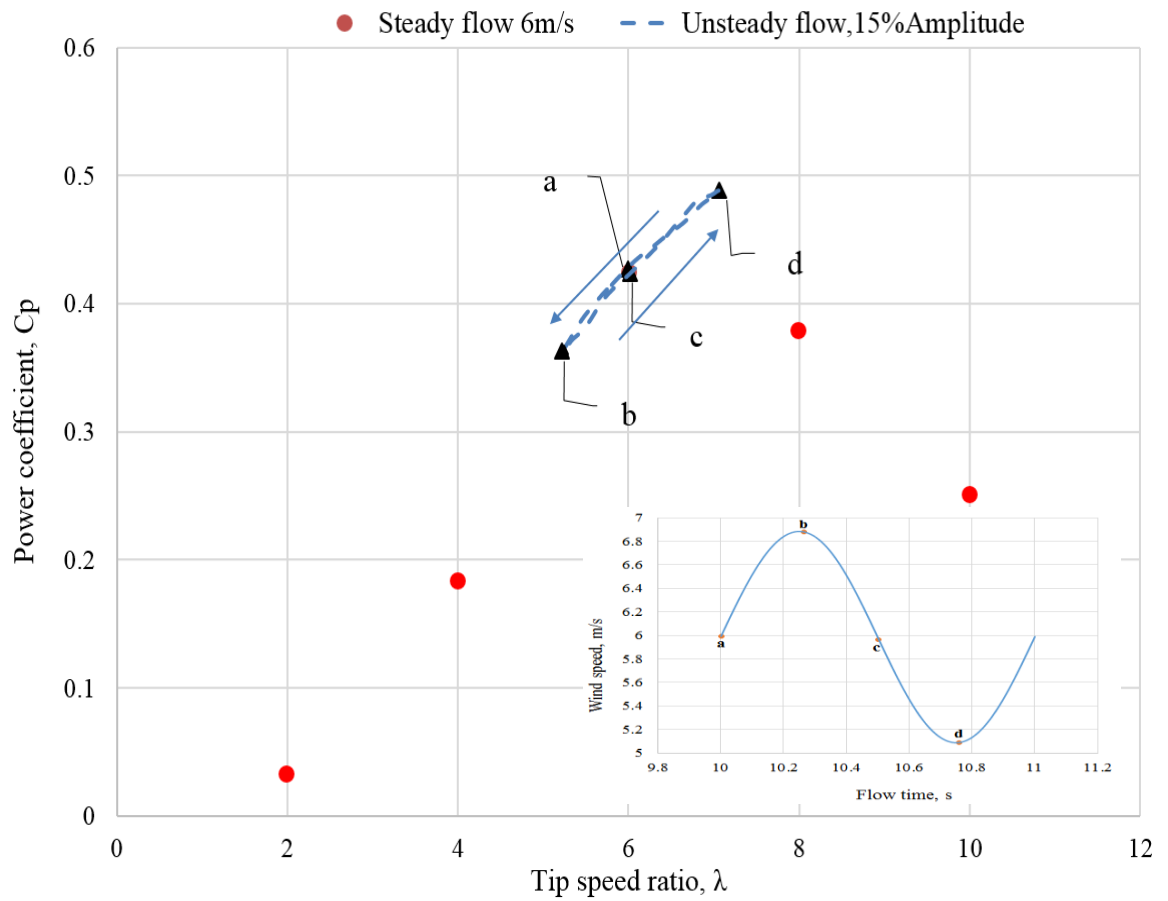
6.4 Power performance of the wind turbine with amplitude variations

In order to investigate the influence of the unsteady flow on the power performance of the wind turbine, a consistent comparison study needed to be implemented of the performance of the wind turbine operating in steady state environment conditions. One average cycle of the unsteady flow power performance of the wind turbine ($C_{p_{av}}$) was taken into account in calculations. Also, the unsteady wind speed was calculated according to the time step size ($t=0.00244$ s) which is derived from the rotational blade speed ($\omega=7.158$ rad/s). In general, the unsteady-state computations were carried out for approximately 3600 iterations to have a convergence up to 10^{-6} in some cases. The following paragraphs gradually introduce the 1Hz frequency and various amplitudes of the wind speed and their effect on the rotor performance. As mentioned in the literature review, a variety of wind speed amplitudes were studied. Starting from small values, 7% and 12% amplitudes were used by Danao et al. (2013), whereas Toshimitsu et al. (2012) used 20% amplitude of wind speed, Scheurich and Brown, (2012) used fluctuation amplitudes of $\pm 10\%$ and $\pm 30\%$, and finally, Danao and Howell, (2012) applied 50% of the mean wind speed. Hence, this study will attempt to cover this wide range. The following sequence of figures represents the hysteresis loop at each amplitude.

(a)



(b)



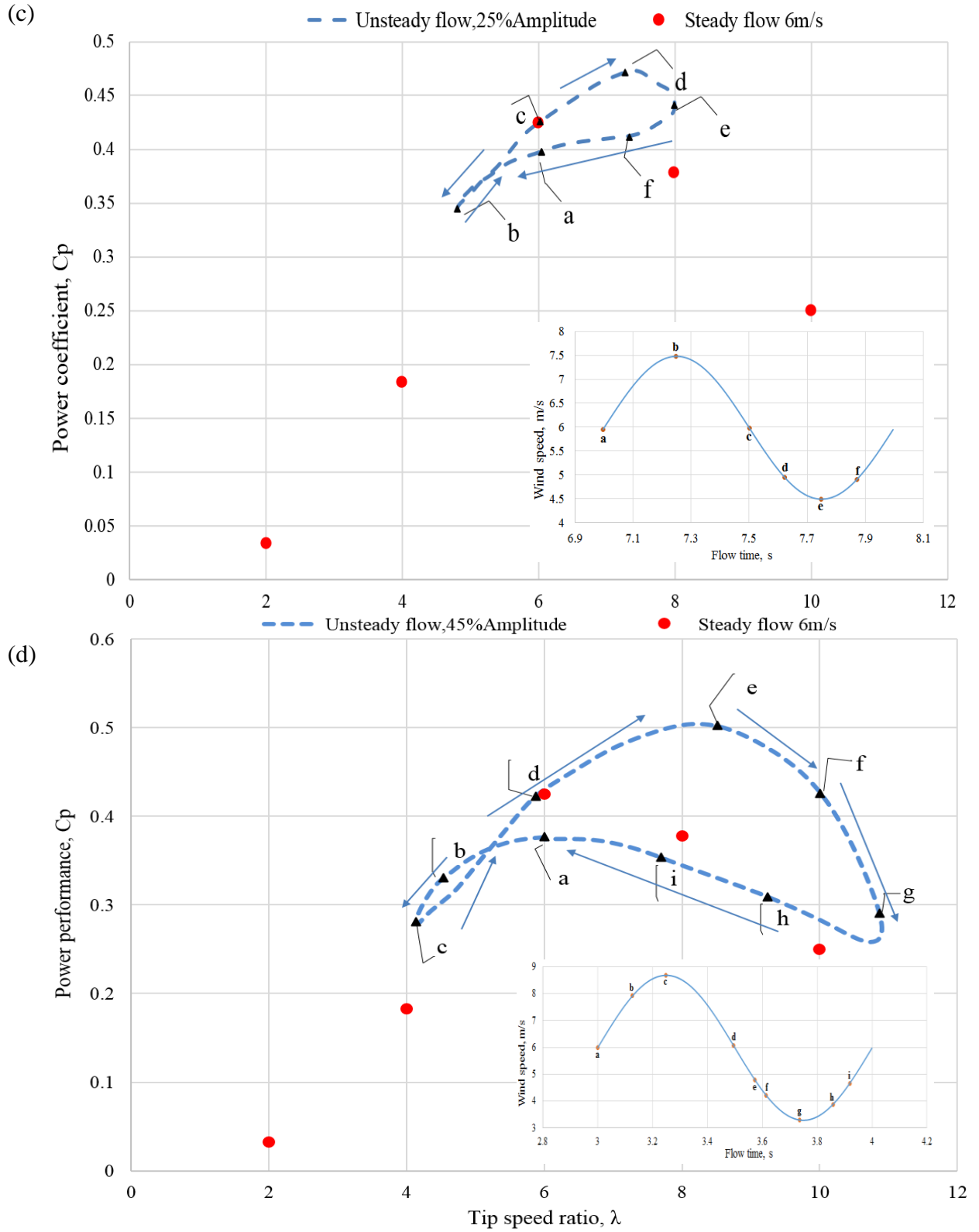


Figure 6.4: Effect of steady and unsteady flow on the performance of the HAWT at various amplitude.

6.4.1 Power curve at $f=1\text{Hz}$ and 7% amplitude

The data from Figure 6.4 generally clarify that there is relatively little difference in C_p despite the wind turbine being slightly advantaged by steady state flow conditions, which is generally similar to findings in previous works by Scheurich and Brown (2013) and Danao et al. (2014).

Starting with low amplitude of the oscillation and 1Hz frequency, as shown in Figure 6.4(a), this case displays the C_p - λ plot of the NREL rotor for both steady and unsteady flow conditions. From chapter five, the peak of the steady flow performance case, which is denoted by the red dots, locates at $\lambda=6$ which is 0.425. The unsteady flow case is indicated by the blue dashed loop, which is also called “a hysteresis loop”. In addition, points (**a**, **b**, **c** and **d**), shown in black dots superimposed on the current trace, will be focused on over the next paragraphs. In general, the unsteady flow loop has a little deviation from the reference case trend in $\lambda=6$ region which means there is a little deviation in TSR.

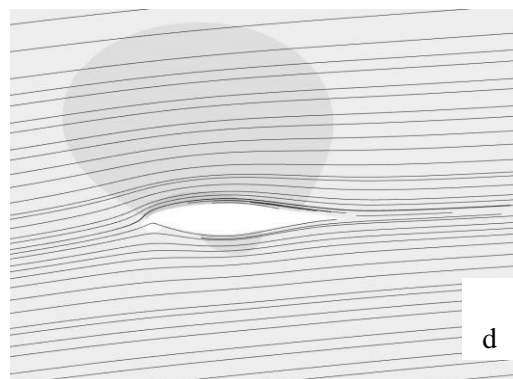
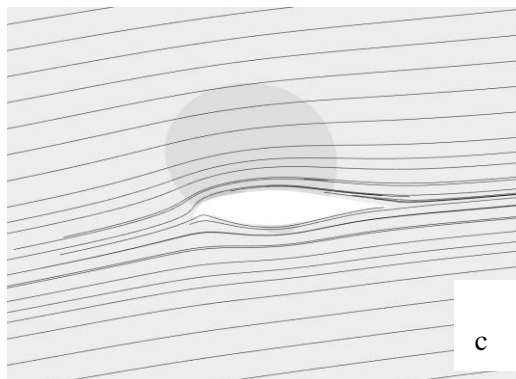
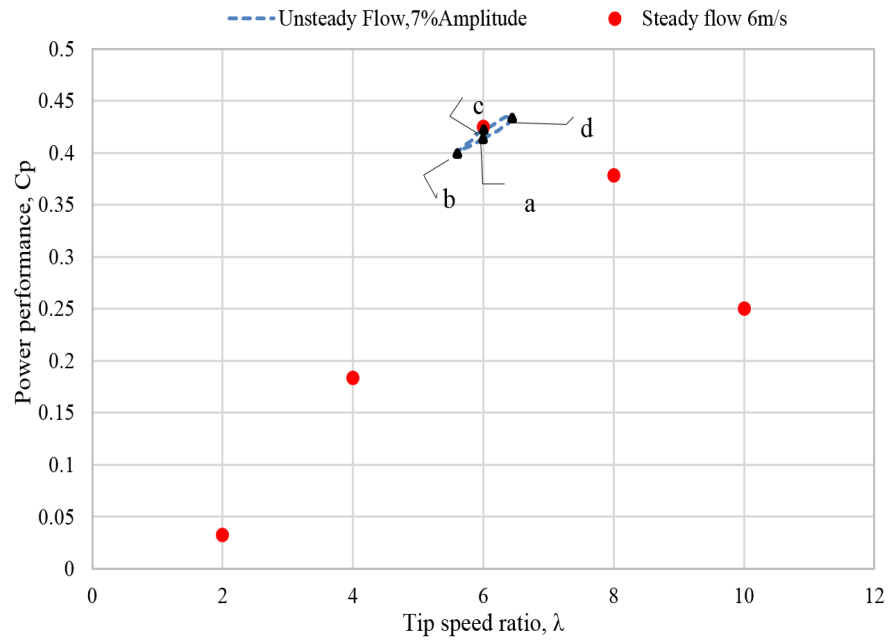
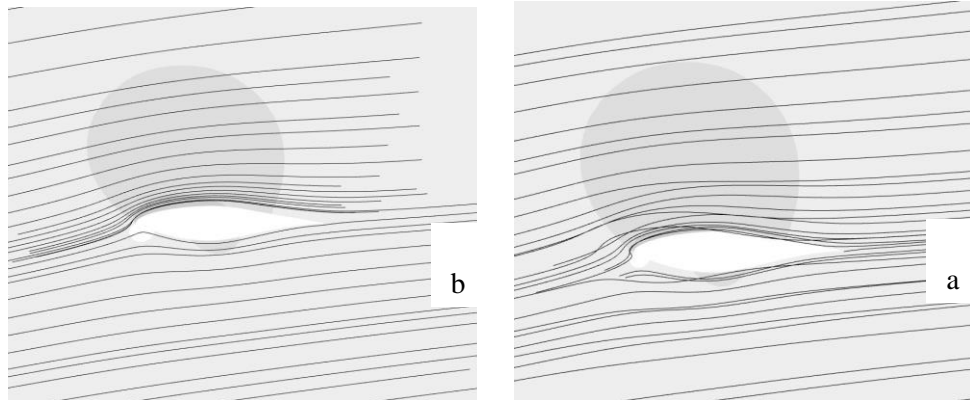
From Figure 6.4(a), it can also be seen that the unsteady flow loop locates, as was almost expected, close by the peak of the steady case band and it generally falls within the limits of that band. As mentioned above, the $C_{p_{av}}$ was calculated by averaging the C_p values which are confined between points (**a** and **d**) within the wind cycle with a fluctuating wind speed of 0.417.

The maximum $C_{p_{av}}$ value, which was obtained from the unsteady flow curve, was 0.432 at $\lambda=6.45$, and is denoted by the letter **d**, whereas the lowest $C_{p_{av}}$ value was 0.398 at $\lambda=5.6$, and is identified by the letter **b**. This finding also revealed clearly that the performance was relatively high at some points on the unsteady loop, even from the steady state flow curve; hence, that the aerodynamic behaviour on the selected points will be fully discussed in the next paragraphs.

Referring back to the discussion in chapter five, 75% and 30% of blade-span were selected for examining the flow behaviour of the hysteresis loop as shown in Figure 6.4(a). To visualise that behaviour, streamlines were plotted around the blade surface at four points around that loop, as presented in the two parts (a) and (b) of Figure 6.5. In general, the first part includes the flow visualisation at the power production position of the blade, whereas the second one shows the 30% of the blade region details. Figures 6.5(a) and 6.5(b)

reveal the nature of the flow around the blade at 75% and 30% locations respectively. It can be clearly seen that the flow is fully attached to the surface of the blade in both locations and at all points in the loop. This attachment could be as a result of the low effect of the low amplitude on the wind turbine when the flow behaves as a steady flow, although the flow is expected to face high angle of attacks at the area which is next to the root.

(a)



(b)

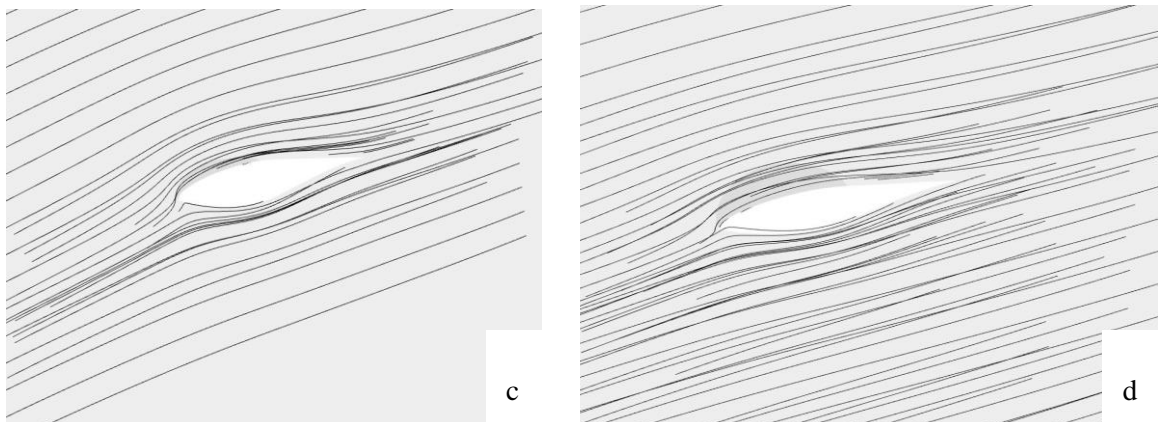
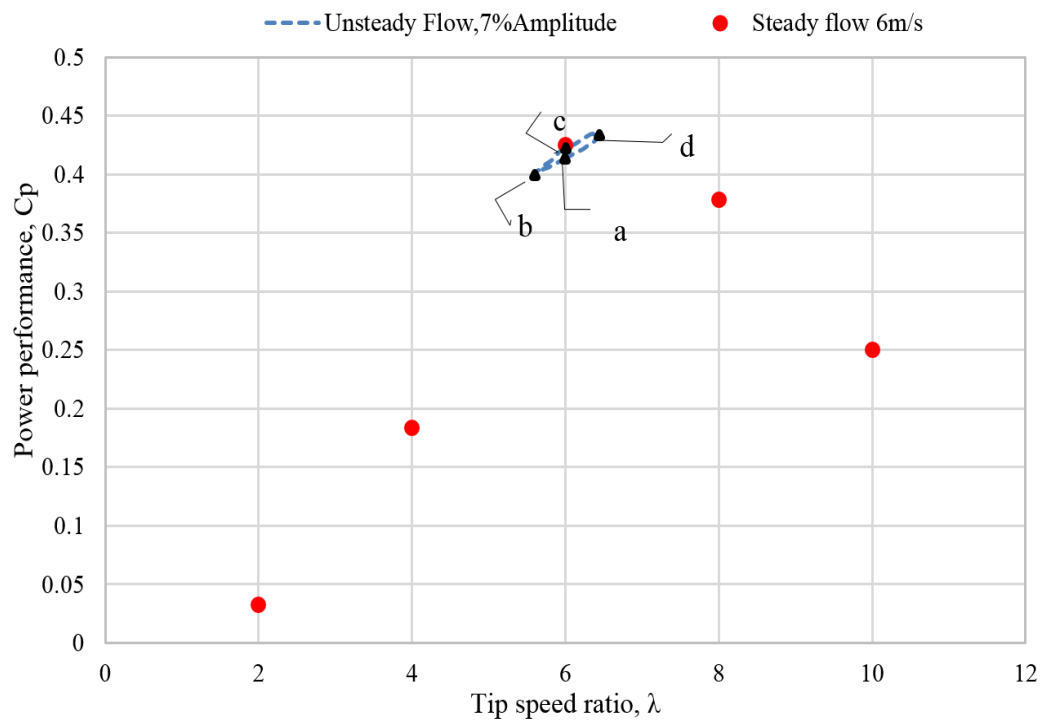
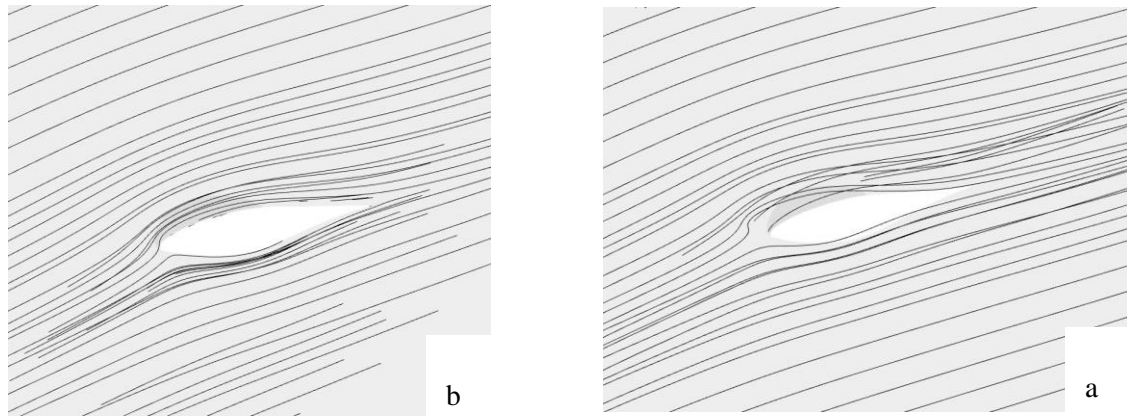


Figure 6.5: The plot and streamline performance curve of the full-scale NREL wind turbine at 1Hz and 7% amplitude of unsteady wind speed (a) at 75% and (b) at 30% of the blade.

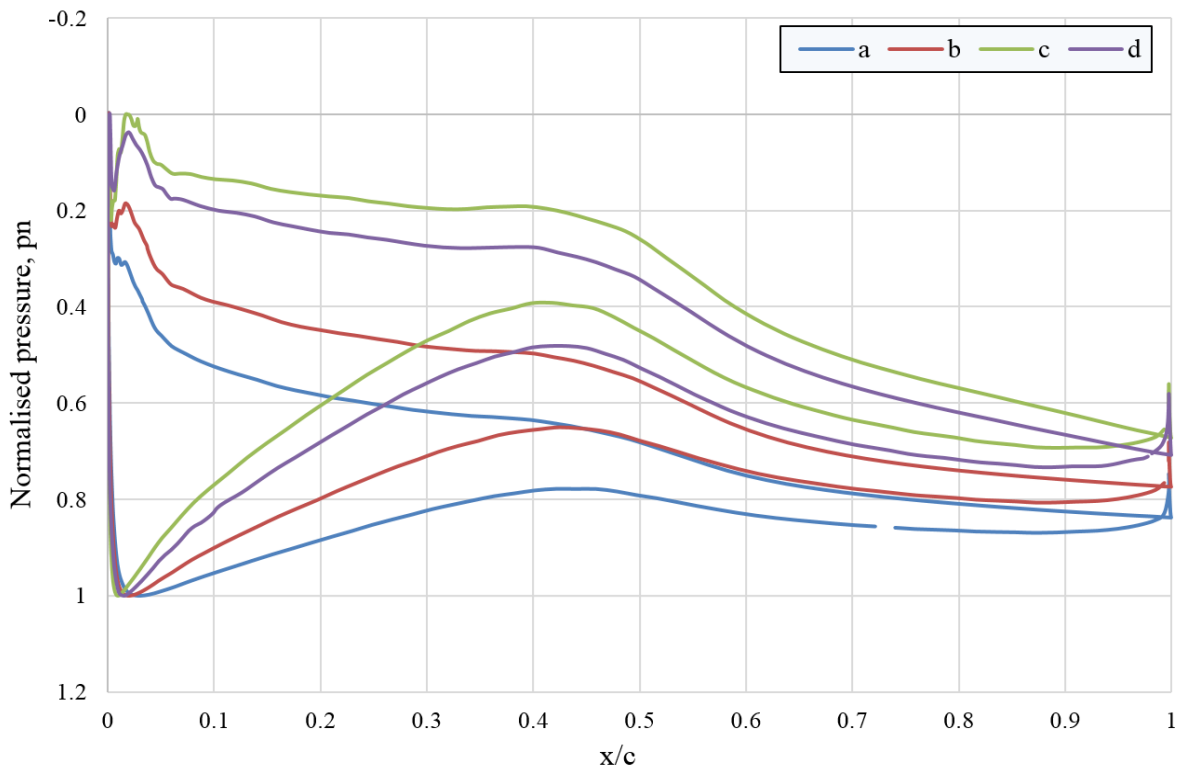


Figure 6.6: The pressure distribution around the rotor blade at different locations around the hysteresis loop of the full-scale NREL wind turbine. Conditions are 1Hz and 7% amplitude of unsteady wind speed at 75% of the blade.

The surface pressure distributions were also employed, especially at 75% the span-wise, to give more insight into how the flow develops in the unsteady wind flow. The results, as shown in Figure 6.6, indicate a slight discrepancy in the pressure behaviour in the performance loop and a consistently large change in the shape and size of it.

In Figure 6.6, it can also be noted that all shapes of the normalised pressure are relatively similar at the selected cross-section of the blade. The trend of the curves for the two points, **a** and **b**, is roughly similar to that shown in chapter four, in particular at low wind speeds when no separation in flow should be appearing. All curves are identical except at the 45% location where there is an apparent lag between the curves of the points. In addition, the pressure curves indicate that the pressure difference is high at the leading edge at points **c** and **d** and then decreases when the flow goes towards the trailing edge. The following table displays the difference in area then in lift force between points **a** and **b** and also between **c** and **d** in Figure 6.6.

Table 6.1 The area under the pressure curve at each point on the loop ($f=1\text{Hz}$ and $A=7\%$).

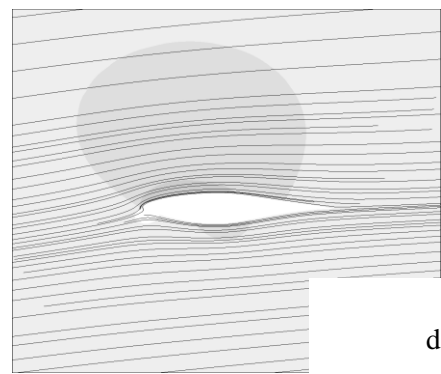
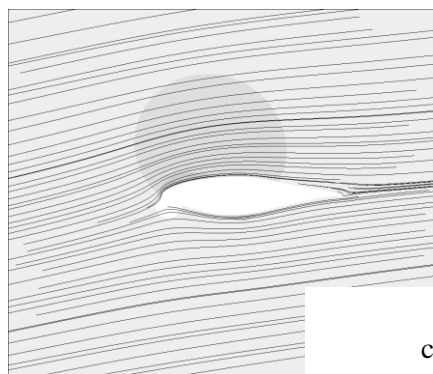
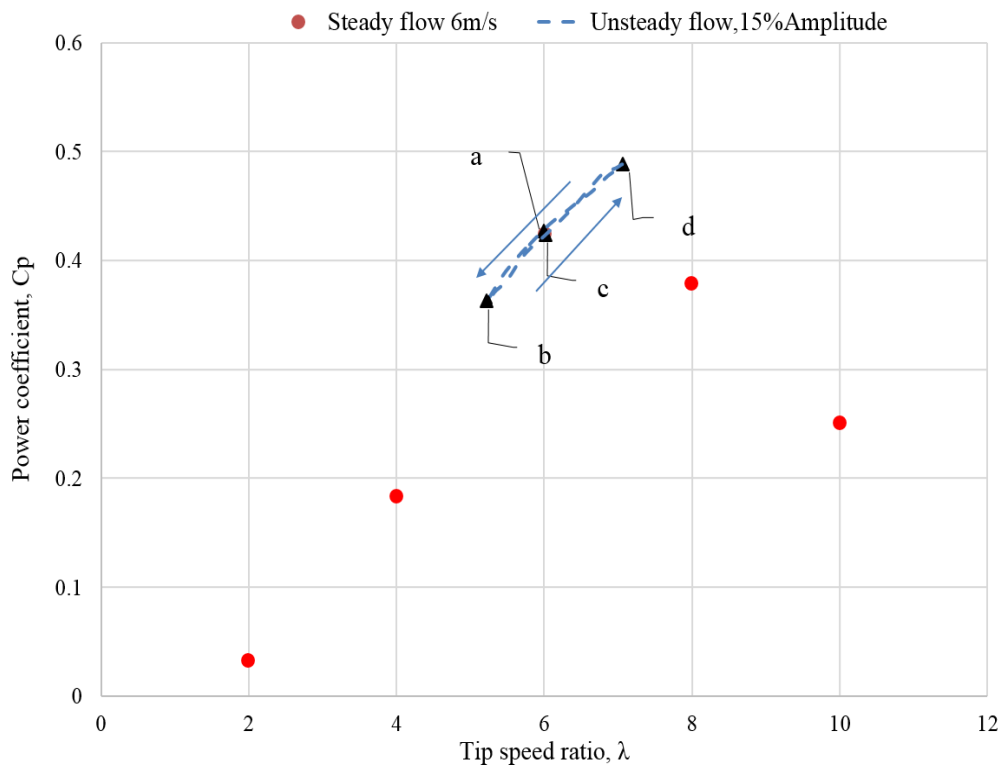
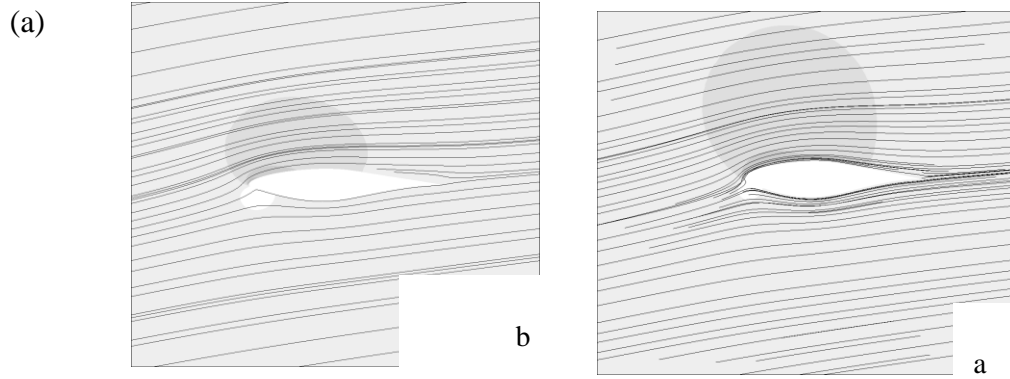
Point	a	b	c	d
Area	0.1747	0.1998	0.2638	0.2608

It is clear that the area surrounding by the pressure curve at point **c** is the highest one in this case. However, the performance of the turbine is high at point **d** which has very close area to that of point **c**.

6.4.2 Power curve at $f=1\text{Hz}$ and 15% amplitude

Maintaining the same wind oscillation (1Hz), but this time at 15% amplitude, the steady flow curve is also presented as a comparative case to the $C_p-\lambda$ plot of the unsteady flow conditions. The hysteresis loop of the unsteady flow case, as shown in Figure 6.4(b), which is denoted by the blue dashed line, locates around $\lambda=6$. The hysteresis loop is wider than in the case of the 7% amplitude curve as one would expect. The four points (**a**, **b**, **c** and **d**) also represent the flow behaviour along that loop. As before, the point **a** represents the beginning of the curve while the point **d** is the end point.

As shown in Figure 6.4(b), the unsteady flow loop is almost entirely based around the maximum value of the steady flow curve. As mentioned earlier, the $C_{p_{av}}$ was obtained by averaging the C_p values which are confined between points (a and d) of one wind cycle with fluctuating wind speed. The $C_{p_{av}}$ is found at about 0.425, which implies that there is no change in the wind turbine performance in either wind cases. The high $C_{p_{av}}$ value is 0.489 at $\lambda=7.05$, and denoted by the letter d, while the $C_{p_{av}}$ in low point b is 0.3628 at $\lambda=5.22$. The unsteady flow curve, in fact, is unsmooth and shows kinks along the loop which can be attributed to changes in wind speeds. Moreover, there is no big change in the C_p value at $\lambda=6$ between point **a** and **c**. The increase in TSR leads to decrease in the angle of attack which achieves high lift as shown in point **d**. The full details of the unsteady flow condition at this amplitude will be discussed in the next paragraphs by plotting streamlines and taking the pressure distribution around the blade.



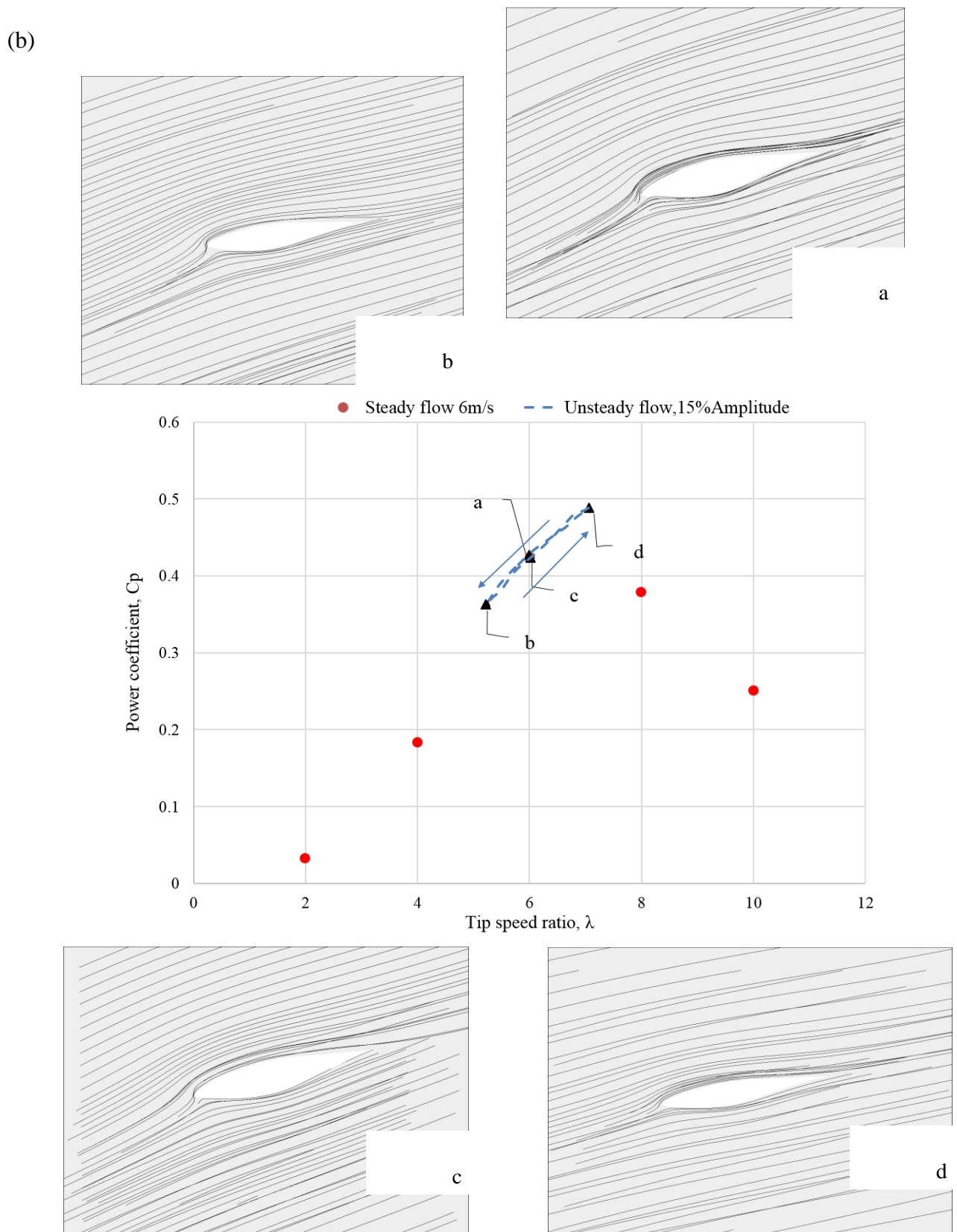


Figure 6.7: The plot and streamline performance curve of the full-scale NREL wind turbine at 1Hz and 15% amplitude of unsteady wind speed (a) at 75% and (b) at 30% of the blade.

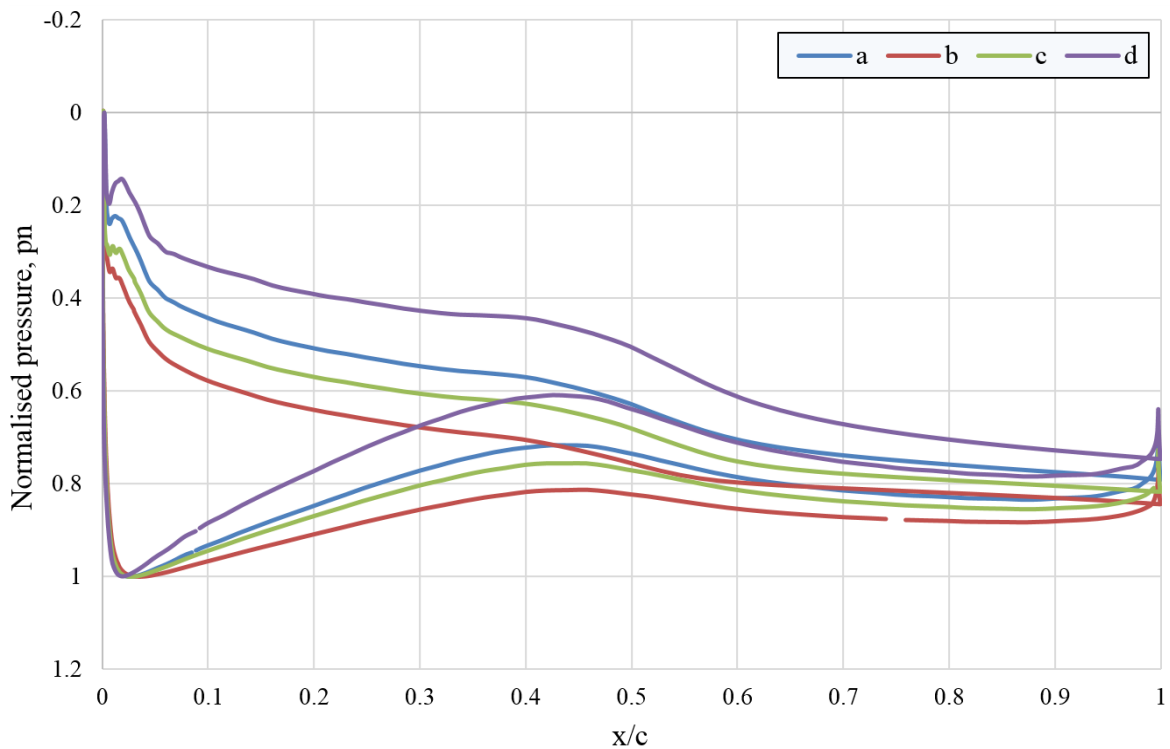


Figure 6.8: The pressure distribution around the rotor blade at different locations around the hysteresis loop of the full-scale NREL wind turbine. Conditions are 1Hz and 15% amplitude of unsteady wind speed at 75% of the blade.

Firstly, it can be seen that Figure 6.7 is similar to Figure 6.5 where streamlines were drawn around the cross-sections of the blade at the four points, as shown clearly in Figure 6.8(a) and (b). The flow visualisations in both parts reveal that the flow is still attached to the surface of the blade in both locations along the blade and at all points in the loop. Similar to an explanation given earlier, the low effect of the low amplitude on the wind turbine might result in the attachment of flow along the blade surface. Even the loop of this case is wider than that from the previous case, the AOA is still below the stall angle spatially at points **b** and **d**.

Secondly, Figure 6.8 highlights the areas under the normalised pressure curves, which are distributed around the blade at 75% of the span-wise. The tendency of the curves in the two points **a** and **c**, when these points is noticeably sharing the same performance of the turbine and at the same TSR.

From the table below, it is shown that the area under the **d** point pressure curve is the highest in this case. So, the lift is high and hence the generated power is also high.

Table 6.2 The area under the pressure curve at each point on the loop ($f=1\text{Hz}$ and $A=15\%$).

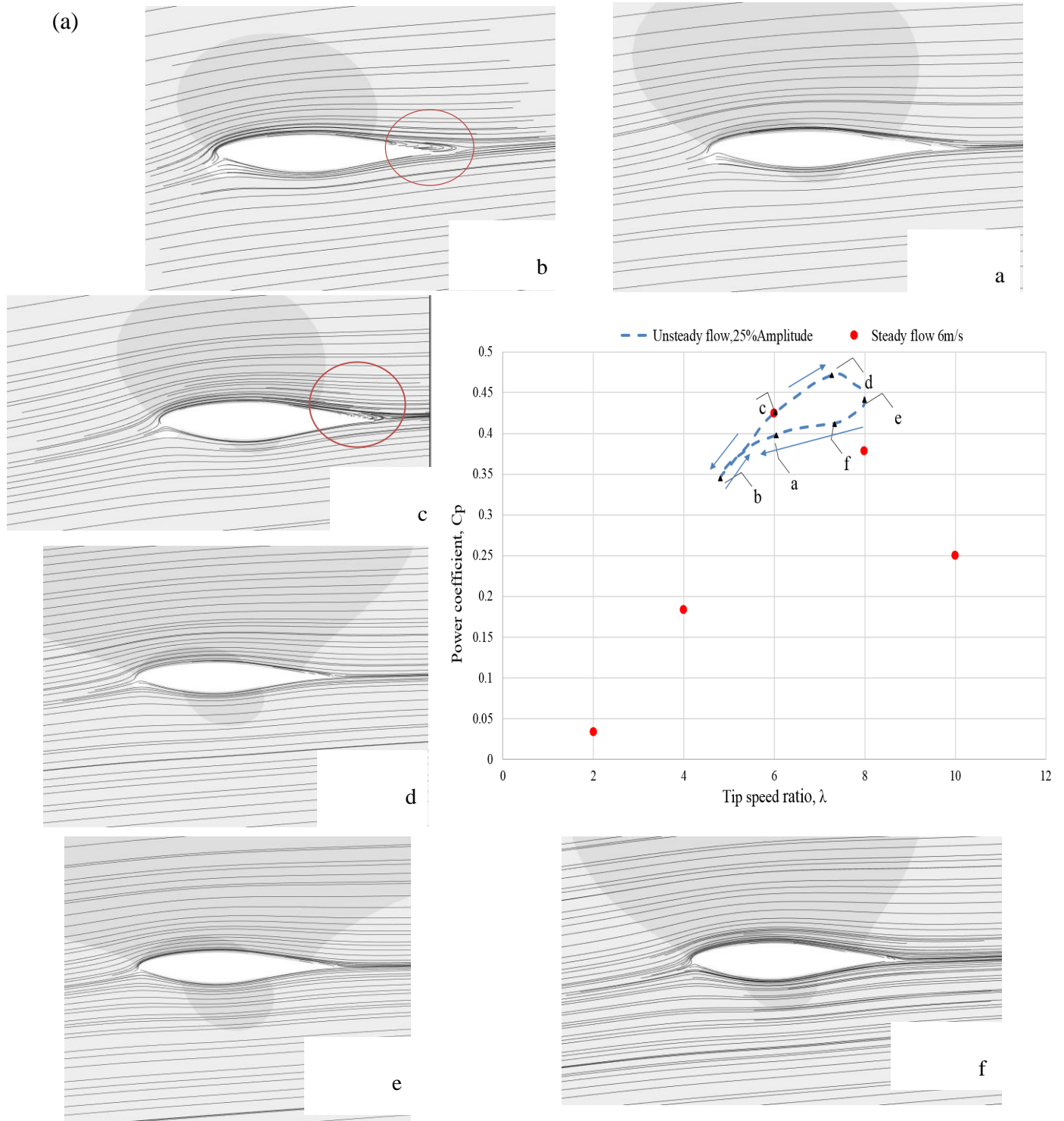
Point	a	b	c	d
Area	0.1951	0.1531	0.1702	0.2187

On the other hand, at point **b**, the area under the curve is the lowest among areas at this wind flow condition.

6.4.3 Power curve at $f=1\text{Hz}$ and 25% amplitude

The same procedure was repeated with wind oscillation (1Hz), but this time at higher amplitude (15%). Here, six points (**a**, **b**, **c**, **d**, **e** and **f**) are used to symbolise the flow locations along the hysteresis loop and more interesting behaviour. This increase in points is implemented because of the relatively high width of the loop. The comparative case to the C_p - λ plot of the unsteady flow conditions can be seen in Figure 6.4(c). As before, the hysteresis loop of the unsteady flow case is denoted by the blue dashed line and locates around the $\lambda=6$. The point **a** represents the initial point of the curve, while the point **f** is the end of this curve.

The peak point of the steady flow curve, which is clearly visible, lies on the unsteady flow loop at roughly point **c**. The average $C_{p_{av}}$ of the unsteady flow loop is 0.403 which is lower than the performance of the wind turbine 0.4245 in steady wind flow. In Figure 6.4(c), the high $C_{p_{av}}$ value is 0.472 at $\lambda=7.4$ which is indicated by the letter **d**, while the $C_{p_{av}}$ at low point **b** is 0.3444 at $\lambda=4.8$. The unsteady flow curve shows twisting down of the loop at $\lambda=5.22$. Moreover, the angle of attack during the separation is mostly higher than that when the flow reattaches on the suction side of the blade, while the twisting down could have occurred as a result of fluctuating in instantaneous wind speeds. It is also noticed that the hysteresis loop have different loading at two points (**a,c** and **d,f**) having the same TSR. More details will be given of the unsteady flow condition at this amplitude in the next paragraphs by plotting streamlines and examining the pressure distribution around the blade.



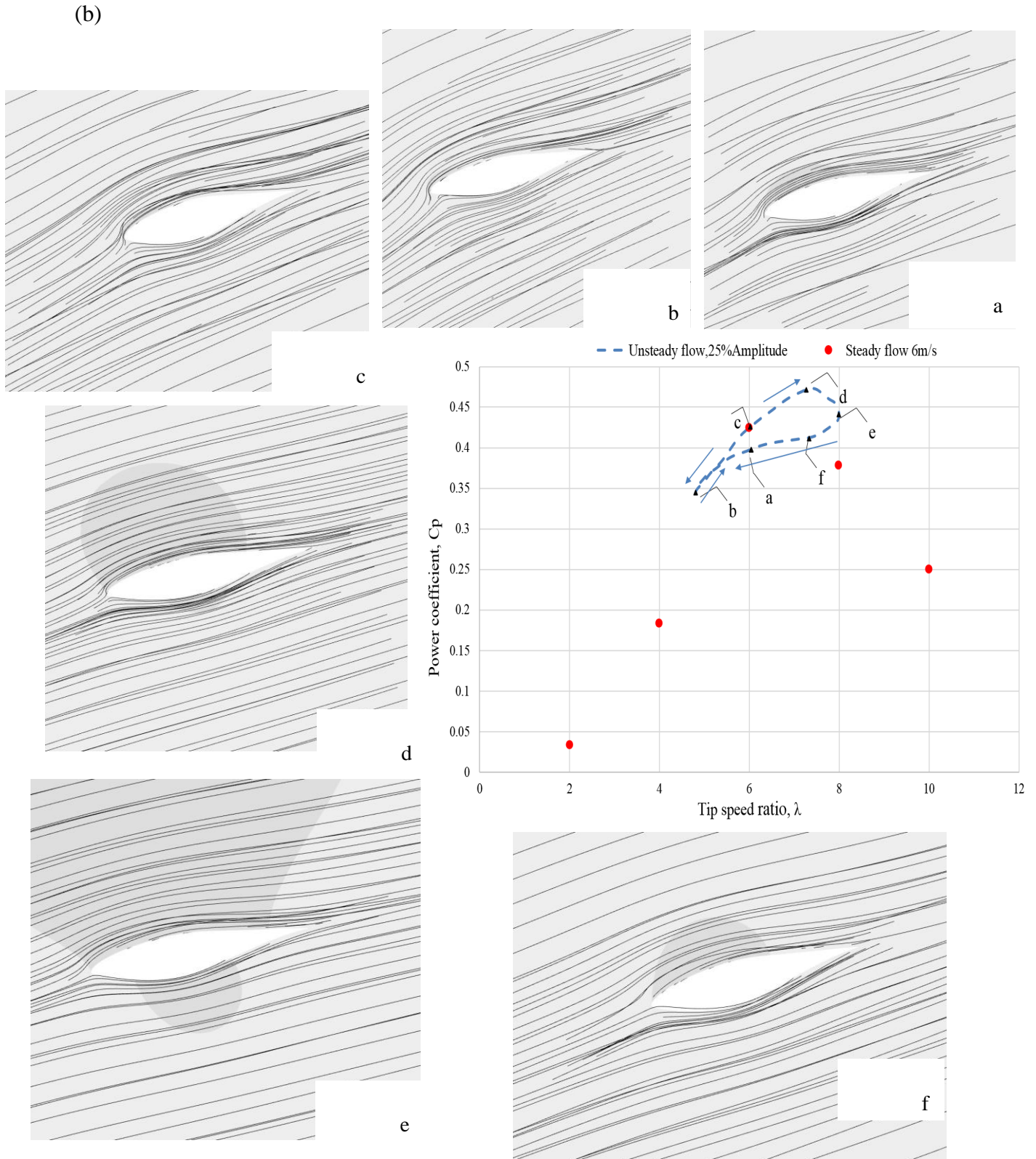


Figure 6.9: The plot and streamline performance curve of the full scale NREL wind turbine at 1Hz and 25% amplitude of unsteady wind speed (a) at 75% and (b) at 30% of the blade.

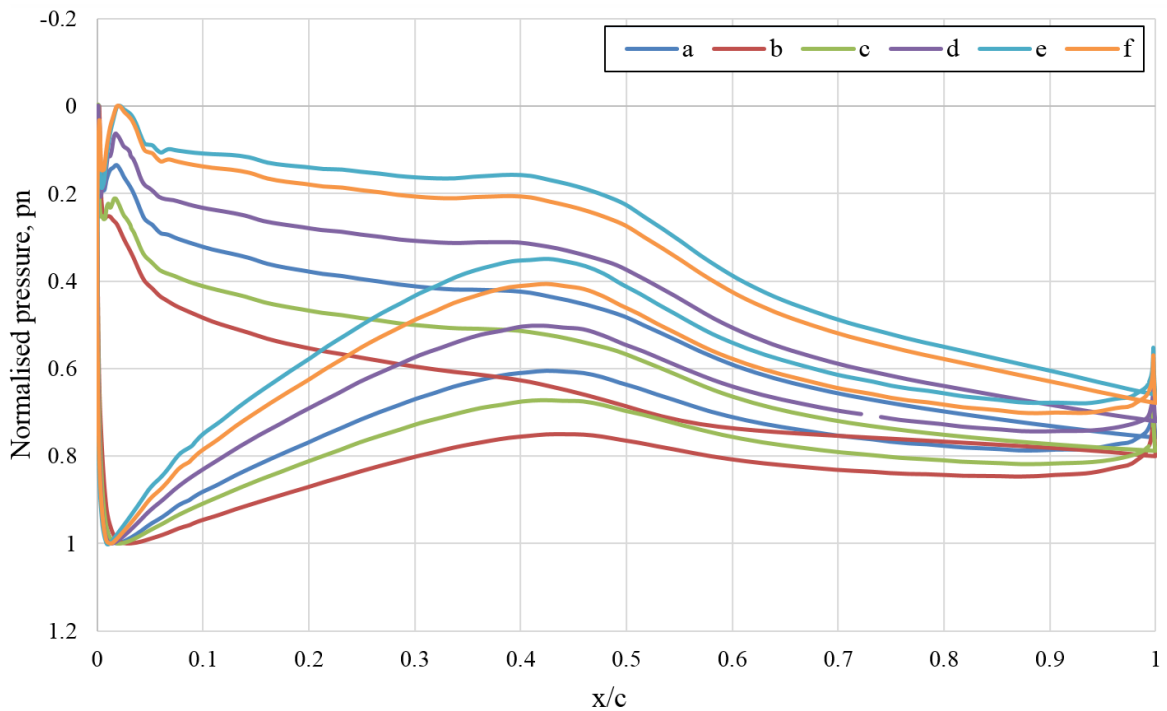


Figure 6.10: The pressure distribution around the rotor blade at different locations around the hysteresis loop of the full-scale NREL wind turbine. Conditions are 1Hz and 25% amplitude of unsteady wind speed at 75% of the blade.

Figure 6.9 shows that the streamlines were set up around the cross-sections of the blade at the six points, as was made clear in Figure 6.8(a) and (b). Six points are used here because the four points used with the asymmetric hysteresis loop at 25% amplitude, as previous cases, may not be sufficient to describe properly the flow visualisations along that loop. Figure 6.9 (a) reveals that the flow begins to separate at $\lambda=5$, which causes a power drop as indicated in the red dashed circle. Whereas the flow is still attached to the surface at 30% of the blade and at all points in the loop.

The pressure distribution around two locations of the blade length, 75% and 30%, is highlighted in Figure 6.10. The areas under the pressure, as it is known, show the lift force value. In general, the tendency of the point **b** and **c** curves at 75% is approximately identical along the chord length. However, at 45% of the chord length, the other pressure curves show a widening difference in pressure. This difference may signify a high lift force between the selected points.

Table 6.3 The area under the pressure curve at each point on the loop ($f=1\text{Hz}$ and $A=25\%$).

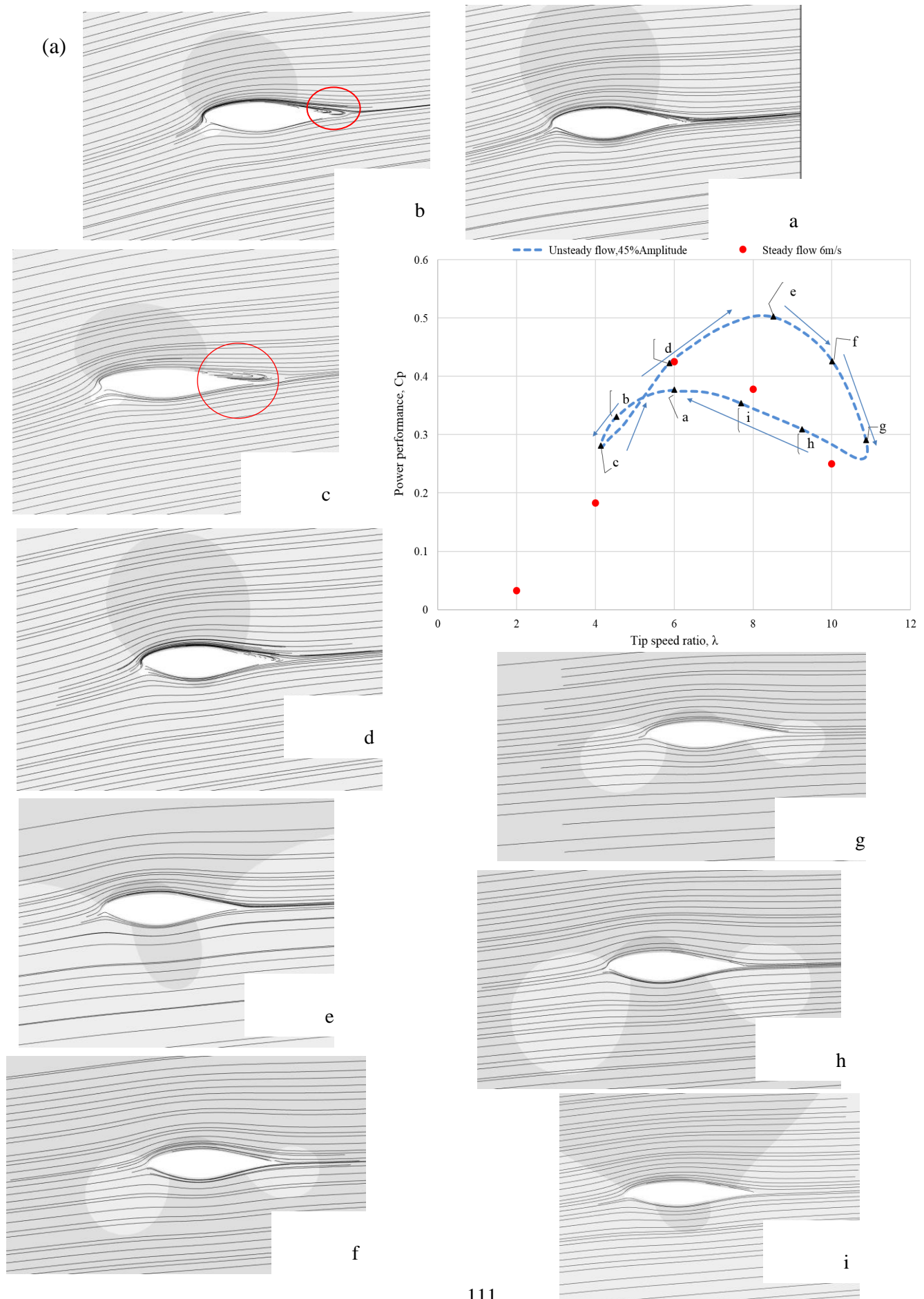
Point	a	b	c	d	e	f
Area	0.2294	0.1817	0.1985	0.2456	0.2636	0.2456

Table 6.3 shows that the lift generated at point **c** and **b** are relatively low and that is clear also from Figure 6.9(a) where the flow starts to detach from the surface due to high angle of attack. On the other hand, the lift for point **a** seems high although the performance is low which could mean that the lift to drag ratio at this point seems high. The behaviour of the flow for point **e** and **f** could be similar to that at **a** when the lift generated is high and high relatively performance.

6.4.4 Power curve at $f=1\text{Hz}$ and 45% amplitude

Figure 6.4(d) elucidates the hysteresis loop with wind oscillation (1Hz) at relatively high 45% amplitude of the average wind speed. First, nine points (**a**, **b**, **c**, **d**, **e**, **f**, **g**, **h** and **i**) were set up along the unsteady flow loop. Like the previous case, this increase in points is because of the relatively high width of the loop. The steady flow trend is set up first and then the hysteresis loop of the unsteady flow case which appears on the blue dashed line around the $\lambda=6$. The loop starts from point **a** and ends at point **i**.

The unsteady flow loop which clearly follows the trend of the steady flow curve. Moreover, the loop twists down, as in the case of 25% amplitude curve, but is wider than that loop. It can definitely be confirmed that the hysteresis loop is highly affected by the amplitude of the wind speed. Figure 6.4(d) demonstrates that the peak point of the steady flow curve lies on the unsteady flow loop and the obtained average $C_{p_{av}}$ of the unsteady flow loop is 0.352 which is still lower than the steady state performance of the wind turbine. The highest $C_{p_{av}}$ value is 0.5044 at $\lambda=8.2$ which is close to point **e**, while the smallest $C_{p_{av}}$ value point, seen close to point **g**, is 0.258 at high tip speed ratio $\lambda=10.73$ and low angle of attack. Therefore, it can be concluded that increase in amplitudes is likely to seriously disrupt the performance of the wind turbine. Further detailed discussion of this unsteady flow condition is provided in the next paragraphs.



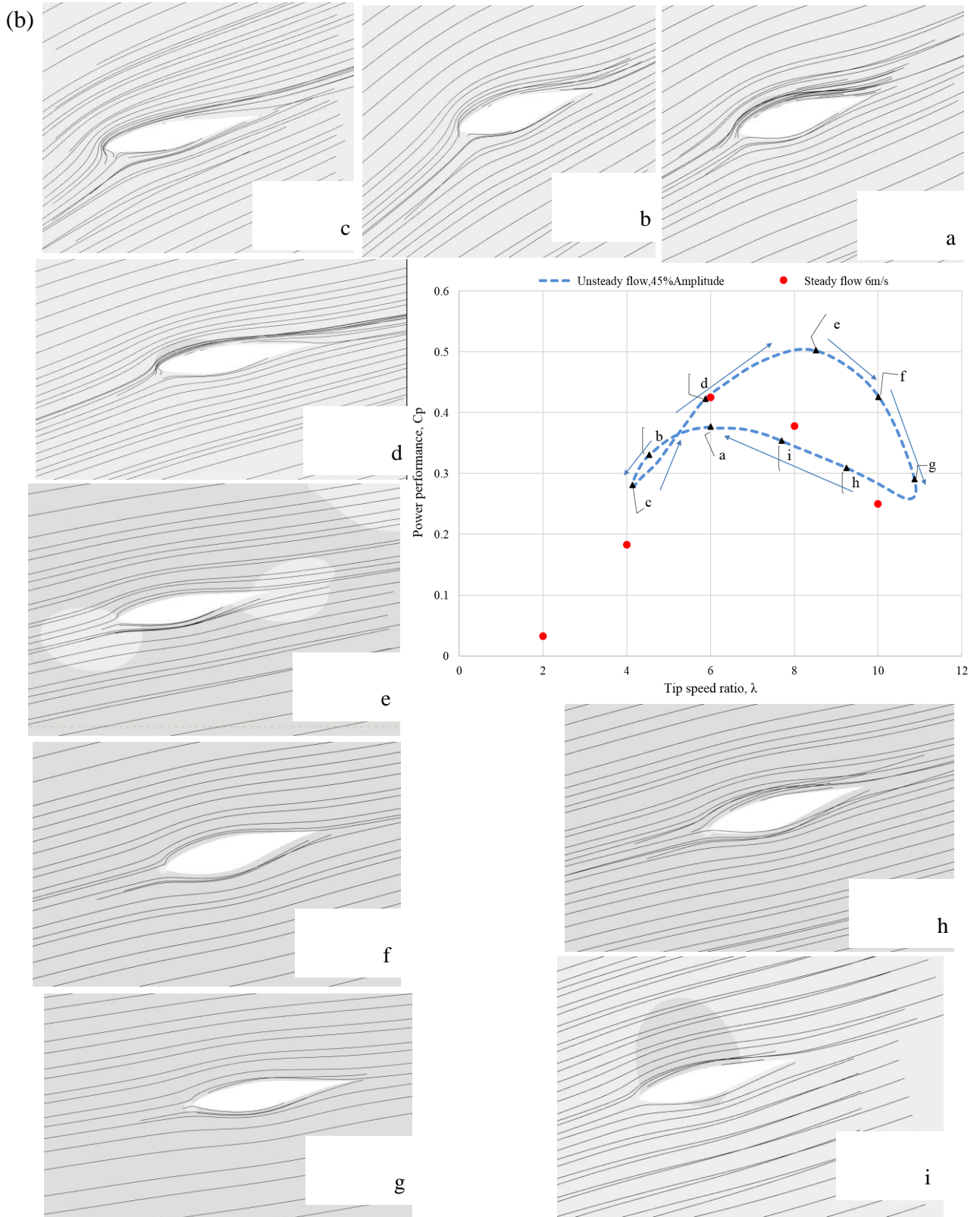


Figure 6.11: The plot and streamline performance curve of the full-scale NREL wind turbine at 1Hz and 45% amplitude of unsteady wind speed (a) at 75% and (b) at 30% of the blade.

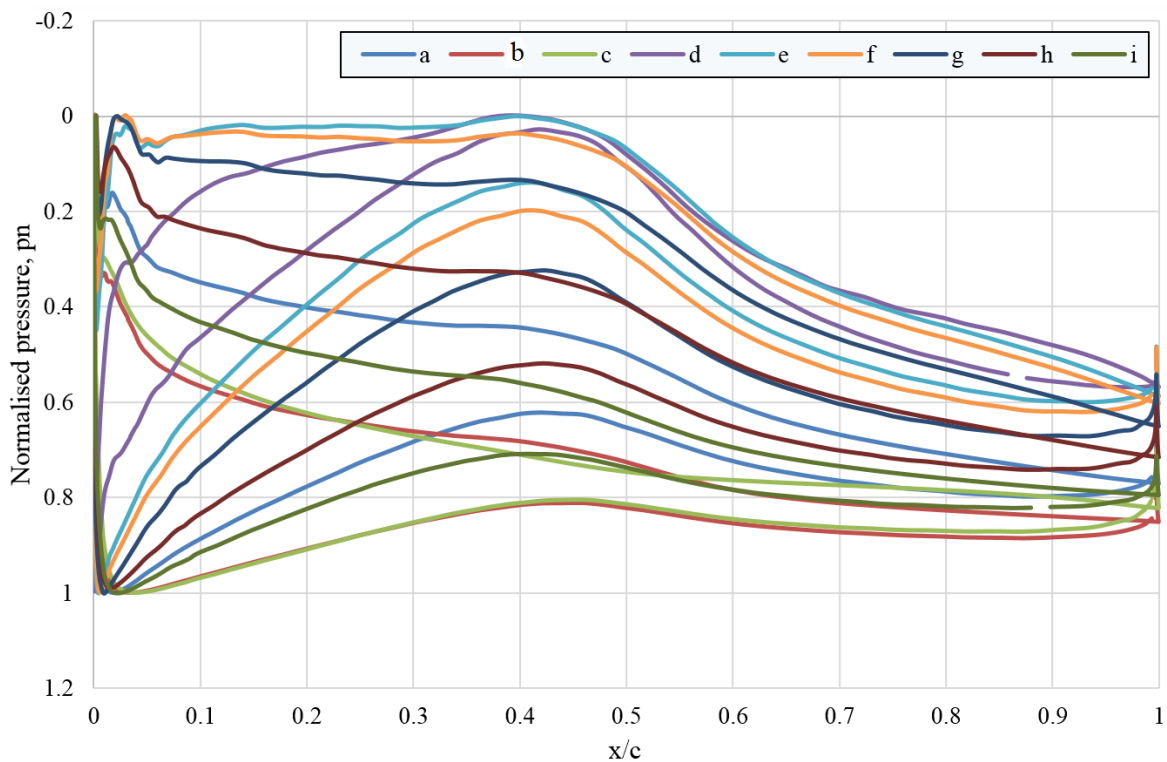


Figure 6.12: The pressure distribution around the rotor blade at different locations around the hysteresis loop of the full-scale NREL wind turbine. Conditions are 1Hz and 45% amplitude of unsteady wind speed at 75% of the blade.

Figure 6.11 shows the nine points selected along the hysteresis loop. Figure 6.11(a) illustrates the streamlines around the cross-sections of the blade at the nine points. The flow visualisations at 75% of the blade indicate that the flow is still attached to the surface of the blade except a small separation that can be sighted next to the trailing edge of blade at two points in the unsteady flow loop (**b** and **c**). Similar to the previous cases, the amplitude of the wind flow has not result in the attachment of flow along the blade surface.

The second Figure 6.12 shows that the normalised pressure curves were plotted in the same way around the blade at 75% of the blade's length. As in the previous test, the general trend of the all curves are mostly compatible at 45% of the chord, except point **b** and **c** as shown on Figure 6.12. Nevertheless, the processes **e** to **f** exposes a salient behaviour compared to the others and this could explain why the wind turbine power dropped during this process. However, Table 6.4 reveals that there is no clear different behaviour of flow at points **e**, **f**, **g** and **h** from each other when they all exhibit high lift force generated. The possible explanation for this is that the drag force is dominated when the rate of decrease in

drag is high making the lift to drag ratio lower. The small areas confined between the curves may generate a lift force that is not enough to produce high power.

Table 6.4 The area under the pressure curve at each point on the loop ($f=1\text{Hz}$ and $A=45\%$).

Point	a	b	c	d	e	f	g	h	i
Area	0.2232	0.1625	0.1691	0.1115	0.2353	0.2534	0.2669	0.2456	0.1904

6.5 Power performance of the wind turbine at different TSR

In order to investigate the influence of the unsteady flow on the performance of the wind turbine in more depth, two different tip speed ratios were studied. Tip speed ratios higher and lower than 6, 4 and 8, respectively, were selected for conducting a comparison to the performance of the wind turbine operating in steady state conditions. The base case of this study was set to be 25% of the mean flow ($A = 25\%$) with frequency of 1 ($f = 1$). The potential reason beyond choosing this amplitude was to obtain an obvious advantage of seeing the performance curve as this was relatively moderate value for the incoming wind flow. One average cycle of the unsteady flow power performance of the wind turbine ($C_{p_{av}}$) would be calculated.

6.5.1 Power performance of the wind turbine at $\lambda=4$

First the low tip speed ratio $\lambda=4$, was investigated. The unsteady wind speed was calculated according to the time-step size ($t= 0.00366$ s) which was derived from the rotational blade speed ($\omega=4.7604$ rad/s). The 1Hz frequency and 25% amplitude was used as a base case. The hysteresis loop with steady state flow curve can be seen in Figure 6.13.

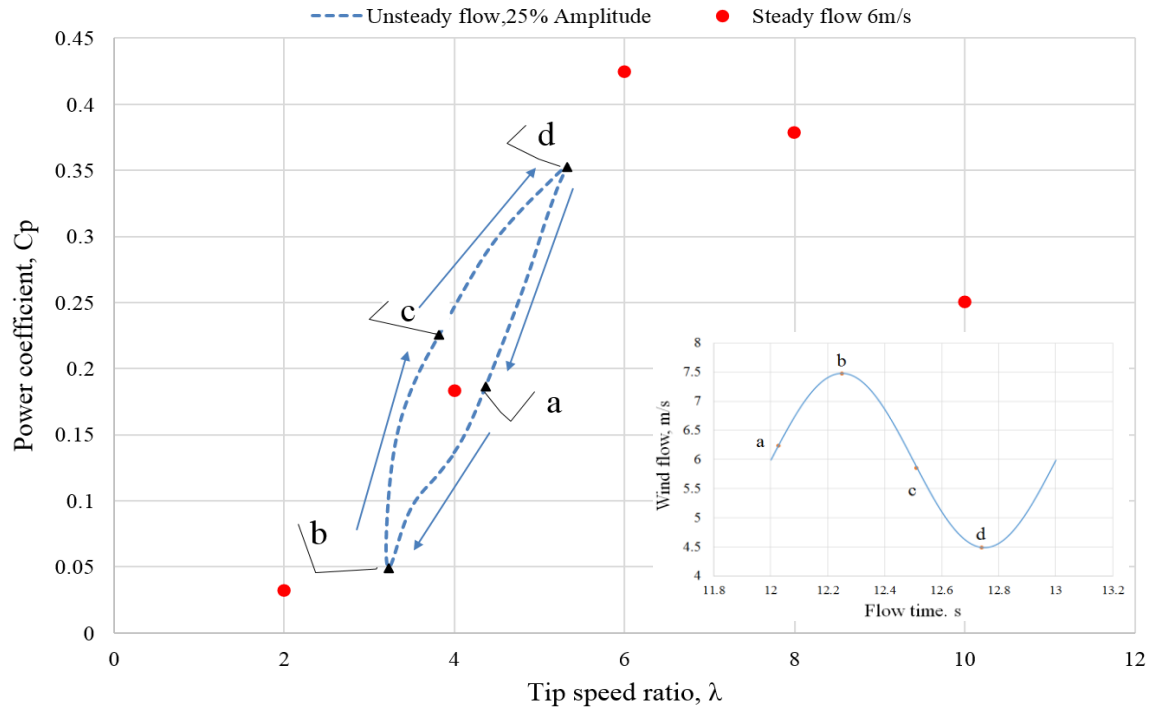
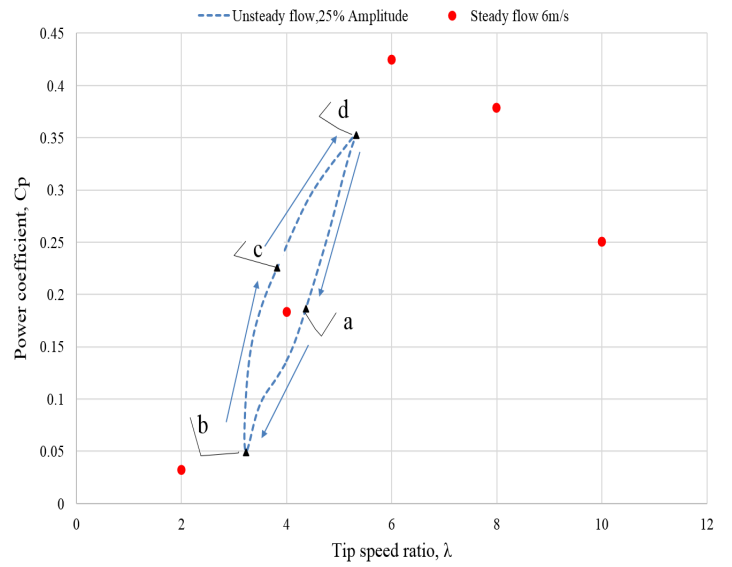
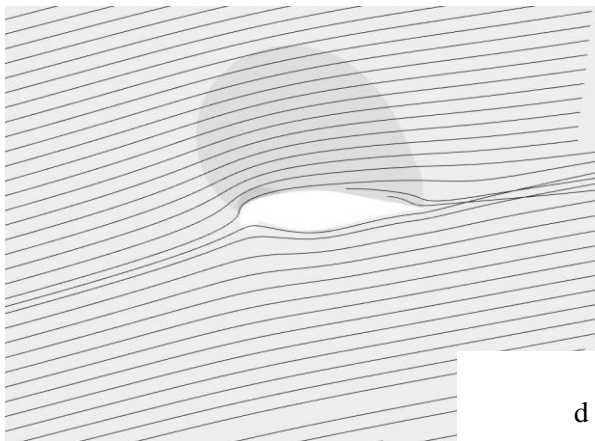
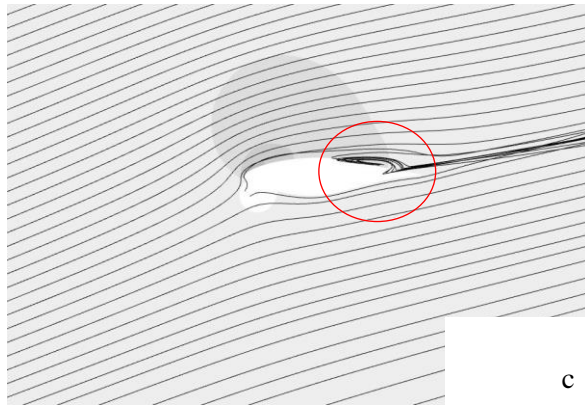
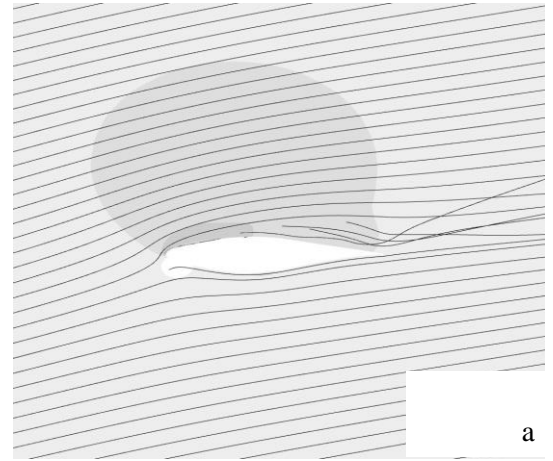
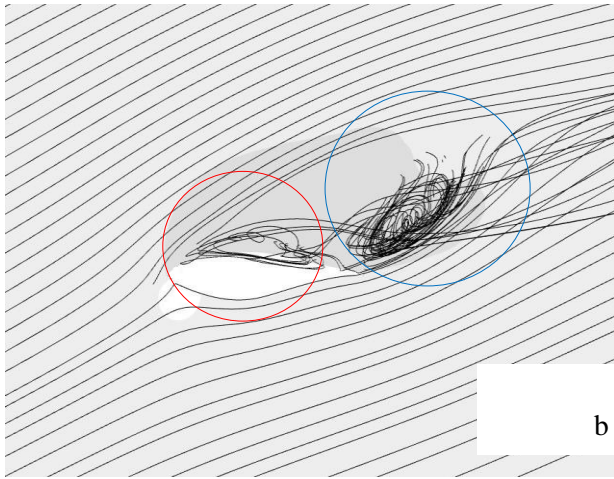


Figure 6.13: Effect of unsteady flow on the performance of the HAWT at 25% amplitude and $\lambda=4$.

Only four points (**a**, **b**, **c** and **d**) were designated along the hysteresis loop, as it was considered this number would be sufficient to provide more specifics about the flow behaviour in this case. Figure 6.13, shows generally that the hysteresis loop follows the trend of the steady state performance case. Furthermore, the loop is wide at approximately $\lambda=4$ and then it goes up until point **d** when the wind turbine approaches the highest performance $C_p= 0.35$ at $\lambda=5.33$. Meanwhile, at point **b** the rotor is operating at low tip speed ratio $\lambda=3.25$ and its value is about 5%. The obtained average $C_{p_{av}}$ of the unsteady flow loop is 0.205, which appears higher than the peak value of the steady flow trend performance of the wind turbine. This could be related back to the possible reason for decline in the performance of the rotor in the steady flow state discussed in chapter five. Hence, in fact, the two values might be either convergent or the steady flow value may be slightly above the unsteady flow state value. Streamlines and pressure distributions will now be discussed to provide more details on this unsteady flow condition.

(a)



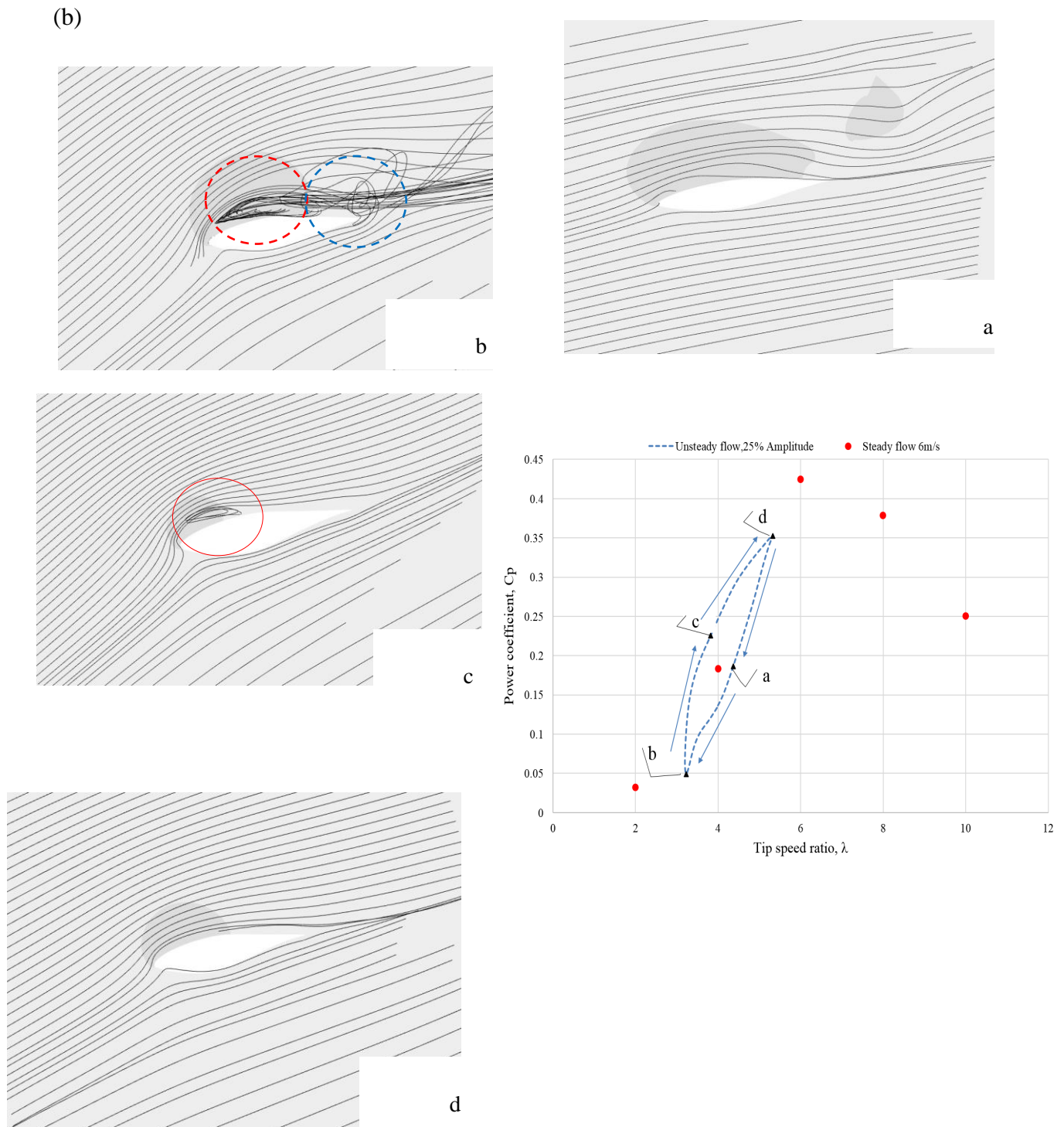


Figure 6.14: The plot and streamline performance curve of the full-scale NREL wind turbine at 1Hz and 25% amplitude of unsteady wind speed at $\lambda = 4$ (a) at 75% and (b) at 30% of the blade.

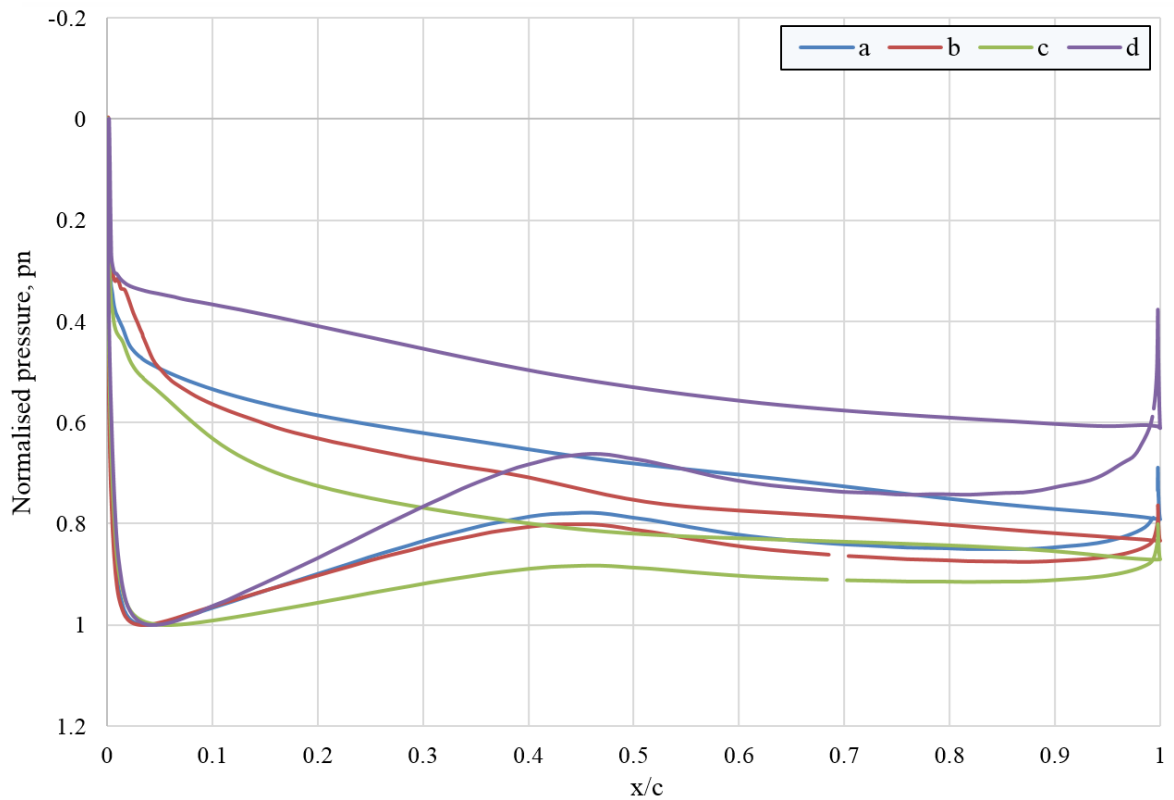


Figure 6.15: The pressure distribution around the rotor blade at different locations around the hysteresis loop of the full-scale NREL wind turbine at $\lambda=4$. Conditions are 1Hz and 25% amplitude of unsteady wind speed at 75% of the blade.

First, Figure 6.14 outlines the streamlines around the cross-section of the blade at 75% and 30% of the four points is shown. In part (a) of Figure 6.14, the flow visualisations at 75% of the blade show clearly that the flow is fully attached to the surface of the blade at point **d**, where the performance is highest in this part of the hysteresis loop. Whereas at point **c**, in the area next to the trailing edge, the flow circulates and then to get steady after the blade as it is surrounded by the red circle. The flow at point **b** is observed to be sharply circulating over the suction side of the blade, especially at the trailing edge. The effect of the lift force on the blade at this point is likely to be decreasing when the angle of attack of the blade is also decreasing. This finding was reported by Yang et al. (2008) at the low part of the hysteresis loop when the flow separated after occurrence of the stall close to the leading edge. Similarly, in part (b), the flow visualisations at 30% of the blade display that the flow is fully attached to the surface of the blade at points **a** and **b**. However, the flow separates gently from the blade at point **c** and the performance deteriorates slightly. Moreover, the main circulation over the surface of the blade next to the leading edge can be

seen at point **d** which is indicated by the red dashed circle. The flow re-separates and reverse circulation process (blue dashed circle) begins, apparently as the result of changes in pressure distribution along the pressure side of the blade at this point. This behaviour pattern is likely to occur at this point which lies in the relatively low tip speed ratio range ($\lambda \leq 3$). This could excite the dynamic stall accompanying the decreasing of lift to drag ratio (Zhou, 2013).

Figure 6.15, as before, illustrates the pressure distribution around the chosen locations along the blade. The trend of the pressure curve at points **a**, **b** and **c** looks distinctly different from that of the point **a**. The pressure gradient appears to be constant at the suction side after 70% of the blade. The lift value at point **c** seems insignificant, although there is a noticeable increase in the performance, as shown in Table 6.5. Nevertheless, the pressure curve at points **d** at 75% of the blade goes down close to the leading edge and this could provide a general impression of why the wind turbine's power high at this point.

Table 6.5 The area under the pressure curve at each point on the loop ($f=1\text{Hz}$, $A=25\%$ and $\lambda=4$).

Point	a	b	c	d
Area	0.1877	0.1570	0.1419	0.2608

Moreover, there is a noticeable difference in the angle of attack visually in the plot between the fluctuated wind flow and of the angle of attack at each instantons wind speed. Excluding a small part of the 30 % angle of attack line, the whole line lies on the stall region ($\alpha > 16$) (see Appendix B).

6.5.2 Power performance of the wind turbine at $\lambda=8$

This investigation focused on $\lambda=8$ which is the high tip speed ratio adjoins the other side of the $\lambda=6$. The hysteresis loop with steady state flow trend can be observed in Figure 6.19. The unsteady wind speed was calculated according to the time-step size ($t= 0.001833$ s)

which is derived from the rotational blade speed ($\omega=9.5208$ rad/s). The 1Hz frequency and 25% amplitudes represents a base case.

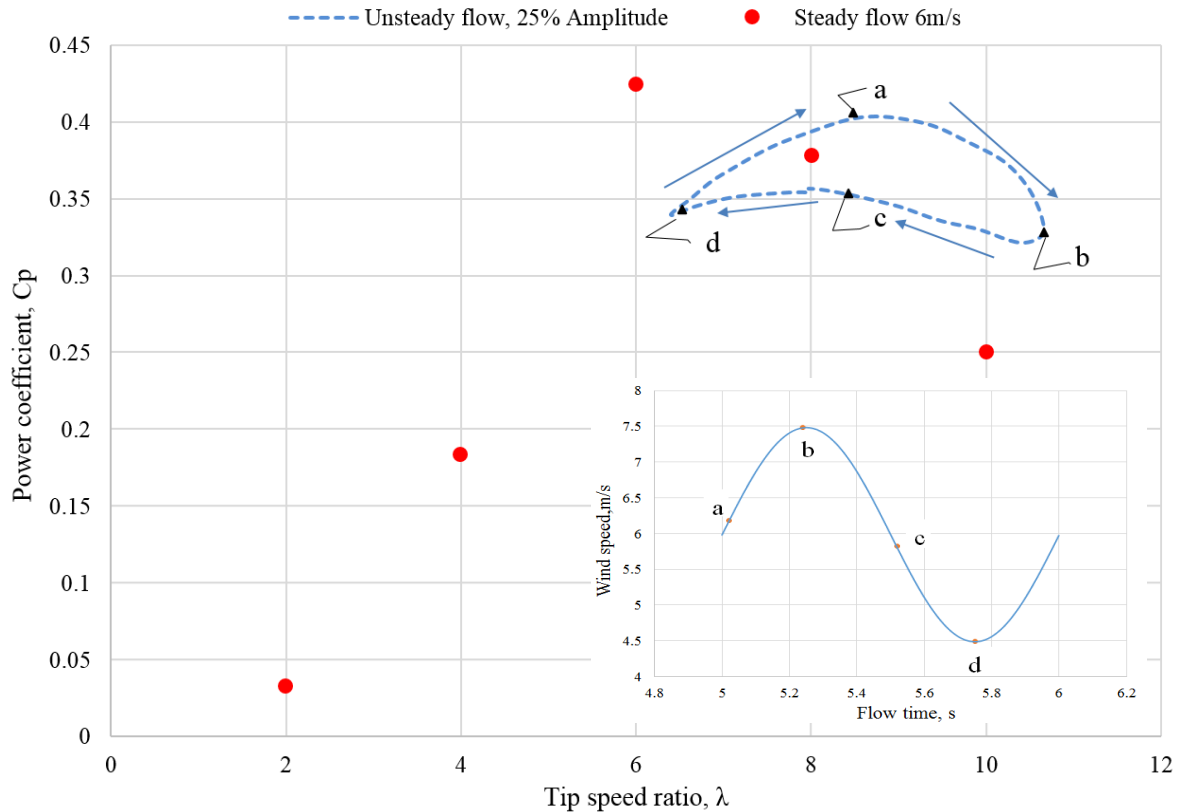
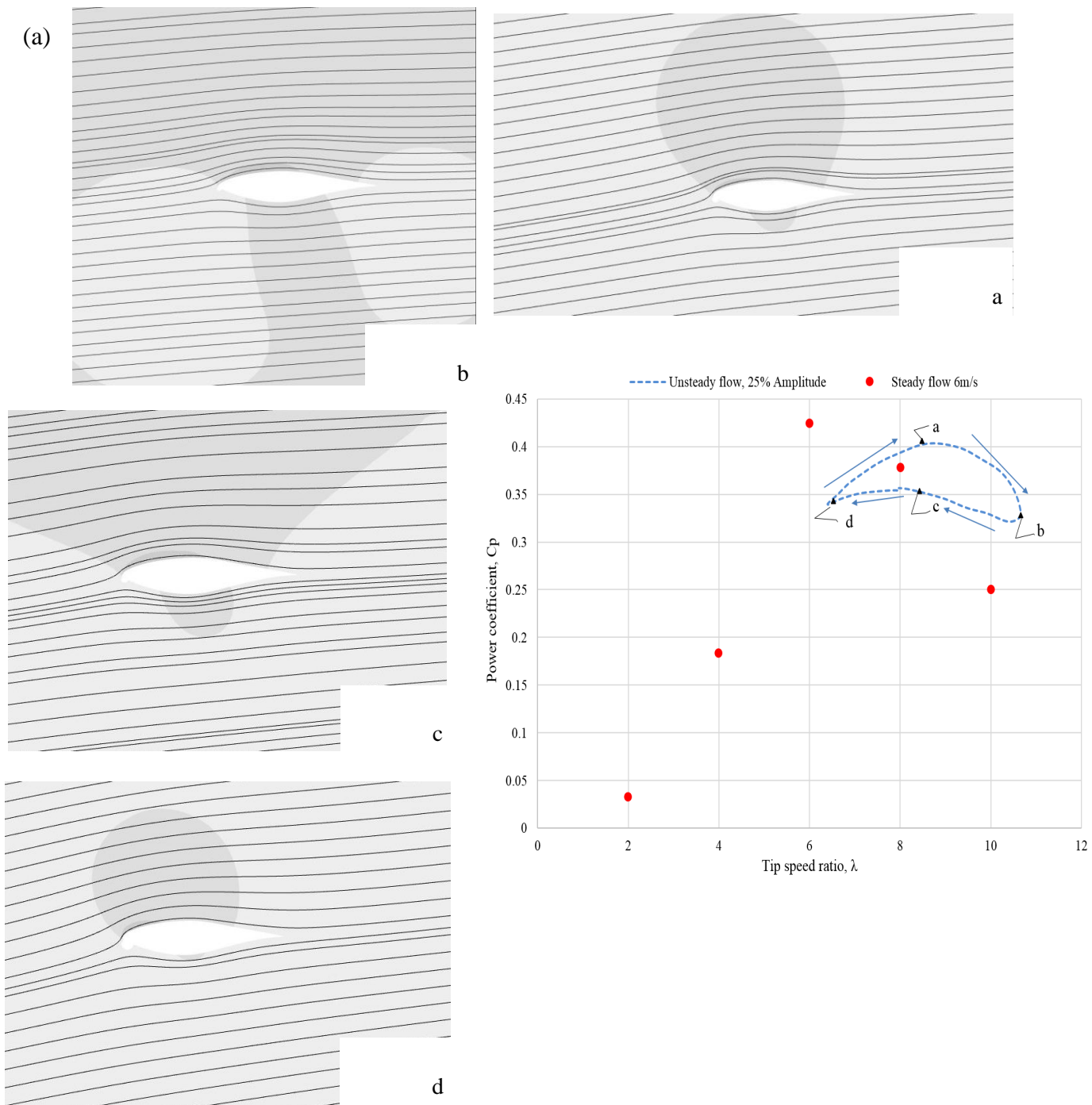


Figure 6.16: Effect of unsteady flow on the performance of the HAWT at 25% amplitude and $\lambda=8$.

Figure 6.16 shows the four points (**a**, **b**, **c** and **d**) placed on the hysteresis loop in order to gain more specifics about the flow behaviour in this case. In general, it can be noticed that the hysteresis loop follows the second half of the steady state performance trend. This loop is also wide in the middle at approximately $\lambda=8.75$ and then goes down until point **b** and **d**. The wind turbine approximates the peak value of the loop ($C_p= 0.4009$) at $\lambda=8.75$ and at point **a**. On the other hand, the turbine in this case is operating at low tip speed ratio $\lambda=10.7$ and its value is 0.335 which is close to point **b**. Additionally, the gained average $C_{p_{av}}$ of the unsteady flow loop is 0.357 which is lower than the peak value of the steady flow case performance of the wind turbine value. This corresponds to the finding obtained from the same case at $\lambda=6$ when the average $C_{p_{av}}$ was lower than C_p . The following figures show the plotting of a range of streamlines and calculation of the pressure distribution on the

surface of the aerofoil section that were utilised to gain more details about this unsteady flow condition.



(b)

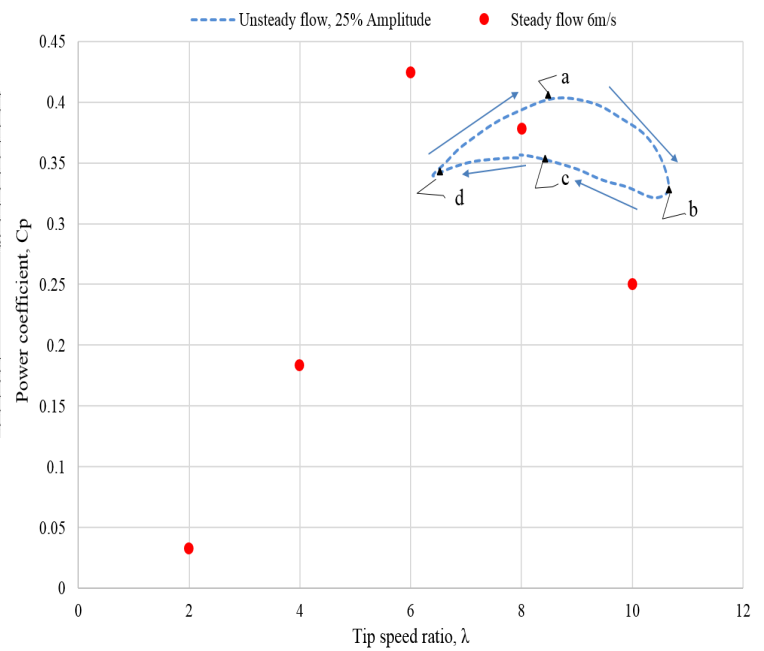
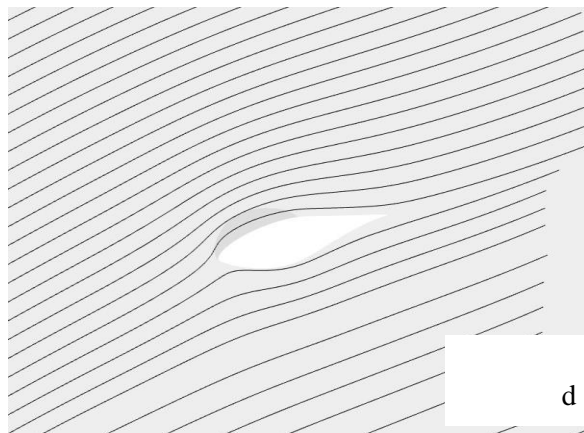
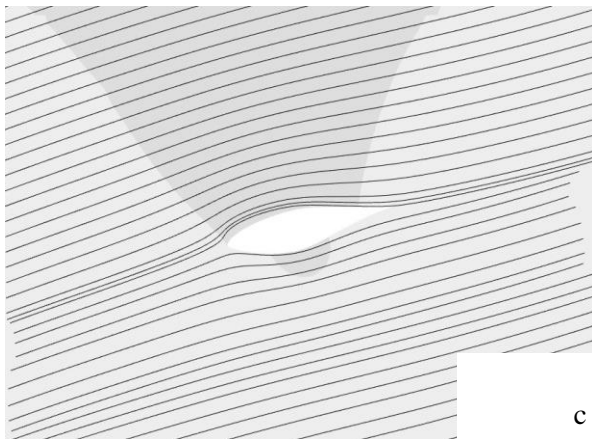
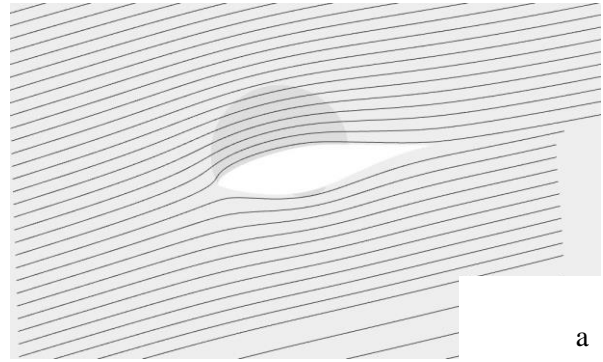
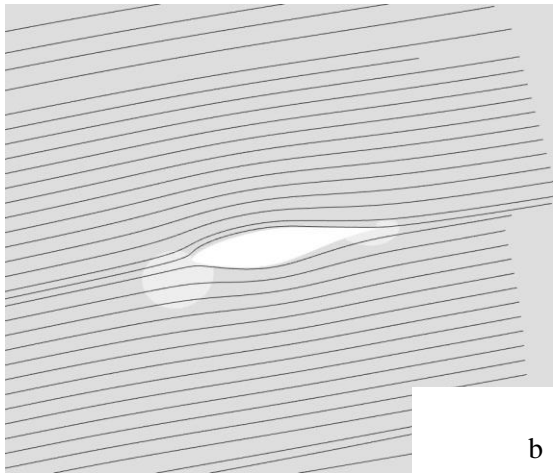


Figure 6.17: The plot and streamline performance curve of the full-scale NREL wind turbine at 1Hz and 25% amplitude of unsteady wind speed at $\lambda=8$ (a) at 75% and (b) at 30% of the blade.

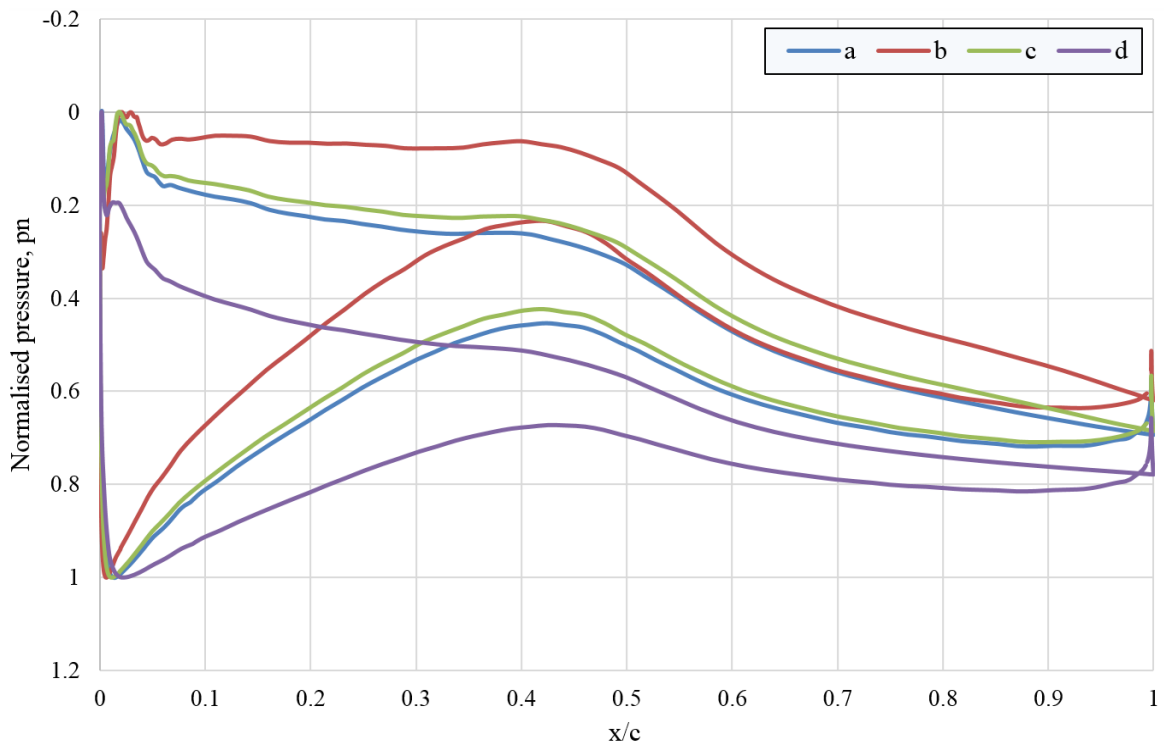


Figure 6.18: The pressure distribution around the rotor blade at different locations around the hysteresis loop of the full-scale NREL wind turbine at $\lambda=8$. Conditions are 1Hz and 25% amplitude of unsteady wind speed at 75% of the blade.

The streamlines are shown in Figure 6.17 at the 75% and 30% span-wise locations of the blade for the five points. In parts (a) and (b) of Figure 6.17, the flow visualisations display that the flow over the two chosen locations of the blade is fully attached at all points when the angle of attack decreases as tip speed ratio increases. It can be easily detected that there is neither separation nor circulating within the flow over the blade and this differs from the findings observed at $\lambda=4$.

Figure 6.18 indicates that there is significant difference in the pressure distribution around the 45% of the blade except that for point **d**. Whereas, after the 60% of the blade shows high similarity in the behaviour among whole processes. Although the pressure curve of point **a** is small and could generate low lift, the performance is shown in the high value at this point. This could happen due to low lift to drag ratio when the drag force might be high.

Table 6.6 The area under the pressure curve at each point on the loop ($f=1\text{Hz}$, $A=25\%$ and $\lambda=8$).

Point	a	b	c	d
Area	0.2549	0.2567	0.2649	0.2061

Going back to Appendix B, it is obvious that whole values of angle of attack are within the attach region ($\alpha < 16$).

6.6 Effects of amplitudes in summary

The performance of the NREL phase VI wind turbine in oscillating wind flow conditions was simulated as mentioned above and the findings will be summarised in the following paragraphs. The results revealed that increase in the amplitude of the unsteady wind flow can negatively affect the performance. Concise of results can be tracked on Table 6.7:

Table 6.7. Performance at various amplitudes.

Amplitudes (%)	C_p , CFD	$C_{p_{av}}$, CFD	$V_{(t)max}$ (m/s)	$V_{(t)min}$ (m/s)
0	0.42457	-	-	-
7	-	0.41691	6.404	5.56605
15	-	0.42582	6.8827	5.08725
25	-	0.4029	7.48125	4.48875
45	-	0.352146	8.6782	3.29176

In general, the performance decreased at high amplitudes compared to the steady state case (0% amplitude). However, it was found that at the moderate amplitude values of 7 and 15%, performance either approached to the value of 0% amplitude or slightly improved on it. The values in the last two columns could explain why the performance was relatively high at low amplitude compared to the others. It can be observed that at 7% amplitude, the difference between instantaneous wind speeds is small compared to the difference between maximum and minimum instantaneous wind speed values at 45%

amplitude. That means the power coefficient was not strongly changed with relatively small fluctuating of wind speeds.

The shape of hysteresis unsteady state wind flow differs between the 7 and 45% amplitudes. It was found that at 7% amplitude the curve was in the shape of a small loop in a small range of the tip speed ratio. The curve of the 15% amplitude was similar in shape to the 7% amplitude curve, but it was longer and the instantaneous C_p values more widely distribute over tip speed ratios. Regarding the high amplitudes, the curves of the 25% and 45% amplitudes generally exhibited different shapes from the low amplitudes curves. The two shapes have a noticeable width and they twisted at a certain tip speed ratio. Therefore, additional points were required along the loop in order to provide more details on how the wind turbine behaves at these amplitudes of the incoming wind speed.

The main power curve up to this point in the chapter needs to be mentioned and is clearly exhibited in Figure 6.19.

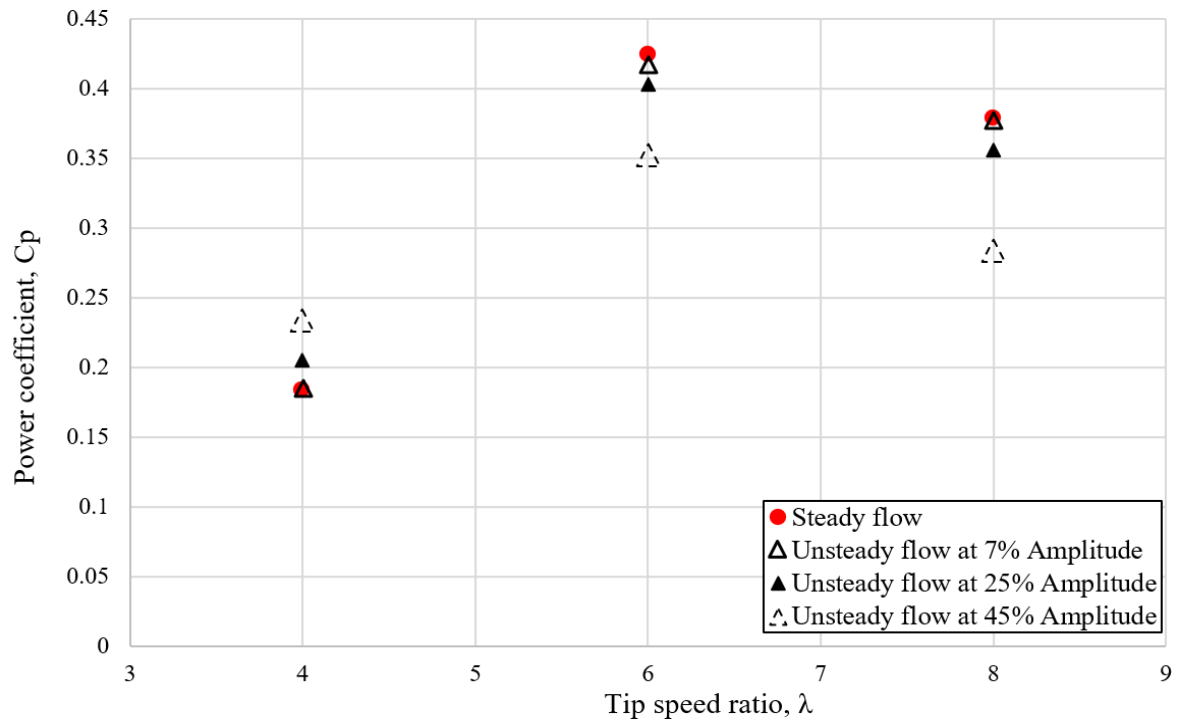


Figure 6.19: Effect of various amplitudes at 1Hz unsteady wind flow on the wind turbine.

Figure 6.19 presents the performance of the turbine for the three different amplitudes (7, 25 and 45%) of the wind speed and 1Hz at the three tip speed ratios ($\lambda=4, 6$ and 8). As mentioned above, 7% and 25% amplitudes were similar in shape, so the 15%

amplitude effect was dropped. It shows that the power values at the 7% amplitude, which are shown in hollow triangles, and the steady state flow values are highly compatible at all tip speed ratios. The performance of the 25% amplitude wind speed, in solid triangles, is shown to be disproportionate to the steady state values. The wind turbine performed poorly at 45% amplitude of the wind speed except at $\lambda=4$. This exception can possibly be explained in terms of the findings in chapter five that the performance value at $\lambda=4$ was relatively lower than other sources, for the reason mentioned earlier.

The last sections consider the effect produced by two additional tip speed ratios positioned close to the main base case $\lambda=6$. Rather than presenting the three hysteresis loops separately, they are combined in one figure in order to gain more insight into their behaviour, as shown in Figure 6.20.

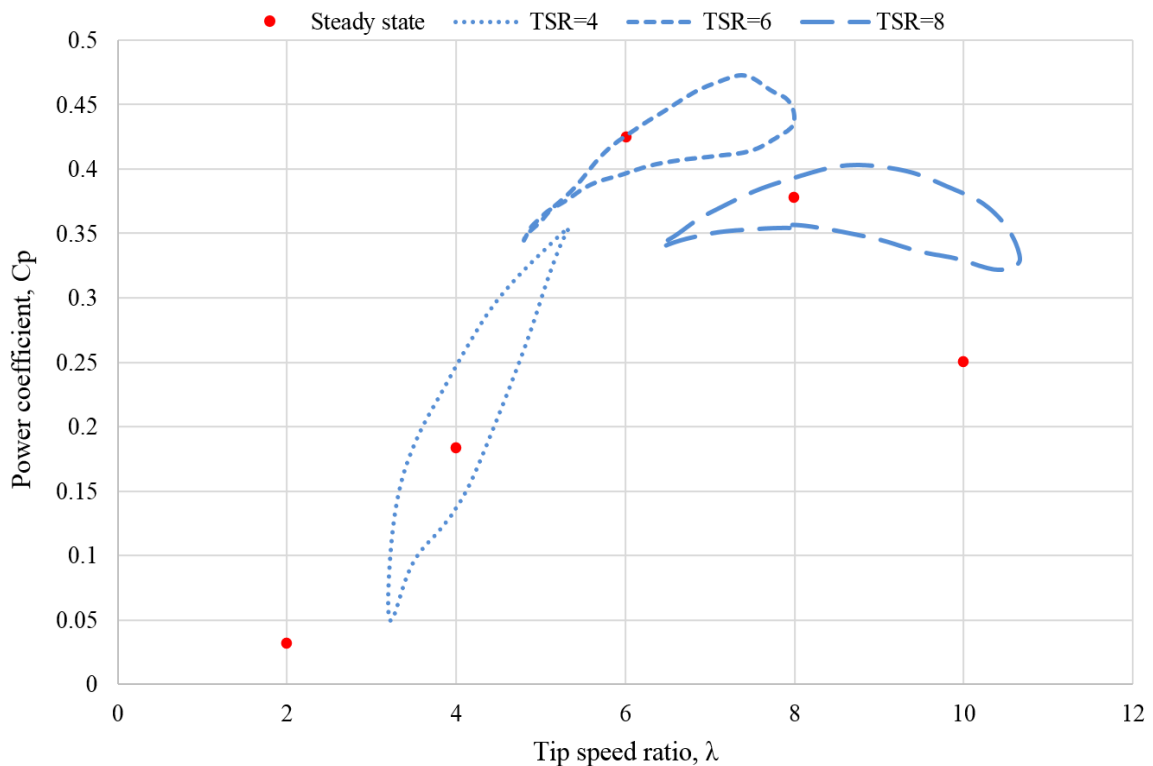


Figure 6.20: The hysteresis curve for the three unsteady cases at $\lambda=4$, 6, and 8.

The hysteresis loop at $\lambda=4$ is mainly concentrated on the left hand-side of the steady state curve; however, at $\lambda=8$ it follows the right hand-side of that curve. The loop at $\lambda=6$ ranges from the left to the right side of the curve and is centred almost at the top of that

curve. The results of the simulation at $\lambda=4$ show that at stall the wind flow separates from the surface near the tip and the root of the blade. In addition, when streamlines were applied around the blade sections, circulations were clearly apparent that could have side effects on the performance in total. In contrast, at $\lambda=8$ the use of the streamlines revealed that the flow still attached to the surface along the blade and could provide compelling evidence the rotor's performance is relatively higher than that at $\lambda=4$.

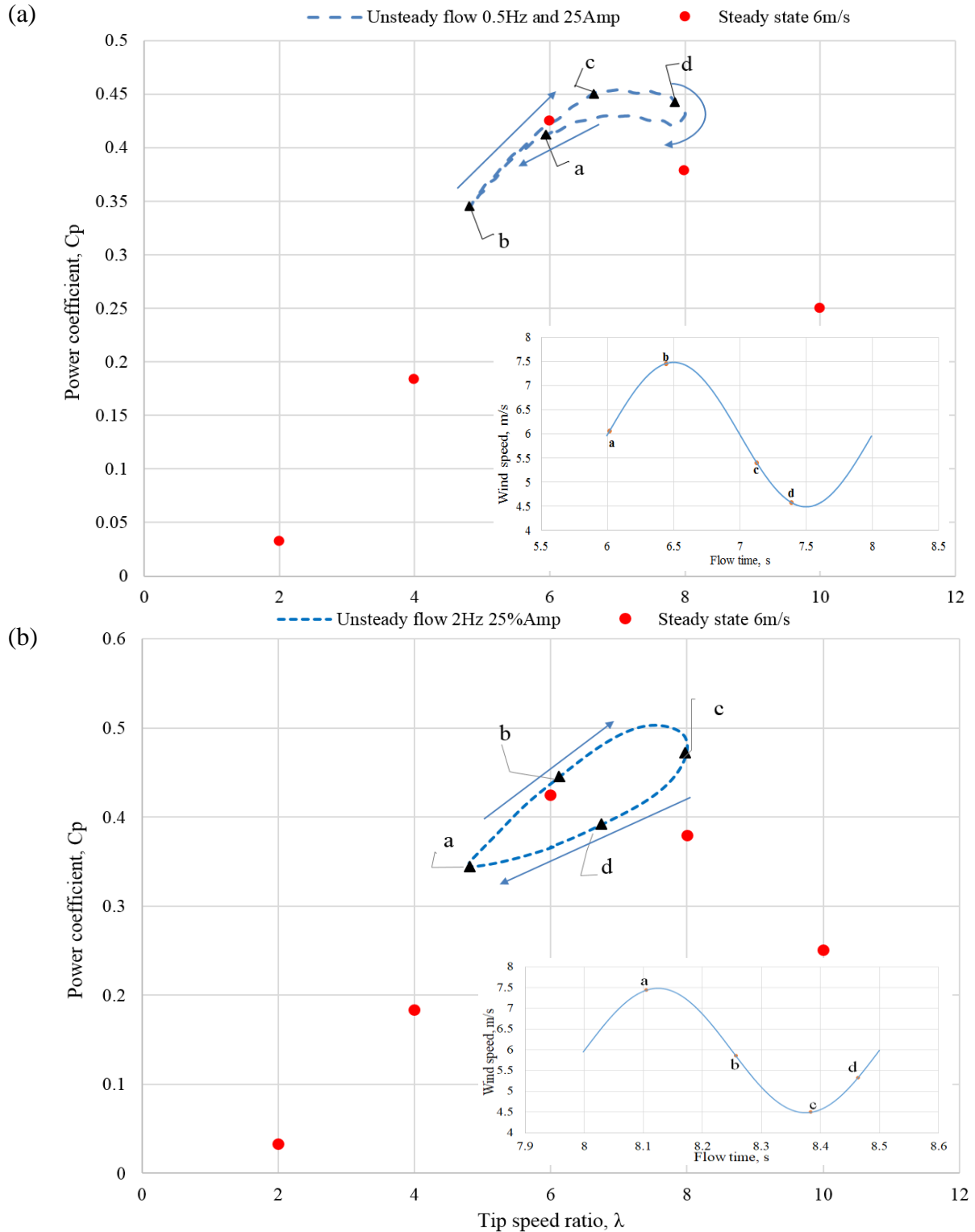
The next part in this chapter will investigate the influence of frequency variation on the performance of the current wind turbine rotor, taking into consideration the rotor's optimum operating condition of $\lambda=6$. Moreover, the same analytical procedures as those utilised for the streamlines and pressure distribution around two locations along the blade, will be employed in order to gain more insight into that investigation.

6.7 Power performance of the wind turbine with frequency variations

This part of the chapter will focus on the impact of wind speed frequencies on the wind turbine. Various frequencies will be investigated and analysed and then compared to the steady flow base case (1Hz and 25% amplitude), and results discussed in detail as in the previous part. The base case was chosen due to the 25% amplitude wind speed is the average of the low and high amplitudes (7% and 45%) respectively. In addition, the 15% amplitude wind speed was dropped because of its high similarity with the 7% amplitude case. One average cycle of the unsteady flow power performance of the wind turbine ($C_{p_{av}}$) will be calculated by taking the C_m value then go to excel to obtain the performance value. Also, the same solver and running jobs procedure will be used for all simulations. The unsteady wind speed will be produced using the time-step size ($t=0.00244$ s) which is derived from the rotational blade speed ($\omega=7.158$ rad/s) at $\lambda=6$ by compiling the UDF file to Fluent tool. The parameter f , which was mentioned in equation 6.1, will likely play an essential role in forming the shape and behaviour of the hysteresis loop.

Each of the following sections will shed light on the diversity of frequencies and their influence on the rotor performance. As mentioned in chapter two, five different frequencies (0.5, 2, 5, and 10Hz) were chosen to accomplish this study, in an attempt to fill the gaps identified in the previous research in the frequencies range covered. Briefly, among those previous studies, Toshimitsu, et al. (2012) covered the range below 0.5Hz, although they

applied a different wind turbine model. Additionally, Scheurich and Brown (2013) analysed the performance of the VAWT using 1Hz to investigate its performance. Finally, Steinkohl et al. (2013) employed 8Hz to examine the behaviour of the high wind speed. The following sequence of figures represents the hysteresis loop at various frequencies.



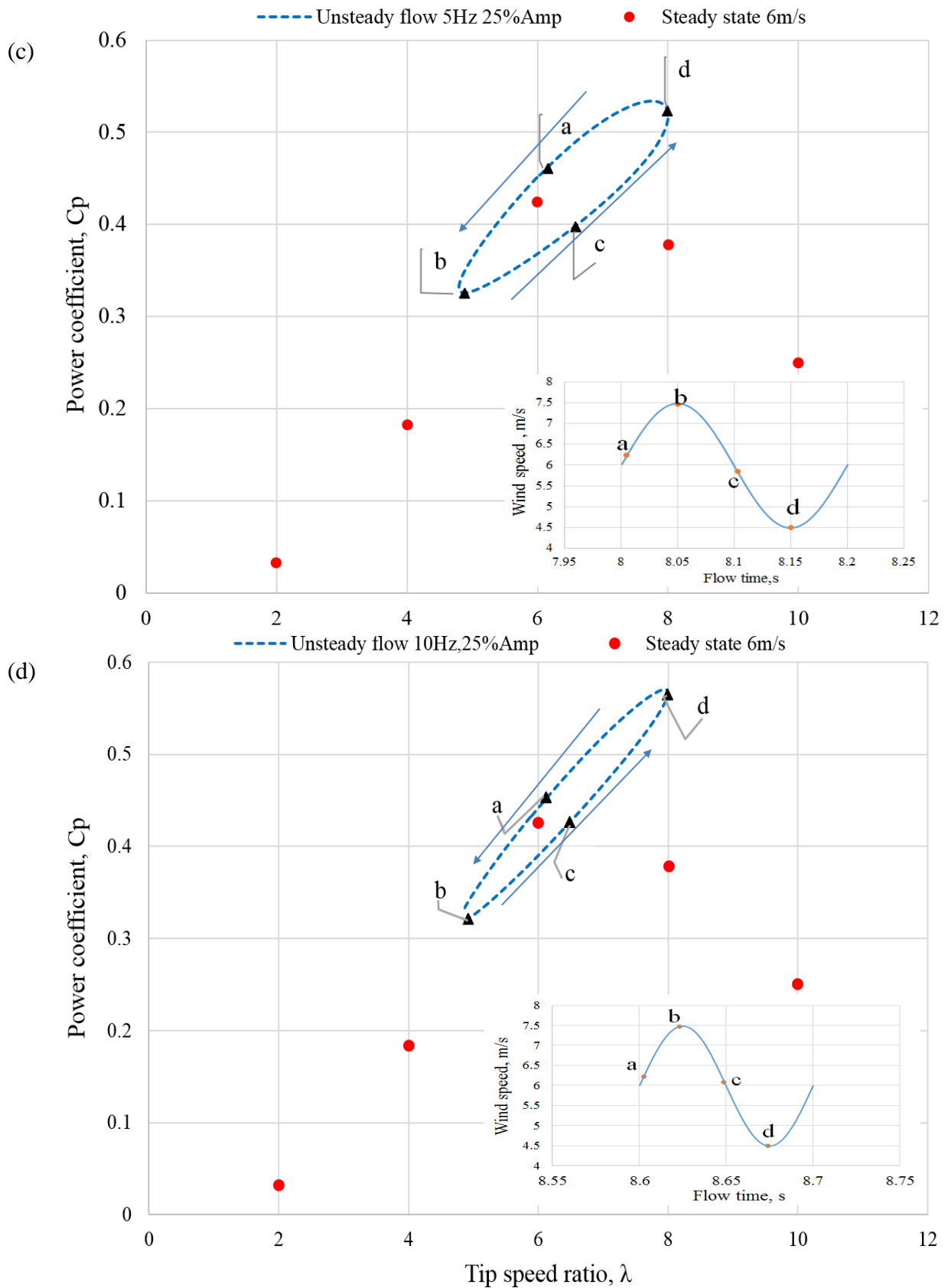


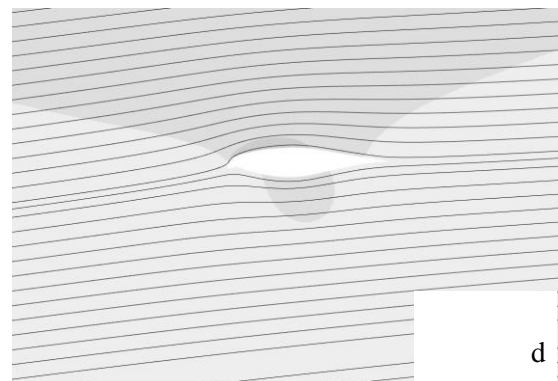
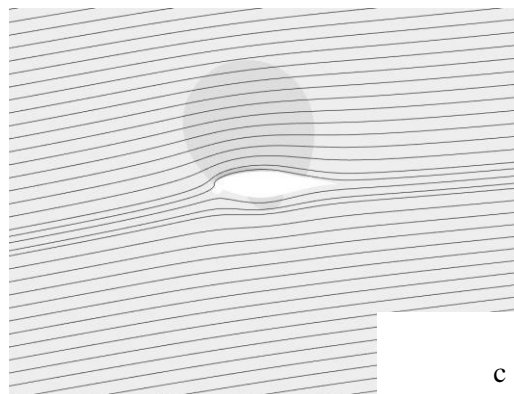
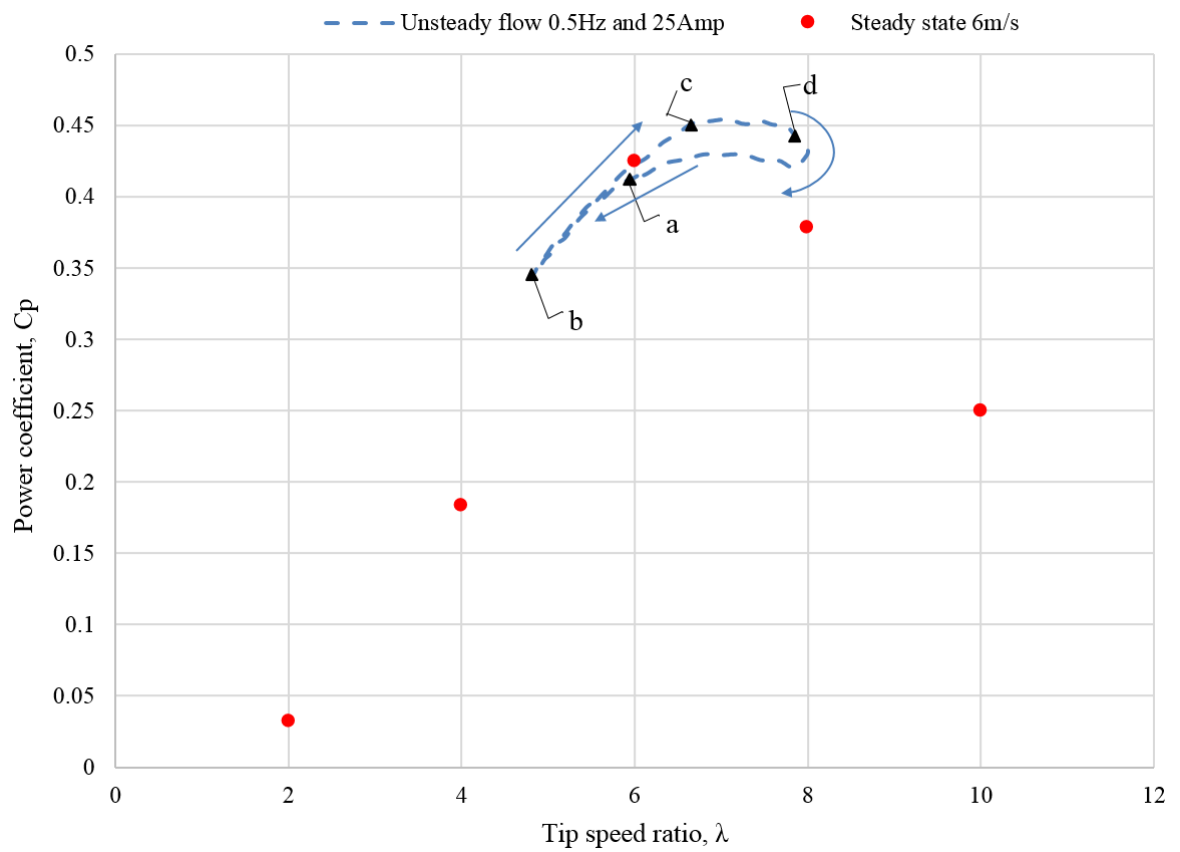
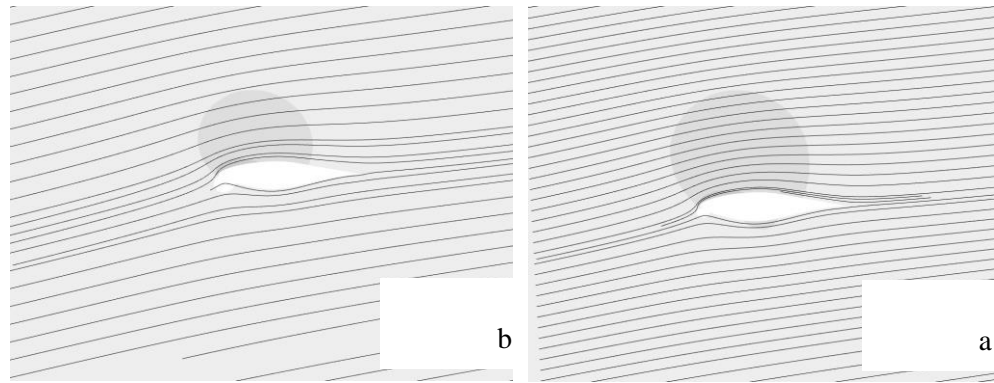
Figure 6.21: Effect of steady and unsteady flow on the performance of the HAWT at 25% amplitude and various wind speed frequencies.

6.7.1 Power curve at $f=0.5\text{Hz}$ and 25% amplitude

In line with the previous amplitudes procedures and starting with low oscillation of flow at 0.5Hz frequency, the C_p - λ curve of the wind turbine for both steady and unsteady flow conditions will be presented, as shown in Figure 6.21(a). As is customary in this study, the red points refer to the steady flow trend, while the blue dashed loop plots show the unsteady flow loop. In addition, the points (**a**, **b**, **c**, and **d**), located in the black triangles, are superimposed on the current trend to give the opportunity to take a closer and broader look at the performance of the rotor at this frequency.

Figure 6.21(a) reveals that the hysteresis loop generally follows the trend of the steady state performance curve. The prominent points (**a**, **b**, **c** and **d**) were located along the hysteresis loop gain more visualization of the flow behaviour. The hysteresis loop shows twist-down of 0.3463 at the tip speed ratio lower than 6 where the performance is at the lowest point in the loop at **b**. Clearly, point **b** is within the high angle of attack region, therefore; the lift force decreases and hence the rotor performance drops. Then, the $C_{p_{av}}$ value goes up until point **d** when the wind turbine performance shows recovery, $C_p= 0.4542$ at $\lambda=7.045$. The average $C_{p_{av}}$ value of the unsteady flow loop is found to be 0.4037 which is clearly lower than the peak value of the steady flow trend performance of the wind turbine. The streamlines and pressure distributions presented considerable detail on this unsteady flow condition as can be seen in Figure 6.22 and Figure 6.23 respectively.

(a)



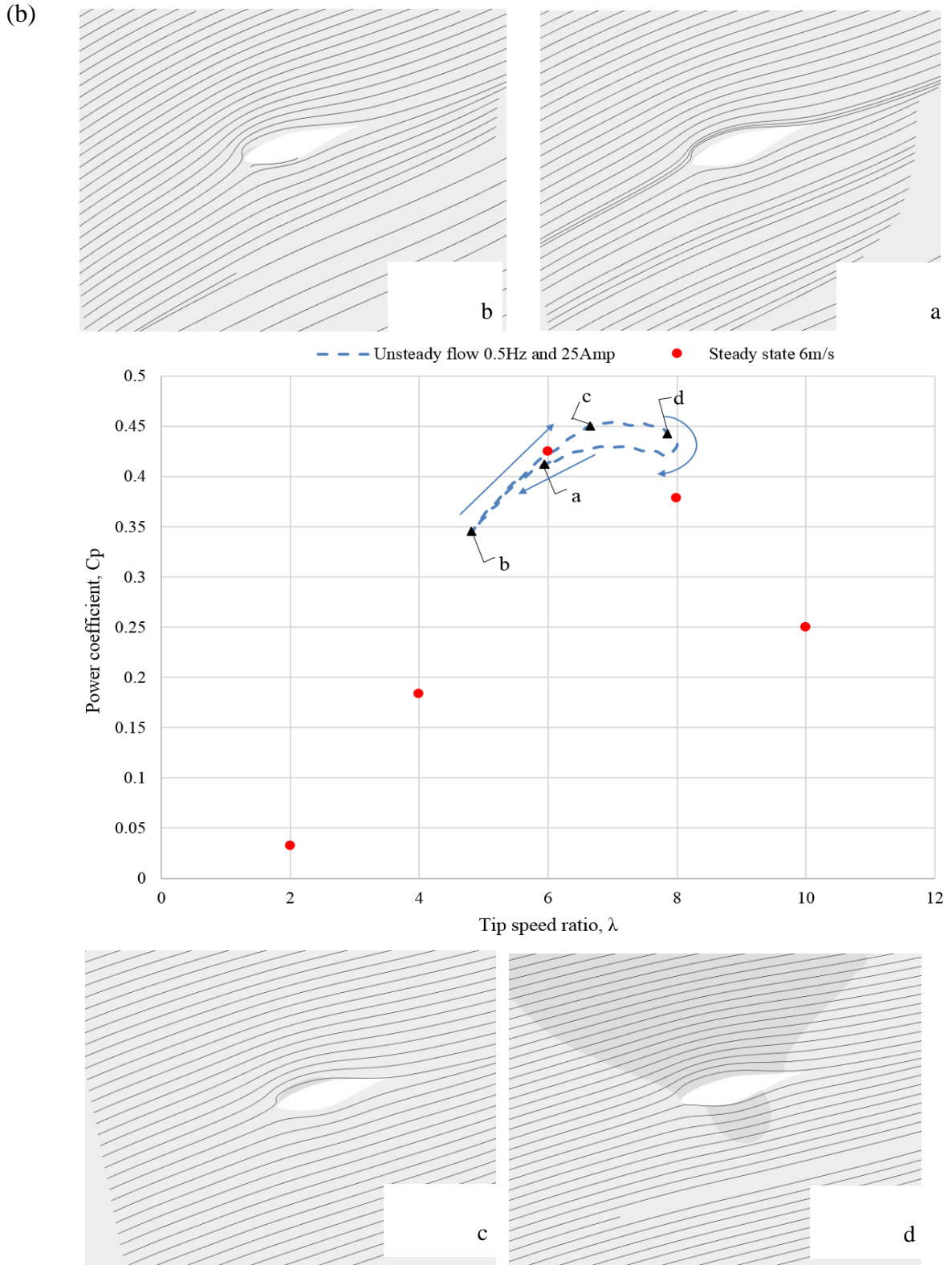


Figure 6.22: The plot and streamline performance curve of the full-scale NREL wind turbine at 0.5Hz and 25% amplitude of unsteady wind speed at $\lambda= 6$ (a) at 75% and (b) at 30% of the blade.

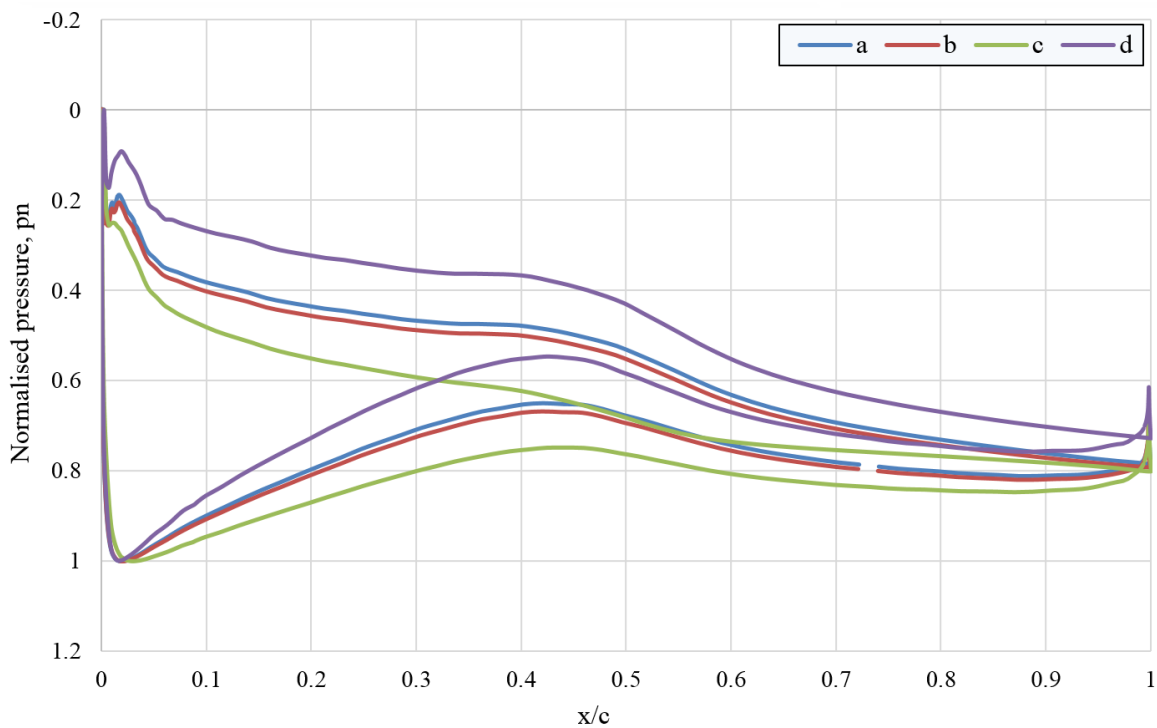


Figure 6.23: The pressure distribution of the hysteresis loop of the full-scale NREL wind turbine at 0.5Hz and 25% amplitude unsteady wind speed at 75% of the blade.

In Figure 6.22 shows that the flow passes smoothly around the blade at the two locations along the blade (75% and 30%). It seems that the flow is still attached to the blade in all points along the hysteresis loop even point **b** lies on the low tip speed ratio region and the angle of attack is expected to be high. This could occur due to a low instantaneous wind speed which may hit the rotor at this point.

Figure 6.23 shows that there is a visible difference in shapes among the normalised pressure curves except points **a** and **b**. This difference, however, does not reveal a significant difference in areas, excluding the area of point **c**, as shown in Table 6.8. It can be concluded that the flow here behaves in exactly the same manner as at 7% amplitude and 1Hz unsteady wind speed. So, it is clear that has a more dominate effect on the hysteresis loop than the amplitudes.

Table 6.8 The area under the pressure curve at each point on the loop ($f=0.5\text{Hz}$ and $A=25\%$).

Point	a	b	c	d
Area	0.2131	0.2079	0.1823	0.2344

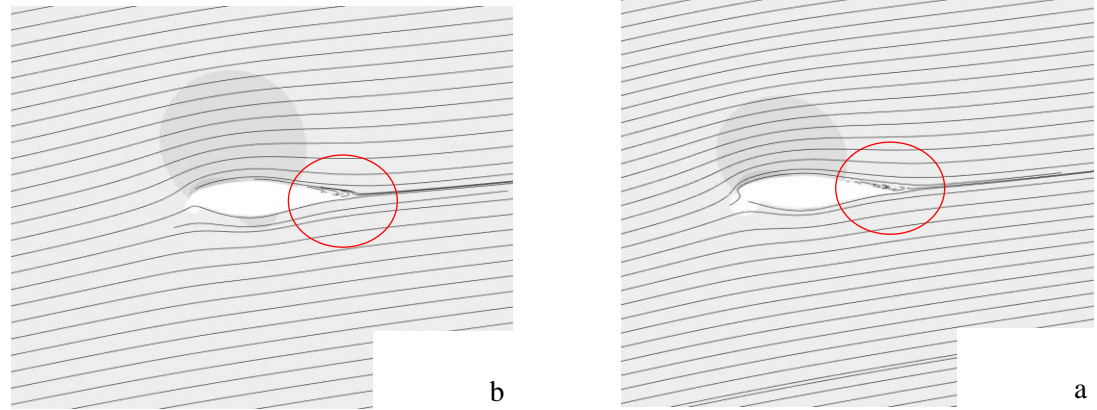
6.7.2 Power curve at $f=2\text{Hz}$ and 25% amplitude

As in the previous low frequency case, four points were set up along the hysteresis loop as illustrated in Figure 6.21(b). In this case, the 2Hz wind speed frequency, which is higher than previous frequencies, was studied and the results are shown in the following paragraphs.

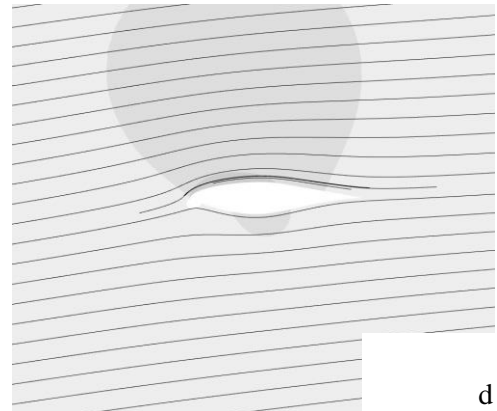
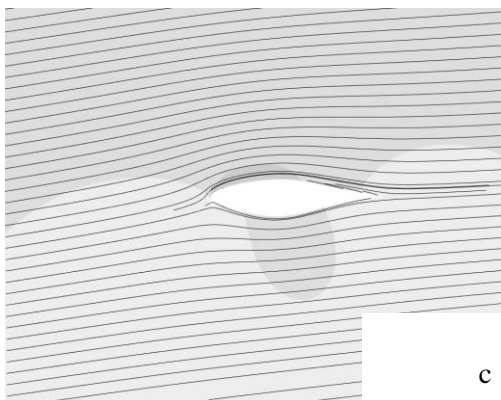
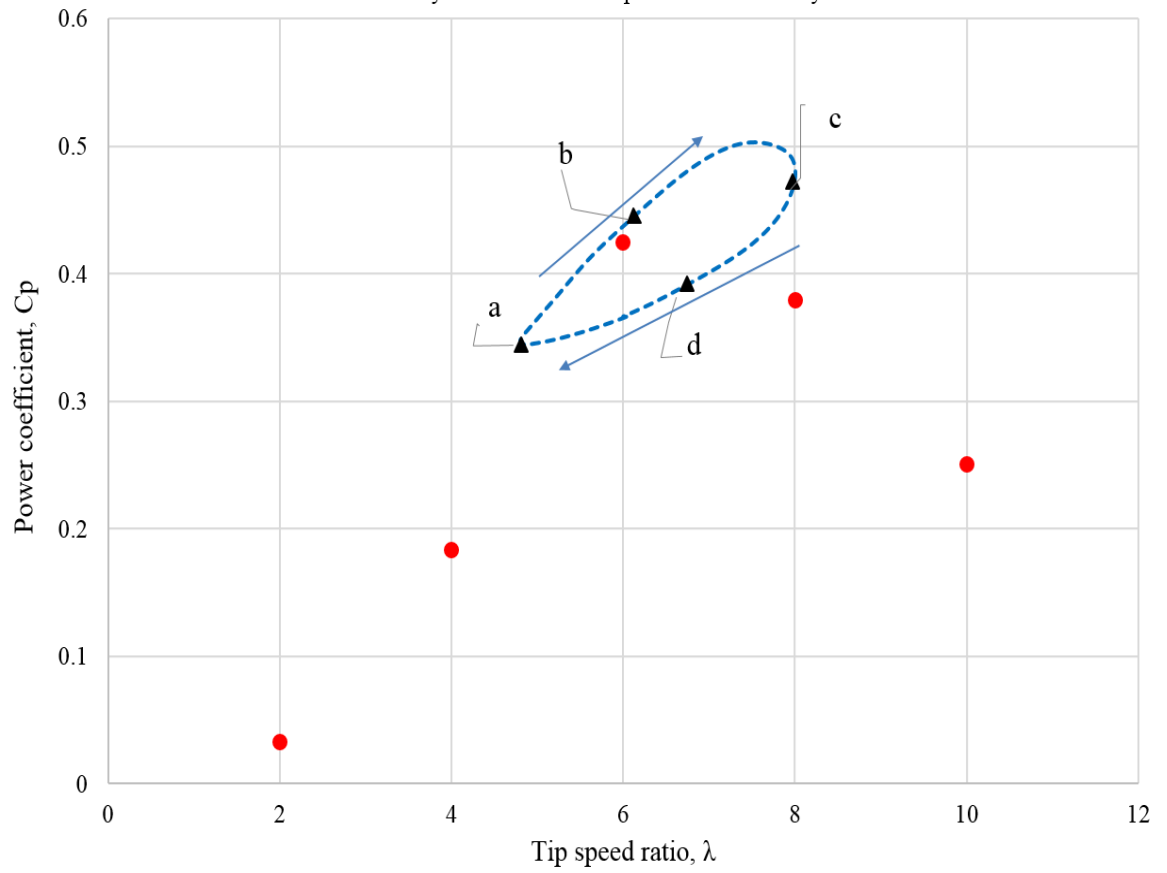
Figure 6.21(b) simply delineates the hysteresis loop in 2Hz wind speed. The loop generally takes an elliptic form and it completely surrounds the peak value of the steady state trend. Moreover, it does not seem to resemble the behaviour of the preceding hysteresis loops that were wider and untwisted. The lowest performance of the wind turbine C_p lies on the lowest point in the loop **a** and is 0.344 at $\lambda=4.83$, while the highest performance is 0.5033 at $\lambda=7.98$ close to point **c**. In total, the average $C_{p_{av}}$ value of the unsteady flow loop is 0.4073 which is clearly lower than the peak value of the steady flow trend performance. So, comparing this result with the 0.5Hz wind speed result it is clear that there is little difference in performance between the two, which could imply that the wind turbine could not respond to the increase in the wind speed frequency.

This unsteady flow condition with streamlines and pressure distributions will now be presented separately in Figure 6.24 parts a and b, and Figure 6.25.

(a)



--- Unsteady flow 2Hz 25%Amp ● Steady state 6m/s



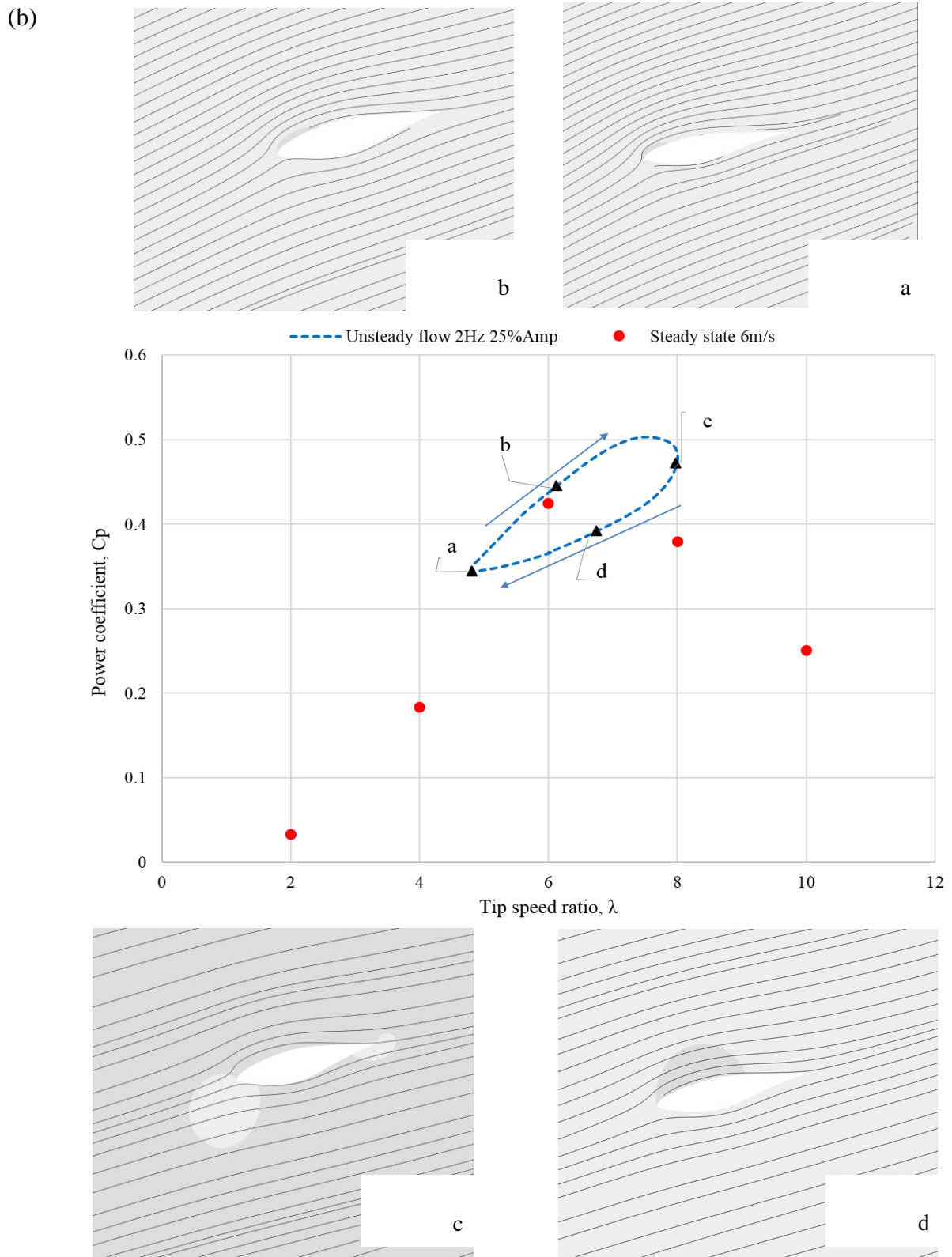


Figure 6.24: The plot and streamline performance curve of the full-scale NREL wind turbine at 2Hz and 25% amplitude of unsteady wind speed at $\lambda=6$ (a) at 75% and (b) at 30% of the blade.

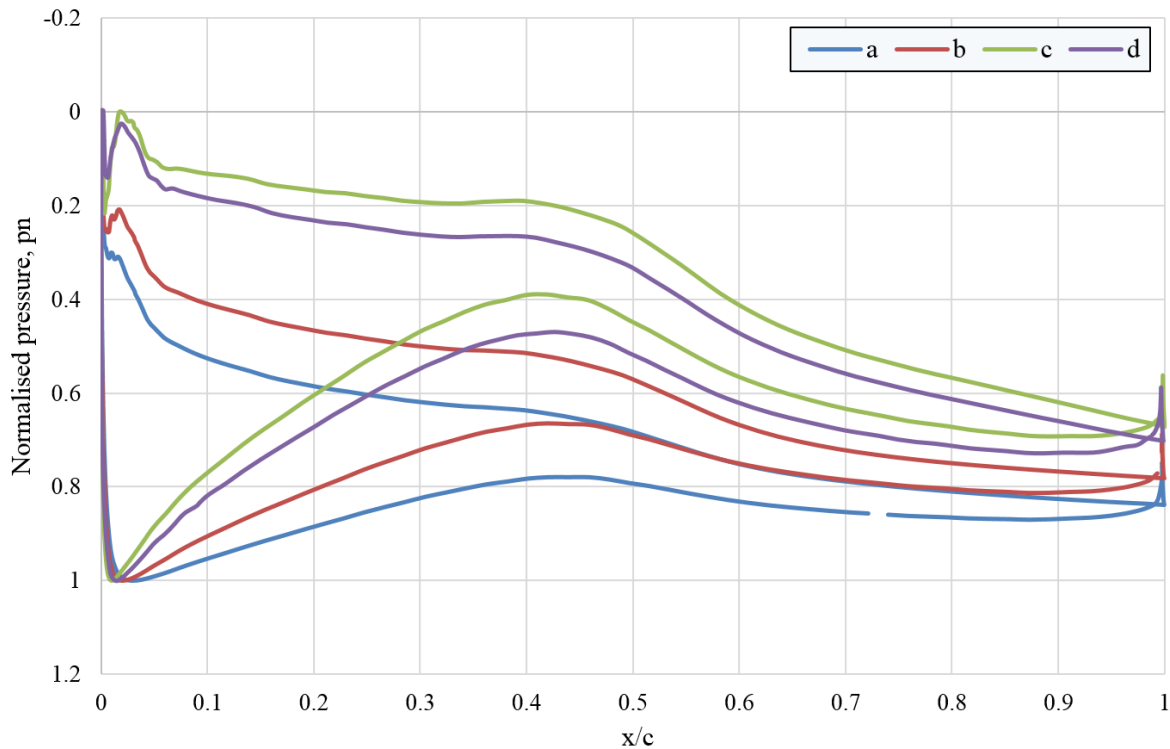


Figure 6.25: The pressure distribution of the hysteresis loop of the full-scale NREL wind turbine at 2Hz and 25% amplitude unsteady wind speed at 75% of the blade.

Figure 6.24, in particularly part (a), it is obvious that the flow moves steadily along the suction side of the blade, but it is suddenly separated next to the trailing edge as denoted by the red circle in two points, **a** and **b**. This could have occurred as a result of high angle of attack in this region ($\lambda < 6$). However, it is completely attached to the blade in all other points at 75% and 30% positions along the blade.

Finally, Figure 6.25 exhibits that there is considerable difference in the behaviour of normalised pressure curves between the two large areas (**c** and **d**) and the two small areas (**a** and **b**) on the hysteresis loop. This divergence could have occurred because of the drop in the lift force for point (**c** and **d**). Furthermore, the curve of point **a** and **b** at 75% of the blade, the pressure curve is relatively straight towards the trailing edge which implies the gradual pressure gradient is constant and this is an indication of separation. Table 6.9 supports the findings by showing the area under the pressure curves.

Table 6.9 The area under the pressure curve at each point on the loop ($f=2\text{Hz}$ and $A=25\%$).

Point	a	b	c	d
Area	0.1740	0.1935	0.2646	0.2633

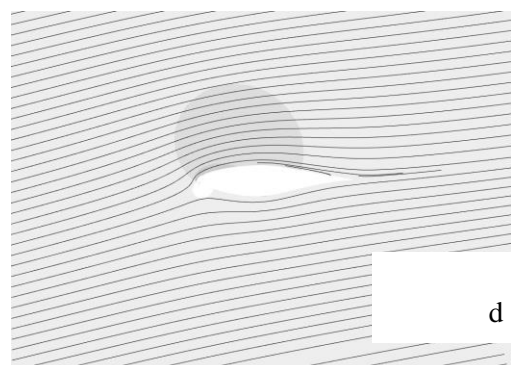
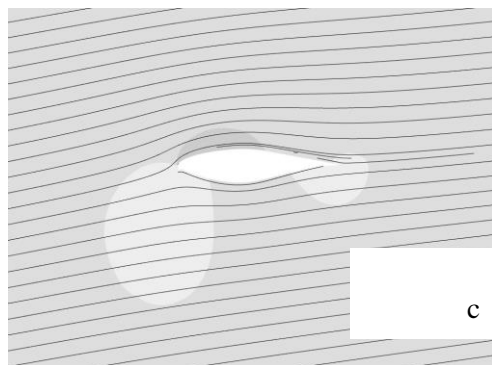
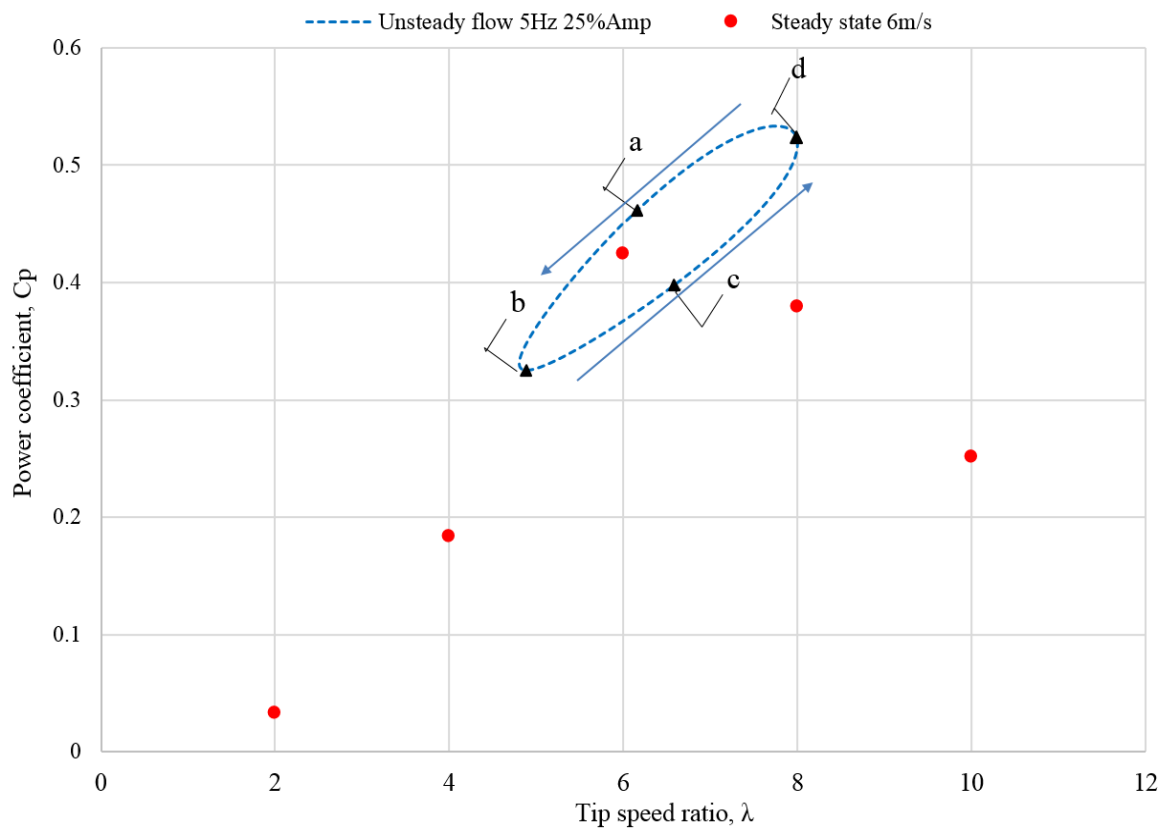
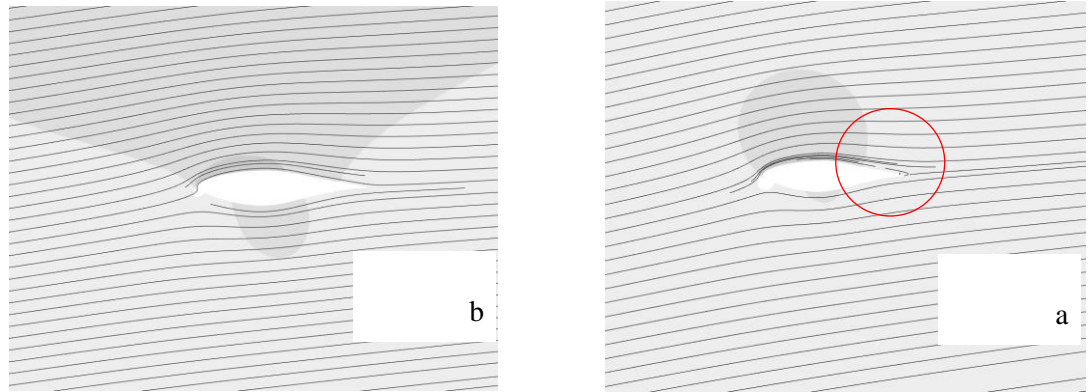
6.7.3 Power curve at $f=5\text{Hz}$ and 25% amplitude

Next, the 5Hz frequency was tested. Similar to the above procedure, four points were set up along the hysteresis loop (blue dashed loop) to highlight the flow behaviour on this loop, as demonstrated in Figure 6.21(c).

The hysteresis loop in 5Hz wind speed generally shows a similarity to that produced for the 2Hz wind speed with a little variation width-wise. The elliptic form also surrounds the peak value of the steady wind speed trend. It is found that the lowest performance of the wind turbine C_p is on the lowest point in the loop **d** and is 0.33 at $\lambda=4.8$, while the highest performance is 0.5336 at $\lambda=7.715$ on point **b**. Overall, the obtained average $C_{p_{av}}$ value of the unsteady flow loop is 0.4175 which is also lower than the maximum value of the steady flow curve performance. Comparing this result with the 0.5Hz and 2Hz wind speeds results there is clearly an increase in performance which could imply that the wind turbine this time could accommodate the increase in the wind speed frequency.

The streamlines and the pressure distribution will be presented as shown in the following figures.

(a)



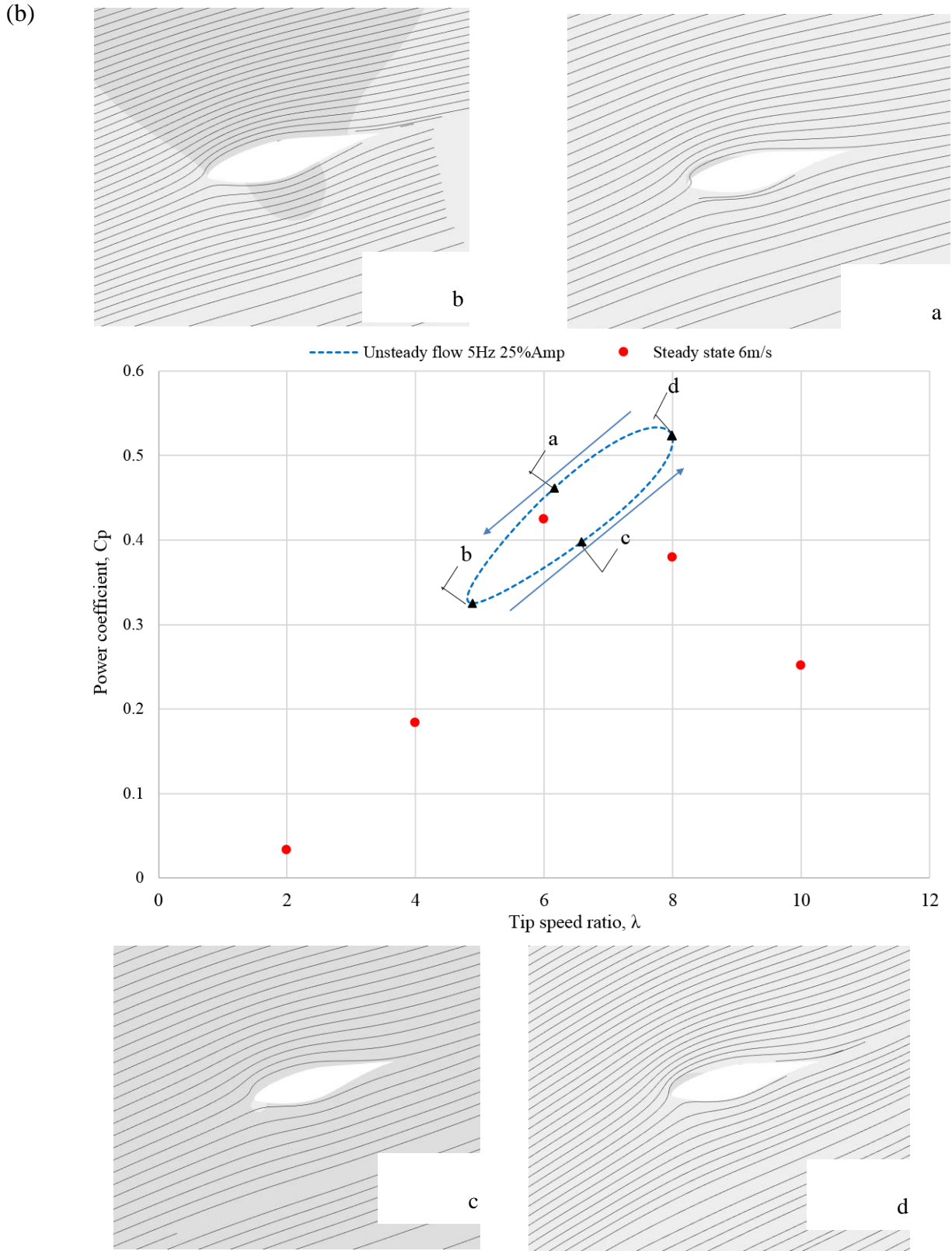


Figure 6.26: The plot and streamline performance curve of the full scale NREL wind turbine at 5Hz and 25% amplitude of unsteady wind speed at $\lambda=6$ (a) at 75% and (b) at 30% of the blade.

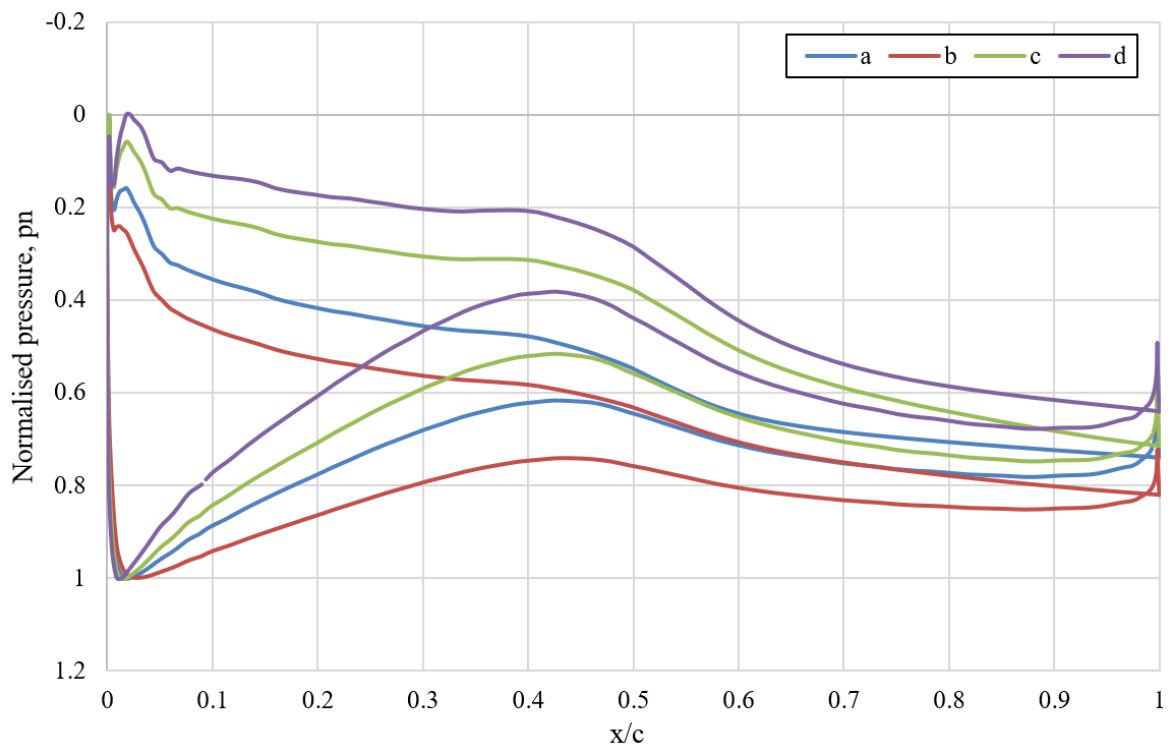


Figure 6.27: The pressure distribution of the hysteresis loop of the full scale NREL wind turbine at 5Hz and 25% amplitude unsteady wind speed at 75% of the blade.

Part a in Figure 6.26 shows the streamlines that were plotted at 75% of the blade. It reveals that the flow starts to separate slightly at trailing edge of the blade as indicated by the red circle. Whereas, it is completely attached to the blade at all other points on the 75% and 30% positions along the blade in a manner somewhat similar to the case described above.

A remarkable difference in the normalised pressure curves can be noted between the highest and the lowest point **d** and **b** respectively, as stated in Figure 6.27. The curve of point **a** at 75% of the blade, the pressure curve is not completely straight towards the trailing edge which implies the gradual pressure gradient is constant and this is an indication of separation. Table 6.10 declares that the turbine produced sufficient lift at point **d** where the area is clearly higher than others.

Table 6.10 The area under the pressure curve at each point on the loop ($f=5\text{Hz}$ and $A=25\%$).

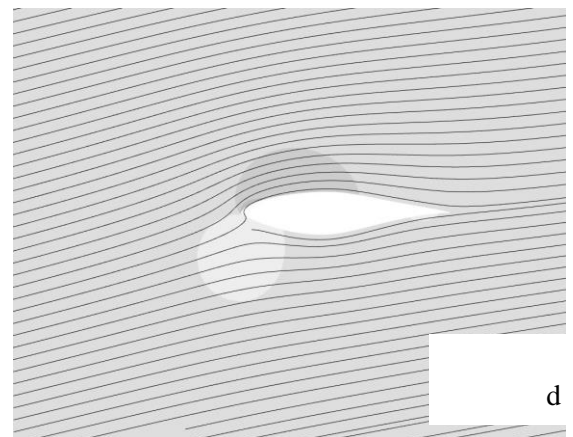
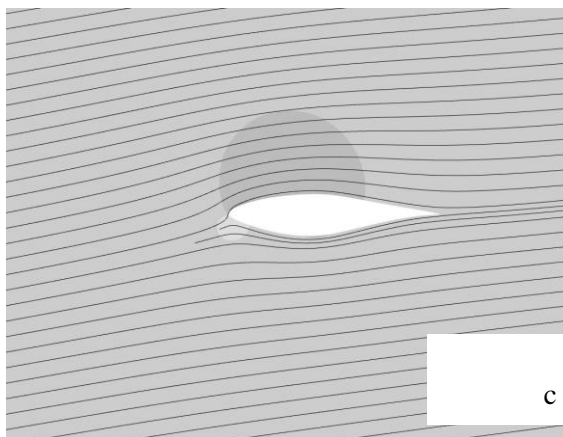
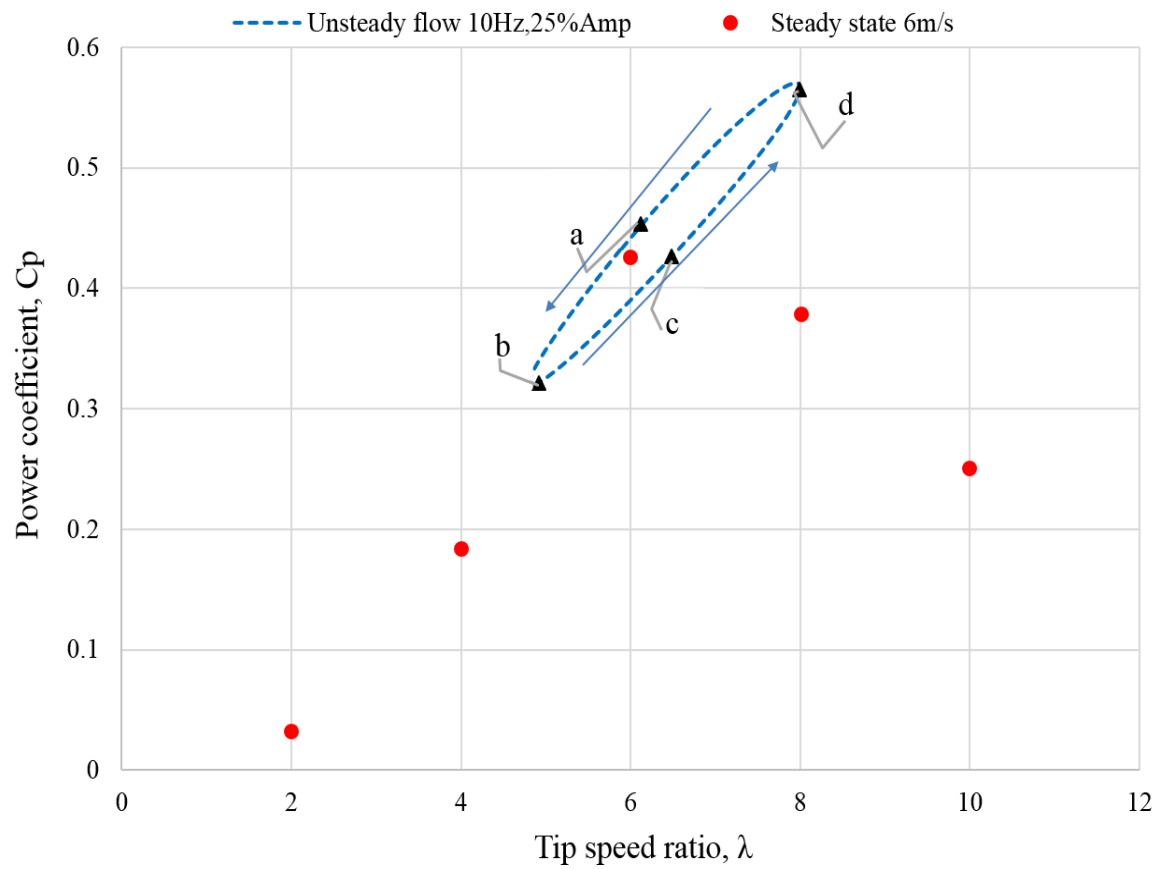
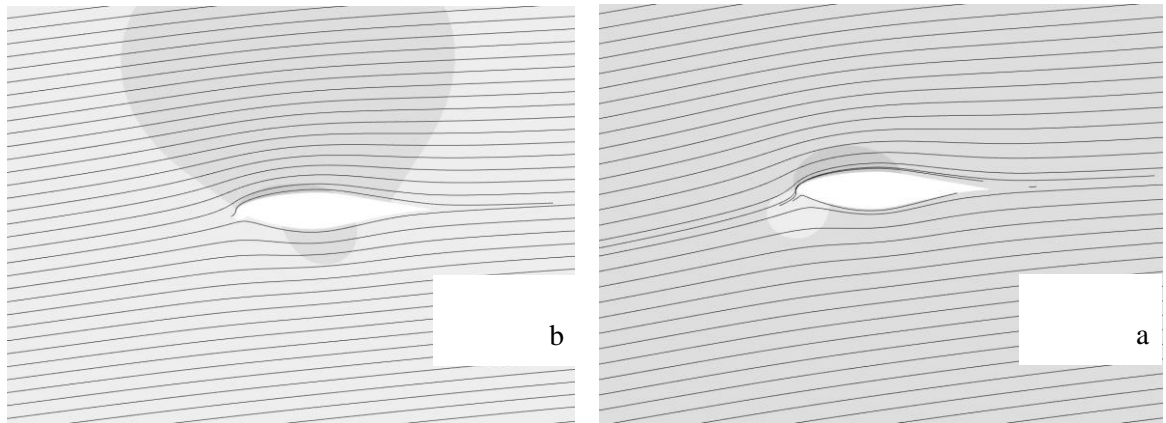
Point	a	b	c	d
Area	0.2001	0.1974	0.2575	0.2450

6.7.4 Power curve at $f=10\text{Hz}$ and 25% amplitude

The results of the investigation of the highest wind speed frequency in this study, which is 10Hz, are shown in Figure 6.21(d), which demonstrates clearly the hysteresis loop at this wind condition, and then explained below in detail.

Comparing the 10Hz wind speed with the last two studied wind speed frequencies, the hysteresis loop seems to behave in a fairly similar way. The peak value of the steady wind speed trend is also surrounded by the elliptic loop. The elliptic loop is rather narrow compared to that given in the two studies above. The lowest performance of the wind turbine C_p is at the lowest point in the loop **b**, and is 0.3195 at $\lambda=4.81$; by contrast, the highest performance is 0.5698 at $\lambda=7.91$ on point **d**. The average $C_{p_{av}}$ value of the unsteady flow loop is approximately 0.43, which is greater than the maximum value of the steady flow trend performance. In comparison to the 0.5Hz, 2Hz and 5Hz wind speed frequencies, this percentage seems high and clearly means the performance increases with increases in the wind speed frequency.

(a)



(b)

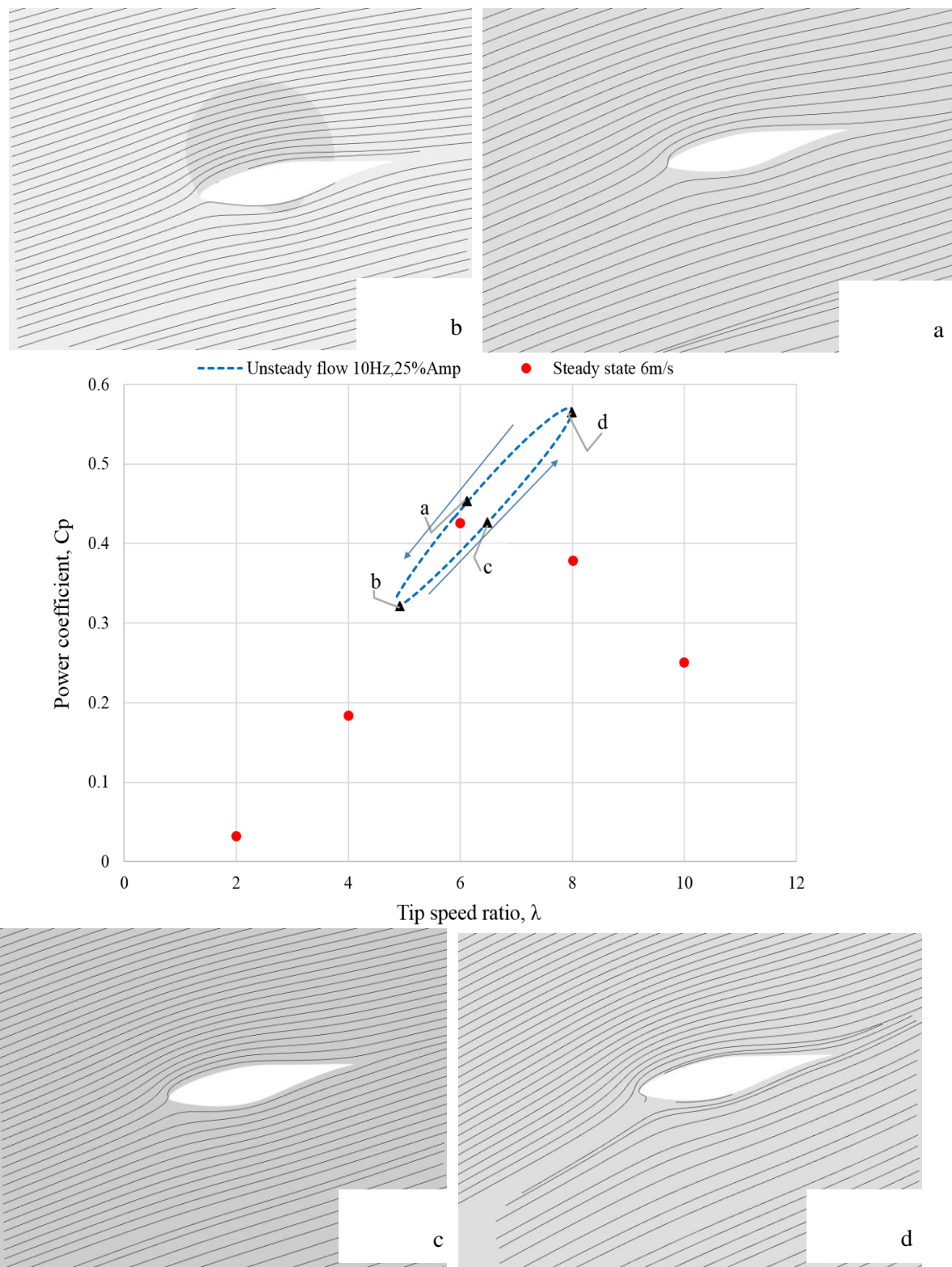


Figure 6.28: The plot and streamline performance curve of the full scale NREL wind turbine at 10Hz and 25% amplitude of unsteady wind speed at $\lambda=6$ (a) at 75% and (b) at 30% of the blade.

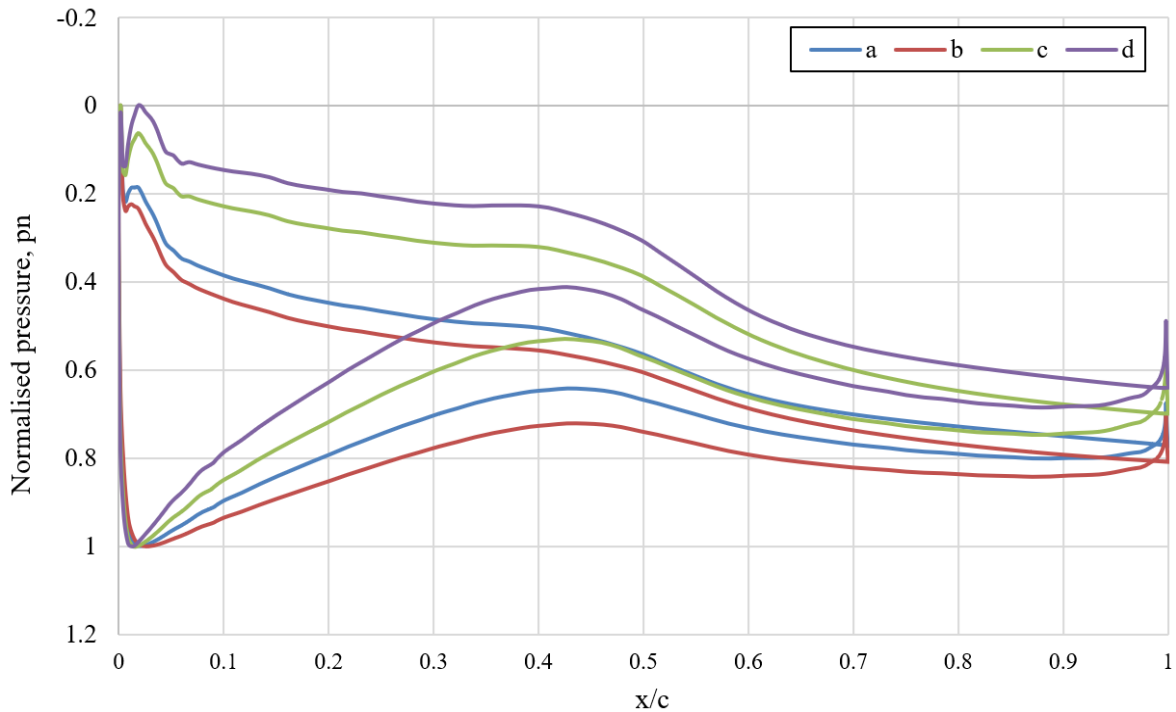


Figure 6.29: The pressure distribution of the hysteresis loop of the full scale NREL wind turbine at 10Hz and 25% amplitude unsteady wind speed at 75% of the blade.

Parts (a) and (b) in Figure 6.28 reveal the flow behaviour at 75% and 30% locations along the blade for all points. It appears clear that the flow around these positions are fully attached to the blade, which means there is no difference in behaviour of wind flow at this frequency compared to those mentioned above.

Similar to the previous case, **a**, **b**, **c** and **d**, the pressure distribution curves at 75% of the blade show a distinct variance at all points, as seen in Figure 6.29. The generated lift force at points **a** and **b** was relatively low. However, the lift to drag ratio at point **c** could be high which led to high performance of the turbine more than that at point **d**, as seen in the table below.

Table 6.11 The area under the pressure curve at each point on the loop ($f=10\text{Hz}$ and $A=25\%$).

Point	a	b	c	d
Area	0.1956	0.2049	0.2589	0.2491

6.8 Summary of findings

The effect of various wind speed frequencies on the performance of the horizontal rotor in at 25% amplitude oscillating wind flow conditions was investigated as described above, and the results are summarised in the table below.

Table 6.12. Performance at 25% amplitudes and various frequencies.

Amplitude (%)	Frequency (Hz)	$C_{p_{av}}$, CFD	C_p , CFD
0	0	-	0.42457
7	0.50	0.4284	-
	1.0	0.4169	-
	2.0	0.4278	-
	5.0	0.4186	-
	10.0	0.4195	-
25	0.50	0.4037	-
	1.0	0.4029	-
	2.0	0.4073	-
	5.0	0.4175	-
	10.0	0.4299	-
45	0.50	0.3782	-
	1.0	0.3521	-
	2.0	0.3810	-
	5.0	0.4015	-
	10.0	0.4458	-

The final conclusion is that the performance of the full wind turbine rotor is to some extent sensitive and responsive to change in the amplitude value at one frequency, as shown in

Table 6.12. However, the findings exhibit that the performance increases is roughly consistent with the increase in frequency of wind speed at the average amplitude 25%. Moreover, it was found that there was an equal or slightly greater increase in performance at the high wind speed frequency (10Hz) when compared to the maximum performance of the steady flow case. This may indicate that the performance of the wind turbine is generally lower than its maximum value in the case of steady state at low amplitudes. Table 6.12 also presents the results for the other investigated wind speed amplitudes, and these appear at first sight to approach those in the table. The lowest amplitude (7%) of the wind machine in general has far high performance than the 25% amplitude illustrated in the table. In contrast, the findings presented in the table for the high amplitude (45%) exhibit an overall decline in comparison to the other amplitudes.

Overall, however, it can be stated that the performance of the horizontal wind machine can be broadly affected by different frequencies with various amplitudes of the unsteady flow wind speed. The essential points to be drawn from these findings are, firstly, the trend of the power coefficients is directly proportional both to the increase in the wind frequencies and increasing in amplitudes. Secondly, the overall power coefficients at these frequencies and 7% amplitude showed a remarkable convergence with the maximum steady wind flow value. Finally, Table 6.12 also divulges further details regarding the highest frequency in the current study, and it shows a visible increase in performance in all assigned amplitudes compared to the other calculated frequencies. This might signify that the rotor would behave differently if it were to face such aspects of wind conditions.

6.9 The effect of changes in wind turbine scale in unsteady flow

As discussed at the end of chapter five, the effect of wind turbine size on performance was tested at steady state wind flow (6 m/s). This study can be complemented by conducting a further investigation into the effect of the unsteady flow on the performance of the scaled-down rotor. The highest instantaneous C_p performance was recorded by the 0.2671 wind turbine at the same tip speed ratio $\lambda=6$ of the full-size machine. Correspondingly, 7, 25 and 45% wind speed amplitude were employed in this investigation, while the base case frequency was increased 17 times to obtain the reduced frequency k value of 0.05. The trend of the unsteady flow with various amplitudes can be observed in Figure 6.30.

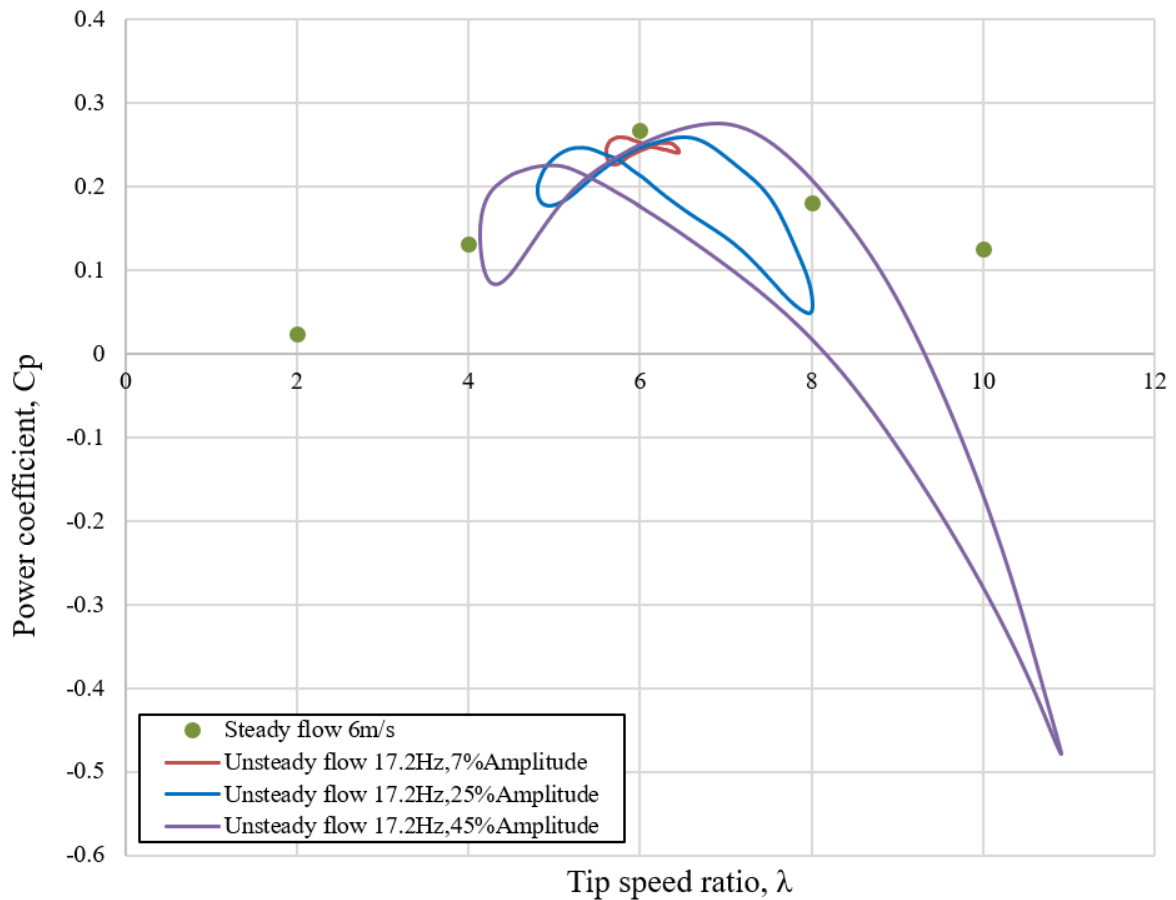


Figure 6.30: Operation of the small NREL rotor at $V_\infty = 6\text{m/s}$ against various wind speed amplitudes.

Oscillations in wind speed were simulated numerically at average wind speed with period of fluctuation using the following form:

$$V(t) = 5.995 + 1.49875 \sin(2\pi t) \quad \text{Equation 6-6}$$

The simulation jobs in ICEBERG required a running time of roughly 144 hours and 4.5 turns of the wind turbine to reach the fully convergence. It was also observed that the convergence initiates at less than 3 seconds from the starting point of the run which is after about 1/3 turn of the wind turbine.

As shown in the figure above, the hysteresis loops in this wind speed condition generally indicate a relative similar trend, especially between the 25% and 45% amplitudes loops. The peak of the steady state trend, moreover, is outside of the surrounding of all loops but they broadly follow this trend. The average performance $C_{p,av}$, which was

produced by the small wind turbine, was 0.2445 and then 0.1826 and 0.548 at the 7, 25 and 45% wind speed amplitude respectively. It is clearly apparent that the small amplitude achieved higher performance than the others, whereas the lowest performance was produced at the high amplitude in this study. These results may seem anticipated and reasonable when the high amplitude loop exceeds the zero line and moves into the negative power zone, possibly generating low average performance. Therefore, further increasing amplitudes of wind speed could lead to a rather more pronounced deterioration in performance. This study now moves on to further and more detailed analysis of the flow behaviour, selecting the 25% amplitude hysteresis loop to gain general insights into the performance of the small size rotor in real wind conditions, as shown Figure 6.31.

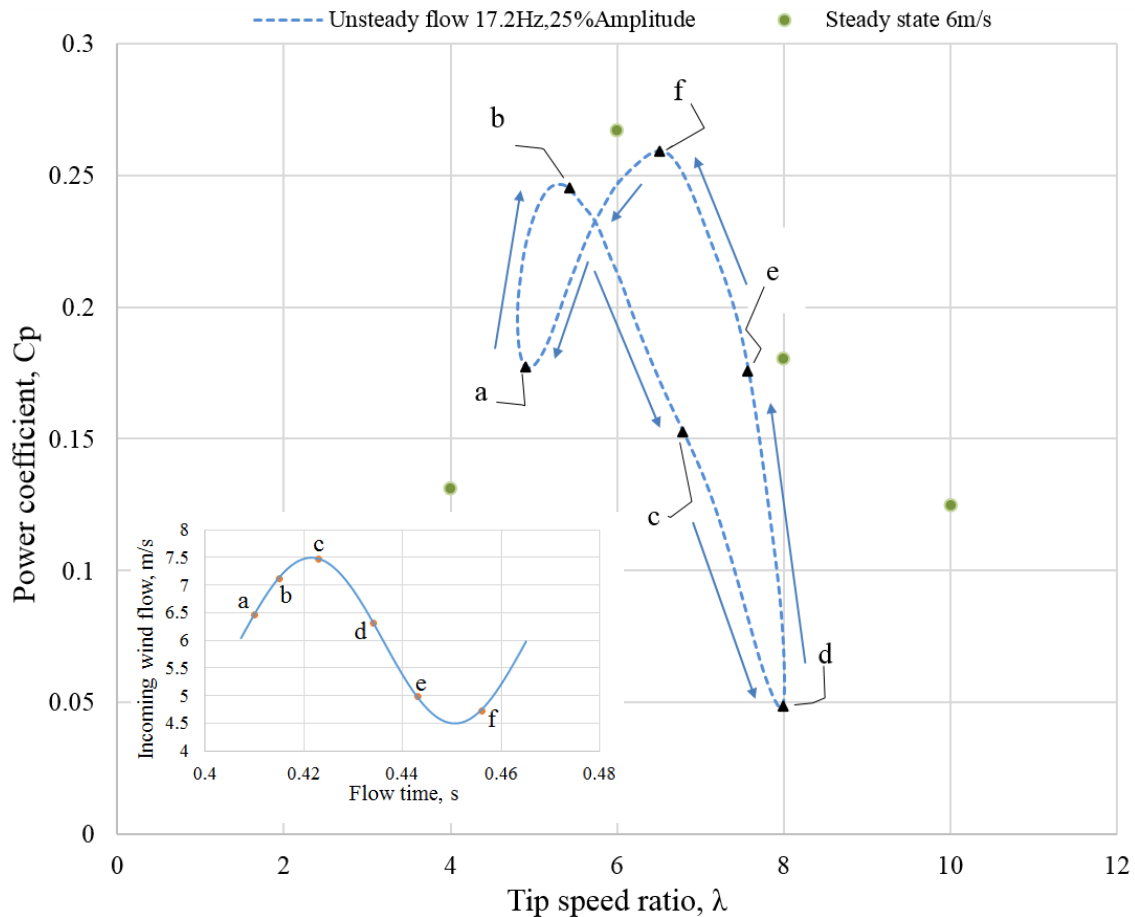
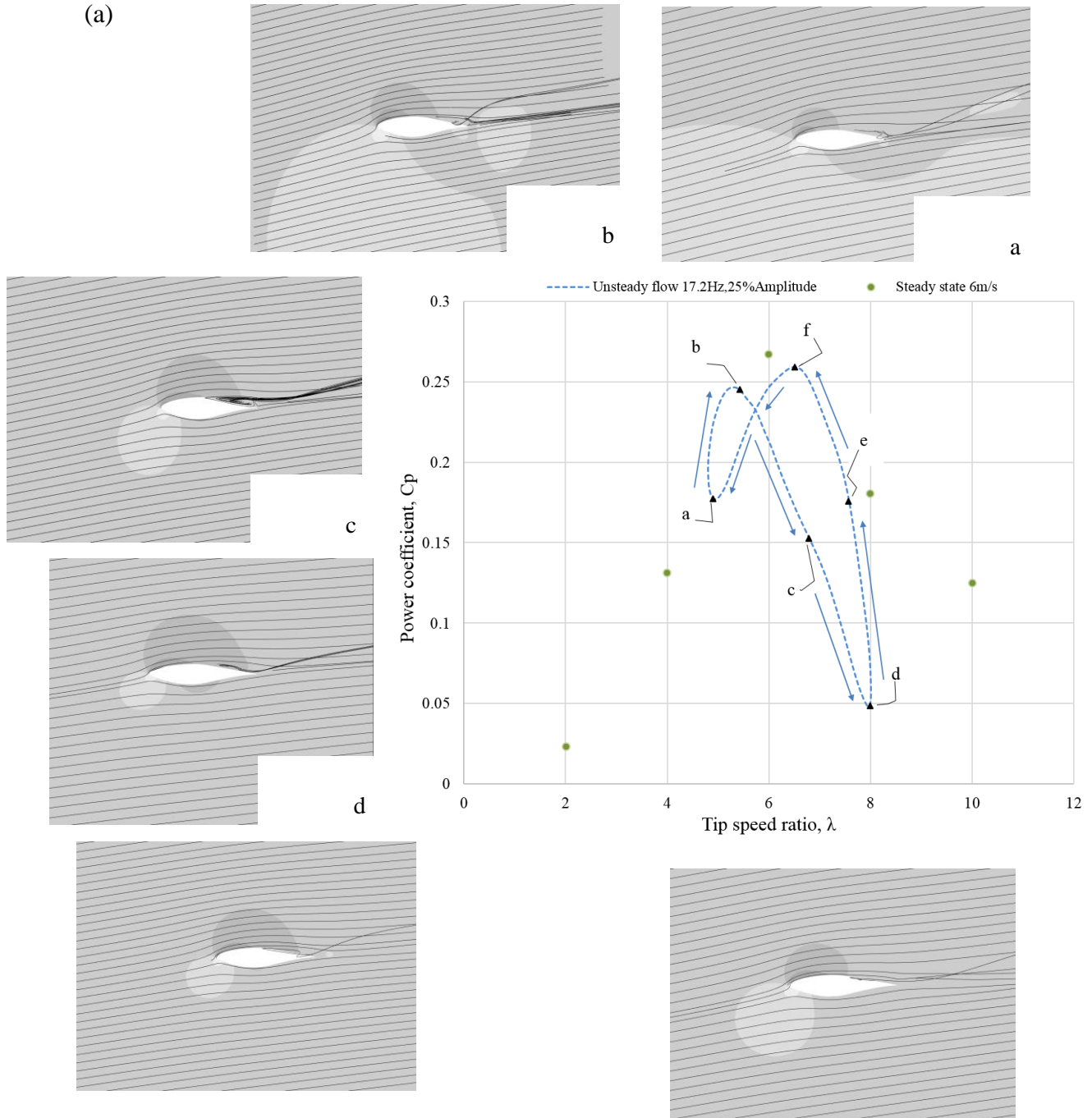


Figure 6.31: Effect of steady and unsteady flow on the performance of the HAWT at 25% amplitude and 17.2Hz wind speed scaled-down NREL.

The same previous analysis which was used with full-size wind turbine was carried out here to investigate the behaviour of the unsteady flow. Six points were placed along the 25% wind speed amplitude hysteresis loop to conduct the investigation. As mentioned above, the average wind cycle performance is $C_{p_{av}}=0.1826$ and the maximum performance is 0.2592 at $\lambda=6.5$, whereas the minimum value is 0.477 at $\lambda=7.96$. Following is the streamlines plot and pressure distribution around the cut plan at the two positions.



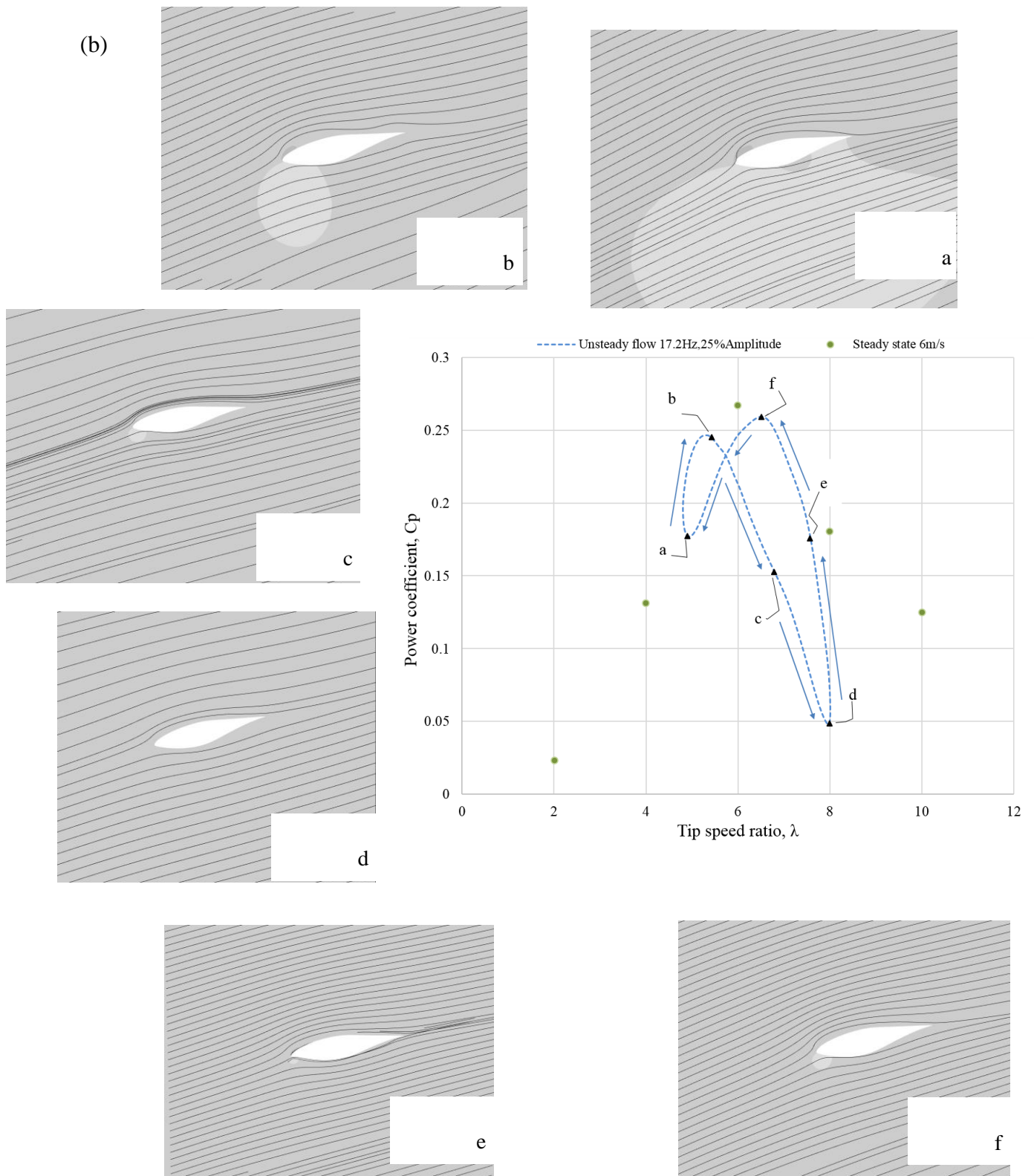


Figure 6.32: The plot and streamline performance curve of the scale-down NREL wind turbine at 17.2Hz and 25% amplitude of unsteady wind speed at $\lambda=6$ (a) at 75% and (b) at 30% of the blade.

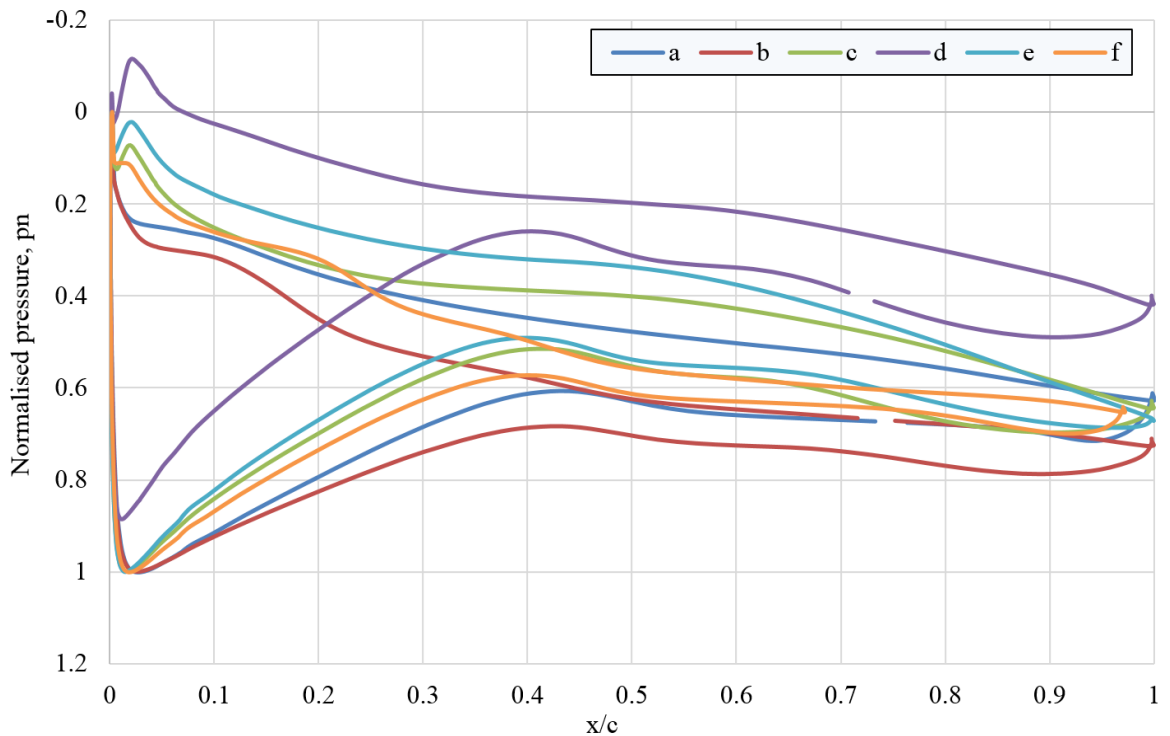


Figure 6.33: The pressure distribution of the hysteresis loop of the scaled-down NREL wind turbine at 17.2Hz and 25% amplitude unsteady wind speed at 75% of the blade.

Figure 6.32, parts (a) and (b), shows the flow behaviour at 75% and 30% of the blade span for the six points on the hysteresis loop. Figure 6.32(a) illustrates that the flow around these positions is still attached to the blade except on the surface next to the trailing edge of the aerofoil, which may mean the angle of attack is relatively high at the high tip speed ratio region and the flow has insufficient momentum to overcome the unfavourable pressure at this area of the blade. In contrast, Figure 6.32(b) illustrates that the flow seems attached to the surface at all points, for the reason mentioned previously.

Figure 6.33 displays that there is no significant difference in the behaviour of the whole pressure curves except that they are beyond ($x/c = 0.7$) which is roughly constant. Table 6.13 shows that the area under the pressure curves for point **f** is lower than other at all points, however, the generated lift may overwhelm the drag force leading to high rate of C_L/C_D value and generates high performance. On the other hand, the drag force for point **d** seems high which is negatively affecting the turbine's performance and that may give an impression of the poor performance during this case.

Table 6.13 The area under the pressure curve at each point on the loop ($f=17.2\text{Hz}$ and $A=25\%$).

Point	a	b	c	d	e	f
Area	0.2853	0.2053	0.2426	0.2434	0.2269	0.2027

The following paragraphs are going to elucidate the effect of two additional tip speed ratios close to the main base case $\lambda=6$ as done for the full-size rotor. The three hysteresis loops are also gathered in one figure, as shown in Figure 6.34.

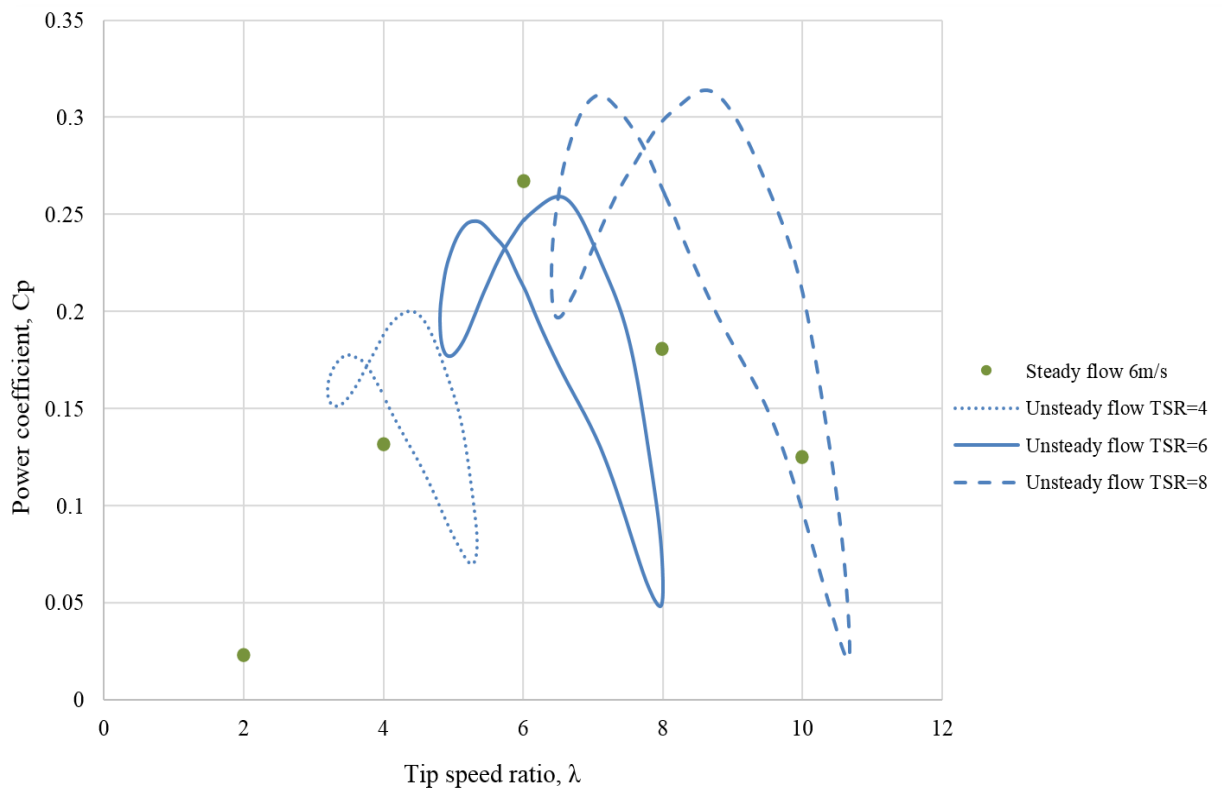


Figure 6.34: The hysteresis curve for the small-size rotor at three unsteady cases at $\lambda=4, 6,$ and 8 and at 25% amplitude 17.2Hz .

Figure 6.34 demonstrates that all hysteresis loops exhibit a similar trend and shape but the loop at $\lambda=8$ seems larger than the others for the same amplitude of 17.2% . They are surrounded the peak steady state values, except at $\lambda=6$ when the range of the hysteresis loop is completely below its steady value.

The main power curve required for the case of the small size rotor is clearly exhibited in Figure 6.35.

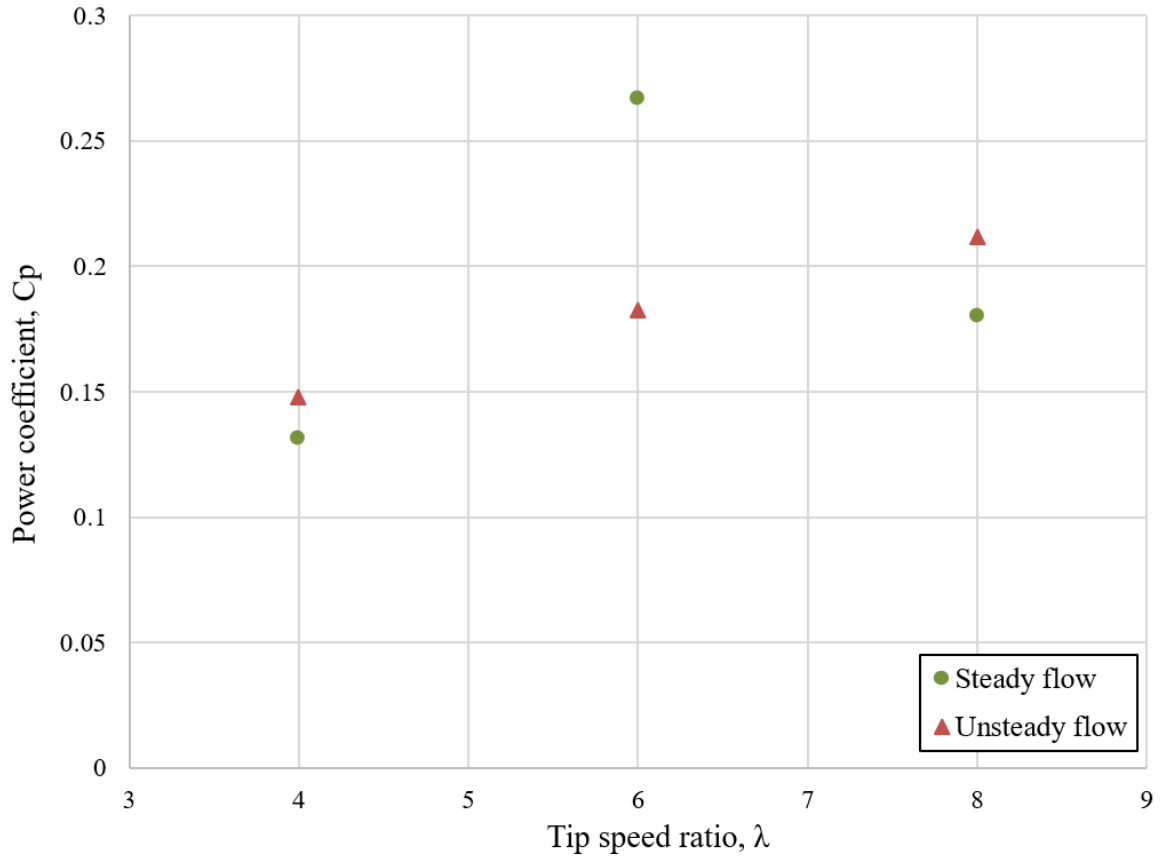


Figure 6.35: Performance of small rotor at three tip speed ratios at 17.2Hz and 25% amplitude.

In Figure 6.35, it can be noticed that the findings of the unsteady flow in all cases is still on the increase as the TSR increases even for the low angle of attack region. This could induce a different impression from that of the full-scale rotor. It also shows that the rotor performed better at the unsteady flow conditions except at $\lambda=6$ which is well below the steady state case. It was found that the unsteady performance is increasing with increasing values of tip speed ratios. This could happen due to an ascending decline in the coefficient of torque (C_m) for one cycle of the velocity with increasing the tip speed ratio, as seen in Table 6.14.

Table 6.14. Coefficient of torque from three different tip speed ratio.

Tip speed ratio, λ	Coefficient of torque (C_m) $\times 10^{-3}$, steady flow case	Coefficient of torque (C_m) $\times 10^{-3}$, unsteady flow case
4	3.8	5.02
6	5.17	4.22
8	2.68	3.73

According to the following performance formula:

$$C_p = C_m \lambda \quad \text{Equation 6-7}$$

Small values of coefficient of torque and hence low torque can cause retardation in the performance. However, the angular velocity of the rotor ($U = \omega R$) increases when the tip speed ratio increases that could cause a considerable variation in the estimated power performance at $\lambda=8$ and so on.

6.10 Summary of this chapter

The performance of the NREL phase VI rotor at various frequencies and amplitudes was investigated then compared to the value of the steady state wind conditions which was $C_p = 0.424$ at $\lambda=6$. The findings generally indicate that the performance of the wind rotor is decreasingly affected by increasing the amplitude of the wind speed. The plots of streamlines exposed the behaviour of the flow around the blades and as expected at high angles of attack (at low tip speed ratios) the flow separates that means increasing drag, decreasing lift and so reducing torque, while at low angles of attack the flow remains attached to the surface of the blades. In addition, the unsteady wind flow at high wind speed frequency was studied for the scaled-down wind turbine. In general, increasing the wind speed amplitudes was found to lead to deterioration in performance.

CHAPTER 7

Conclusions and Recommendations

7.1 Introduction

This chapter draws together the main findings of this thesis and provides suggestions for how future studies can build on this work. It will also identify limitations which have surfaced during the study period.

7.2 Conclusions

The effects of unsteady wind flow on the aerodynamics and performance of a horizontal axis wind turbine was investigated numerically for various amplitudes and frequencies at 6 m/s mean wind speed. The effect of unsteady flows on the performance of the HAWT has received much less research investigation and is still an open-ended research question.

In this thesis, CFD based on the RANS equations to conduct modelling and simulation the performance of the NREL phase VI wind turbine rotor. To further understanding, both steady wind and unsteady wind flow conditions were simulated using the CFD model and then the steady wind was validated against the experimental work by utilising the NREL/ NASA-Ames wind tunnel. Various wind speeds were applied with a constant rotor rotational speed. The ANSYS ICEM CFD was used for meshing to perform the CFD simulation. The marked agreement of the CFD results with the experimental data showed that the model was suitable for the work in this thesis.

Before initiating the jobs in Fluent, the quality of the mesh needed to be checked to ensure the solutions were independent of that mesh. Three mesh sizes were examined, at 4 million, more than 6 million and roughly 9 million grids, and these were tested at wind speeds of 7, 10, 13 and 15 m/s with $k-\omega$ SST turbulence model, which showed much better results and matched the experimental C_p values. A 6 million grids were selected when they achieved the goal and being close to the experimental data except at $\lambda=3.79$ ($V_\infty=10\text{m/s}$). This wind speed was considered as “critical point” when the hard to predict stall started to dominate.

The current 3D CFD wind turbine blades may be considered to be one of the first times that a full turbine simulation has been carried out with unsteady flow. Most of the

previous simulations were conducted for just one blade of the turbine using periodic boundary conditions where the same wind flow conditions were applied for all the blades.

The influence of Reynolds numbers has been tested when full and small size of the NREL phase VI wind turbine model were built and set up in the above mentioned wind tunnel. Generally, the coupling of the full and scaled-down models gave a valuable insight into the HAWT's behaviour and further understanding of its performance and the aerodynamics under fluctuating wind flow conditions.

Overall, the findings of this thesis can be divided into some sections on the basis of the wind flow conditions.

- The performance of the wind turbine at the 6m/s wind speed at various tip speed ratios was studied. The peak performance C_p value, gained from calculations, was 0.4245 at $\lambda=6$. Then, they were validated versus the BEM simulation which was represented by the QBlade tool. The findings revealed that there is a good agreement between the steady wind flow performance trend and all performance values of the steady flow are above that from the QBlade findings except at $\lambda=4$ when the C_p value drops down. The CFD findings, moreover, showed an acceptable tendency with that from a previous study conducted by Tadamas and Zangeneh (2011). However, C_p value at $\lambda=4$ is still far from the reference values as mentioned in chapter five.
- Wind flow around two sections of the blade (30% and 75%) was examined using flow streamlines around the aerofoil section. Flow separation were clearly seen at $\lambda=2$ for both sections of the blade due to high angle of attack. At this low tip speed ratio, all C_p values showed low magnitude when high AOA generated low lift and high drag which caused the lower C_p observed at this ratio. Whereas, at high tip speed ratios, $\lambda=8$, the flow was fully attached to the surface area of the blade and C_p values went down as the AOA decreased which generating slighter lift force.
- The NREL phase VI rotor was scaled-down to investigate the effect of the Reynolds number on the performance of the turbine. The scaled-down CFD performance curve matched the trend of the full-scale rotor curve perfectly. Furthermore, the C_p value at $\lambda=6$ at approximately 60% was identified as the peak performance value.

The flow around the two sections of the blade was also studied and the streamlines showed that the flow starts to separate early close to the trailing edge at 75% span from the root at high TSR. This could happen when the airflow in the boundary layer no longer has ability to withstand the adverse pressure gradient. However, the flow at 30% span is still attached to the surface except at low TSR as the AOA decreased.

In a similar way, the NREL phase VI wind turbine rotor was simulated under unsteady state wind flow. The sinusoidal wind speed form, which was coded in a UDF file, was employed to mimic the varying wind conditions. A sine wave variation of wind velocity was used because it allowed a more simplified approach to the problem. Using real unsteady wind profiles makes the job of understanding the causes of the changes in wind turbine performance unnecessarily complicated.

- The performance of the wind turbine rotor is to some extent sensitive and responsive to change in the amplitude value at one frequency. The CFD findings indicated that the rotor can in total give higher performance at low amplitudes, based on the average $C_{p_{av}}$ taken for all frequencies included in this study compared to the steady wind equivalent condition which was 0.4245 at $\lambda=6$. The average $C_{p_{av}}$ at 7% wind amplitude was 0.4222, at 25% wind amplitude it was 0.4125, while at 45% wind amplitude it was 0.3917.
- The findings exhibit that the performance increase is roughly consistent with the increase in frequency of wind speed at the average amplitude 25%. Moreover, it was found that there was an equal or slightly greater increase in performance at the high wind speed frequency 10Hz especially at 45% which was 0.4458 at $\lambda=6$ amplitude when compared to the maximum performance of the steady flow case. This could lead to the conclusion that low amplitudes and high frequencies are the optimal wind conditions for enabling the wind rotor to achieve higher performance levels.
- Unsteady simulations at $\lambda=4$ and $\lambda=8$ have also been carried out to gain more information about how the unsteady flow will behave at both sides of the peak value ($\lambda=6$) of the wind turbine's power curve. The results revealed that the power

coefficients for both $\lambda=4$ and $\lambda=8$ at 7% amplitude were so closed to their counterparts in the steady state case. At $\lambda=4$, the wind turbine showed better performance at high amplitudes, whereas the performance had lessened at $\lambda=8$.

- The scaled-down wind turbine performance at unsteady state flow was also simulated at three various amplitudes and the high frequency. The outputs from the CFD showed that the small rotor at $\lambda=6$ and 7% amplitude can perform better than the other two selected amplitudes. In addition, the results revealed that working in high wind speed amplitude (45%) caused a massive performance deterioration. The base case ($\lambda=6$ and 25% amplitude) was utilised to accomplish a comparative study with two different tip speed ratios 4 and 8. The performance of the turbine at $\lambda=4$ and $\lambda=8$ was above its counterpart at steady state case. Nevertheless, there was a high divergence between the steady and unsteady power value at $\lambda=6$.

7.3 Limitation and recommendations for future work

The current work has lead to a better understanding of the horizontal wind turbine's performance and aerodynamics in unsteady wind flow conditions. However, the unsteady wind assumed in the current unsteady could not match wind conditions in the natural environment. Although the CFD simulations conducted in this thesis presented valuable data compared to other previous works, the unsteady wind flow behaviour needs to be tested experimentally in order to assess it more deeply. Nevertheless, the CFD work can allow testing of various horizontal wind turbine scales which could reduce costly, time-consuming and labour-intensive experiments. Following are some suggestions from the author for interesting topics for future research:

- Although CFD simulations can be useful for testing multi-scale models of wind turbines, true experimental testing, despite being considered an arduous endeavour, is still favourable. Wind tunnels could be used for tests for various rotors scales which could highly mimic actual reality. Consequently, a large wind tunnel, like the NREL/ NASA-Ames, could be used again to retest the NREL phase VI rotor by supplying a sinusoidal air flow shape over the blade to support the validity of numerical solutions. This could be performed by using a shutter mechanism to

manipulate and control the incoming wind flow, as used by Danao et al. (2013). Furthermore, studies could examine the effects of unsteady winds of various amplitudes and frequencies on the performance of three blades models with different aerofoils and chord thicknesses provide more data about the most commonly used rotor.

- Because of its complexity, it has not been possible to use CFD work to study the effect of changing the pitch angle by different degrees on the performance of the rotor in the testing of unsteady wind conditions. Therefore, pitch angle simply refers to the flexibility of the blade to rotate around its own axis. This difficulty derives from the fact that no axial rotating cylinder was built over the blades to allow them to manoeuvre freely. That effect could be studied with various wind speed frequencies but a rotating cylinder would need primarily to be set up. In fact, many attempts were made but they failed because of overlapping of the meshes which occurs as a result of ignoring the presence of available neighbouring blocking.
- This thesis has studied two sizes (6 and 100%) of the NREL rotor, so the door is still open to investigate numerically the influence of the unsteady wind flow on the performance and aerodynamics of other sizes rotors. This could be linked to studying the effect of various Reynolds numbers on the wind turbine rotor in these wind conditions. The CFD simulation can provide more predictions on the behaviour of wind machines which would save time and cost when conducting lab work to examine various wind turbine scales. Additionally, although the effect of the hub and tower was ignored to minimise the size of the mesh and thereby to save simulating time, it would still be worthwhile to study further unsteady conditions in relation to the full geometry of the horizontal wind turbine.
- In this research, the sine wave wind speeds, as it was added earlier, were utilised because they are relatively simple and therefore allow researchers to more easily understand what is going on. Using real wind conditions or something more complicated than a sine wave could substantially mimic the real environment. For instance, it can be conducted using mathematical methods on virtually any fluctuating signal that varies with respect to time. It could be based on a waveform of a series of sinusoidal terms, each with a unique amplitude and frequency.

However, it is important to match the capacity of computers when the ability of personal computers could not be sufficient to evaluate large quantities of numbers with these methods.

References

- Aldo Vieira Da Rosa, 7 May 2009. *Fundamentals of renewable energy process*. 2nd Ed ed. Amsterdam ; London: Academic Press;
- Ali Z. and Tucker P.G., 2014. Multiblock Structured Mesh Generation for Turbomachinery Flows. In: Sarrate J., Staten M. (eds) *Proceedings of the 22nd International Meshing Roundtable*. Springer, Cham, pp. 165-182.
- Anderson, J., 2008. *Introduction to Flight*. 6th edition ed. USA: Mc Graw Hill International Edition.
- ANSYS FLUENT Guid, 2016. *ANSYS FLUENT 16.1 UDF Manual*. [Online].
- Bai C. J., Hsiao F. B., Li, M. H., Huang G. Y., and Chen Y. J., 2013. Design of 10 kW horizontal-axis wind turbine (HAWT) blade and aerodynamic investigation using numerical simulation. *ScienceDirect. In Procedia Engineering*, Volume 67, p. 279 – 287.
- Bakker.org, 2015. *Retriver from <http://www.bakker.org/dartmouth06/engs150/11-bl.pdf>*. [Online].
- Belamadi R., Mdouki R. , Ilinca A. and Djemili A., 2015. CFD study of a horizontal axis wind turbine NREL Phase II. *Revue des Energies Renouvelables*, Volume 18 N°4, pp. 683-700.
- Beri. H. and Yao Y., 2011. Numerical Simulation of Unsteady Flow to Show Self-Starting Of Vertical Axis Wind Turbine Using Fluent. *Journal Of Applied Sciences*, Volume 11(6), pp. 962-970.
- Bolin K., Bluhm G., Eriksson G., and Nilsson M.E. , 2011. Infrasound and low frequency noise from wind turbines: exposure and health effects. *Environmental Research Letters, IOP PUBLISHING*, Volume 6(3), p. 035103.
- Brawley.D., 2008. Performance of a Horizontal Axis Wind Turbine. *M.Sc dissertation, University Of Sheffield*.
- Bryce S. Richardsa, Gavin L. Parka, and Andrea I. Schäferb, 2010. Renewable Energy Powered Membrane Technology: The effect of wind speed fluctuations on the performance of a wind-powered membrane system for brackish water desalination. *Journal of Membrane Science*.
- Burton, T., Sharpe, D., Jenkins. N. and Bossanyi,E., 2001. *Wind energy handbook*. West Sussex, England: John Wiley & Sons, Ltd.
- Byron Inouye, 2018. <https://manoa.hawaii.edu>. [Online]
Available at: <https://manoa.hawaii.edu/exploringourfluidearth/physical/atmospheric-effects/wind-formation>
[Accessed 01 08 2018].

-
-
- Carcangiu C. E., Sørensen J. N., Cambuli F., and, 2007. *CFD-RANS analysis of the rotational effects on the boundary layer of wind turbine blades*. 75(1), Journal of Physics: Conference Series 75 (2007) 012031. IOP Publishing.
- Chaviaropoulos, P. K., Nikolaou, I. G., Aggelis, K. A., Soerensen, N. N., Johansen, J., Hansen, M. O. L., Gaunaa, Mac, Hambaas, T., Von Geyr, H., Hirsch, Ch., Shun, K., Voutsinas, S. G., Tzabiras, G., Perivolaris, Y., and Dyrmoose, S. Z., 2003. Viscous and aeroelastic effects on wind turbine blades. The VISCEL project. Part I: 3D Navier-Stokes rotor simulations. *Wind Energy*, Volume 6(4), p. 365–385.
- Chen, H., 2016. Numerical Study of Trailing Edge Flow Control for Horizontal Axis Wind Turbines. *Ph.D. Thesis, University of Sheffield*.
- Cho T. and Kim C., 2014. Wind tunnel test for the NREL phase VI rotor with 2m diameter. *Renewable Energy*, Volume 65, p. pp.265–274.
- Cho T., Kim C. and Lee D., 2010. Acoustic measurement for 12% scaled model of NREL Phase VI wind turbine by using beam forming. *Current Applied Physics*, Volume 10(2), p. S320–S325.
- Danao L., Eboibi O. and Howell R., 2013. An experimental investigation into the influence of unsteady wind on the performance of a vertical axis wind turbine. *Applied Energy*, Volume 107, p. 403–411.
- Danao L., Eboibi O. and Howell R., 2014. A numerical investigation into the influence of unsteady wind on the performance and aerodynamics of a vertical axis wind turbine. *Applied Energy*, Volume 116, p. 111–124.
- Danao L., Edwards J., Eboibi O., and Howell R., 2013. A numerical investigation into the effects of fluctuating wind on the performance of a small scale vertical axis wind turbine. *Engineering Letters*, Volume 21(3), p. 149–157.
- Danao LA, Howell R., 2012. Effects on the performance of vertical axis wind turbines with unsteady wind inflow: a numerical study. In: *50th AIAA aerospace sciences meeting including the new horizons forum and aerospace exposition, Nashville, Tennessee*.
- Danmei Hu Ouyang Hua and Zhaohui Du, May 2006. A study on stall-delay for horizontal axis wind turbine. *Renewable Energy*, 31(6), p. 821–836.
- Delbaere M., 2015. Aerodynamics and Aerostructures. Performance prediction of Vertical Axis Wind Turbine. *M.Sc dissertation, University Of Sheffield*.
- Devinant P., Laverne T. and Hureau J., 2002. Experimental study of wind-turbine airfoil aerodynamics in high turbulence. *Journal of Wind Engineering and Industrial Aerodynamics*, Volume 90(6), p. pp.689–707.
- Du Gang and Wu Chun Kau, 2015. Unsteady Flow Numerical Simulation of Vertical Axis Wind Turbine. *Procedia Engineering*, 99(Elsevier Ltd), p. 734 – 740.
- Eboibi, O., 2013. The Influence of Blade Chord on the Aerodynamics and Performance of Vertical Axis Wind Turbines. *Ph.D Thesis, University of Sheffield*.

Edwards, J., Danao, L. and Howell, R. , 2012. Novel Experimental Power Curve Determination and Computational Methods for the Performance Analysis of Vertical Axis Wind Turbines. *The Solar Energy Division of ASME*, 134(Spyros Voutsinas), pp. 031008-2-11.

Ekaterinaris, J.A. and Menter, F.R, 1994. Computation of oscillating airfoil flows with one- and two-equation turbulence models. *AIAA Journal*, Volume 32(12), p. pp.2359–2365.

Eleni C. Douvi, Dionissios P. Margaritis, 4-7 July, 2012. *AERODYNAMIC CHARACTERISTICS OF S809 vs. NACA 0012 AIRFOIL FOR WIND TURBINE APPLICATIONS*. Athens, Greece, 5 th International Conference from Scientific Computing to Computational Engineering, 5th IC-SCCE.

Erich, H., 2006. *Wind Turbines: Fundamentals, Technologies, application and Economies*. 2nd Ed. ed. Germany: Production GmbH.

Gigueere P. and Selig M.S., 1999. *Design of a Tapered and Twisted Blade for the NREL Combined Experiment Rotor Design of a Tapered and Twisted Blade for the NREL Combined Experiment Rotor*, U.S.A: The National Renewable Energy Laboratory (NREL).

Gilooly S. and Taylor-Power G. , 2016. *Physical Modeling of the Atmospheric Boundary Layer in the University of New Hampshire's flow physics facility*, Durham ,USA: University of New Hampshire Scholars Repository.

Guide, 2012. *Fluent 12.0 User's*.

Han, C., 2011. *Aerodynamics Analysis of Small Horizontal Axis Wind Turbine Blades by Using 2D and 3D CFD Modelling Engineering and Physical Sciences at the University of Central Lancashire*.

Hand, M.M. Simms, L.J. Fingersh, D.W. Jager, J.R. Cotrell, S. Schreck, and S.M. Larwood, 2001. *Unsteady Aerodynamics Experiment Phase VI: Wind Tunnel Test Configurations and Available Data Campaigns*, 1617 Cole Boulevard Golden, Colorado 80401-3393: National Renewable Energy Laboratory (NREL).

Hansen, M. O.L., 2008. *Aerodynamics of Wind Turbines*. 2nd Edition ed. the UK and USA: Earthscan .

Hau, E., 2006. *Wind Turbines: Fundamentals, technologies, application, economics*. 2nd edition ed. Berlin : Springer.

Hsu M., Akkerman I. and Bazilevs Y., 2014. Finite element simulation of wind turbine aerodynamics: validation study using NREL Phase VI experiment. *Wind Energy*, Volume 17, p. 461–481.

[http://airfoiltools.com/airfoil/details airfoil=s809-nr](http://airfoiltools.com/airfoil/details%20airfoil=s809-nr), 2012. <http://wind.nrel.gov/airfoils/>, USA: National Renewable energy Laboratory.

Huyer, S.A., Simms, D. & Robinson, M.C., 1996. Unsteady aerodynamics associated with a horizontal-axis wind turbine. *AIAA Journal*, 34(7), p. 1410–1419.

- International Renewable Energy Agency, 2018. Retrieved from <http://www.irena.org>.
- Johnson, D. & G. K., 2012. Numerical modelling of an S809 airfoil under dynamic stall, erosion and high reduced frequencies. *Applied Energy*, Volume 93, p. 45–52.
- Jones, W. a. L. B., 1972. The prediction of Laminarization With a two-equation model of turbulence. *International journal heat and mass transfer* , Volume 15, p. pp.301–314.
- Jonkman, J. M., 2003. Modeling of the UAE wind turbine for refinement of FAST_AD. *Master's thesis, Colorado State University*.
- Khan, Md. Zulfequar Ahmad, 2017. Causes and Consequences of Greenhouse Effect & Its Catastrophic Problems for Earth.. *International Journal of Sustainability Management and Information Technologies.*, Volume Vol. 3, No. 4., pp. pp. 34-39..
- Kyoungsoo Lee , Shrabanti Roy , Ziaul Huque , Raghava Kommalapati and SangEul Han, 2017. Effect on Torque and Thrust of the Pointed Tip Shape.. www.mdpi.com/journal/energies, doi:10.3390/en10010079(Frede Blaabjerg), pp. 10, 79.
- Ladson, C. L., 1988. Effects of Independent Variation of Mach and Reynolds Numbers on the Low-Speed Aerodynamic Characteristics of the NACA 0012 Airfoil Section. *NASA TM 4074*.
- Leishman, J., 2002. Challenges in modelling the unsteady aerodynamics of wind turbines. *Wind Energy*, Volume 5(2-3), p. 85–132.
- Leishmann, J. G., 2006. *Principle of Helicopter Aerodynamics*. s.l.:Cambridge University Press.
- Lindenburg C., 2003. *Investigation into rotor blade aerodynamics*, The Netherlands Society for Energy and the Environmen: Analysis of the stationary measurements.ECN-C-03-025.
- Mahmuddin, F., 2017. Rotor Blade Performance Analysis with Blade Element Momentum Theory. *Energy Procedia*, Volume 105, p. pp.1123–1129.
- Manwell, J. F. R., 2009. *Wind Energy Explained: theory, design, and application*. 2nd Ed. ed. UK: John Wiley and sons.
- Marten D., Wendler J., Wendler G., Nayeri C.N., and Paschereit C.O., 2013. Qblade: an Open Source Tool for Design and Simulation of Horizontal and Vertical Axis Wind Turbines. *International Journal of Emerging Technology and Advanced Engineering*, Volume 3, p. 264–269.
- McIntosh, S., Babinsky, H., and Bertenyi, T., 2007. Unsteady power output of vertical axis wind turbines operating within a fluctuating free-stream. *In: Forty-sixth AIAA Aerospace Sciences Meeting and Exhibit, Reno, Nevada*, pp. 1-13.
- Menter, F., 1994. Two-equation eddy-viscosity turbulence models for engineering applications. *AIAA Journal*, Volume 32(8), p. pp.1598–1605.

- Milne, I., Day, A., Sharma, R., & Flay, R. , 2013. Blade loads on tidal turbines in planar oscillatory flow. *Ocean Engineering*, 60(Elsevier Ltd), pp. 163-174.
- Mo, J.O. and Lee, Y.H., 2012. CFD Investigation on the aerodynamic characteristics of a small-sized wind turbine of NREL PHASE VI operating with a stall-regulated method. *Journal of Mechanical Science and Technology*, Volume 26(1), p. 81–92.
- Moir, I. and Seabridge, A., 2008. *Introduction to Aircraft Aeroelasticity and Loads*. 1 st ed. Southern Gate, Chichester, England: John Wiley and Sons, Ltd.
- Moukalled F., Mangani L. and Darwish M., 2016. *The Finite Volume Method in Computational Fluid Dynamics*. 1st ed. Switzerland: Springer International Publishing, ISBN 978-3-319-16874-6 (eBook).
- Pablo M. Carrica, Yuwei Li, Kwang-Jun Paik and Tao Xing, 2012. Dynamic overset CFD simulations of wind turbine aerodynamics. *Renewable Energy*, Volume 37(1), p. 285–298.
- Park, Y. Cho, T. and Chang, B., 2007. Numerical Simulation of Wind Turbine Scale Effects by using CFD. *In 45th AIAA Aerospace Sciences Meeting and Exhibit. Reno, Nevada.*
- Robinson M.C., Hand M.M., Simms D.A, and Schreck S.J., 1999. *Horizontal axis wind turbine aerodynamics: Three dimensional, unsteady and separated flow influences*. San Francisco, California, USA, Presented at the 3rd ASME/JSME Joint Fluids Engineering Conference.
- Rubinstein, Robert, 2004. *Tuncer Cebeci: Analysis of Turbulent Flows*. ISSN: 0935-4964 ; E-ISSN: 1432-2250 ; DOI: 10.1007/s00162-005-0168-2 ed. USA: Elsevier.
- Ryi J., Choi J.S., Lee Se., and Lee So. , 2014. A full-scale prediction method for wind turbine rotor noise by using wind tunnel test data. *Renewable Energy*, Volume 65, p. 257–264.
- Scheurich, F. and Brown, R.E., 2013. Modelling the aerodynamics of vertical-axis wind turbines in unsteady wind conditions. *WIND ENERGY*, 16(Published online 24 February 2012 in Wiley Online Library (wileyonlinelibrary.com). DOI: 10.1002/we.532), p. 91–107.
- Sobotta, D., 2015. *The Aerodynamics and Performance of Small Scale Wind Turbine Starting. A Dissertation Submitted for the Degree of Doctor of Philosophy, University of Sheffield.*
- Somers, D., 1997. Design and Experimental Results for the S809 Airfoil. p. 103.
- Song Y. and Perot J., 2015. CFD Simulation of the NREL Phase VI Rotor. *Wind energy*, 39(available in <http://arxiv.org/abs/1404.6183>), p. 299–310.
- Sørensen, N.N., Michelsen, J.A. and Schreck, S., 2002. Navier-Stokes predictions of the NREL phase VI rotor in the NASA Ames 80 ft × 120 ft wind tunnel. *Wind Energy*, Volume 5(2–3), p. 151–169.

- Steinkohl, C., Davis, R.A. & Klüppelberg, C., 2013. Extreme value analysis of multivariate high-frequency wind speed data. *Journal of Statistical Theory and Practice*, Volume 7(1), p. 73–94.
- Tadamasa, A. and Zangeneh, M., 2011. Numerical prediction of wind turbine noise. *Renewable Energy*, Volume 36(7), p. 1902–1912.
- Tominaga, Y., 2015. Flow around a high-rise building using steady and unsteady RANS CFD: Effect of large-scale fluctuations on the velocity statistics. *Journal of Wind Engineering and Industrial Aerodynamics*, Volume 142, p. 93–103.
- Toshimitsu K., Kikugawa H., Sato K., and Sato T., 2012. Experimental Investigation of Performance of the Wind Turbine with the Flanged-Diffuser Shroud in Sinusoidally Oscillating and Fluctuating Velocity Flows. *Open Journal of Fluid Dynamics, Japan*, 02(04)(Published Online December 2012 (<http://www.SciRP.org/journal/ojfd>)), p. 215–221.
- Velamati R.K., Sudhamshu A.R., Pandey M. CH., Sunil N., Satish N.S., and Mugundhan V., , 2016. Numerical study of effect of pitch angle on performance characteristics of a HAWT. *Engineering Science and Technology, an International Journal*, Volume 19(1), p. 632–641.
- Versteeg, H. and Malalasekera, W., 2007. *Introduction to Computational Fluid Dynamics An : The Finite Volume Method*. 2nd Edition ed. Essex, England: Pearson Education Limited.
- Wekesa, D. W., Wang, C., Wei, Y., Kamau, J. N. & Louis Angelo M. Danao, 2015. A Numerical analysis of unsteady inflow wind for site specific vertical axis wind turbine : A case study. *Renewable Energy*, Volume 86, p. 648–661.
- Wekesa, D.W., Wang, C., Wei, Y., and Louis Angelo M. Danao, 2014. Influence of operating conditions on unsteady wind performance of vertical axis wind turbines operating within a fluctuating free-stream: A numerical study. *Journal of Wind Engineering and Industrial Aerodynamics*, Volume 135, p. 76–89.
- Wilcox, D., 1998. *Turbulence Modelling for CFD*. 5354 Palm Drive, La Cañada, California: DCW Industries, Inc..
- Wind energy, 2018. Retrieved from <http://windenergyfoundation.org/about-wind-energy/history/>. [Online].
- Xie Y.H., Moshfeghi M. and Song Y.J., 2012. Effects of near-wall grid spacing on SST-K- ω model using NREL Phase VI horizontal axis wind turbine. *Journal of Wind Engineering and Industrial Aerodynamics*, Volume 107–108, p. 94–105.
- Yelmule M. and Anjuri VSJ, 2013. CFD predictions of NREL Phase VI Rotor Experiments in NASA/AMES Wind tunnel. *INTERNATIONAL JOURNAL of RENEWABLE ENERGY RESEARCH*, 3(2), pp. 261-270.

YutakaHara, KoichiHara, and TsutomuHayashi, 2012. Moment of InertiaDependence ofVertical AxisWind Turbines in PulsatingWinds. *International Journal of RotatingMachinery*, Article ID 910940(Hindawi Publishing Corporation), p. 12.

Zhou, Z. C Li, J B Nie, and Y Chen, 2013. *Effect of oscillation frequency on wind turbine airfoil dynamic stall*. 52(5), p.52012., IOP Conference Series: Materials Science and Engineering.

Zhu J. , Cai X. and Gu R., 2016. Aerodynamic and structural integrated optimization design of horizontal-axis wind turbine blades. *Energies* 2016, 9, 66; doi:10.3390/en9020066 , 9(www.mdpi.com/journal/energies), pp. 1-18.

Zifeng Yang, Hirofumi Igarashi, Mathew Martin and Hui Hu, 2008. An experimental investigation on aerodynamic hysteresis of a low-Reynolds number airfoil. *AIAA Paper 2008-0315, 46th Aerospace Sciences Meeting and Exhibit*, p. 1–11.

Appendices

Table Appendix A.1

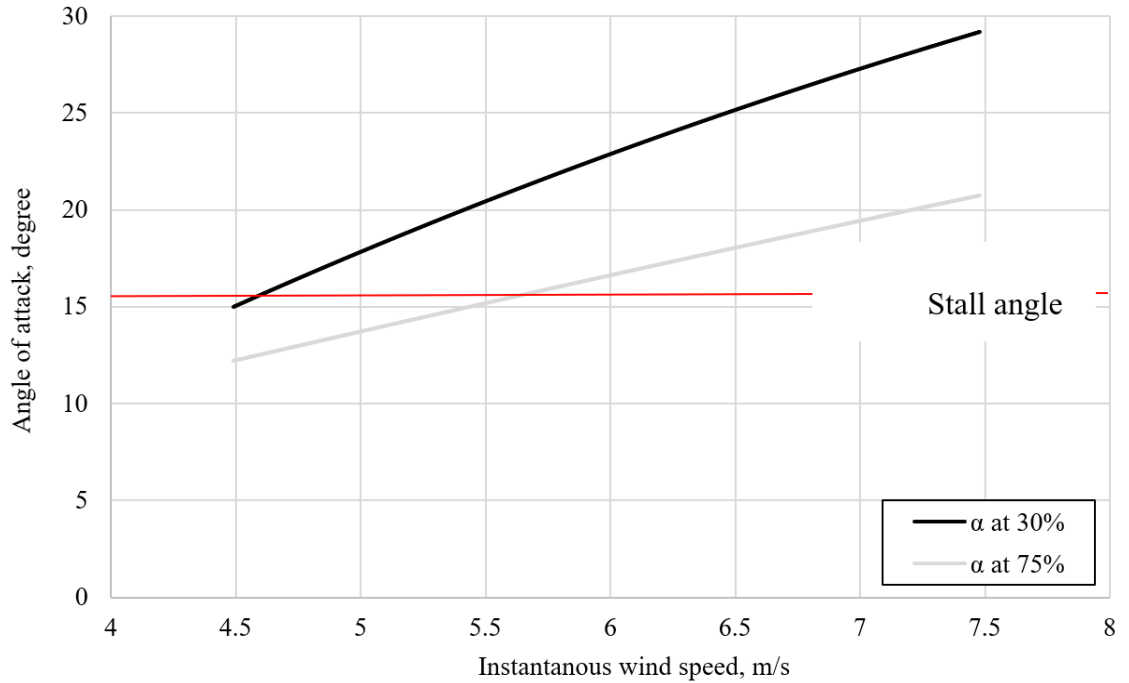
The NREL geometry specifications: full size (left) Hand et al. (2001) and 6% size (right).

	Radius	Chord	Twist	Thickness
1	1.2573	0.737	21.8559	0.154402
2	1.3427	0.728	18.074	0.152516
3	1.5087	0.711	14.292	0.148955
4	1.6495	0.697	11.909	0.146022
5	1.9513	0.666	7.979	0.139527
6	2.258	0.636	5.308	0.133242
7	2.3435	0.627	4.715	0.131357
8	2.5598	0.605	3.425	0.126748
9	2.8665	0.574	2.083	0.120253
10	3.1733	0.543	1.15	0.113759
11	3.1834	0.542	1.115	0.113549
12	3.475	0.512	0.494	0.107264
13	3.7818	0.482	-0.381	0.100979
14	4.0232	0.457	-0.475	0.095742
15	4.0835	0.451	-0.92	0.094485
16	4.3903	0.42	-1.352	0.08799
17	4.6971	0.389	-1.469	0.081496
18	4.7775	0.381	-1.775	0.07982
19	4.9988	0.358	-2.191	0.075001
20	5.029	0.355	-2.5	0.074373

	Radius	Chord	Twist	Thickness
1	0.083485	0.04893	21.8559	0.010252
2	0.089155	0.04833	18.074	0.010127
3	0.100178	0.04721	14.292	0.009891
4	0.109527	0.04628	11.909	0.009696
5	0.129566	0.04422	7.979	0.009265
6	0.149931	0.04220	5.308	0.008847
7	0.155608	0.04163	4.715	0.008722
8	0.169971	0.04017	3.425	0.008416
9	0.190336	0.03811	2.083	0.007985
10	0.210707	0.03605	1.15	0.007554
11	0.211378	0.03399	1.115	0.00754
12	0.23074	0.03200	0.494	0.007122
13	0.251112	0.03034	-0.381	0.006705
14	0.26714	0.02994	-0.475	0.006357
15	0.271144	0.02788	-0.92	0.006274
16	0.291516	0.02583	-1.352	0.005843
17	0.311887	0.02583	-1.469	0.005411
18	0.317226	0.02529	-1.775	0.0053
19	0.33192	0.02377	-2.191	0.00498
20	0.333926	0.02357	-2.5	0.004938

Appendix B

(a) Shown here are the angles of attack for the 30% and the 75% span of the blade for $\lambda=4$:



(b) Shown here are the angles of attack for the 30% and the 75% span of the blade for $\lambda=8$:

